ADAS-EU R(12)PU05

ADAS-EU
ADAS for fusion in Europe

Grant: 224607

Alessandra Giunta, Hugh Summers, Paul Bryans and Martin O'Mullane

# Generalised-collisional-modelling for light- and medium-weight elements

November 12, 2012

Workpackages :
Category : DRAFT

# Generalised-collisional-modelling for light- and medium-weight elements

Alessandra Giunta, Hugh Summers, Paul Bryans and Martin O'Mullane

Department of Physics, University of Strathclyde, Glasgow, UK

**Abstract:** *This work focusses on developments in atomic modelling for light and medium-weight elements in fusion and astrophysical plasmas. These atomic models are suited to and may be used for the interpretation of visible/UV/EUV spectral measurements from fusion plasmas and space-borne instruments such as SoHO/SUMER, SoHO/CDS and Hinode/EIS. Theoretical developments include extension of generalised collisional-radiative (GCR) techniques to heavier and more highly ionised systems where fine structure and other relativistic effects are present. The theory of non-Maxwellian modelling is also assembled in the GCR picture. Attention is given to the generation of fundamental atomic structure and electron impact collisional data to support these developments. New codes are brought into operation in the distorted wave approximation which allow large-scale mass production of data and its full integration with ADAS and its GCR modelling. The new fundamental and derived data increase the ADAS databases by more than a factor four.*

# Contents

# Preface

This article is the one of a series of technical notes which are being prepared as useful extracts during the longer term construction of the next edition of the ADAS user manual. As such it reflects a change in style, planned for the new manual. It will be more book-like, examining and explaining in detail the physics basis behind the commitment to certain approaches in ADAS and how these work out in practice. The new manual will remain technically detailed with extended appendices. However, it is hoped this will be ameliorated by much more emphasis on worked examples. That is to say the actual manoeuvres, adopted by experienced ADAS users in getting the atomic modelling into application scenarios will be mapped, rather as an expert system. It has become clear that, for some, ADAS operates in a somewhat rarefied atmosphere in which too much is assumed. It is this which I wish to improve upon.

Collisional-radiative modelling is at the centre of the ADAS approach and its link to both obsservational spectroscopy and to plasma models.

In the present development is also appropriate to give full attention to dynamical plasmas in which the free electron distribution is not relaxed to Maxwellian form. Such plasmas can occur in both laboratory and astrophysical plasmas when strong electron energy losses or efficient localised (in energy) input mechanisms are present. A number of such possibilities are examined and families of non-Maxwellians are introduced for their description. It is shown how rate coefficients for electron impact reactions must be reworked without the assumption of detailed balance. Care is taken that the fundamental cross-section data required is adequate for this reworking. Excited population modelling based on collisional-radiative theory is modified to cope with non-Maxellian rates. With these modifications, it is demonstrated that much applied modelling and data use can be continued transparently for the non-Maxwellian situation.

**H P Summers**
12 November 2012

# Chapter 1

# Introduction

The solar atmosphere offers a good opportunity to investigate high temperature plasma in general and is one of the few astrophysical plasma sources which can be studied in the highest detail. Most knowledge of outer stellar atmospheres is based on the understanding of plasmas processes in the solar upper atmosphere, especially in the transition region and corona. One of the major unresolved issue in solar physics concerns the morphology and the energy balance through these upper layers of the atmosphere. The solar corona shows a temperature two hundred times or more than the underlying layers, which cannot be explained without the occurrence of non-thermal energy flows between the photosphere/chromosphere and corona. As the interface between the photosphere and corona, the solar transition region plays a key role in mediating the transport and dissipation of such non-thermal energy, which powers the heating of both chromosphere and corona. However, even the nature of the transition region continues to be a subject of significant debate. This problem has been discussed for many years, leading to proposals for different heating mechanisms, ranging recently from the effect of cool loops (1) to field-aligned (2) and cross-field (3) processes. A relevant topic in this context is the study of the intensity and features of emission from neutral and ionised elements in the upper regions of the solar atmosphere. One of the most abundant, but at the same time peculiar, elements in the Sun is helium. The intensity and spatial distribution of helium lines forming in the solar outer atmosphere show a puzzling relative intensity behaviour. These lines are at relatively short wavelengths in the extreme-ultraviolet and soft X-ray regimes and their formation mechanism is still an open issue. Continued work in this thesis on the helium problem may help to solve the bigger problem of coronal heating. Spectral surveys make clear that the extreme-ultraviolet band, namely 100-1,000 Å, offers a rich source of detailed information about physical conditions in the outer layers of the Sun's atmosphere. However, due to the Earth's atmospheric absorption, spectral observations in this band require observations from space. Advances in the understanding of the solar upper atmosphere are closely linked to the ability to study the Sun in the ultraviolet and extreme-ultraviolet with rocket and satellite experiments, such as SERTS (89 and 97), SoHO, TRACE and the new generation of space-borne instruments like STEREO, Solar-B and SDO. The strong resonance lines of ions that should be abundant at transition region and coronal temperatures are located in the ultraviolet and extreme-ultraviolet portions of the spectrum but, unfortunately, in most cases the spatial scale of structures of interest is still well below the resolution of current instruments. Therefore it is also important to reconstruct observed emission in terms of theories for the plasma distribution in temperature and density and for its dynamic state. This is an objective of this thesis. In principle, the analysis of plasmas using observations of their spectra is one of the most precise and informative routes of study. Such study is suitable not only in an astrophysical context, but also for laboratory fusion plasmas. Even if the basic mechanisms of energy input are different in laboratory and space, their spectral emission shows clear similarities, which allow the development of common modelling approaches. Atomic physics provides the link to interpret such spectra in terms of the properties of the source from which they are emitted, whether they originate in an experiment on Earth, such as a laser or tokamak device, or in an astronomical object, ranging from the Sun and stars to planetary nebulae and interstellar medium. The close connection between astrophysical and laboratory plasmas leads to the possibility of making measurements in a more accessible and controlled Earth-based situation to confirm or support results when applying them to astronomy. The present work will strongly exploit these interdisciplinary links.

The intensity of a spectral line depends on the excited atomic population of the emitting atoms. In general, a plasma contains atoms, ions, free electrons and radiation and may be permeated by a magnetic field. Interaction between these species collectively through collisional and radiative processes establishes the population structure of the emitting

atom or ion. As a consequence, diagnostic models developed as tools to analyse line intensity are based on atomic population modelling. In turn, the excited population structure of the ions reflects key parameters of the plasma, especially electron density, electron temperature, species density and magnetic field. The radiation produced in the interior of a plasma can interact with the plasma as it travels out of the plasma boundary. When the probability that the produced photons escape from the volume of the plasma without being re-absorbed is very small, the plasma is said to be optically thin. The difficulty occurs when "radiation trapping" is not negligible. In this case, the plasma becomes optically thick and it entails that in optically thick conditions a plasma can release radiation from a thin layer near the surface only. This alters the emergent flux, because of the loss of photons out of the line of sight due to scattering and absorption. Moreover, the opacity affects the population distribution within the absorbing atoms, leading to modification to the population structure caused by photo-absorptions. Further, the optical thickness may cause partial frequency redistribution, which can modify the emission profiles and again influence the populations and emergent intensities. Fortunately for a high temperature ($T_e \geq 2 \times 10^4$ K) and low density ($N_e \leq 10^{13}$ cm$^{-3}$) plasma of modest extent (in the astrophysical sense), which describes the solar corona, many assumptions can be applied, making the model relatively simple. Optical thickness effects can be generally neglected and the dominant atomic processes that have to be considered are those caused by electron collisions and spontaneous radiative decays both bound and free. Moving towards the inner layers of the atmosphere, that is upper chromosphere/lower transition region, plasmas of greater density are observed. This has the consequence that optical thickness effects become significant for strong resonance lines of abundant elements such as helium. In the case of a moderate optical depth, such as for Si II and C II lines observed by SoHO/SUMER, the escape factor method can be used ((4); (5)). This approach treats the equation of radiative transfer in a linear approximation and so is easily integrated into other models, to diagnose for example plasma densities in fusion divertors as well as optical depths in solar atmosphere.

Another important problem is related to the fact that the plasma in the solar transition region and corona is dynamic and inhomogeneous. Observations by SoHO/CDS and SoHO/SUMER spectrometers show evidence that there is considerable dynamic activity and spectral variability not only during explosive events but even in apparently inactive solar regions (6). In such conditions, the evolution of the plasma may have time-scales of the same order of or shorter than the ionisation/recombination time-scales, which may invalidate the assumption of ionisation equilibrium. Collisional-radiative theory (7) addresses the issue of time constants of atomic level populations. In that model the ground population of ionisation stages are the dominant slowly relaxing populations. This is an oversimplification for complex atoms and ions, since low lying metastable states, which cannot decay radiatively to the ground, can have populations comparable to the ground. Separation of metastables and their placing on an equal footing with the ground states is the correct procedure for dealing with this dynamic ionisation. This is called generalised collisional-radiative (GCR) theory. Ionisation and recombination time-scales depend on electron density which also influences the relative population of metastable states. Finite plasma density also affects highly excited non-metastable populations by collisional ionisation and redistribution. Such high populations matter in establishing effective ionisation and recombination (especially dielectronic recombination) rate coefficients since substantial recombination can occur through such high states. Dynamic ionisation, metastables and finite density work together in describing transient ionisation and indeed equilibrium ionisation states

These considerations impel us towards generalised collisional-radiative theory ((8), (9) and references therein). A step forward to the solution of the solar astrophysical issues is, in fact, the application of such theory for the collective behaviour of ions together with advanced calculations for relevant cross-sections. An extensive atomic database has been prepared and assembled within the ADAS (Atomic Data and Analysis Structure) project (http://adas.phys.strath.ac.uk) which is continously updated with the most recent results on the relevant physical processes. Important advancements have been achieved on the dielectronic recombination ((10) and references therein). Calculations for iso-electronic sequences up to Mg-like have been already worked out and dielectronic data have been assembled within the GCR framework. The fineness of such data is sufficient for prediction of the dielectronic contribution to individual spectral line emissivities, allowing a precise and accurate spectral analysis. This contribution is of extreme importance for modelling ions of elements in dynamic finite-density plasmas, such as happens in transient astrophysical plasmas (e.g. solar flares) and in the divertors and high transport regions of magnetic fusion devices. Using the ADAS database, GCR theory for light elements (11) has been successfully applied to ions of interest for fusion plasma research. However, in the last few years calculations for numerous ions of astrophysical interest have been implemented more extensively ((12), (13) and references therein), leading to the possibility of more sophisticated modelling of ions in the astrophysical environment, such as the solar outer atmosphere. Recently, interest in the behaviour of heavy species in a plasma has been growing too, mainly due to the new thermonuclear reactor, ITER (International Thermonuclear Experimental Reactor), which will be constructed in Caderache (France). For ITER key parts of the inner wall of the device will be tungsten. Also, new space-borne instruments, such as EIS onboard Solar-B, allow more accurate

observations, compared to previous missions, of strong spectral lines which arise from ions of elements heavier than argon, including calcium and iron.

The urgent requirement to cope with species such as tungsten in the fusion domain has motivated strong efforts to systematise and organise efficient methods for handling the atomic physics, population structure and ionisation states of arbitrarily heavy species. These methods have included automatic procedures for setting up relevant atomic structure for the various complex ions based on configurations and electron promotional rules. Then, from this basis, reaction data for establishing populations, emissivities and ionisation states are created automatically to provide the derived data for plasma modelling.The complexity has necessitated careful consideration of appropriate levels of precision (often called resolution in this context) to make calculations computationally manageable (14). It turns out that some of these methods are helpful for lighter species, for astrophysics and for the developments of this thesis. This aspect will be returned to later (chapter 5).

This thesis will attempt to give a complete and accurate approach to the study and interpretation of the complex problem of helium behaviour in the solar upper atmosphere, concentrating both on the observational and atomic points of view. In chapter 2 an outline of the solar upper atmosphere and the instruments involved will be presented. Also a review of the helium problem will be provided, to emphasize that, although it has been analysed for many years (indeed from 1939) and, although numerous proposals of enhancement mechanisms have been suggested, the issues are still open. Chapter 3 gives a detailed overview of the new simultaneous observations carried out for this work, together with essential information on instrumental characteristics and data calibration. The atomic physics required for the present analysis will be discussed in chapter 4, where a description of the basic theory and a detailed review and update of the atomic data needed for the present purposes will be provided. Observations and atomic data will be discussed in chapter 5, where the estimate of enhancement factors and a comparison with the literature will be presented. Finally, chapter 6 summarises the main conclusions and outlines the future direction of this work.

# Chapter 2

# Background

## 2.1 The solar upper atmosphere

Viewed as a star, the Sun has an effective surface temperature of about 5,800 K. Because the radiation from a blackbody at that temperature peaks at a wavelength of around 5,000 Å, the visible emission from the Sun is dominated by a strong continuum. This emission comes essentially from the lowest, densest level of the solar atmosphere, the *photosphere*. In the ultraviolet range at 1,000 Å the continuum emission is reduced by a factor of approximately $10^5$. This allows observation of emission lines on the solar disc in the ultraviolet with intensities comparable to those seen at visible wavelengths in the corona at eclipses. The advantage of ultraviolet emission is that it offers the opportunity to investigate the complexity of the outer layers of the solar atmosphere from the upper chromosphere to the corona.

A schematic view of the layers of the Sun and its atmosphere is displayed in fig. 2.1. In addition, this figure shows the behaviour of temperature and density along the solar upper atmosphere as will be described below in this section.

The *chromosphere* is a narrow layer, about 2,000 km thick, which takes its name from its reddish appearance during total eclipses. Such red aspect is due to the fact that in the visible part of the spectrum much of chromospheric radiation is emitted by hydrogen atoms at a single red wavelength, called H$\alpha$ (the first line of the Balmer series) at 6,563 Å. The temperature rises from 4,000 K up to about $2 \times 10^4$ K, while the plasma density drops to roughly $10^{11}$ cm$^{-3}$, a million times less than that of the photosphere. The brightness of the chromosphere's hydrogen line confirms the large abundance of this element in the solar atmosphere. The second most abundant element in the Sun is helium. This element was discovered, for the first time, during a solar eclipse in 1868 as an intense yellow emission line at a wavelength of 5,876 Å. H$\alpha$ and calcium H (3,968 Å) and K (3,932 Å) lines reveal a complex dynamic and non-uniform configuration, with an extremely complicated pattern of very small structures, many of them in the form of filaments. Looking at solar limb, the chromosphere appears as an ensemble of numerous fine jet-like features known as spicules. On the disc, the chromosphere seems organised into an overall cellular pattern called the supergranule (or chromospheric) network, which is related to convective cells in the photosphere below. The average diameter of a supergranule cell is typically $3 \times 10^4$ km. The magnetic field is swept from supergranular cell interiors into the cell boundaries, where the chromosphere appears brightest. Such chromospheric network is shown by images of the Sun in He II 304 Å (Fig. 2.2), which corresponds to a temperature of around $8 \times 10^4$ K.

Between the upper chromosphere and the corona there is a region 200 km thick, called the *transition region* (TR). Although it is a very thin layer, the transition region shows unusual characteristics. While the photosphere, chromosphere and corona have a gradual temperature and density gradient, the transition region appears as a discontinuity, where the temperature jumps from $2.5 \times 10^4$ K to $10^6$ K in only a few hundred kilometres and the density decreases from $10^{11}$ to $10^8$ cm$^{-3}$. Also, as the temperature rises the atmosphere changes from predominately neutral to highly ionised. The spectrum is in fact dominated by the hydrogen Lyman series of lines and the neutral helium lines generated in the optically thick regime in the upper chromosphere-lower transition region. By contrast, most of emission lines of the less abundant heavier ions are believed to be produced in the optically thin layer in the upper transition region. It is generally guessed that the transition region is the consequence of two different heating regimes operating in the chromosphere and in the corona, which may indeed derive from different heating mechanisms or be simply

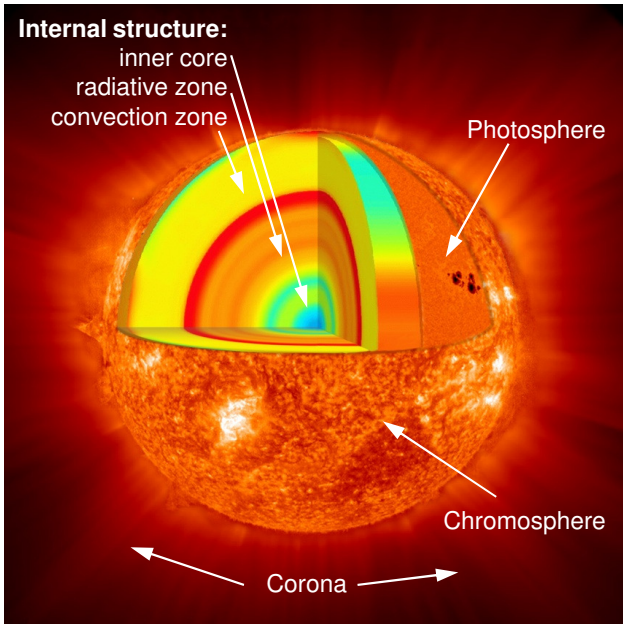


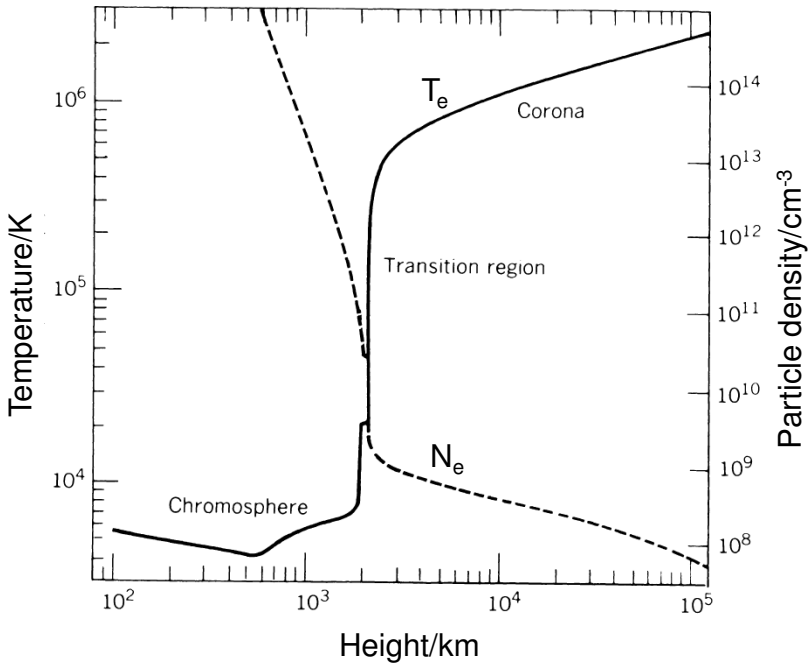


Figure 2.1: The upper image shows schematically the structure of the Sun, from the core to the upper atmosphere. The lower plot illustrates the behaviour of the electron temperature and electron density as a function of the solar radius, assuming that at the photosphere $r = 1R_{\odot}$.

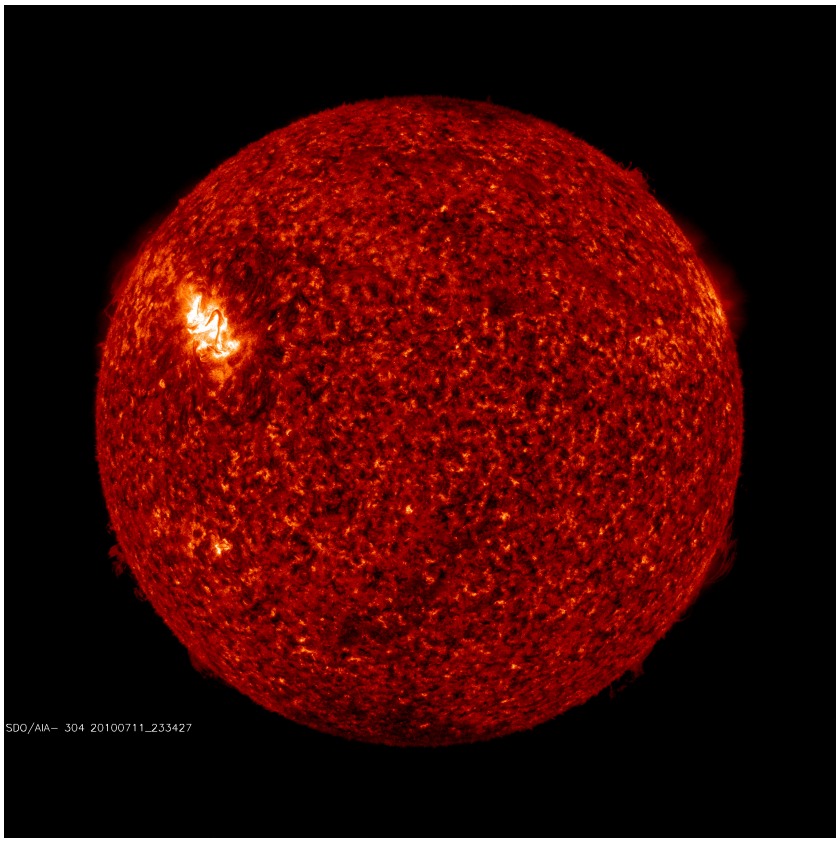


Figure 2.2: Image of the solar disk in He II 304 Å, taken on $11^{th}$ July 2010 by the Atmospheric Imaging Assembly (AIA) on SDO (Solar Dynamics Observatory), revealing the chromospheric network ($\sim 80,000K$). The brighter area on the disk is an active region which is situated above sunspots.

due to different dissipation regimes of the same basic heating process. The large temperature gradient is expected to be the principal factor in the transport of energy in the transition region, whilst the mechanical heating should play a secondary role. However, the problem is not simple because extreme conditions could be found in which a high non-uniformity of the plasma may produce significant departure from local thermodynamic equilibrium conditions.

The *corona*, above the transition region and the chromosphere, is much more extended and diffuse than the colder temperature regions. The emission from the visible spectrum of corona is so faint that it can be observed only during the solar eclipses or with the help of coronagraphs. Nevertheless the solar corona appears much brighter, compared to the photosphere, in X-ray and extreme ultraviolet bands. The coronal emission arises from highly ionised elements, which imply a temperature of the order of $10^6 - 10^7$ K. Then the temperature drops gradually outwards to a value of $10^5$ K at 1 AU[1] in the heliosphere and continues to decrease into the interplanetary space. The physical understanding of the high coronal temperature is still a fundamental problem in astrophysics, because it seems to violate the second thermodynamic law, given the much cooler photospheric boundary, characterised by the temperature of around 5,800 K and even as low as 4,500 K in sunspots. The particle density in the corona ranges from $10^6$ cm$^{-3}$ in the upper corona, at a height of one solar radius, to $10^9$ cm$^{-3}$ in the quiet regions, but can increase up to $10^{13}$ cm$^{-3}$ in flares. The structure of solar corona is highly inhomogeneous. The optically thin emission in soft-X rays and extreme ultraviolet shows features marked by different dimensions and physical conditions. The basic coronal structure is a magnetic loop, overdense arcade structure, filled with heated plasma, of opposite magnetic polarity. The loops can be quite small or very long and extend across a significant fraction of the solar radius. However, loop-like structures do not occur uniformly throughout the corona. Some regions, known as coronal holes, are dominated by open magnetic field lines, being the primary source of the high speed solar wind streams. The coronal holes appear much darker than the quiet Sun, because they are empty of plasma most of the time, due to the efficient transport mechanism that drives heated plasma from the corona into the solar wind. In the regions above the sunspots, the chromosphere and the transition region are very bright in ultraviolet and X-ray ranges, mainly because of a greater electron density. These regions, called active regions, are marked by a complex and strong magnetic field and appear often as complicated sets of loops at different temperatures, as shown in Fig. 2.3. It is in the active regions that most solar flares occur. A flare process is associated with a rapid energy release in the solar corona, probably triggered by an instability in the magnetic configuration and characterised by acceleration of non-thermal particles and heating of coronal/chromospheric plasma (e.g. Fig. 2.4).

There are many other active solar phenomena, such as streamers, soft X-ray jets and coronal mass ejections. However, this work is focused essentially on the study of quiet Sun regions, observed during the solar minimum in 2009, and to the analysis of characteristic extreme ultraviolet lines emitted by these regions.

## 2.2 Spectrometric and related instrumentation for the solar atmosphere

The atmosphere of the Earth filters out emission from the Sun and stars in many wavelengths, except for two windows at optical and radio wavelengths. The major progress in solar upper atmosphere physics involves a number of space missions, allowing observations which avoid the atmosphere absorption. These space missions provide unprecedented information over the entire wavelength spectrum, covering gamma-rays, hard X-rays, soft X-rays, X-ray ultraviolet (XUV), extreme ultraviolet (EUV) and ultraviolet (UV). This thesis is principally involved with three important instruments onboard two spacecrafts:

(a) Solar Ultraviolet Measurements of Emitted Radiation, SUMER, onboard the Solar and Heliospheric Observatory, SoHO;

(b) Coronal Diagnostic Spectrometer, CDS, again onboard SoHO;

(c) Extreme-ultraviolet Imaging Spectrometer, EIS, onboard Hinode (also called Solar-B).

These spectrometers are designed to analyse the solar upper atmosphere and to investigate the heating mechanisms and the active regions using the UV and EUV spectral ranges.

The ESA/NASA jointly-built spacecraft SoHO was launched on $2^{nd}$ December 1995 and it is still operational. Two of its goals, concerned with the solar atmosphere, are the understanding of the coronal heating and the study of

[1] 1 AU=149,590,000 km, approximately the mean Earth-Sun distance.

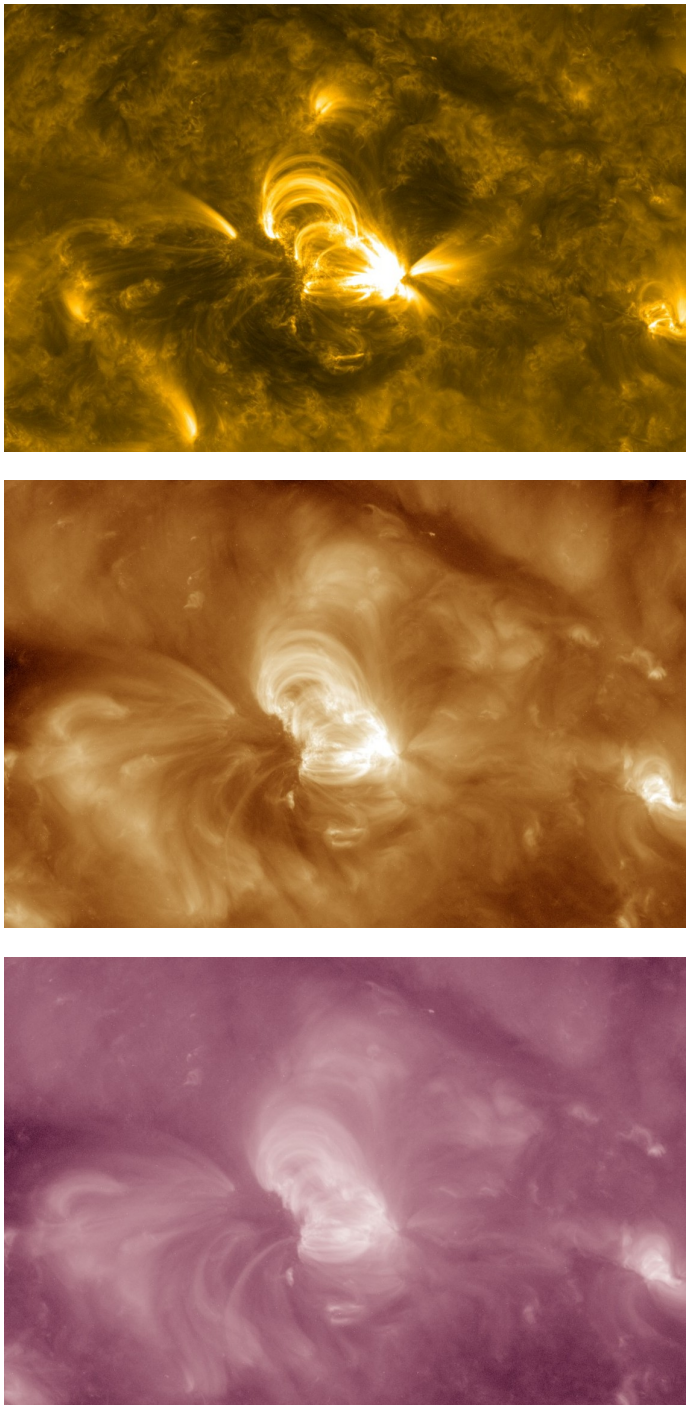

Figure 2.3: Images of large magnetic loops obtained by AIA onboard SDO on $5^{th}$ July 2010. They illustrate the behaviour of the loop structure at different wavelengths and so in different temperature regimes. Starting from the top: the first image shows the complex set of loops in Fe IX 171 Å (quiet corona/upper transition region at ~ 630,000 K); the second image shows the same loop structure in Fe XII, XXIV 193 Å (corona and hot flare plasma at ~ $1,300,000$ and 20,000,000 K respectively); finally, the third image shows such an active region in Fe XVI 211 Å (active region corona at ~ $2,000,000$ K).

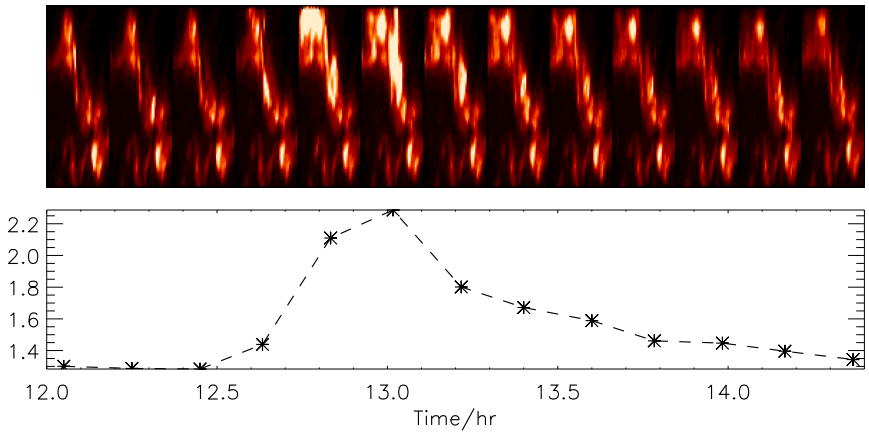


Figure 2.4: Sequence of images which illustrates the evolution of an active region (NOAA AR 10759) as observed by SoHO/CDS on $13^{th}$ May 2005 before and after a C1.5 flare which occurred at 12:45 UT. The lower plot shows the intensity-time curve for He I 584 Å emission line. The intensity is in photons $s^{-1}$ $cm^{-2}$ $sr^{-1}$, scaled by a factor $10^{14}$. The time is in hours starting from 00:00 UT on $13^{th}$ May 2005. The increase of the averaged intensity at around 13:00 UT is the evidence of the flare.

the solar wind. These objectives underpin a detailed analysis of the solar atmosphere: the determination of plasma characteristics (temperature, density, abundance) with appropriate spatial, temporal, spectral resolution ranges in order to study its structure and evolution. The SUMER and CDS instruments are designed to assist this task through the detection of spectral emission lines in the extreme ultraviolet wavelength range 600–1600 Å and 150–800 Å, including lines from ions formed in the temperature range $10^4 - \sim 10^6$ K. The SUMER spectrograph (15) is based on two parabolic mirrors. The first one projects the light from the Sun to the spectrometer entrance slit, while the second one collimates the beam that leaves the slit. Then this beam is deflected by a plane mirror onto a spherical concave grating. Two detectors (detector A and B) collect the images of the spectrometer entrance slit. Only one detector can be operated at a time, covering a wavelength range 780–1610 Å if the detector A is used or 660–1500 Å if the detector B is chosen instead. CDS (16) is a double spectrometer, having the advantages of the wide wavelength of a grazing incidence device and the stigmatic imaging performance of a normal incidence instrument. A grazing incidence telescope feeds simultaneously a normal incidence spectrometer (NIS) and a grazing incidence spectrometer (GIS) which share a common slit. In the grazing incidence spectrometer, radiation is dispersed onto four detectors, GIS1, GIS2, GIS3 and GIS4, which cover respectively the wavelength ranges 151–221 Å, 256–341 Å, 393–492 Å and 659–785 Å, while, in the normal incidence spectrometer, the two NIS gratings disperse two different wavelength bands, 310–381 Å (NIS1) and 513–633 Å (NIS2). For their general characteristic and performance (wavelength range covered, spatial, temporal and spectral resolution), as shown in Table 4.1, SUMER and CDS represent the first thorough examination of the EUV Sun, significantly improving on past EUV space borne instrumentation (EUV OSO VII, Skylab, CHASE and SERTS).

Hinode (Solar-B), a Japan Aerospace Exploration Agency Solar mission with USA and UK collaboration, was launched on $22^{nd}$ September 2006 UT. The aim of the Hinode mission is to determine the mechanisms responsible for heating the corona in active regions and in the quiet Sun, to establish the mechanisms that cause transient phenomena (flares, coronal mass ejections etc.) and to investigate processes for energy transfer from the photosphere to the corona. The EIS (17) contribution to these goals involves the measurement of line intensities, Doppler velocities, line widths for the Sun's atmosphere in the wavelength ranges 170–210 Å (EISA) and 250–290 Å (EISB). Also these spectra will allow accurate determination of differential emission measure and element abundances within a variety of corona and transition region structures. The wavelength ranges discussed above and covered by the three spectrometers (SUMER, CDS and EIS) employed in this thesis work are shown in Fig. 2.5.

The advantage in performing observations using these three instruments is that they cover all together a large range of temperatures, which is appropriate for a complete analysis of the solar atmosphere from the upper chromosphere to the corona. Also, they allow observation of the strong EUV resonance lines both of neutral and singly ionised helium, to which this thesis is mainly addressed. Accurate details on the observation data and the atomic transitions involved will be provided in chapters 4 and 5.

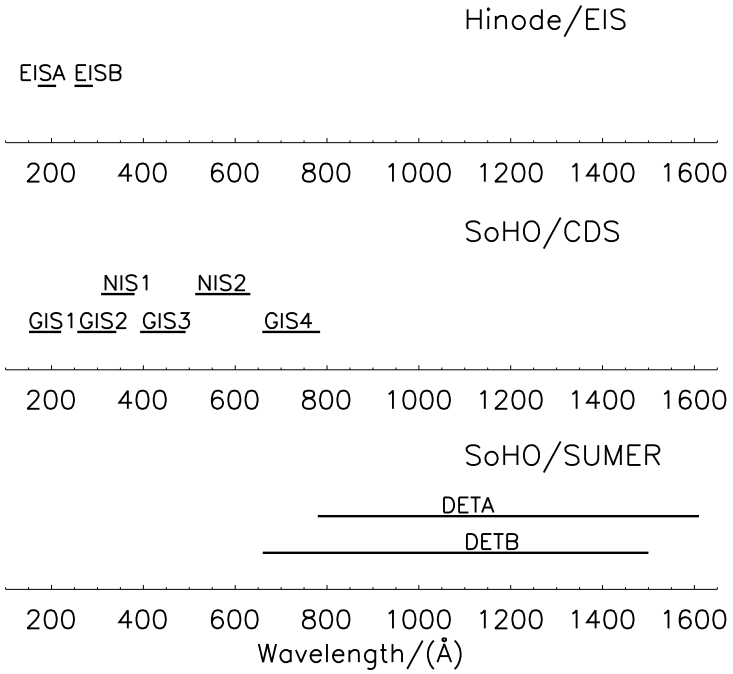


Figure 2.5: SoHO/SUMER, SoHO/CDS and Hinode/EIS wavelength ranges.

Regarding the notation employed in this thesis, the ions will be specified by $X^{+z}$, where X is the element and $z$ the ionisation stage, while if it refers to a spectral line, the spectroscopic notation will be used, so that the element X is followed by a roman number. Note that in the latter case X I corresponds to $X^{+0}$. Each level in a transition is specified using the notation $nl^{x\ 2S+1}L_J$, where $n$ is the principal quantum number, $l$ indicates the orbital of electron ($l = s, p, d, f, g, ...$), $x$ is the number of electron in that orbital, so that $nl^x$ is the electronic configuration. Additionally, $S$ is the quantum number related to the total electron spin and $2S + 1$ is called multiplicity, $L$ represents the total orbital angular momentum and $J$ represents the total angular momentum, which is the vector sum of $L$ and $S$. A *level* is specified by a combination of $S$, $L$ and $J$, while a *term* is characterised by specific $S$ and $L$.

Following the notation above, a general overview of EUV He I and He II lines, as observed by CDS and EIS, is given here in figure 2.6. The lines marked in red in full CDS and EIS spectra are the He I and He II lines which arise from the transitions illustrated in the panel on the left. The Coronal Diagnostic Spectrometer allows observation of neutral helium EUV resonance lines, related to transitions between the ground level $1s^2\ ^1S$ and the levels $1snp\ ^1P$ with $n$=2,3,4,5, giving the wavelengths respectively 584.33 Å, 537.03 Å, 522.21 Å and 515.62 Å. In addition, the doublet of He II at 303.78 Å is observed by CDS in the second order. It is a blend which arises from the transitions between the ground level $1s\ ^2S_{1/2}$ and the levels $2p\ ^2P_{1/2,3/2}$. The resonance doublet of singly ionised helium, which involves the term $3p\ ^2P$, is observed by EIS, as visible in figure 2.6. Also, the intercombination multiplet of neutral helium between the terms $1s^2\ ^1S$ and $1s2p\ ^3P$ at 591.41 Å is observed by CDS. It was identified, for the first time, by (18). They analysed the measured and predicted line ratios between $n$=2 to $n$=5 members of the $1s^2\ ^1S - 1snp\ ^1P$ series of He I and the intercombination line and estimated them both in the optically thin approximation and in the optically thick case, using the non-local thermodynamic equilibrium (NLTE) radiative transfer code MULTI (19). They found that the optically thin ratio I(591)/I(584) was too low compared with the observations, while the optically thick ratios were much closer to the observations, as expected for the 584.33 Å line[2] being affected by opacity and the 591.41 Å line remaining optically thin, because of its very low radiative transition probability (A-value). Even if its intensity is very low compared with the helium resonance lines, since it is the only optically thin helium line in both the CDS and EIS spectra, the intercombination line can help to investigate the anomalous behaviour of helium lines without including opacity effects. If the helium problem involves some processes that preferentially enhance the helium line intensities

[2]The same consideration can be done for the other lines of the $1s^2\ ^1S - 1snp\ ^1P$ series at 537.03 Å, 522.21 Å and 515.62 Å.

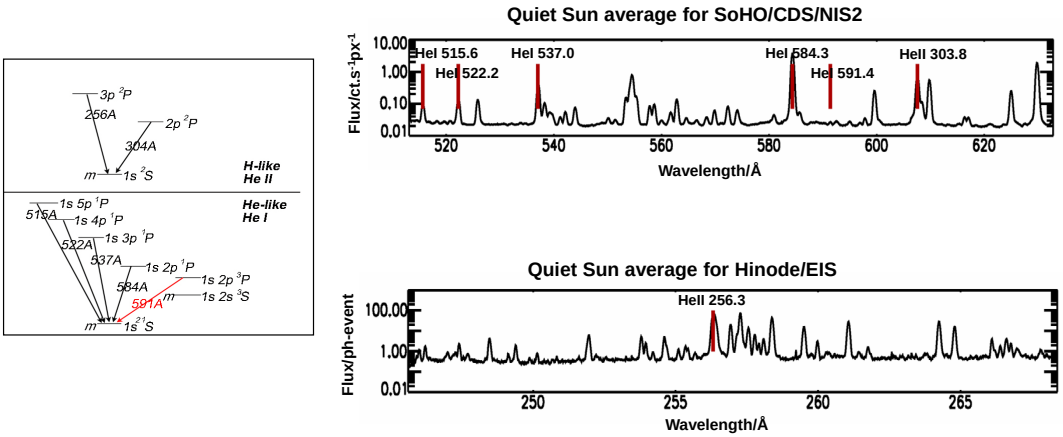


Figure 2.6: Example of SoHO/CDS and Hinode/EIS quiet Sun spectra (respectively on the upper right and on the lower right of the image), with identifications of the resonance lines of the $n$=2 to $n$=5 members of the $1s^2\,{}^1S - 1snp\,{}^1P$ series of He I and the resonance doublets of the $n$=2,3 members of the $1s\,{}^2S - np\,{}^2P$ series of He II. On the left, the scheme of atomic transitions is reported. The line marked in red is the intercombination line of neutral helium between a singlet and triplet states. It is the small line at 591.41 Å, which is possible to see in the CDS spectrum on the upper right.

with respect to the other characteristic transition region lines, the same effect should be present in the intercombination line. The next section will give a detailed review of the helium problem and consider the extensive literature involved.

## 2.3 The behaviour of EUV helium line intensities

The formation of helium lines in the solar spectrum is still not well understood, although the subject has been discussed for many years. One of the most important problems is due to the different behaviour of resonance lines of neutral and singly ionised helium in the solar EUV spectrum, when compared with lines of other ions formed at similar temperatures. Such lines have anomalously high intensity, which cannot be explained using models of other transition region lines. This discrepancy has led to proposals for the formation of the helium spectrum by different processes at different temperatures.

A purely radiative mechanism (*PR mechanism*) has been suggested first by (20) and later by (21) and (22). They proposed that coronal photons, at a wavelength near to the photoionisation threshold for the ground state (504 Å), penetrate into the chromosphere and photoionise helium atoms. These ions recombine to He I excited levels and produce the He I lines. By studying the lines between 5876 Å and 4009 Å, (20) showed that the lines at 4922 Å and 4388 Å (singlets) are faint compared with the triplets and maybe also the 4144 Å line (which is strong but probably because it is blended with an Fe I line). He interpreted this behaviour as being due to metastability of the lowest triplet level of helium ($1s2s\,{}^3S_1$) and an excess of ultraviolet solar radiation ($\sim$ 500 Å). Because of the excess UV radiation, the ground level will be depleted (in fact the ionisation potential of the ground state $1s^2\,{}^1S$ is around 25 eV $\Rightarrow \lambda \simeq$ 500 Å) and, consequently, the singlet lines will be weakened with respect to the triplet. (21) concluded that the neutral helium lines are emitted from the same region as hydrogen and metal lines, because the width and the intensity of these lines can be explained in terms of ionisation due to UV radiation, even if the kinetic temperature is as low as 5,000 K. (22) computed a model in which all helium is photoionised by coronal radiation and populates upper states by recombination at the local kinetic temperature of 8,000 K. Then, in his formulation, the photoionisation-recombination mechanism would be responsible for the formation of the entire helium spectrum in the Sun. The consequences of this model for the line profiles have been examined by (23). He showed that the mechanism related to photoionisation and recombination, described by (22), leads to very strong self-absorption in the cores of the resonance lines. Such

absorption cannot be eliminated by changing the parameters of the model. Furthermore, observations of He I and He II resonance lines (early observations - (24) and (25) - and also following observations through SERTS and SoHO - (26) and (27) -) did not detect this phenomenon.

Another extreme in excitation mechanism for the helium transitions is presented by *collisional excitation at higher temperature* ($T_e$ > 20,000 K, intermediate between chromosphere and corona), described by (28) and (29). However, such a model requires too high densities ($N_e \geq 10^{12}$ cm$^{-3}$), incompatible with other transition region diagnostics.

An attempt to understand the details of the physical processes responsible for exciting the helium, taking into account both extreme (radiative and collisional) mechanisms, was carried out by (30). They concentrated on the study of the resonance and the subordinate lines of neutral helium with a treatment of radiative transfer and statistical equilibrium calculations using a homogeneous model atmosphere representative of the solar chromosphere (from (31)'s model, with the addition of a second temperature plateau at 45,000 K to their plateau at 22,000 K). Assuming that triplet levels are populated primarily by *radiative recombination of ionised helium* in the lower temperature regions ($T \leq$ 10,000 K) and by *collisional excitation* in the higher temperature regions ($T \geq$ 20,000 K), where the 584 Å resonance line is formed, they stated that the populations of these levels are sensitive to the over-ionisation produced by excess ultraviolet radiation at lower temperature. They interpreted, moreover, that the underpopulation of the excited singlet levels with respect to their triplet counterparts is due to the provision for radiative decay of the singlets by escape of resonance-line photons. However, the agreement with observations concerning ultraviolet helium transitions from OSO-VI (32) is poor. The homogeneous model gives, in fact, a reasonable representation of quiet Sun, disc centre conditions, but fails to reproduce the eclipse data.

The (31)'s model (VAL) is used also by (33), who calculated some of the main He I and He II emission lines for the quiet Sun with a detailed NLTE analysis. They drew the conclusion that changes in the temperature gradient in the transition region are able to reproduce a large part of the helium observations (such as He II 304 Å and He I 584 Å resonance lines). Also, even though the collisional excitations play a major role in the process of photon creation, the coronal flux can introduce a non-negligible contribution to the line intensities. Finally, they examined the possible role of the *overlapping of the radiation at 304 Å with the 504 Å He I continuum*, finding out that it is not effective in the solar chromosphere.

(34) suggested an alternative model, pointing out that the helium lines (He I and He II) in the EUV spectrum have high intensities with respect to lines of other ions, but their intensities decrease in coronal holes. As said above, the problem is the large discrepancy between the observed and predicted He I and He II emission for the resonance lines. She proposed that the big increase observed in the absolute intensities of He I and He II lines should be the consequence of *mixing low temperature helium atoms and ions with higher temperature electrons*. The decrease in the He I and He II intensities in coronal holes can be explained by the reduced efficiency of such process. From Hearn's calculations (35; 36), (34) showed that, over the electron density range $10^8$ - 7×$10^{10}$ cm$^{-3}$, the 30-50 per cent of population of $1s2p\,^1P_1$ level in He I originates from the ground level $1s^2\,^1S_0$ by collisional excitation. At the same time the ground state is being depopulated by collisional excitation to $1s2s\,^3S_1$, from where the photoionisation occurs. Raising the electron temperature where the $1s^2\,^1S_0$-$1s2p\,^1P_1$ (584 Å) line is formed will not increase the intensity, because $1s^2\,^1S_0$ is depleted by about the same amount. The population of $1s2p\,^1P_1$ is therefore insensitive to $T_e$ for $T_e$>2.5×$10^4$ K (where the emission function peak for He I 584 Å is). However, if a process occurred that moved ions formed at one temperature rapidly to a region of higher temperature (or if the local electron temperature became higher than in equilibrium) then the excitation and decay of $1s2p\,^1P_1$ could take place before the ionisation returned to equilibrium. The emission would be greater than in the equilibrium situation since the ground state population would be higher for a given temperature. Furthermore, this process would raise the intensity of He I and He II lines without causing large increases in the intensity of other lines formed at similar temperatures.

(37) proposed that *ion diffusion effects* can provide such a mechanism. Their numerical calculations showed that diffusion can produce significant changes in the ionisation distribution in transition region models. These changes can in turn affect line intensities. In particular, the resonance line of He I and He II, which are especially sensitive, are greatly enhanced as helium diffuses into regions of higher temperature. It is unlikely, moreover, that many lines will show effects comparable to He lines, because diffusibility decreases with increasing ion charge and the temperature gradient decreases with increasing temperature in the upper transition region. The helium lines may appear weak in coronal holes due to the weakness of diffusion. However, despite qualitative agreement between their calculations and helium observations, it cannot be taken as strong evidence that diffusion effects are responsible. Furthermore, such effects were proposed mainly to justify the EUV lines, without solving the problem of subordinate He I lines.

A detailed analysis of the effects of diffusion on NLTE radiative transfer and statistical equilibrium calculations has been carried out by (38). They computed energy-balance models of the low transition regions including ambipolar diffusion for hydrogen and helium diffusion in the solution of the NLTE radiative transfer problem, for one-dimensional, hydrostatic atmospheric models, called FAL (39; 40; 38). The diffusion process increases the intensities of helium lines, especially He I resonance line emission. However, it has a less important effect on the He II lines. In fact, the resulting intensities and profiles are generally consistent with current observations, but the absolute intensity of He II 304 Å line is low compared with observations. The radiation shining down from the corona upon the transition region and upper chromosphere has also been considered in their calculations. They showed how incident radiation from coronal lines affects various EUV lines and the He I 10830 Å line.

(41) studied in detail the *process exciting the He I spectrum in a grid of models*, varying parameters such as chromospheric pressure, thickness of the transition region and level of coronal illumination to include predominance of either extreme in the excitation mechanism (expressly PR and collisional) and intermediate combinations. A modified VAL model (31) has been used to describe the thermal structure of the atmosphere, considering, as boundary conditions, the incident radiation field from the corona (EUV radiation) and the photosphere, that plays a role in photoexiting and photoionising the excited levels. The fine structure of triplet levels is not included in their atomic model, which is a valid approximation in the rate equations because in most of the triplet levels the energy separation of the J-sublevels is small enough for collisional interchange between them to maintain relative populations in proportion to their statistical weights. They concentrated on the strength and spectral distribution of He I 584 Å, 537 Å and the ionising continuum shortward 504 Å, 10830 Å and 5876 Å. Their calculations showed that coronal illumination evidently affects the spectrum in general, but it has weak influence on He I 584 Å in the presence of a transition region. Also they found that the population balance of neutral helium atom is strongly influenced by the photospheric radiation field, while the UV radiation field below 2600 Å can have a significant effect on the strength of the He I 10830 Å line. A mixed formation mechanism has finally been investigated, concluding that PR process does not necessarily lead to a strengthening of He I lines. In fact, for temperatures above $2 \times 10^4$ K photoionisations compete with direct excitation mechanisms in depleting the ground state of He I and the result can be a weakening of the helium spectrum with increasing EUV illuminance.

The capabilities of the Coronal Diagnostic Spectrometer CDS (16) and the Solar Ultraviolet Measurements of Emitted Radiation SUMER spectrometer (15), on board Solar and Heliospheric Observatory SoHO (27), have allowed new observations of the lines of the He I resonance series and the He II resonance line, improving their observed profiles. Such observations support the evidence that PR is not the principal mechanism which controls the formation of the EUV resonance He lines and that collisional excitation processes play a significant role in the quiet Sun. The relevance of *PR mechanism in active regions*, where the coronal EUV radiation field is much more intense than in quiet areas, has been analysed by (42). They concentrated on the study of the helium line formation in a specific active region prior to a two ribbon flare. Such analysis has been extended to the data taken during the flare by (43). To their aim, they planned an observing campaign coordinated between ground-based and space-borne instruments to obtain simultaneous spectroheliograms of the same area in several spectral lines, including four He lines (He I 5876 Å and 10830 Å from the Horizontal spectrograph at the Dunn Solar telescope DST of the National Solar Observatory at Sacramento Peak; He I 584 Å and He II 304 Å from the Normal Incidence Spectrometer NIS of the Coronal Diagnostic Spectrometer CDS onboard SoHO). They presented semiempirical models of the line profiles from the chromosphere to the transition region, using the program PANDORA (44; 45). The calculations have taken into account the estimated total number of photoionising photons impinging on the target active region (EUV radiation in the wavelength range below the photoionisation threshold at 504 Å) and their spectral distribution. The standard photospheric helium abundance [He]=0.1, as a starting point, and a modified distribution of microturbulence have also been included. They concluded that, similarly to the quiescent case, in an active region the incident coronal radiation has a limited effect on the UV helium lines, whereas it fundamentally affects the D3 (5876 Å) and 10830 Å lines. Moreover, they tested how the helium abundance influenced the computed profiles, building two more models for [He]=0.15 and [He]=0.07, only where the temperatures are greater than $10^4$ K. All these three models provides a good agreement with the observations. The differences in the computed lines for the model with the extreme [He] values are mostly evident for 584 Å and 304 Å lines, but, due to the spectral resolution of CDS, they are not appreciable in the observations and consequently do not provide enough constraints to choose between helium abundance values.

Observations made with the Coronal Diagnostic Spectrometer CDS are used also by (46) to investigate whether or not *photon scattering* plays a significant role in determining the behaviour of intensity ratios involving the helium and oxygen lines. They have examined separately supergranulation cell boundaries and cell interiors, already studied by (47) to derive mean enhancement factor for the He I and He II resonance lines. (47) found that these lines are increased

by a factor of 10 in the cell boundaries and by a factor of 14 in the cell interiors, using the intensity calibration of CDS by (48) and assuming that all the photons created in the He I and He II lines escape in the line of sight. The more recent CDS calibration by (49) reduces these values by a factor of about 1.3. It was suggested that such a different behaviour between cell boundaries and interiors may be due to the scattering of photons from the boundaries into the cell interiors. (46) analysed the overall trend for HeI(584Å)/OIII(600Å) and HeII(304Å)/OIII(600Å) intensity ratios to decrease as I(OIII) increases, taking into account the photon scattering, in order to explain how the enhancement in a given cell interior can be related to the enhancements in the nearby cell boundaries. They found that the gradients of the observed HeI(584Å)/OIII and HeII/OIII intensity ratios in individual boundary to cell interior scans can be determined by the different spatial variations of the optically thick helium lines and optically thin oxygen line and hence can depend on the local opacities. However, the intrinsic opacities in the cell interior and boundary regions must differ by at least an order of magnitude and would not lead to unique gradients for all the points in an individual scan. This observational result can be accounted for if photons observed from cell interiors originate in the cell boundary regions. Furthermore, they concentrated on the behaviour of HeII(304Å)/HeI(584Å), HeI(537Å)/HeI(584Å) and HeI(537Å)/HeII(304Å) intensity ratios, which show that these lines have very similar optical depth, as found also by (50).

Taking into account the study on the formation of the helium line and enhancement mechanisms before the launch of SOHO, the subsequent work related to diffusion processes concentrate essentially on the presence of *turbulent motions*, the role of *non-thermal transport* of helium ions and *non-Maxwellian electron distributions* and finally the study of the *effects of mass flow*.

The transport of helium atoms and ions through the steep temperature gradients in the transition region due to turbulent motions has been analysed by (51). They gave a detailed treatment of the effect of "microturbulent" velocities increasing the intensity of the He II 304 Å line with respect to other transition region emission lines and termed such process "velocity redistribution". They considered, as starting point, the possibility of production of non-thermal hot electrons in the transition region, studied more recently by (52). The latter proposed a mechanism for the generation of non-Maxwellian electron distribution in the upper regions of the solar atmosphere in the presence of collisional damping. Their purpose was to focus on the ideas implied by the velocity filtration process[3] (53) and to study how such non-Maxwellian distribution functions are generated and maintained in the solar environment. They suggested that parallel electrical field associated with low-frequency, obliquely propagating electromagnetic waves can be the source of high-frequency electron plasma and ion acoustic-like turbulence, which can be damped out by the background plasma electrons, resulting in the generation of non-Maxwellian suprathermal components on very fast time-scales. This hypothesis was explored using the chromosphere-coronal model. (51) believed that such a mechanism can contribute significantly to the HeII(304Å) intensity enhancement. To that goal, they exhibited evidence from the two flights of SERTS (Solar EUV Rocket Telescope and Spectrograph) in 1991 and 1993, showing that He II 304 Å line profiles observed in quiet and active regions appear to be very nearly Gaussian, in support of collisional excitation processes rather than the PR mechanism. The anticorrelation observed between intensity and residual line width in the He II 304 Å line suggests that the small-scale velocities of emitting ions may be greater in the quieter radiating elements than in and near the active regions. If it is true, then the mechanism of velocity redistribution could be important for the intensity enhancement of He II line in the quiet Sun, considering that this line is most likely optically thick. Because the velocity redistribution mechanism is identified not by an absolute intensity enhancement but rather by a relative enhancement with respect to transition region line emission, (51) investigated the ratio between the He II 304 Å line and the O III 600 Å line, which is formed under very similar conditions to the 304 Å line. This was tested by a coordinated campaign, using SOHO/CDS and H$\alpha$ spectroheliograms from Coimbra Observatory. They concluded that velocity redistribution, supported by all these observations, and velocity filtration appear to be the two candidate possibilities to explain the problem of the 304 Å enhancement. They also showed that there might be a contribution from the PR mechanisms in bright network elements, but it seems to be playing only a secondary role in the quiet Sun and even in active regions, as indicated by SERTS-97 observations and the analysis of the HeII/OIII ratio. Finally they left an open question concerning the observed anticorrelation between the HeII/OIII ratio and the O III line, explained by (46) through photon scattering.

(54) have also studied the effects on He I and He II lines, considering the transport of helium atoms and ions by turbulent motions to regions of higher electron temperature. Although the photoionisation-recombination mechanism appears to be important in the formation of some lines of helium spectrum, such as He II 1640 Å (55), He I 5876 Å and

[3]The basic nature of velocity filtration mechanism is that, given a non-Maxwellian particle distribution subject to stationary gravitational or electrostatic fields, the distribution function can have a temperature moment which increases with height across the transition region between the chromosphere and the corona, without the need of any local heating source.

He I 10830 Å (41), and probably contributes to the He I 584 Å evidence (23; 41) suggests that the He II 304 Å and He I 584 Å lines are formed mainly by collisional excitation. Hence, because the helium resonance lines have larger values of $W/kT_e$, where $W$ is the excitation energy, any process which involves larger populations of suprathermal electrons than in equilibrium will tend to increase the collisional excitation rates of lines. (54)'s calculations followed the approaches of (51), but a new emission measure distribution, determined from observed line fluxes and the appropriate atomic data, was used to calculate the temperature gradient. Moreover, they adopted a distribution of velocities working in terms of the initial life times of the He I and He II ground states, $\tau = [C_{ij}(T_i)]^{-1}$, where $C_{ij}$ is the collisional excitation rate. They considered such a time-scale to reflect better the dependence of the enhancement process on the long excitation and ionisation times of the helium ions at the equilibrium temperatures of resonance line formation. It is this long time-scale with respect to those for other transition region lines that allow unresolved turbulent motions to carry helium ions to higher temperatures where excitation occurs. They found out that turbulent transport can explain the enhancements of He I and He II resonance lines and the effects of this non-thermal motions are more consistent with the observed spatial distribution of helium emission than are those of excitation by non-Maxwellian distribution alone. Their formulation is also qualitatively consistent with observed variations in the HeI(537Å)/HeI(584Å) intensity ratio. However their calculations didn't include radiative transfer, that could be relevant especially to He I.

Investigation through extensive radiative transfer calculations including non-thermal motions and non-Maxwellian distributions has been done by (56). His simulations on the He II resonance line at 304 Å and the first two lines of He I resonance series (584 Å and 537 Å) lead to significant enhancements of the helium resonance line intensities compared with models assuming Maxwellian electron distributions. However, many of the predictions of the models tested are inconsistent with line ratio observations and do not reproduce simultaneously the observed intensities of the three lines studied. He concluded that, although small departures from Maxwellian distributions are not excluded, the collisional excitation by suprathermal electron in electron velocity distribution functions of the form which has been examined in this paper is unlikely to dominate the formation of the helium resonance lines. This is a further support to the enhancement by non-thermal transport of helium atoms and ions, already investigated in the previous paper of (54).

The effect of diffusion and mass flows on hydrogen and helium have been investigated by (2). Their calculations involve models based on a full treatment of the radiative transfer, statistical equilibrium and energy balance, for the solar transition region, that include mass flows as well as particle diffusion. Detailed calculations have been performed only for hydrogen and helium, while other elements have not been treated in a fully self-consistent manner. This implies that their models are appropriate mainly for the low transition region at temperatures between $10^4$ and $10^5$ K, since in such a regime hydrogen and helium are the main contributors to energy transport and radiative losses. At higher temperatures, hydrogen and helium become completely ionised and other species dominate. Considering these limitations, they evidenced that energy balance can be achieved through field-aligned diffusion of hydrogen and helium atoms. For illustrative purposes, they presented several cases to show how the flow velocities affect the emitted spectral lines of hydrogen and helium. Their line intensities and profiles are generally consistent with observations, but any detailed comparison would require specific adjustment of the boundary conditions for the observed case.

A new component to the mechanism for the enhanced helium emission has been proposed by (57). Again the diffusion of helium atoms along the magnetic field lines have been taken into account, but also the diffusion of neutral helium *across* magnetic field lines has been included. (57) based their work on two main aspects: the study of spatio-temporal behaviour of the helium lines, other relevant lines and continua and the investigation of some spectroheliograms obtained in the He I line at 584 Å, the multiplet of C III at 1175 Å and the MDI (Michelson Doppler Imager onboard SoHO) magnetogram. They found that helium lines behave differently from both typical chromosphere and transition region lines. In particular, the integrated helium line intensities show no oscillations, while their Doppler shifts do. They explained this result with the diffusion of neutral helium across the magnetic "canopy", which marks the location of a thin current sheet that separates the cooler regions from the overlying corona. This current sheet inhibits any charged particles from moving across it. However, neutral particles have long free paths and move freely across the current sheet to the higher temperature plasma and then they can be excited there by the hot coronal electrons. Moreover, (57) found that the integrated helium line intensities vary very slowly with respect both to the chromosphere oscillations and to the transient brightenings detected in transition region lines, but they vary rapidly compared to the coronal radiation. They interpreted the former evidence considering the anomalously long relaxation times of helium atoms under the condition of the upper chromosphere. Concerning the latter result, they concluded that photoionisation followed by recombination gives only a little contribution to the formation of helium lines.

The new suggestion for the enhancement mechanism, proposed by (57), has been followed more recently by (3), who examined the diffusion of neutral particles into the corona across magnetic fields in a more comprehensive scenario.

His purpose was, in fact, to give an explanation for the problem of structure and energy balance in the solar transition region using, as "ingredients", simply cross-field diffusion of neutral atoms from cool threads extending into the corona and the subsequent excitation, radiation and ionisation of these atoms via electron impact. Although he speculated that his new scenario might bring theoretical and observed intensity values into agreement, more observations, which connect chromosphere, transition region and corona, should be done. Also, their relation with theoretical models and available atomic data should be investigated to give more accurate conclusions both to the general problem of the structure of the transition region and to the specific problem of the origins of helium line enhancement.

The purpose of this thesis is to give a contribution to the above "problem" by revisiting atomic data and using new joint observations of both extreme-ultraviolet helium lines and other characteristic chromospheric/transition region lines.

## 2.4 Relating atomic physics to solar physics analysis

In the following chapters a substantial development of atomic physics will be made to enable detailed spectral analysis of the solar atmosphere observations. Information, such as electron and ion temperature, electron density, the thermal structures of the plasma, its chemical composition and ionisation state, its dynamics and the velocity distributions of its electrons, requires appreciation of the atomic processes in the solar plasma, as well as accurate atomic data.

Errors in the underlying atomic physics put severe constraints on the distinguishing of the physical processes which take place in the transition region or inner corona. For instance, uncertainties in the fundamental theoretical atomic data can make ambiguous the interpretation of non equilibrium signatures and affect the reliability of the elemental abundances derived from a specific spectral analysis. Moreover, the investigation of velocity fields deduced by Doppler shifts of observed spectral lines depends on precise energy values of the bound levels for the ions involved. Lack of accurate energy levels creates uncertainty in the identification of spectral lines based on their wavelengths.

In the optically thin regime (which is usually assumed in upper transition region and corona), several simplifications can be applied by reducing the complex radiative transfer equation to a well known expression for the integrated line intensity. This permits the use of a differential emission measure analysis to extract the plasma physical properties. This diagnostic method can be supported by other spectroscopic techniques for determining the electron temperature and electron density of the emitting plasma, such as line ratios. Progressing down into the more dense chromosphere, the radiation emitted cannot be treated in the optically thin approximation and the non-local thermodynamic equilibrium (NLTE) approach must be employed. This consists in the simultaneous solution of the radiative transfer and the statistical equilibrium equations for the atomic population densities. However, these techniques for deriving the temperature and density structure of the emiting plasma again depend on the quality of atomic data adopted and the validity of the atomic models (e.g. the analysis performed in chapter 6).

The analysis of dynamic plasmas is also a concern. Such study usually requires knowledge of cross-sections of the individual process (particularly ionisation and recombination) rather than the values deduced under the ionisation equilibrium assumption (e.g. fractional abundance). In a dynamic plasma, such as during a flare, the atomic relaxation time-scales for ground and metastable states are not short enough to allow the plasma to reach equilibrium. So, it is necessary to take into account explicitly the role of metastable states in a specific density regime.

This thesis addresses these issues in the context of atomic data and models assembled within the ADAS framework. In particular, the observed intensities of the EUV helium resonance lines, present in the CDS and EIS wavelength ranges and discussed in section 2.2 from a purely observational point of view, will be analysed using the sophisticated GCR theory and by revisiting the atomic data collected in the ADAS database.

# Chapter 3

# Non-Maxwellian collisional-radiative modelling

## 3.1 Introduction

The present paper is an extension of Summers *et al.*(2004), hereafter called *GCR - paper I*. In most modelling of excited populations and emission by ions in plasmas, it is assumed that the free electrons have an isotropic Maxwellian distribution of speeds. This assumption is based on the short time-scale for energy redistribution in e-e collisions (Spitzer, 1956)

$$\tau_{e-e} = [3.3 \times 10^5](kT_e/eV)^{3/2}(\mathrm{cm}^{-3}/\mathrm{N_e}) \ \ \mathrm{s}, \tag{3.1}$$

in comparison with other time-scales, such as those for establishing the state of ionisation of elements and the excited populations of their ions. In equation 3.1, $T_e$ is the electron temperature and $N_e$ the electron density, and, as indicated, we shall normally work with $kT_e$ in electron-volts and number densities in $\mathrm{cm}^{-3}$. The free electrons are key participants in the flow of energy from input sources such as ion kinetic energy from shocks, wave-particle interactions and plasma instabilities, through to radiant losses. Our interest for this paper is in situations when the inputs and outputs to the free-electron energy are sufficiently large and rapid that energy re-distribution is incomplete, non-Maxwellian distribution functions result and collisional-radiative modelling of excited populations and emission driven by electron collisions must be re-worked. Such a situation is well known in weakly ionised laboratory discharge plasmas when electron energy gain in the accelerating electric fields is lost in neutral atom or molecule excitation or by the electrons diffusing to the walls. Steady state distribution functions with the high energy tail depleted relative to a Maxwellian result, tending to the Druyvesteyn form in the pure elastic and diffusion limit. The detailed shape of such a distribution function is however quite sensitive to the actual neutral molecular species (and hence the particular vibrational excitations which occur) as illustrated in figure 3.1a.

In broad terms, the time scale for energy transfer from thermal free electrons to bound state excitation of ions is

$$\tau_{exc} = [6.3 \times 10^4](kT_e/eV)^{1/2}(\Delta E/eV)e^{\Delta E/kT_e}(\mathrm{cm}^{-3}/\mathrm{N^{(z)}}) \ \ \mathrm{s}, \tag{3.2}$$

with the transfer to neutral atoms about a factor $\sim 10$ longer. It is relevant also to note that the timescale for ionisation of ions by electrons is

$$\tau_{ion} = [4.4 \times 10^5](eV/kT_e)^{1/2}(I_{ion}/eV)^2 e^{I_{ion}/kT_e}(\mathrm{cm}^{-3}/\mathrm{N^{(z)}}) \ \ \mathrm{s}. \tag{3.3}$$

A contrasting situation of enhancement of the high energy tail of Maxwellians occurs in magnetically confined fusion experiments with neutral beam and lower hybrid heating. It also occurs in astrophysics. Topical at this time is the role of the modified two-stream instability in planetary atmospheres, comets and supernova remnants. Consequential energised electron distribution functions (see figure 3.1b) are believed to lead to x-ray line and continuum emission as observed by the CHANDRA and XMM spacecraft. Taking the cometary case as an example, the time-scales are very different. Introduce the plasma oscillation time (reciprocal plasma frequency) as

$$\tau_{pe} = 1/\omega_{pe} = [1.1 \times 10^{-4}](\mathrm{cm}^{-3}/\mathrm{N_e})^{1/2} \ \ \mathrm{s}, \tag{3.4}$$

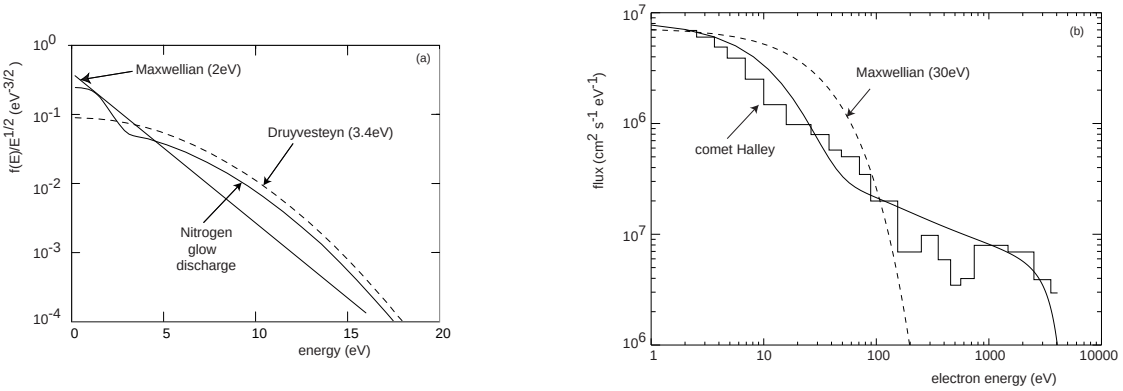


Figure 3.1: (a) Electron distribution functions typical of low temperature discharges. The Maxwell and Druvesteyn patterns are shown and a modelled case for a nitrogen plasma. The kink at $\sim$ 0.8 eV reflects the energy loss to vibrational excitation of the molecule (Behringer and Fantz, 1994). (b) Electron flux measurements in the vicinity of comet Halley by the VEGA 1, 2 spacecrafts in Comet Halley (Gringauz and Verigin, 1990). The measurements suggest the development of a non-Maxwellian tail parallel to the magnetic field of an initial Maxwellian electron distribution function in the presence of a lower-hybrid wave field. Such fields are expected to be energised by the interaction of the solar wind with an ebullient cometary plasma and lead to x-ray emission. For comparison a Maxwellian (dashed line) at 30eV and a synthesised distribution (solid line). The latter comprises a Maxwellian at 10 eV combined with a 70 eV Maxwellian Landau damped with a Gaussian wave of resonant velocity 4 times the thermal speed, and the half-width of the wave is 2 times the thermal speed (see section 3.2.2).

then a typical evolution time for the electron distribution function due to Landau damping of waves generated by the modified two-stream instability for a comet is $\sim 10^2 \tau_{pe}$ with $N_e \sim 30$ cm$^{-3}$ (Dawson *et al.*, 1997), that is $\sim 3$ msec. On the other hand, for a comet at $\sim 0.7$ a.u., the electron thermalisation time $\tau_{e-e} \sim 3-4$ days and the time-scale to establish the high ionisation states of light elements C, N and O in a 200 eV plasma is $\sim 80$ days. Evidently, both excited population and ionisation stage fractional abundances are dynamic and incomplete in cometary transit. Handling of non-Maxwellians must not presuppose quasi-static populations and only return the usual effective collisional-radiative coefficients. The precise character of the electron distribution in the cometary case remains ambiguous, but depends on the total energy flow and the 'duty cycle' of wave-particle energy input events.

## 3.2 Distribution functions

It is a purpose of this paper to enable use of non-Maxwellian distributions in both predictive modelling and in deductive spectral analysis. In the former, we shall wish to explore the effect of different degrees of non-Maxwellian character on predicted emission, ionisation state etc. In the latter, the typical progress of analysis is that one should deduce, from spectral line ratios, some sort of non-Maxellian parameter, analogous to electron temperature itself. For both these purposes, we introduce 'families of non-Maxwellians' designed to be helpful for investigations.

### 3.2.1 Analytic non-Maxwellian distributions

We work with (nominally) isotropic distribution functions, $f(E)$ defined with respect to electron kinetic energy, $E$, so that $\int f(E)\,dE = 1$. With mean energy $\bar{E} = \int Ef(E)\,dE$ and variance $\sigma_f = \int (E-\bar{E})^2 f(E)\,dE$, the effective temperature, $T_{eff}$, is defined by $kT_{eff} = 2\bar{E}/3$. Thus the Maxwellian electron distribution is

$$f_{T_e}(E) = \frac{1}{\mathrm{kT_e}} \frac{2}{\sqrt{\pi}} \left(\frac{E}{\mathrm{k}T_e}\right)^{1/2} \exp\left(-\frac{E}{\mathrm{k}T_e}\right). \tag{3.5}$$

where we have set $T_e = T_{eff}$, so that $\bar{E} = 3kT_e/2$ and $\sigma_{f^m} = kT_e$. Since typical electron impact excitation cross-sections are such that the collision strength $\Omega$ is approximately constant with energy for non-neutral targets, it is the variation of the functional $f(E)/E^{1/2}$ which is most important for the calculation of Maxwellian and non-Maxwellian reaction rate coefficients.

The simplest non-Maxwellian distributions are simply superpositions of Maxwellians. Such superpositions can represent local power-law-like behaviours, etc.

The most common non-Maxwellian situations are over-population of the high energy Maxwellian tail typical of many astrophysical plasmas and under-population of the tail typical of discharge plasmas. The analytic paradigms are the $\kappa$ and Druyvesteyn distribution function families respectively.

The $\kappa$ distribution (or generalised Lorentzian) form of distribution function, introduced by Vasyliunas (1968), has been shown to arise, for example, in the presence of suprathermal radiation fields (Hasegawa *et al.*, 1985) and is also connected with generalised entropy formalisms (Leubner, 2001). The family takes the form

$$f_{\kappa,E_\kappa}(E) = \frac{1}{E_\kappa} \frac{2}{\sqrt{\pi}} \left(\frac{E}{E_\kappa}\right)^{1/2} \kappa^{-3/2} \frac{\Gamma(\kappa+1)}{\Gamma(\kappa-\frac{1}{2})} \left(1+\frac{E}{\kappa E_\kappa}\right)^{-(\kappa+1)}, \tag{3.6}$$

parametrised by $\kappa$, where $E_\kappa$ is the characteristic energy of the distribution and is such that $\bar{E} = 3\kappa E_\kappa/(2(\kappa-3/2))$. $\kappa$ determines the deviation from the Maxwell distribution of temperature $T_{eff}$. In the limit as $\kappa \to \infty$ the $\kappa$ distribution tends to the Maxwellian. Figure 3.2 illustrates $f_\kappa(E)$ for various values of $\kappa$, with the limiting Maxwellian distribution shown for comparison. The key feature for atomic modelling is the enhanced high energy tail.

In low pressure discharges, the analytic Druyvesteyn electron distribution function form (Druyvesteyn, 1930) arises from velocity independent elastic scattering models. Generalisations to include inelastic processes has led to the Druyvesteyn family

$$f_{x,E_x}(E) = \frac{x}{E_x^{3/2}} \frac{\Gamma(5/2x)^{3/2}}{\Gamma(3/2x)^{5/2}} E^{1/2} \exp\left(-\left[\frac{E\Gamma(5/2x)}{E_x\Gamma(3/2x)}\right]^x\right), \tag{3.7}$$

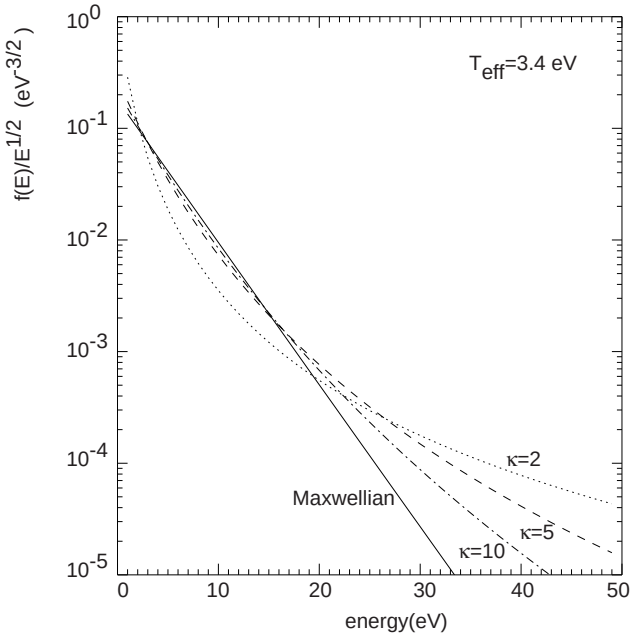


Figure 3.2: $\kappa$ distribution for various $\kappa$ values, and a comparison to a Maxwellian for an (effective) electron temperature of 3.4 eV.

where the parameter $x$ typically varies between 1 and ~3. $x = 1$ gives the Maxwellian and $x = 2$ the classic Druyvesteyn. The characteristic energy $E_x = \bar{E}$. These are used in detailed modelling (e.g. Gudmundsson, 2001). Figure 3.3 illustrates behaviour for various values of $x$, with the Maxwellian distribution shown for comparison. The key feature for atomic modelling is the depleted high energy tail.

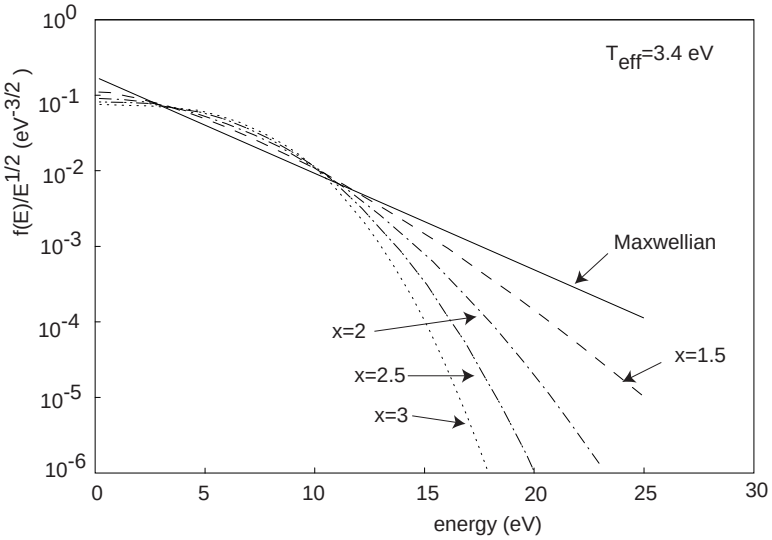


Figure 3.3: Generalised Druyvesteyn distributions for various $x$ values, and a comparison to a Maxwellian for an (effective) electron temperature of 3.4 eV.

### 3.2.2 Numerical non-Maxwellian distributions

The above analytic distribution functions are simplified representations of the actual distributions in real plasmas. Probe measurements or more sophisticated computational solutions of the electron Fokker-Planck equation yield numerical values for the electron distribution function. Following our astrophysical interest of section 3.1, and in illustration, we focus here on Landau damping of lower-hybrid waves. Such electrostatic waves propagate parallel to a magnetic field and, if moving with a velocity $v = \omega/k$ in a plasma, will be travelling at the same velocity as some of the electrons. It is possible for the wave to transfer energy to these electrons and vice versa. The direction of energy

transfer depends on the first derivative of the electron distribution function with respect to velocity in the direction parallel to the magnetic field. If $\partial f/\partial v_{\|} < 0$, electrons will be energised and the waves will be damped, and if $\partial f/\partial v_{\|} > 0$, the waves will grow and the electrons decelerate. If $\partial f/\partial v_{\|} = 0$ then there is no energy transfer. Therefore in the absence of electron collisions, the lower-hybrid waves will cause a plateau region to be formed in the electron velocity distribution in one direction. This can be described by the Fokker-Planck equation:

$$\left(\frac{\partial f}{\partial t}\right)_{w} = \frac{\partial}{\partial v_{\|}}\left(G(v_{\|})\frac{\partial f}{\partial v_{\|}}\right), \tag{3.8}$$

where $G(v_{\|})$ is a normalised wave diffusion operator. Dendy *et al.*(1995) solved eqn. 3.8 for the case of a Gaussian power spectrum,

$$G(v_{\|}) = \frac{\pi^{1/2}}{\omega\nu_{ei}}\left|\frac{eE}{mv_T}\right|^2 \frac{v_{\|}}{\Delta} exp\left[-\frac{(v_{\|}-v_0)^2}{\Delta^2}\right], \tag{3.9}$$

where $\omega$ is the wave frequency, $\nu_{ei}$ is the electron-ion collision rate, $v_{Th}$ is the thermal speed, $\Delta$ is the half-width of the wave power spectrum, which is centred at $v_0$. Here we have continued the work of Dendy *et al.*using Maxwellian and other initial distribution functions. Figure 3.4 shows a contour plot of the evolved distribution function from an initial Maxwellian, after 3ms, in the $v_{\perp}$ and $v_{\|}$ plane with respect to a magnetic field in the parallel direction. It is assumed that the plasma is collisionless. The resulting distribution is non-isotropic: the symmetry in the $v_{\|}$ direction has been broken, although the distribution is still symmetrical around all azimuthal angles. For calculating atomic collision rates we should properly use differential cross sections but have chosen to integrate the distribution function over the pitch ($\phi$) and azimuthal ($\theta$) angles to give a simple distribution over speed (energy) which is tabulated.

The specific organisation of our distribution function files, both analytic, superposition and numeric are tuned to handling within the ADAS Project and are assigned the ADAS data format *adf37* (see section 3.5).

## 3.3 Non-Maxwellian reaction rate coefficients

### 3.3.1 Electron impact excitation and de-excitation

Consider the electron impact excitation and de-excitation of the $z-$times ionised ion $A^{+z}$ between lower state $i$ and upper state $j$

$$A^{+z}(i) + e(\varepsilon_i) \rightleftharpoons A^{+z}(j) + e(\varepsilon_j). \tag{3.10}$$

The excitation energy is $\Delta E_{ij} = \varepsilon_i - \varepsilon_j$ with $\varepsilon_i$ the free electron energy with the ion in the lower state $i$ and $\varepsilon_j$ the free electron energy with the ion in the upper state $j$. For modelling and atomic databases it is most convenient to describe the reaction by a collision strength $\Omega_{ij}$ specified as a function of the threshold parameter $X = \varepsilon_i/\Delta E_{ij}$ with $X \in [1, \infty)$. For Maxwellian electron distributions, the averaged collision strength $\Upsilon_{ij}(T_e)$ is a preferred tabulation as a function of electron temperature $T_e$ and is given by

$$\Upsilon_{ij}(T_e) = \int_0^{\infty} \Omega_{ij}(\varepsilon_j) \exp\left(-\frac{\varepsilon_j}{kT_e}\right) d\left(\frac{\varepsilon_j}{kT_e}\right). \tag{3.11}$$

Note that $\Omega_{ij}$ is symmetrical between $i$ and $j$ from micro-reversibility and likewise $\Upsilon_{ij}$ from detailed balance. Thus in the Maxwellian case both the excitation and de-excitation rate coefficient are obtained from $\Upsilon_{ij}$ as

$$q_{i\rightarrow j}(T_e) = 2\sqrt{\pi}\alpha c a_0{}^2 \left(\frac{I_H}{kT_e}\right)^{1/2} \frac{1}{\omega_i} \exp\left(-\frac{\Delta E_{ij}}{kT_e}\right) \Upsilon_{ij}(T_e), \tag{3.12}$$

$$q_{j\rightarrow i}(T_e) = 2\sqrt{\pi}\alpha c a_0{}^2 \left(\frac{I_H}{kT_e}\right)^{1/2} \frac{1}{\omega_j} \Upsilon_{ij}(T_e), \tag{3.13}$$

where $\alpha$ is the fine structure constant, $c$ the speed of light in vacuum, $a_0$ the Bohr radius, $I_H$ the Rydberg energy, and $\omega_i$ and $\omega_j$ the statistical weights of states $i$ and $j$ respectively.

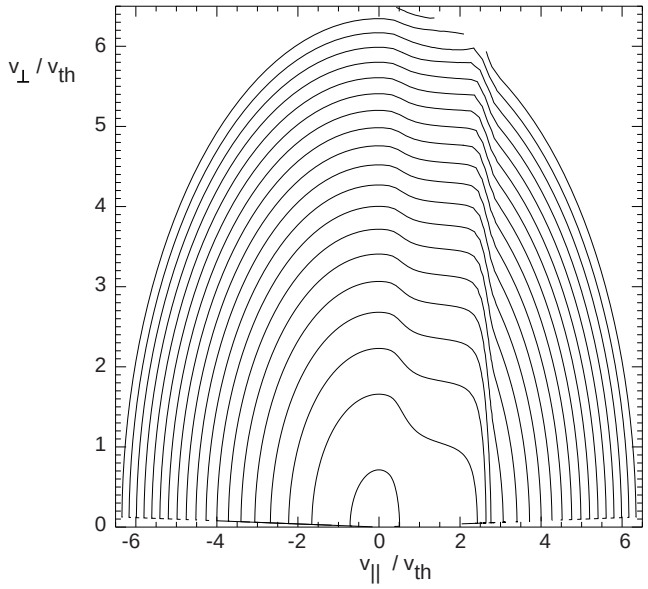


Figure 3.4: Contour plot of an initial Maxwellian at $T_e$ = 1 keV evolving for 3 ms in a lower-hybrid Gaussian wave field of strength 40 *rmmV/m* centred on wave velocity velocity $v_0 = 1.5v_{th}$ with half-width of $\Delta = 0.5v_{th}$. $v_{th}$ is the mean Maxwellian thermal speed.

For the non-Maxwellian case, the averages over the electron distribution must be re-done and there are two issues - whether the precision of tabulation (or functional fitting) of $\Omega_{ij}$ can sustain adequate precision in the non-Maxwellian rates and the lack of symmetry in $\Upsilon$ due to the lack of detailed balance.

### Interval averaged collision strengths

Collision strengths obtained from simple analytic or parametric formulae, non-resonant calculations and from data asessment are smooth functions of energy and the forming of rate coefficients is a further smoothing procedure. It is tacitly assumed that the tabulated collision strength can sustain quadrature over an arbitrary electron distribution function. More precise resonance-including calculations such as *R*-matrix however indicate that for incident electron energies between excitation and ionisation threshold, the true collision strength shows many fine, highly-peaked, resonance features. Even for a neutral target, the typical collision strength shows detailed structure (cf. figure 3.5a for neutral helium). Thus much publically available collision strengths are (unspecified) averages and therefore cannot necessarily support arbitrary non-Maxwellian averaging. The relative variability of the collision strength and the distribution function matters. It seems therefore that *R*-matrix and similar resonance-including collision strengths must be the starting point for computing rate coefficients in the general case. On the other hand the exact delimiting of a collision strength may require tabulation at a very large number of data values - prohibitive for convenient utilisation within database structures such as those of the ADAS Project. For example the most recent *R*-matrix calculation of the collision strength for the transition $1s^2\ ^1S - 1s2p\ ^3P$ in neutral helium used $\sim 37000$ data points over a 2 Ryd energy range. In the present work, when *R*-matrix source data is available, we form a more manageable intermediate data file for an ion (ADAS *adf04 - type 1* as described in section 3.5) in which the collision strength data for each transition is provided as a set of interval averages. More precisely, we work in threshold energies $X = \epsilon_i/\Delta E_{ij}$ and seek a suitable fixed set of $\sim 50$ $X$-values, the same for all transitions, for the tabulation. Interval averages are formed as integrals of the resonant collision strengths between successive mid-way points of the fixed $X$-grid. The first moment is also formed and then used interpolatively to re-position onto the fixed grid for increased precision. For the transition $1s^2\ ^1S - 1s2p\ ^3P$ in neutral helium, the *R*-matrix collision strength can be compared to the interval averaged results as shown in figure 3.5a.

The *adf04 - type 1* file is archived and used for subsequent non-Maxwellian averaging in place of the orginal *R*-matrix data. In forming a non-Maxwellian rate coefficient data set in this way, at issue then is whether the interval-averaging grid is acceptable. We define 'energy' scale lengths for the interval averaged collision strength and the distribution function, namely,

$$X_\Omega = 1/\frac{\mathrm{d}\log\Omega}{\mathrm{d}X}, \quad X_f = 1/\frac{\mathrm{d}\log f}{\mathrm{d}X}. \tag{3.14}$$

In the region below ionisation threshold, where the underlying collision strength is resonant, we require $X_\Omega < X_f$ and above ionisation threshold, where the underlying collision strength is non-resonant, we require $X_f < X_\Omega$. Figure 3.5b illustrates the situation. Any failure of the criterion (executed as a running test during non-Maxwellian averaging) necessitates reworking of the interval averaged *adf04 - type 1* file.

### Effective Collision Strengths

We generalise equations 3.12 and 3.13 by replacing $\Upsilon_{ij}(T_e)$ by new effective collision strengths, $\Upsilon_{i\to j}(T_{eff})$ and $\mathrm{J}_{j\to i}(T_{eff})$ averaged over a general distribution function. We define these non-symmetric effective collision strengths, called *Upsilons* and *Downsilons* respectively, such that the conversion to rate coefficients remains as it was in the Maxwellian case, *viz.*

$$\begin{aligned}
\Upsilon_{i\to j}(T_{eff}) &= \frac{\omega_i}{2\sqrt{\pi}\alpha c {a_0}^2}\left(\frac{kT_{eff}}{I_H}\right)^{1/2}\exp\left(\frac{\Delta E_{ij}}{kT_{eff}}\right)q_{i\to j}(T_{eff}),\\
\mathrm{J}_{j\to i}(T_{eff}) &= \frac{\omega_j}{2\sqrt{\pi}\alpha c {a_0}^2}\left(\frac{kT_{eff}}{I_H}\right)^{1/2}q_{j\to i}(T_{eff}).
\end{aligned} \tag{3.15}$$

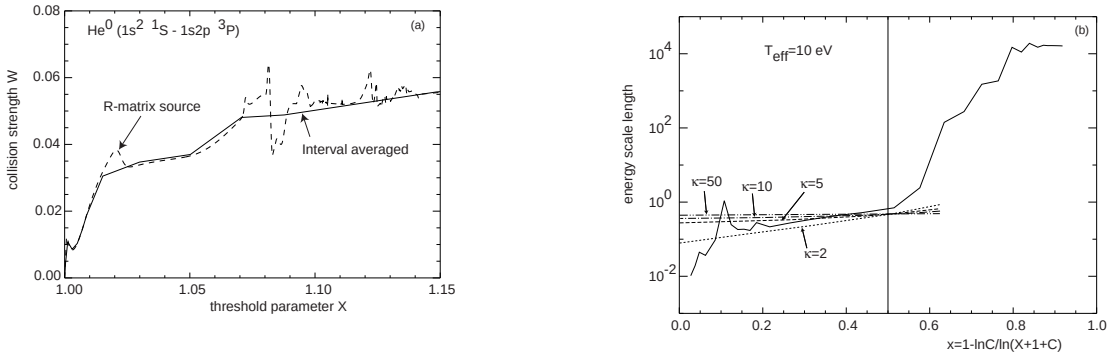


Figure 3.5: (a) The collision strength in the resonant region for the transition $1s^2\ ^1S - 1s2p\ ^3P$ in neutral helium from an *R*-matrix with pseudostates calculation (RMPS) compared with the interval averaged collision strength; (b) 'Energy' scale lengths for the kappa distribution function family compared with that of the interval averaged collisions strength $1s^2\ ^1S - 1s3p\ ^3P$. The independent variable $x$ follows the Burgess $C$-plot transformation with $C$ chosen to place the ionisation threshold at 0.5. The test criterion is satisfied except at $x \sim 0.1$. $X$ is the threshold parameter.

For a general electron energy distribution, $f(E)$, the excitation and de-excitation rate coefficients are given by

$$\begin{aligned} q_{i\to j}(T_{eff}) &= \sqrt{\frac{2}{m_e}}\frac{\pi {a_0}^2}{\omega_i} I_H \int_0^\infty \Omega_{ij}(\varepsilon_i) {\varepsilon_i}^{-1/2} f(\varepsilon_i)\, d\varepsilon_j \\ q_{j\to i}(T_{eff}) &= \sqrt{\frac{2}{m_e}}\frac{\pi {a_0}^2}{\omega_j} I_H \int_0^\infty \Omega_{ij}(\varepsilon_j) {\varepsilon_j}^{-1/2} f(\varepsilon_j)\, d\varepsilon_j \end{aligned} \tag{3.16}$$

which leads to

$$\begin{aligned} \Upsilon_{i\to j}(T_{eff}) &= \frac{\sqrt{\pi}}{2}\exp\left(\frac{\Delta E_{ij}}{kT_{eff}}\right)\int_0^\infty \Omega_{ij}(\varepsilon_i)\left(\frac{\varepsilon_i}{kT_{eff}}\right)^{-1/2} f(\varepsilon_i)\, d\varepsilon_j \\ \mathfrak{Upsilon}_{j\to i}(T_{eff}) &= \frac{\sqrt{\pi}}{2}\int_0^\infty \Omega_{ij}(\varepsilon_j)\left(\frac{\varepsilon_j}{kT_{eff}}\right)^{-1/2} f(\varepsilon_j)\, d\varepsilon_j \end{aligned} \tag{3.17}$$

For example, for the $\kappa$ distribution these become

$$\begin{aligned} \Upsilon_{i\to j}(T_{eff}) &= \sqrt{\frac{2\kappa}{2\kappa-3}}\kappa^{-3/2}\frac{\Gamma(\kappa+1)}{\Gamma(\kappa-\frac{1}{2})}\exp\left(\frac{\Delta E_{ij}}{kT_{eff}}\right) \\ &\quad\times\int_0^\infty \Omega_{ij}(\varepsilon_j)\left[1+\frac{\varepsilon_j+\Delta E_{ij}}{\kappa E_\kappa}\right]^{-(\kappa+1)} d\left(\frac{\varepsilon_j}{E_\kappa}\right), \\ \mathfrak{Upsilon}_{j\to i}(T_{eff}) &= \sqrt{\frac{2\kappa}{2\kappa-3}}\kappa^{-3/2}\frac{\Gamma(\kappa+1)}{\Gamma(\kappa-\frac{1}{2})} \\ &\quad\times\int_0^\infty \Omega_{ij}(\varepsilon_j)\left[1+\frac{\varepsilon_j}{\kappa E_\kappa}\right]^{-(\kappa+1)} d\left(\frac{\varepsilon_j}{E_\kappa}\right). \end{aligned} \tag{3.18}$$

As described in section 3.2, our distribution functions $f(E)$ may be of two possible formats: analytic and numeric. The analytic format includes superpositions of analytic forms as families. Numeric distribution functions are isotropic distributions tabulated against energy. These different classes of distribution function dictate differences in the numerical quadrature method employed in the generation of rate coefficients. Although mainly a computational issue, some points are noted here. For certain analytic distributions the quadrature accuracy can be improved since only the form of the collision strength need be approximated. For example, in evaluation of average collision strengths over a $\kappa$ distribution, the collision strength is locally fitted to a linear or quadratic function of $X$ within each interval. The integrand is thus analytic as $\Omega(X)f(X) \sim (c_0 + c_1X + c_2X^2)(1+X)^{-(\kappa+1)}$ and integrable. It is also important to recognise the asymptotic behaviours of the collision strength. The numerical quadrature procedures take account of dipole, non-dipole and spin-change forms for excitation. These forms remain valid and useful in the interval averaged collision strength case. More detail is given in section 3.5.

### 3.3.2 Radiative recombination

To obtain the non-Maxwellian radiative recombination coefficient and associated stimulated recombination and photoionisation rate coefficients, return to the Milne relations

$$\begin{aligned} Q_c(\bar{\nu}) &= \left(\frac{h\bar{\nu}}{mvc}\right)^2 \frac{\omega_i}{\omega_+} a(\bar{\nu}) \\ \sigma(\bar{\nu}) &= \frac{c^3}{8\pi h\bar{\nu}^3} Q_c(\bar{\nu}) \end{aligned} \tag{3.19}$$

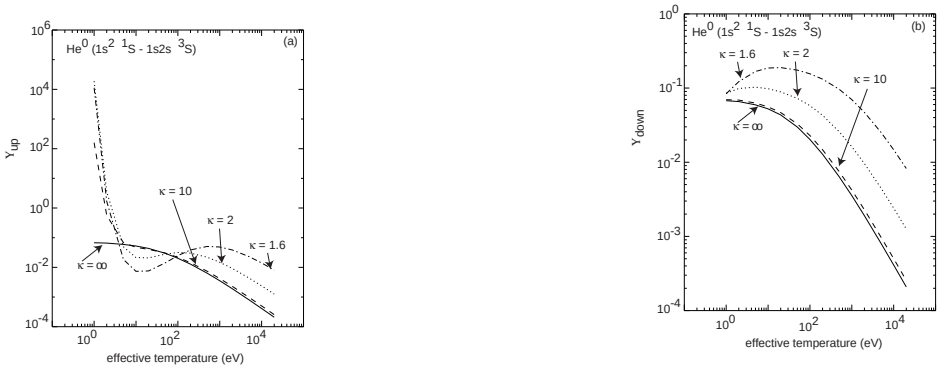


Figure 3.6: (a) Upsilon for the transition $1s^2\ {}^1S - 1s2s\ {}^3S$ in neutral helium for various $\kappa$ distributions (b) Downsilon for the same transition. The curves are generated by numerical quadrature over the interval averaged cross-sections for helium described in section 3.1.1. The x-axis coordinate is $T_{eff} \equiv 2\bar{E}/3$ as described in section 2.1.

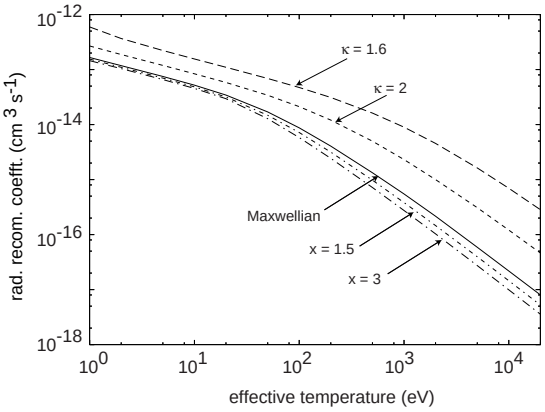


Figure 3.7: Radiative recombination integral for $\kappa$ distributions for capture into the ground state of neutral helium. The curves are generated by numerical quadrature over the distribution function. The free-bound Gaunt factor $g^{II}$ is set to unity. The limiting Maxwellian curve is the analytic expression $e^{I_H/kT}E_1(I_H/kT)/T_e^{3/2}$. The x-axis coordinate is $T_{eff} \equiv 2\bar{E}/3$ as described in section 2.1.

with $Q_c(\bar{\nu})$ the *capture cross-section*, $a(\bar{\nu})$ the *photo-ionisation cross-section* and $\sigma(\bar{\nu})$ the *stimulated capture cross-section*. It is helpful to work in terms of the bound-free Gaunt factor, $g^{II}$ where

$$a(\bar{\nu}) = \frac{128\alpha}{3\sqrt{3}} \frac{z_1^4}{\bar{\nu}^3} \frac{\omega_+}{\omega_i} \frac{g^{II}}{(E/I_H + I_i/I_H)^3} \pi a_0^2 \tag{3.20}$$

Then the recombination coefficient is obtained as

$$\alpha_i^{(r)} = \frac{32\alpha^4 c\pi a_0^2}{3\sqrt{3}} \frac{z_1^4}{\bar{\nu}^3} \int_0^\infty \frac{1}{\sqrt{E/I_H}} \frac{g^{II}}{(E/I_H + I_i/I_H)} f(E)\, dE \tag{3.21}$$

### 3.3.3 Dielectronic recombination

Since dielectronic recombination is a resonant process, then the non-Maxwellian recombination coefficient is

$$\alpha_{i;j,nl:i}^{(d)} = 2I_H \pi^2 a_0^3 \frac{\omega_{j,nl}}{\omega i} \frac{1}{\sqrt{E/I_H}} f(E) \frac{A_a A_r}{A_a + A_r} \tag{3.22}$$

In general, a summation over a manifold of nearly degenerate doubly excited states belonging to a level, term or shell is required and $E$ represents a mean energy for the resonance manifold. We may use dielectronic recombination coefficient tabulations for Maxwellians as a function of temperature for the non-Maxwellian case. Thus the datasets following from the work of Badnell *et al.*(see Badnell *et al.*, 2003 - hereafter called *DR-paper I*) remain applicable. From the non-Maxwellian distribution function with mean energy $\bar{E}$, identify the tabular $kT_e \sim \bar{E}$ and deduce the local mean resonance energy from

$$\alpha_{i;j:i}^{(d)}(T_e) = 4\pi^{3/2} a_0^3 \frac{\omega_{j,nl}}{\omega i} \left(\frac{I_H}{kT_e}\right)^{3/2} e^{-E/kT_e} \frac{A_a A_r}{A_a + A_r} \tag{3.23}$$

Then convert $\alpha_{i;j:i}^{(d)}(T_e)$ with the factor

$$\frac{\sqrt{\pi} I_H}{2} \left(\frac{kT_e}{I_H}\right)^{3/2} \sqrt{\frac{I_H}{E}} e^{E/kT_e} f(E) \tag{3.24}$$

Some error is introduced by this procedure due to outer electron stabilisation. It is safe to assume this is small.

### 3.3.4 Collisional ionisation and three-body recombination

More substantial reworking is required for these processes. The starting point is the Fowler relation for the double differential cross-sections (in energy), namely

$$\omega_i E Q_{i\to+}(E; E', E'') = \frac{16\pi m}{h^3} \omega_+ E' E'' Q_{+\to i}(E', E''; E) \tag{3.25}$$

Where the impacting electron with the target in the state $i$ is $E$ and the projectile and released electron have final energies $E'$ and $E''$. From energy conservation $E = E' + E'' + I_i$. Then the ionisation rate coefficient is

$$q_{i\to+} = \int_{I_i}^\infty \sqrt{\frac{2E}{m}} Q_{i\to+}(E; E', E'') f(E)\, dE \int dE' \int dE''$$

and the three-body recombination coefficient is

$$\begin{aligned} \alpha_{+\to i}^{(3)} \quad = \quad & \int_{I_i}^\infty \sqrt{\frac{2E'}{m}} f(E')\, dE' \int \sqrt{\frac{2E''}{m}} f(E'')\, dE'' \\ & \times \int Q_{+\to i}(E', E''; E)\, dE \end{aligned} \tag{3.26}$$

Re-writing this using the Fowler relation, introducing $kT_{eff}$ and grouping

$$\begin{aligned}\alpha^{(3)}_{+\to i} &= 8\left(\frac{\pi a_0^2 I_H}{kT_{eff}}\right)^{3/2} \frac{\omega_i}{2\omega_+} e^{I_i/kT_{eff}} \\ &\times \int_{I_i}^{\infty} \sqrt{\frac{2E}{m}} Q_{i\to+}(E;E',E'') f(E)\, dE \\ &\times \int\int \left[\frac{\sqrt{\pi}}{2}(kT_{eff})^{3/2} e^{-I_i/kT_{eff}}\right. \\ &\left.\times \sqrt{\frac{E}{E'E''}} \frac{f(E')f(E'')}{f(E)}\right] dE'\, dE'' \end{aligned} \tag{3.27}$$

The term in square brackets tends to unity as $f(E) \to f_{T_e}(E)$ and $T_{eff} \to T_e$.

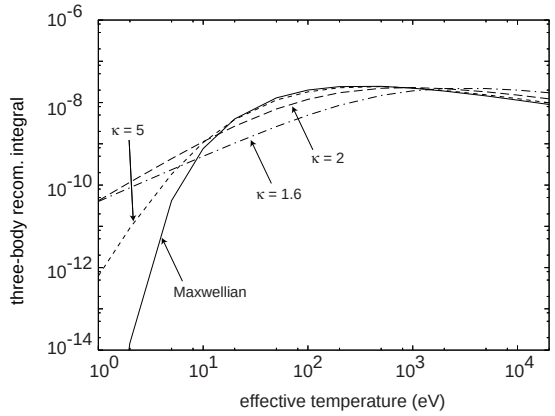


Figure 3.8: The numerical integral in the three-body coefficient of eqn. 29. Curves are for capture to the ground state of neutral helium for the $\kappa$ family excluding the leading terms outside the integral.

If the differential ionisation cross-section is that due to Thomson

$$Q_{i\to+}(E;E',E'') = 4\pi a_0^2 \zeta I_H^2 \frac{1}{EE'^2}\delta(E-E'-E''-I_i) \tag{3.28}$$

then in the Maxwellian case

$$\begin{aligned} q_{i\to+} &= 8\sqrt{\pi}\alpha c a_0^2 \zeta \left(\frac{I_H}{I_i}\right)^{1/2}\left(\frac{I_H}{kT_e}\right)e^{-I_i/kT_e} \\ &\quad \times\left[1-\frac{I_i}{kT_e}e^{I_i/kT_e}E_1(I_i/kT_e)\right] \end{aligned} \tag{3.29}$$

and

$$\begin{aligned} \alpha^{(3)}_{+\to i} &= 8\left(\frac{\pi a_0^2 I_H}{kT_e}\right)^{3/2}\frac{\omega_i}{2\omega_+}e^{I_i/kT_e}q_{i\to+} \\ &= \frac{N_i^{saha}}{N_e N_+}q_{i\to+} \end{aligned} \tag{3.30}$$

as expected. In the non-Maxwellian case a double integral must be evaluated numerically. It is generally the case that double-differential ionisation cross-sections are not available. Then we make the simplifying assumption that an $E$ dependent correction factor

$$g(E) = Q_{i\to+}(E)/Q^{thomson}_{i\to+}(E) \tag{3.31}$$

may be introduced in the final quadrature over $E$. The $Q$s in the above equation are the total ionisation cross-sections. This assumption preserves detailed balance in the Maxwellian limit and allows some improvement in the rate coefficients.

## 3.4 Population structure and ionisation state

The set of non-Maxwellian rate coefficients enters the equations of statistical balance for the excited populations of an ion within the generalised-collisional-radiative ($\mathcal{GCR}$) context (Summers, 2002; *DR-paper I*). That is, we are concerned not only with equilibrium level populations, but also with effective coefficients for line emission, ionisation, recombination and radiated power 'driven' by the various metastables of the different ionisation stages of an element. These effective coefficients, which in the Maxwellian case are functions of electron temperature, $T_e$, and electron density, $N_e$, are functions also of a 'non-Maxwellian parameter' in the present case. It is noted that for $\mathcal{GCR}$ modelling in finite density plasma, especially when dielectronic recombination is active, very highly excited populations must be taken into account in the statistical balance equations. Within the ADAS Project, this is done by the method of condensation and projection matrices which give the influence of highly excited populations on a set of low levels. The latter, typically including all levels (specified in *LS* or *IC* coupling) up to some principal quantum shell, must span excited levels which are the upper levels of observed spectrum lines. Modelling for diagnostic spectroscopy requires high precision in rate coefficients for the low-level group. The highly excited populations, handled by projection in a quasi-static assumption, require less precision. High quality rate coefficient data for the low-level group is provided in tabular data sets (*adf04* format in the ADAS Project). The high levels and projection are computed using simpler analytic approximations for the various rate coefficients.

For our non-Maxwellian treatment, the techniques of section 3.3 are used to create a non-Maxwellian *adf04* file (called an *adf04 type 4* file). This is drawn into the low-level population modelling and combined with the (existing) Maxwellian treatment (at the effective temperature $T_{eff}$ defined in section 3.2.1) of the high-level projection. The simplification allows us to focus economically on the primary effects of non-Maxwellians on spectral emission while retaining the $\mathcal{GCR}$ completeness - at a small reduction in precision.

## 3.5 Computational procedures

Figure 3.9 show a schematic of the main computations. The *adf04* data format has been used for many years in the ADAS Project and has become one of the common formats for delivery of the results of fundamental electron-ion collision and atomic structure calculations. Prior to the present development virtually all *adf04* files composed

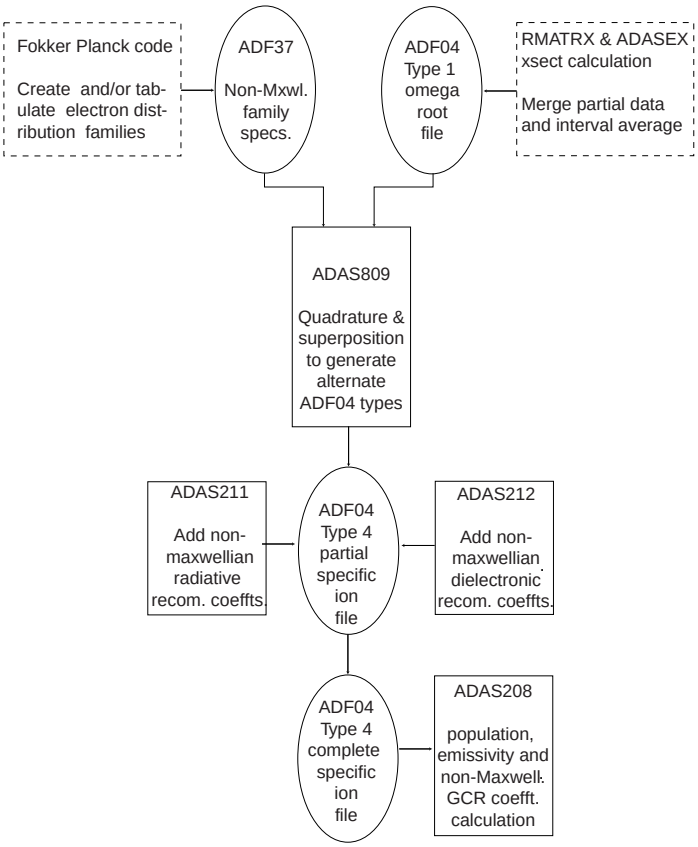


Figure 3.9: Flow chart showing the steps used to create distribution averaged collision strengths.

of Maxwell averaged rate coefficients (held as $\Upsilon$s), called *type 3* files. Here the new *type 1* version is introduced composed of cross-sections (held as $\Omega$s). The latter are interval averaged for compactness but are unaveraged over a distribution function. *R*-matrix codes and associated structure codes such as the versions in use by Badnell and co-workers are indicated as RMATRX/AUTOS in the schematic. Griffin *et al.*(1998) prepared a post-processing code, ADASEX, which assembled raw *R*-matrix outputs, executed Maxwell averaging and delivered a fully formed *adf04 - type 3* dataset. ADASEX has been extended, with inclusion of interval averaging so as to deliver an *adf04 - type 1* dataset. The collisional data in this file type includes only electron impact excitation and ionisation. The code ADAS809 converts *type 1* to *type 3* or *type 4* by quadratures over distribution function families. The specific analytic $\kappa$ and Druyvestyn families are internally generated while true numerical distribution function families and superposition families are supplied in the data format *adf37*. For complete $\mathcal{GCR}$ modelling, additional collisional reactions must be added to the *adf04* file - specifically state selective radiative recombination and dielectronic recombination. The latter are supplied by extensions to the existing ADAS codes ADAS211 and ADAS212 as described in *GCR-paper I*. It is noted that the evaluation of bound-free, $g^{II}$ Gaunt factors by Gaussian quadratures used there delimits the Gaunt factor precisely over the whole energy range. Numerical non-Maxwellian averaging is then rapid. For dielectronic recombination, the procedures of *GCR-paper I* and *DR-paper I* remain applicable and the *BBGP* support function is effective for the transfer to the non-Maxwellian case.

An extension to the main ADAS population code, ADAS208, is required to recognise and pair up/down transition lines from the *adf04 - type 4* dataset. Thereafter, final generation of population structure, effective recombination and ionisation coefficients and line emissivities follow exactly the procedures of *GCR-paper I*

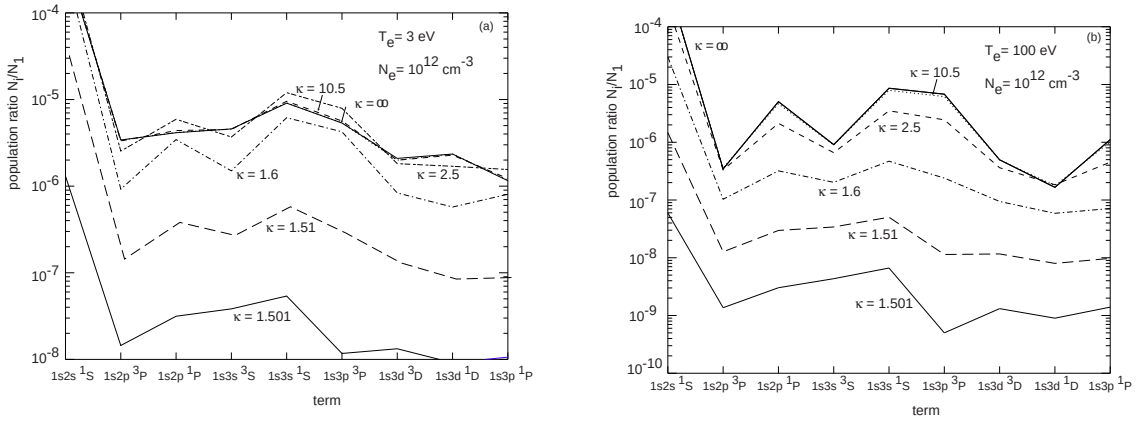


Figure 3.10: Variation of the excitation-driven parts of the populations of the $n = 3$ shell of $He^0$ with electron temperature and $\kappa$. The sub-parts of the populations driven by (a) the ground state $He^0(1s^2\ ^1S)$ and by (b) the metastable $He^0(1s^2\ ^1S)$ are distinguished. Note that for the two values of $\kappa$, some fractional populations are increased and some decreased. At the fixed electron density $N_e = 10^{13}$ cm$^{-3}$, there is only partial re-distribution amongst the $n = 3$ $l$-substates.

## 3.6 Illustrative results

Illustrations are drawn from neutral helium. The underlying collision strength data which underpin the results (Paton *et al.*, 2005) merge assessed experimental data (cf. De Heer *et al.*, 1998) with converged close coupling calculations (Ralchenko *et al.*, 2000) at intermediate and high energy, and with the recent calculations of Ballance *et al.*(2004) at low energies. The latter *RMPS* (*R*-matrix with pseudostates) calculations span levels up to $n = 4$, resolve fine resonance structure and match correctly to the intermediate energy region. The resulting *adf04 - type 1* file is the 2004 preferred ADAS dataset. The dataset energy grid will support all non-Maxwellian averaging required here. It is also to be noted that the additional structure and detail, arising principally from the improved low energy region in the new dataset, does alter the rate coefficients even in the pure Maxwellian case over those heretofore. Two studies are relevant, namely, Smith (2003) and Behringer and Fantz (2000). The former work sought to interpret discrepancies in helium line ratios from the solar atmosphere in terms of non-Maxwellians. This model is, however, less complete than the present one, using a simplified description of the electron distribution function and failing to renormalise the distribution when calculating the collisional excitation rate. In addition, the atomic collision strength data is much older and less reliable. The latter work was associated with RF heated discharge plasmas in which helium served as a diagnostic species. The interpretation of the neutral helium emission in the discharge case is complicated by opacity and the non-equilibrium metastable ($1s2s\ ^3S$) fraction (due to wall quenching). Re-analysis of these experimental measurements is not possible in this paper, rather we have investigated the variations in the key spectrum lines due to non-Maxwellians which could influence the interpretations.

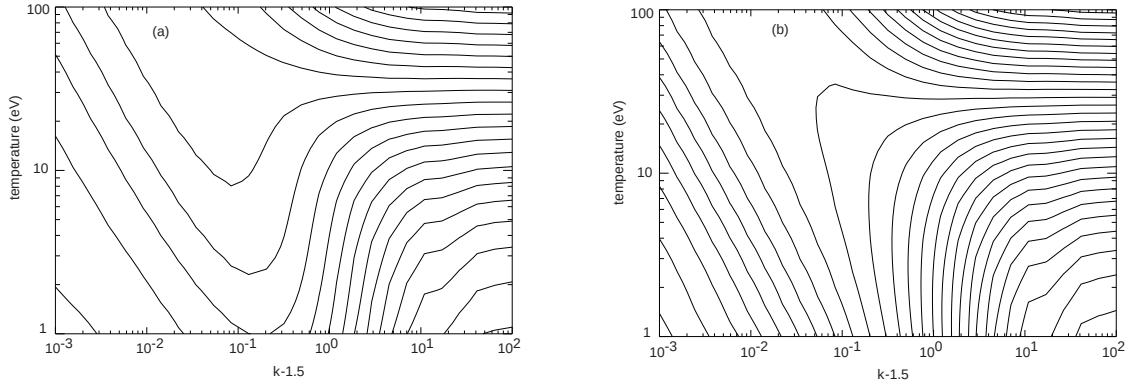


Figure 3.11: 2-D surfaces and contours of selected line ratios in the $T_e$ and $\kappa$ plane. Results are at the fixed electron density, $N_e = \text{cm}^{-3}$. (a) HeI(1s2s $^3$S − 1s3p $^3$P)/HeI(1s2s $^1$S − 1s3p $^1$P). (b) HeI(1s2p $^3$P − 1s3d $^3$D)/HeI(1s2s $^1$S − 1s3p $^1$P). The difference between the two surfaces indicate that $T_e$ and $\kappa$ may be extracted from line ratio observations although insight into the appropriate non-Maxwellian family is required.

In general, it is expected that separation of the effective temperature parameter and a non-Maxwellian parameter from spectral line ratios will be ambiguous since the first order effect of a non-Maxwellian parameter is a mean energy shift. This weak orthogonality is countered by the differential variation of dipole, non-dipole and spin change collision strengths with energy. Figures 3.10a and 3.10b show that the latter effect remains present, at electron densities $\sim 10^{10} - 10^{14}$ cm$^{-3}$, in the relative populations of the $n = 3$ terms. The putative electron temperature and density

diagnostic from neutral helium uses the line ratios HeI(1s2p $^1$P – 1s3d $^1$D)/HeI(1s2s $^1$S – 1s3p $^1$P) and HeI(1s2s $^3$S – 1s3p $^3$P)/HeI(1s2s $^1$S – 1s3p $^1$P). To the latter we add the HeI(1s2p $^3$P – 1s3d $^3$D)/HeI(1s2s $^1$S – 1s3p $^1$P) ratio and seek parameter discrimination for the $\kappa$ family. Results are illustrated in figures 3.11a and 3.11b. This demonstration of principle falls short of establishing a working diagnostic for non-Maxwellians. That will be the subject of a separate work.

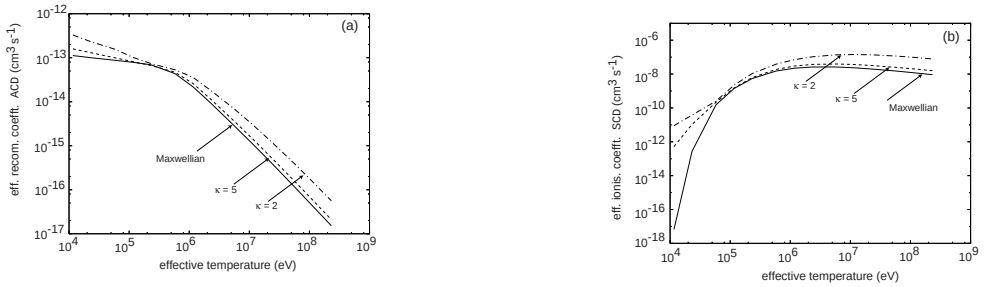


Figure 3.12: (a) Variation of $\alpha_{cd}$ for $He^{+1} + e \leftrightarrow He^0$ with electron temperature and $\kappa$ for an electron density of $10^{14}$cm$^{-3}$. (b) Variation of $S_{cd}$ for $He^0 + e \leftrightarrow He^{+1} + e + e$ with electron temperature and $\kappa$ for an electron density of $10^{14}$cm$^{-3}$.

In figures 3.12a and 3.12b, the effect of the non-Maxwellian parameter on collisional-radiative recombination ($\mathcal{ACD}$) and ionisation ($\mathcal{SCD}$) coefficients is shown. The sensitivity of the ionisation balance to electron temperature and the relatively lower accuracy of electron impact ionisation coefficients compared with excitation rate coefficients makes unambiguous detection of non-Maxwellians from ionisation state alone more elusive than from line ratios.

## 3.7 Conclusions

It has been shown how generalised collisional-radiative modelling may be extended comprehensively to handle non-Maxwellian electron distributions. The new procedures are largely transparent to the applied modeller once an initial collision strength file of format *adf04 - type 1* is set up. A new ADAS data format *adf37* has been defined to describe non-Maxwellian distribution functions.

The suitability of collision strength data for non-Maxwellian collisional-radiative modelling has been addressed. New initiatives are underway to deliver fundamental collision data according to these requirements. For existing databases of Maxwellian averaged collision strengths, only the superposition route to non-Maxwellians is available. Maxwellian superpositions which involve cancellation between components of the superposition are unsound due to (in general) unknown implicit averaging assumptions.

An initial demonstration of the potential for non-Maxwellian line ratio diagnostics has been made based on helium.

Further work is in progress to show effectiveness in spectroscopic experiment analysis.

The present development has been made in the context of the ADAS Project.

# Chapter 4

# New observations

The need of performing joint observations using the three spectrometers SoHO/SUMER, SoHO/CDS and Hinode/EIS has been already mentioned in section 2.2. For the purpose of this thesis, on one hand it is central to analyse lines formed at the lower temperatures characteristic of the upper chromosphere/lower transition region. These lines include, as discussed, the EUV helium resonance lines and some other lines formed in the temperature range of $10^4 - 10^5$ K, such as lines from $Si^{+1}$ and $C^{+1}$. On the other hand, it is essential to extend the range of observations at higher temperatures, including upper transition region and coronal lines. This allows us to explore the connection between the chromosphere and the corona through the thin atmospheric layer that is the transition region. Also, this permits us to investigate whether the anomalous emission of helium is related to mechanisms which involve coronal plasma.

In the following section, an overview of the missions and instrumentation is given. Then, the chapter is focussed on a new set of joint observations carried out in April 2009. Firstly, it concentrates on each single instrument, in order to describe the data reduction and calibration procedures and to show how images and spectra have been built up. Secondly, the use of the three instruments together is illustrated, dwelling on the co-alignment and cross-calibration procedures employed and on the fit of line profiles.

## 4.1 Missions and instrumentation

### 4.1.1 Outline of capabilities of SUMER and CDS on SoHO

After the launch in December 1995, the Solar and Heliospheric Observatory (27), SoHO, was inserted into a 180-day period halo orbit around the gravitational equilibrium L1 Lagrangian point, about $1.5\times10^6$ km sunward from the Earth. It started to be operational in April 1996. The choice of the halo orbit is strictly related to the objectives for which SoHO has been designed. Thus, it provides a smooth Sun-spacecraft velocity change throughout the orbit, appropriate for helioseismology measurements to study the solar interior. Moreover, it is outside the magnetosphere and allows continuous observations of the Sun, suitable for the analysis of solar wind and particles and for solar atmosphere observations to achieve a better understanding of the physical processes that form and heat the solar corona.

Of the twelve instruments onboard the spacecraft (as shown in figure 4.1), two in particular deal with the provision of diagnostic information concerning the structure of the solar atmosphere from the upper chromosphere through to the low corona. These are the Solar Ultraviolet Measurements of Emitted Radiation (SUMER) spectrometer and the Coronal Diagnostic Spectrometer (CDS). In the context of EUV experiments, EUV observations have been made since the early '60s, but all missions prior to SoHO have been severely constrained by project, instrumentation design and current technology (for an overview of EUV missions until SoHO see (58)). As an example, the OSO (Orbiting Solar Observatory) series 1-8, which ran between 1962 and 1975, used, in many cases, integrated solar disc images or integrated spectral bands and had a spatial, spectral and temporal resolution (e.g. 20-60 arcsec, 0.8-3.2 Å and 120-900 s respectively) more than an order of magnitude worse than the instruments on SoHO. Also the wavelength coverage did not extend adequately to wavelengths shorter than $\sim$ 300 Å. An improvement regarding both the spectral range and the resolution has been done by Skylab (1973-74), but it used film as detector and thus the temporal capabilities were

very limited. Also, the Skylab SO82A instrument was a slitless spectrograph. As a consequence, it produced overlapping spectroheliograms that could only provide clear spectral information for bright, compact features such as flares. Only SERTS (Solar Extreme ultraviolet Rocket Telescope and Spectrograph) (1989,91,93,95) and CHASE (Coronal Helium Abundance Spacelab Experiment) (1985), which were flown on short-duration rocket and shuttle flights, had characteristics comparable with SUMER and CDS. Hence, SUMER and CDS spectrometers provide the first opportunity, with respect to the previous missions, for a more accurate and detailed investigation of the EUV Sun, followed by the improvement in spatial and spectral resolution and wavelength range, compared to CDS, of Hinode/EIS, which will be described later.

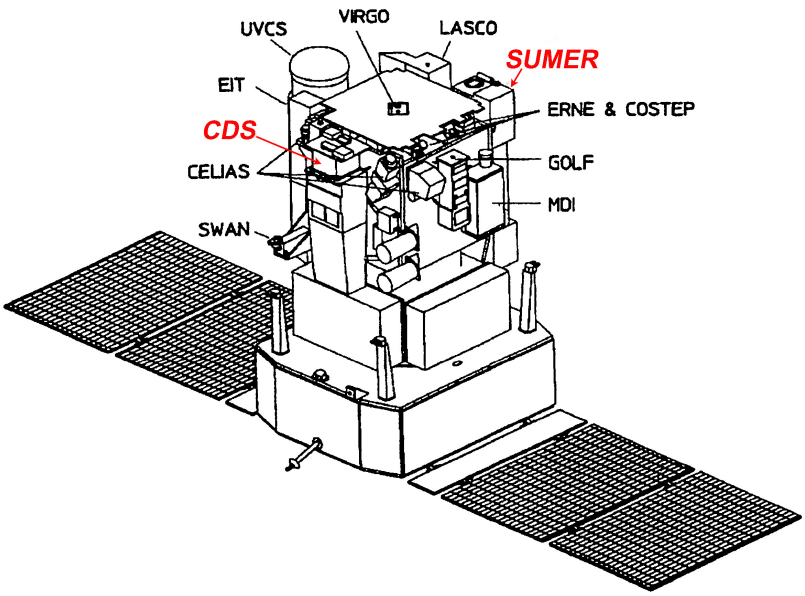


Figure 4.1: SoHO spacecraft schematic view. The two instruments, SUMER and CDS, with which the thesis is concerned are indicated in red.

The SoHO spacecraft performed very well for two years before its attitude control was lost for a four month period, from June to September 1998. Recovery of onboard instrumentation ended in October 1998 and SoHO became again fully operational. During the loss and much of the recovery time the payload experienced extreme temperature conditions, which in most cases affected the radiometric response of the instruments. During the accident, CDS was held at a temperature of ~100 °C, much higher than the range over which it had been tested before launch, while SUMER was on the cold side of the spacecraft, where the temperature was estimated to have dropped to -80 °C. The unusual temperature conditions caused an irreversible distorsion in the CDS, affecting the shape of the spectral line profiles and inducing relatively strong burn-in effects. Also, the SUMER instrument experienced an overall loss of sensitivity, due to a permanent contamination on various optical parts. However, for both the instruments the loss of efficiency have been partially compensated by determining, through subsequent analysis, a correction factor between preloss and postloss efficiency.

### Solar Ultraviolet Measurement of Emitted Radiation (SUMER)

SUMER is a stigmatic normal-incidence spectrograph operating in the range from 465 Å to 1610 Å. Figure 4.2 shows the instrument optical design, which is fully described by (15). SUMER consists essentially of three parts: a telescope mirror, a spectrometer and two detectors. The off-axis parabolic telescope mirror images the Sun into the spectrometer entrance slit plane. It has pointing and scan capabilities of ±32 arcmin in two perpendicular directions (the fastest rate is 300 step$^{-1}$ with 0.375 arcsec step$^{-1}$). Consequently, the total geometric field of view is $64 \times 64$ arcmin$^2$. The spatial resolution, which depends on wavelength, is close to 1 arcsec. The instrument thus can resolve spatial elements on the Sun with dimension down to 1,000 km. A second parabolic mirror collimates the beam leaving the slit. This beam is then deflected by a plane mirror onto the grating. The slit assembly, at the focus of the telescope, is narrow

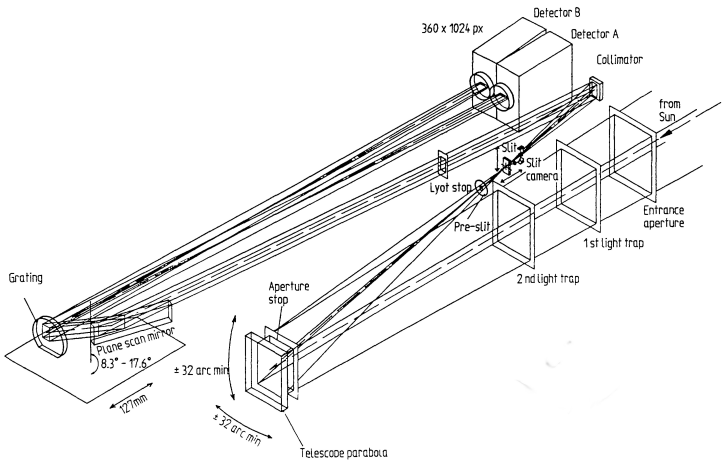


Figure 4.2: Optical layout of SUMER instrument.

in the direction of the wavelength dispersion to obtain good wavelength resolution. Spectroheliograms are built up by using the motion of the plane mirror perpendicular to the long extension of the slit. Four slits with angular dimensions $4 \times 300$ arcsec$^2$ (slit 1), $1 \times 300$ arcsec$^2$ (slit 2), $1 \times 120$ arcsec$^2$ (slit 4) and $0.3 \times 120$ arcsec$^2$ (slit 7) are available. The wide slit (slit 1) allows an increase of counts, at the expense of spatial and spectral resolutions, and is used for off-limb observations. The slit 2 is for standard use to achieve the best possible spatial and spectral resolution. The last two slits (slits 4 and 7) are employed for intense lines. All slits are parallel to CDS normal-incidence (NIS) slits and extend in the solar North-South direction. Also, the slits are centred on the spatial dimension of the detectors, but the two short slits (slit 4 and 7) can be placed off the centre in three different spatial positions. For the observations performed for this work, the slit 4 in top position (slit# 5) has been used. Two diffraction orders can be observed by SUMER, with first order and second order superimposed in the spectrum. Two photon-counting detectors (A and B), with image encoding using cross-delay-line (XDL) technology, are positioned in the focal plane of the grating, in order to collect the images of the slit. Each detectors has an array of 1024(spectral)×360(spatial) pixels. Visible opaque kBr (potassium bromide) photocathode material is deposited on the central area of the detector, increasing the efficiency mainly in the range from 900 Å to 1500 Å. The spectral resolution of the spectrometer can be derived from the grating equation:

$$n\lambda = d(sin\theta + sin\alpha) \tag{4.1}$$

where $n$ is the diffraction order, $d$ is the grating space, $\theta$ is the angle of incidence on the grating and $\alpha$ is the angle of reflection off the grating. Assuming that the angle of incidence is fixed and differentiating the equation 4.1, the relation for angular dispersion is obtained:

$$n\,d\lambda = d\,cos\alpha\,d\alpha \Rightarrow \frac{d\alpha}{d\lambda} = \frac{n}{d\,cos\alpha} \tag{4.2}$$

The linear dispersion of a grating system is the product of the angular dispersion and the effective focal length $f$ of the system, for a given diffracted wavelength $\lambda$:

$$f\,\frac{d\alpha}{d\lambda} = \frac{f\,n}{d\,cos\alpha} \tag{4.3}$$

In the SUMER case, the effective focal length of the grating depends on the angle of incidence, and thus on the wavelength, according to $f = r_a/(1 + cos\theta)$ (where $r_a$ is the radius of the spherical concave grating), while in the CDS case $f = 2R$, where $R$ is the radius of the Rowland circle. From the equation 4.3 an expression for the resolving power is obtained:

$$\frac{\lambda}{\delta\lambda} = \frac{n\,f\,\lambda}{d\,cos\alpha\,\delta x} \tag{4.4}$$

where $\delta x$ is the scale of resolution, usually given as the pixel size. The theoretical resolving power can be considered a characteristic of the grating and the angles at which it is used. However, in practice, the ability to resolve two adjacent wavelengths generally depends not only on the grating, but it is the convoluted result of all optical elements in the system, as well as the quality of these elements. Their effects on resolving power measurements are necessarily superimposed on those of the grating, giving the ”real” spectral resolution $\delta\lambda$. Table 4.1 lists the main characteristics of the three instruments used in this thesis, allowing a comparison of their capabilities.

| Instrument | Wavelength range (Å) | Slit (arcsec$^2$) | Spatial resolution (arcsec px$^{-1}$) | Spectral dispersion (Å px$^{-1}$) | Field of view (arcmin$^2$) |
|---|---|---|---|---|---|
| **SoHO/SUMER** | Det. A : 780-1610Å (1st order)<br>390-805Å (2nd order)<br>Det. B : 660-1500Å (1st order)<br>330-750Å (2nd order) | $4 \times 300$<br>$1 \times 300$<br>$1 \times 120$<br>$0.3 \times 120$ | 1.03 at 800Å<br>0.95 at 1600Å | 0.0450 at 800Å (1st order)<br>0.0418 at 1600Å (1st order)<br>0.0228 at 500Å (2nd order)<br>0.0209 at 800Å (2nd order) | $64 \times 64$ |
| **SoHO/CDS** | NIS1 : 308-381Å (1st order)<br>154-191Å (2nd order)<br>NIS2 : 513-633Å (1st order)<br>257-317Å (2nd order) | $90 \times 240$<br>$4 \times 240$<br>$2 \times 240$ | 1.2 along $\lambda$ disp.<br>1.5 perp. to $\lambda$ disp. | 0.08 for NIS1<br>0.14 for NIS2 | $4 \times 4$ |
| **Hinode/EIS** | EISA : 170-210Å<br>EISB : 250-290Å | $266 \times 512$<br>$40 \times 512$<br>$2 \times 512$<br>$1 \times 512$ | 1<br>2 | 0.047 at 185Å | $6 \times 8.5$ |

Table 4.1: Summary of the relevant characteristics of SoHO/SUMER, SoHO/CDS and Hinode/EIS.

### Coronal Diagnostic Spectrometer (CDS)

The CDS instrument (16) consists of a telescope and two spectrometers with entrance slits which have a common location at the telescope focal plane. The optical layout is given in figure 4.3.

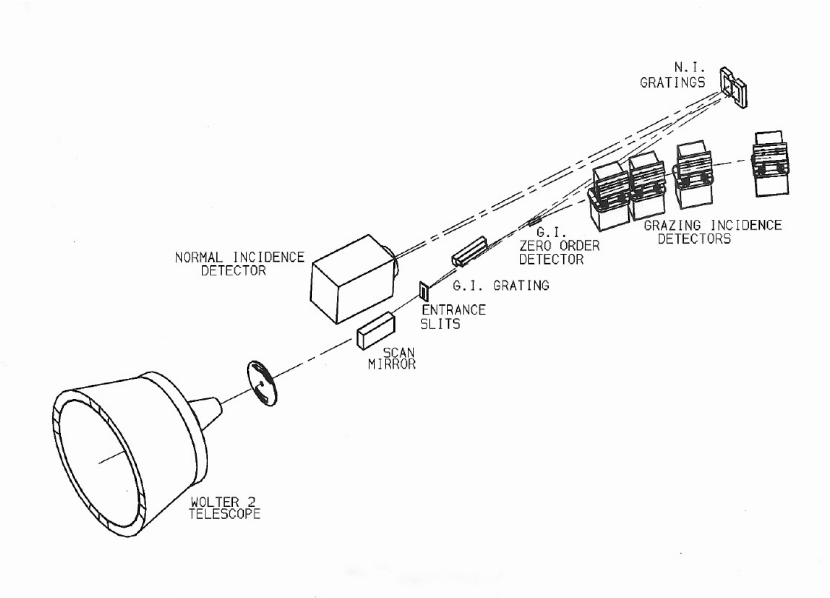


Figure 4.3: Optical layout of CDS instrument.

The telescope is a Wolter-Schwartzchild type 2 design. Only two portions of the telescope are used, one feeding each of the two spectrometers. Two apertures in a front panel define two light paths which feed separately a normal-incidence spectrometer (NIS) and a grazing-incidence spectrometer (GIS). The need of a double spectrometer is explained by the fact that for wavelengths less than ~300 Å the reflection efficiency in normal incidence becomes very small and thus grazing reflections must be used. However, for the purpose of this work, only the normal-incidence spectrometer has been involved in the observations. For lines with wavelengths shorter than 300 Å, in fact, the EIS instrument onboard Hinode has been used. Hence, the grazing incidence spectrometer will not be described here and only the characteristics of NIS have been reported in table 4.1. The spatial resolution of the CDS telescope is defined by the full width at half maximum intensity (FWHM) of the point spread function, that is the intensity distribution which results from the observation of an infinitely distant point source. For each of the NIS and GIS apertures of the telescope, the spatial resolution is given in the direction of wavelength dispersion and perpendicularly to it. For the NIS aperture, the FWHM values are 1.2 and 1.5 arcsec respectively. Before forming an image at the spetrometer's entrance slit, the beam from the telescope is reflected from a plane mirror which can scan over the slit the region of interest in the solar image through a rotation of up to ±2 arcmin. So, the maximum field of view is $4 \times 4$ arcmin$^2$. The entrance

slit is usually aligned North-South, thus images can be built up by moving the scan mirror in the East-West direction through a small angle in 2 arcsec steps. Three slits are available for the stigmatic normal incidence system: $90 \times 240$ arcsec$^2$, $4 \times 240$ arcsec$^2$, $2 \times 240$ arcsec$^2$. The largest slit is used as a feature locator, while the two narrowest slits provide the highest spectral resolution. The NIS spectrometer is basically a Rowland circle design with the exit beam direction along the Rowland circle diameter. The beam passes from the entrance slit onto two toroidal gratings (NIS1 and NIS2), mounted side by side as two parts of the same surface. The radiation is then dispersed by the pair of NIS gratings onto a two-dimensional CCD detector, known as the View finder Detector Subsystem (VDS), which consists of an array of 1024×1024 pixels with the two NIS bands illuminating 1024(spectral)×512(spatial) pixels. Finally, the spectral resolution is derived again from the grating equation (eq. 4.1), as described above for SUMER, and is given in table 4.1.

### 4.1.2 Outline of capabilities of EIS on Hinode

Hinode (59) is the successor to the Solar-A mission, named Yohkoh ("sunlight"). The spacecraft was called, in fact, by its development name Solar-B and the name Hinode was given after successful launch according to the Japanese satellite tradition. Hinode is, as Yohkoh, a Japanese word which means "sunrise". Yohkoh obtained results of extreme importance on the study of the dynamic structure of the corona, the explosive events, such as flares, and their strong connection with magnetic reconnection phenomena. In such a context, Hinode is designed to address the fundamental question of how magnetic field interacts with solar atmospheric plasmas to produce solar variability. Three instruments (Fig. 4.4) have been selected for this purpose: the Solar Optical Telescope (SOT), the EUV Imaging Spectrometer (EIS) and the X-Ray Telescope (XRT). These instruments usually work together studying the same target at which the spacecraft is pointed. However, EIS can offset its own pointing and XRT has the ability to observe its own region of interest. In this thesis only EIS has been used.

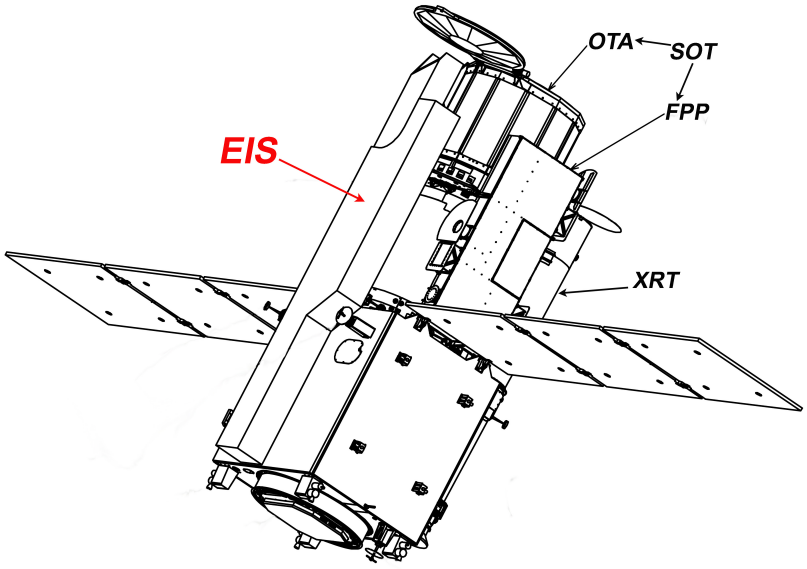


Figure 4.4: Hinode spacecraft schematic view. The instrument, EIS, with which the thesis is concerned is indicated in red.

After the launch, the Hinode spacecraft acquired a circular, Sun-synchronous, polar orbit at about 680 km attitude. With this orbit, Hinode can observe the Sun continuously for nine months each year. However, like other satellites in similar orbits (such as RHESSI and TRACE), there is an eclipse season, from late April until early September, during which the Sun is occasionally occluded by the Earth's atmosphere. It causes, during that period, attenuation and finally complete absorption of the radiation that would reach the instruments onboard Hinode. The data collected by the instruments, during the non eclipse periods, were downlinked to ground stations by two channels, the S-band,

which transmits real-time status, and the X-band, which transmits the data from a data recorder. For EIS, in particular, the data volume allocation was around 3 Gbits in 24 hours. Unfortunately, early in 2008 the X-band was lost and only the S-band can be now used. As a consequence, the data volume downloaded everyday was reduced to only a few hundred megabits. In order to improve the S-band performance, the level of data compression has been increased without significantly affecting the quality of the data and additional ground stations have been brought into operation, allowing an EIS allocation of 600 Mbits per day. Nevertheless, such an allocation puts severe constraints in the choice of the spectral lines when planning observations using EIS and it does not allow now the gathering of a full spectrum from the instrument, in practice.

**Extreme-ultraviolet Imaging Spectrometer (EIS)**

Following the CDS instrument on SoHO, EIS (17) provides the next step in EUV spectral imaging of the solar corona and upper transition region. This instrument achieves a large effective area in the two EUV wavelength bands 170-210 Å and 250-290 Å through the use of Mo/Si multilayer coatings[1], applied to both the telescope mirror and the grating. Optimum response is reached for each band by selection of thickness for the individual Si and Mo layers. Before the development of such multilayer coating technology, the only devices capable of high spectral resolution and sensitivity at wavelengths less than ~300 Å were essentially grazing incidence diffraction gratings, such as the CDS/GIS. However, they focus well only in the dispersion direction. The use of grazing incidence gratings has in fact limited focus capabilities. For instance, CDS/GIS uses a "Pin-Hole" slit and it is necessary to raster in two dimensions to produce an image. By contrast, normal incidence systems with toroidal gratings allow a focus along the slit, producing stigmatic images, while grazing incidence systems do not. Thus, the development of multilayer coating tool permits the implementation of normal-incidence gratings covering the shorter wavelengths and temperature ranges for high-resolution spectroscopic diagnostics. Additionally, a multilayer approach has been employed for EUV images in both the Extreme Ultraviolet Imaging Telescope (EIT) on SoHO and the Transition Region and Coronal Explorer (TRACE) satellite instruments as well as the Atmospheric Imaging Assembly (AIA) onboard the recently launched (on February 2010) Solar Dynamic Observatory (SDO). The optical design of the EIS instrument is shown in Fig. 4.5.

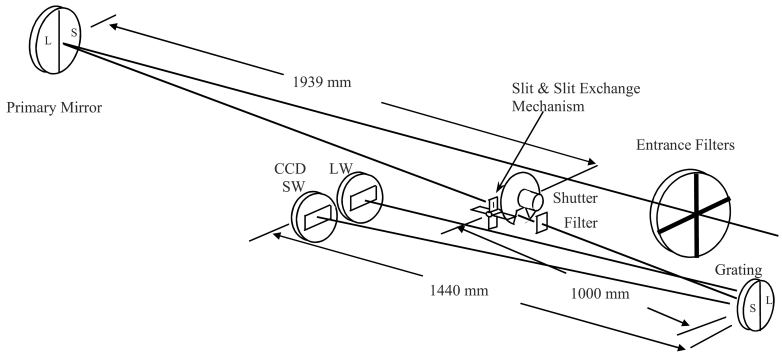


Figure 4.5: Optical layout of EIS instrument. SW and LW indicate respectively the short and long wavelength bands.

Solar radiation enters through an entrance filter, which stops the transmission of visible light. The paraboloid telescope primary mirror images the EUV radiation from the Sun to the spectrograph slit. The beam which passes through the slit is dispersed by the toroidal grating onto two CCD detectors, forming a stigmatic image. An interchange mechanism enables the selection of one of the four instrument slits/slots to support various observation programs. Two slots of 266 and 40 arcsec width and two slits of 2 and 1 arcsec width are available. Both slots and slits are 512 arcsec height. The largest slot is affected by significant spectral overlap, but it may be used to obtain images of large areas of the Sun with a single exposure, allowing the detection of transient events. For the 40 arcsec wide slot, effectively monochromatic images are available for several strong lines that do not overlap in the dispersion plane. The best resolution is obtained when the 1 arcsec slit is used, with a spectral dispersion of 0.047 Å $px^{-1}$ at 185 Å (Table 4.1), while for low brightness targets the 2 arcsec slit can be used instead in order to increase the photon flux. Raster scanning capability is provided

[1]Note that such coatings were not available at the time of SoHO.

by a system which rotates the primary mirror, covering a field of view of up to 6 arcmin in the dispersion direction and of 8.5 arcmin perpendicularly to the dispersion direction, along the slit height. There is, in addition, a coarse mechanism that can offset the mirror by ±15 arcmin from the spacecraft pointing axis in an E-W direction. Finally, the two CCD detectors, which consist of an array of 1024(spatial)×2048(spectral) pixels, are back-illuminated and thinned to maximise the efficiency.

## 4.2 Observations

### 4.2.1 Solar Joint Program

Since multiple instrument studies, using two SoHO instruments and an instrument onboard Hinode, have been involved in this work, a Joint Observing Program (JOP) proposal was necessary. A JOP proposal requires a fairly good knowledge of the capabilities of each instrument involved for compatible objectives within instrument limitations and restrictions. The JOP requires the participating SoHO instruments (SUMER and CDS in this case) and the other observatories (EIS onboard Hinode in this case), the scientific objective and justification (in order to explain why existing observations cannot fulfill the proposed aim) and the detailed observing sequences by instrument. Once the JOP has been accepted by the Science Operations Coordinators (SOCs), a JOP number is assigned and the JOP is reviewed at the SoHO monthly meetings, to be scheduled for a number of runs during one or more days. After the JOP run, a brief report on the data collected is given. At the same time as the JOP proposal, the use of an instrument onboard Hinode requires a further proposal, called Hinode Operation Plan (HOP), to be submitted to the Science Schedule Coordinators (SSCs). For this work, new JOP and HOP proposals have been written, submitted and accepted by the SOCs and SSCs. They include new *ad hoc* observational sequences, which have been designed taking into account the objective that this thesis wanted to achieve. Then, such sequences have been built up with the essential help of the expert team of each instrument involved. In this context, the present thesis explores a new data set obtained under Joint Observing Program 220 (JOP220) and Hinode Operation Plan 109 (HOP109), which aim to predict the EUV helium line intensities in the solar atmosphere. Having recognised what observations are required for this work, an original proposal for a combined SoHO JOP and Hinode HOP was made and constructed especially for this thesis. The joint observing campaign, to which this work is concerned, took place during April 2009. Two sets of observations have been provided, the first on $17^{th}$ April from 12:00 to 16:00 UT and the second on $28^{th}$ April from 20:00 to 24:00 UT. Only the first set has been selected and analysed hereinafter.

The Sun was very quiet in that period - it was a quite deep solar minimum of Solar Cycle 23/24 - so a pointing near the Sun centre for both the two sets of observations was chosen respectively about (0,-40) and (0,0)[2]. Hence, all images and spectra were obtained in quiet regions on the disk, but sometimes included small scale bright points[3], as happens in the first observation set.

The data have been taken by SoHO/SUMER, SoHO/CDS normal incidence spectrometer (NIS) and Hinode/EIS, using respectively 1×120 arcsec$^2$, 2×240 arcsec$^2$ and 1(/2)×256 arcsec$^2$ slits. The field of view covered by the three instruments are 90×120 arcsec$^2$ for SUMER, 80×240 arcsec$^2$ for CDS/NIS (except for the study `s40677r00` which covers instead the area 80×150 arcsec$^2$) and 60×256 arcsec$^2$ for EIS. Solar tracking was not active for CDS and EIS scans, while it was on for the two SUMER scans. However, because of the very quiet conditions during these observations, the general pattern of observed structures is very stable over extended periods of time. Moreover, the analysis is concentrated on the average of a large spatial area of the Sun (the common scanned regions). This reduces substantially the effects of small-scale and short-time fluctuactions, which are an intrinsic characteristic of the transition region and lower corona. Figure 4.6 shows the Sun's disk as seen in the He II 303.78 Å band of the EUV Imaging Telescope (EIT) onboard SoHO at 08:19:19 UT and includes the approximate locations of the SUMER, CDS and EIS first scans.

The new observation sequences have been written to cover the temperature range needed for the purpose of this thesis. They include the following line sets:

[2]The coordinates are given in arcseconds. The Sun centre is (Solar-X=0 arcsec, Solar-Y=0 arcsec). Positive X-values are westward and positive Y-values are northward.

[3]The bright points are small regions of intense emission observed in the quiet transition region and corona. EUV and soft-X ray observations suggest that they are associated with rapidly evolving magnetic bipolar regions and consist of a system of small-scale magnetic loops.

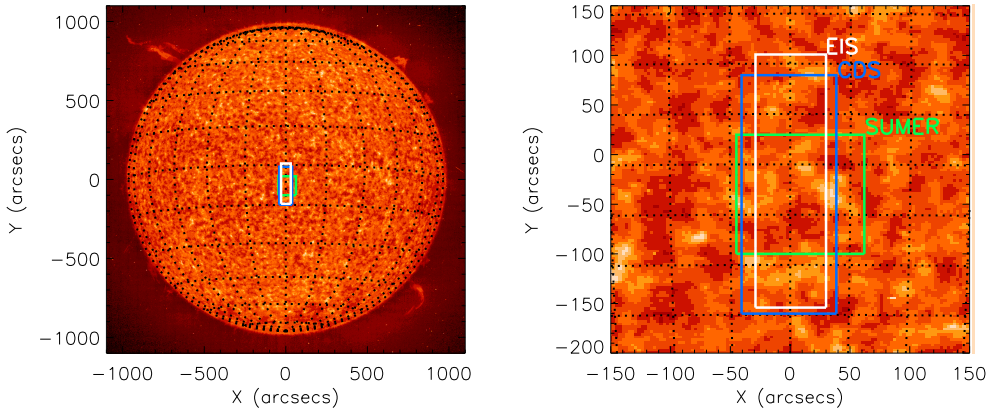


Figure 4.6: Regions observed by the three spectrometers, SUMER, CDS and EIS, on $17^{th}$ April 2009. The full disk image shows the Sun as observed in the He II 304 Å band. It was obtained by the EUV Imaging Telescope (EIT) onboard SoHO on the same date at 08:19:17 UT. The field of view and the pointing of the SUMER, CDS and EIS slits are marked with different colors, respectively green, blue and white. Only the first scan for each instrument has been shown. However, the pointing was fixed for the entire duration of the observations.

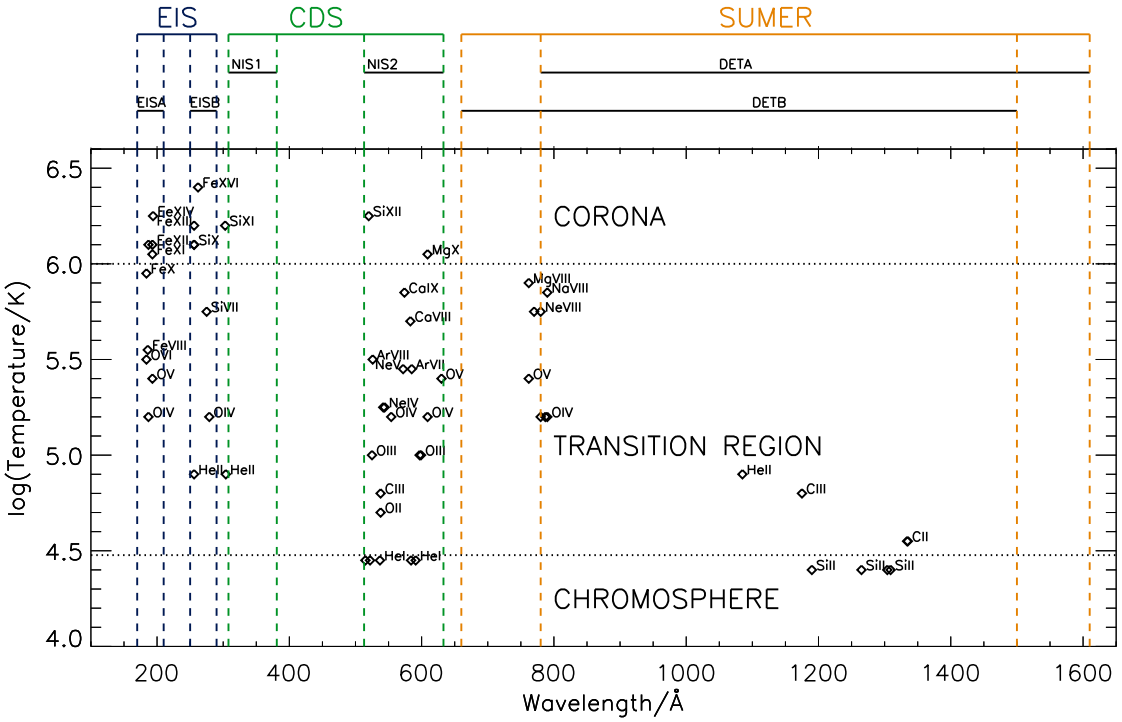


Figure 4.7: Emission lines observed by SUMER, CDS and EIS in the JOP220/HOP109 on $17^{th}$ April 2009 together with the instrument wavelength coverages. Also, the temperatures of line formation have been shown, in order to indicate the atmosphere layer from where the considered lines arise. The second order has not been plotted, but it is important to notice that SUMER observes both O V 629.7 Å and He I 584.3 Å in the second order. The overlap in such wavelength bands is essential for the inter-calibration between SUMER and CDS. Furthermore, CDS observes He II 304.8 Å in the second order which can help to co-align CDS and EIS.

- the EUV He I and He II lines, observed by CDS and EIS;
- *chromospheric* lines at $\log(T/\mathrm{K}) \leq 4.5$, including Si II and C II, observed by SUMER;

- *transition region* lines at intermediate temperatures, 4.5≤log($T$/K)≤6.0, including O III, O IV, OV, Ne V, observed mainly by CDS;
- *coronal* lines at log($T$/K)≥6.0, including Fe X and Fe XII, observed by EIS;
- lines for co-alignment and cross-calibration, that is lines which are in common for at least two instruments, such as O V 629.73 Å and He I 584.33 Å, observed by both CDS and SUMER in the second order, or lines formed by the same ion, such as O IV (e.g.: 790 Å doublet from SUMER, 554 Å multiplet from CDS and 279.93 Å from EIS), O V (e.g.: 762.00 Å from SUMER, 629.73 Å from CDS and 192.9 Å multiplet from EIS), He II (e.g.: 303.78 Å doublet from CDS and 256.3 Å doublet from EIS).

A complete summary of the observed lines as function of temperature and wavelength is illustrated in figure 4.7. More details about the specific lines and transitions involved are listed in the following subsections in tables 4.4, 4.5, 4.6.

Figure 4.8 shows an example of SUMER, CDS and EIS scans. Comparing the field of view observed by these three spectrometers, it is possible to see that they show a quiet Sun region with typical network structures, as seen in the chromospheric/transition region line images (Si II and C II) on the left, with a small coronal bright point located near the right edge of EIS field of view, as seen in the two EIS images (Fe X and Fe XII) on the right.

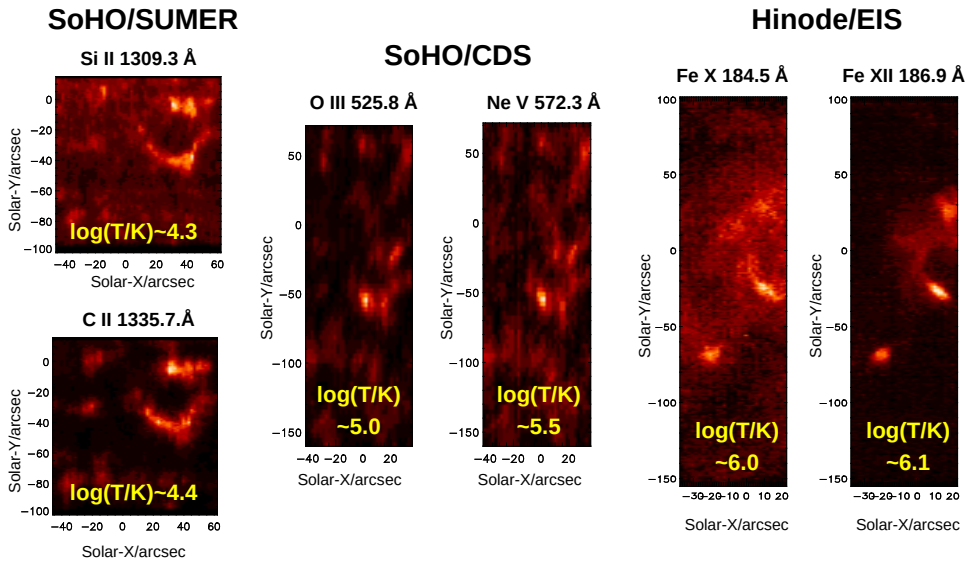


Figure 4.8: Examples of SUMER, CDS and EIS scans. The first two images on the left show Si II 1309.3 Å and C II 1335.7 Å lines, which are formed at temperatures around log($T$/K)~4.2-4.6. The two central images of O III 525.8 Å and Ne V 572.3 Å come from CDS. They show how the intensity distribution changes for lines formed at these higher temperatures (log($T$/K)~5.0-5.5) and this temperature dependence is illustrated in the last two images on the right, which display two EIS scans in Fe X 184.5 Å and Fe XII 186.9Å wavelength bands. A small bright point, located near the right of field of view, is seen in the latter two coronal images.

The SUMER, CDS and EIS new sequences were designed to guarantee the spatial and temporal overlap between the instruments and this is shown in fig. 4.9 and table 4.2 for $17^{th}$ April. Two raster maps were made with SUMER, by moving the slit in the east-west direction. The first scan includes the bands with wavelengths shorter than the Lyman-$\alpha$ limit ($\lambda_{Ly-\alpha}$=1215.7 Å), while the second scan includes the wavelength ranges greater than that limit. By contrast, the six CDS and the nine EIS scans were built up moving their respective slits in the west-east direction. Each scan contains the whole set of wavelength bands, selected for the CDS and EIS observation sequences.

The first SUMER scan ovelaps roughly with the first three CDS and EIS rasters. The second SUMER scan overlaps with the fourth and part of the fifth CDS rasters and the fourth, fifth and part of the sixth EIS rasters. To mitigate the effects of the lack of completely co-temporal alignment, the CDS and EIS rasters can be averaged together and then analysed with the two SUMER rasters. Again, this can be done because the observed region, with which this thesis is concerned, is a quiet Sun region.

| **SUMER** | | |
|---|---|---|
| Scan number | Scan sequence | Time interval/UT |
| 1 | raster_1 | 12:00-14:00 |
| 2 | raster_2 | 14:05-15:17 |
| **CDS** | | |
| Scan number | Scan sequence | Time interval/UT |
| 1 | s40676r00 | 12:00-12:47 |
| 2 | s40676r01 | 12:47:13:34 |
| 3 | s40676r02 | 13:34-14:21 |
| 4 | s40676r03 | 14:21-15:08 |
| 5 | s40677r00 | 15:09-15:50 |
| 6 | s40678r00 | 15:50-16:37 |
| **EIS** | | |
| Scan number | Scan sequence | Time interval/UT |
| 1 | eis_l0_20090417_120241 | 12:02-12:43 |
| 2 | eis_l0_20090417_124423 | 12:44-12:25 |
| 3 | eis_l0_20090417_132605 | 13:26-14:07 |
| 4 | eis_l0_20090417_140748 | 14:07-14:48 |
| 5 | eis_l0_20090417_145842 | 14:58-15:09 |
| 6 | eis_l0_20090417_150933 | 15:09-15:20 |
| 7 | eis_l0_20090417_152025 | 15:20-15:30 |
| 8 | eis_l0_20090417_153117 | 15:31-15:41 |
| 9 | eis_l0_20090417_154209 | 15:42-15:52 |

Table 4.2: Time covered by each scan of SUMER, CDS and EIS.

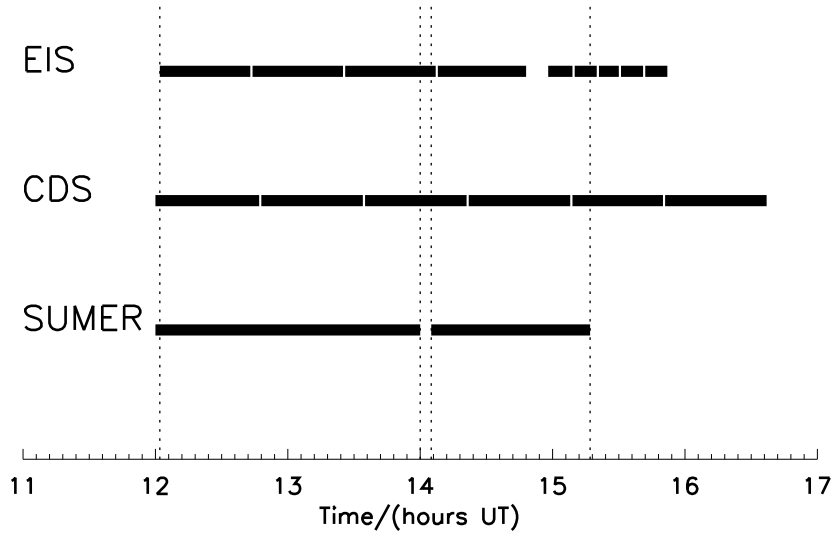


Figure 4.9: Timing of the various SUMER, CDS and EIS scans obtained during the JOP220/HOP109 on $17^{th}$ April 2009.

The exposure time at each location was 30 s for SUMER, 55 s for CDS and 40 s for EIS. For each instrument, it was large enough to ensure a quite high signal-to-noise ratio in the observed fluxes.

A final table (Table 4.3) summarises the main details of the joint observations used in this thesis.

| Observing parameter | SUMER | CDS | EIS |
|---|---|---|---|
| Start | 12:00 UT | 12:00 UT | 12:02 UT |
| End | 15:17 UT | 16:37 UT | 15:52 UT |
| Pointing center | ~(0",-40") | ~(-1",-40") | ~(0.9",-26") |
| Slit size | 1"×120" | 2"×240" | 1"(/2")×256" |
| Field of view | 90"×120" | 80"×240"(/150") | 60"×256" |
| Exposure time | 30 s | 55 s | 40 s |
| Spectral windows | 19 | 14 | 7 |
| Number of scans | 2 | 6 | 9 |
| Name of sequence | HELI80N/HELI34W | RAL_HE_INT_1(/2)SLIT | Giunta.scl |

Table 4.3: General details of joint SUMER/CDS/EIS observations gathered on $17^{th}$ April 2009.

**SUMER**

As explained, new observation sequences have been written for the three spectrometers, in order to cover the wavelength range needed to study the EUV helium line intensities and perform an accurate differential emission measure analysis (see later). In particular, SUMER provides, *inter alia*, lines formed at the low temperatures typical of upper chromosphere/lower transition region, such as lines from Si II and C II. These lines fall in the wavelength range between 1260 Å and 1336 Å. In addition, lines for co-alignment with CDS and EIS are needed. Hence, lines such as He I 584.33 Å, which is in common with CDS, and lines from ions like O IV and O V, which are observed by CDS and EIS too, must be included in the sequence. This last set of lines fall in the wavelength range between 770 Å and 1190 Å. So the first line set covers a spectral region with wavelengths greater than the Lyman-$\alpha$ limit, whereas the second line set includes wavelengths shorter than $\lambda_{Ly-\alpha}$. Each time that the Lyman-$\alpha$ is crossed the detector High-Voltage (HV) has to be lowered. As a consequence, it was convenient to split the observations into two parts, one towards "blue" of Lyman-$\alpha$ and one towards "red" of that limit. The first part includes three sets of spectral windows:

1. band_07704, band_07803,band_7901, band_07619, band_07877;
2. band_10857, band_10836, band_10770, band_10729;
3. band_11686[4], band_11748, band_10770, band_11904.

The second part includes two sets of spectral windows:

1. band_06297[5], band_12648;
2. band_13043, band_13092, band_13345, band_13357.

Therefore, SUMER built up a first raster in three bands (the first three sets of spectral windows), then crossed the Lyman-$\alpha$ limit and built up a second raster in the two remaining bands (the second two sets of spectral windows). The observation study resulted into 1140 images, which have been made up by 19 spectral windows and 60 increments. So, each raster was built up by repeating 60 times the sequence of the bands followed by a movement of the azimuth drive of 1.5 arcsec (that is four elementary steps of 0.37 arcsec each) along the direction East-to-West. Since the exposure time was 30 s at each position, the first complete raster scan took ~2 hours and 1 minute while the second raster scan took ~1 hour and 13 minutes. After the first raster sequence was made up, the Lyman-$\alpha$ was crossed with HV off and the second raster was done with the same pointing. Furthermore, due to the rotation compensation, the instrument introduced a 0.75 arcsec step every about 5 minutes to track the solar rotation. However, those 0.75 arcsec increments are practically smeared within the instrument resolution, because the SUMER point spread function is ~ 1.5 arcsec.

The spectra have been acquired by the detector B and compressed during the downlink. After the decompression, the standard data reduction has been applied. The images have been flatfielded, destretched and corrected for geometric distorsion, deadtime and local gain depression effects. The next step was the radiometric calibration, in order to convert the intensity from counts into physical units. The procedure described by (60) has been used, including

[4]Note that this band contains the He I 584.33 Å at the second order.

[5]As for He I 584.33 Å, this band contains the O V 629.73 Å line, which is observed in the SUMER second order.

a correction factor of 43% to take into account the decrease of sensitivity due to the loss of SoHO. This suggests an uncertainty of the radiometric calibration of about 30% after the SoHO recovery. Regarding the units, it has been decided to adopt $photons\,cm^{-2}\,s^{-1}\,sr^{-1}$ for all the data from the three spectrometers, in order to get easier the subsequent comparison and joint use. Finally, spectral pixels have been converted to wavelengths. Since there is no absolute wavelength reference available in the spectrometer, various paths can be followed to establish a wavelength scale. Firstly, reference wavelength positions have to be identified. Then, the knowledge of the dispersion curve on the detector is used to measure the wavelengths of emission lines from their relative positions to the reference lines in the same detector field. Here, the pixel-to-wavelength relation for each spectral window is achieved through three main steps:

1. A reference wavelength has been selected, using preferably emission lines which are enough strong and unblended and for which the absolute wavelength are known with high accuracy. They can be "cool" chromospheric lines, from neutral or singly ionised species, or "hot" coronal lines with relatively negligible average absolute shifts.
2. The centroids of the reference lines have been determined by comparing shifts along various parts of the slit length.
3. The wavelength scale is obtained using the reference wavelengths and the correlated line centroids by means of the dispersion curve. It should be noted that for SUMER the dispersion changes as a function of wavelength.

Figures 4.11 and 4.12 show the 19 spectral windows calibrated in wavelengths. The first 13 bands are observed in the first raster, the other six bands are from the second raster. The lines observed are specified in red. Both C II and C III multiplets are split into two differents windows: `band_11748` and `band_11770` for C III and `band_13345` and `band_13357` for C II. Unfortunately, as illustrated by figure 4.10, the overlap of the band pairs does not allow a good reconstruction of the two multiplets. This can affect the fit of some of the lines involved in those multiplets. For this reason, only the lines at 1174.93 Å, 1175.26 Å and 1176.37 for the C III multiplet and the line at 1334.53 Å and 1335.71 Å for the C II multiplet will be included in the subsequent analysis. For the C III multiplet (fig. 4.10(a)), the main problem is that the two strongest lines (1175.59 Å and 1175.71 Å) are close to the edge of the two windows. As a consequence the integrated intensity along the line profiles is not reliable. For the C II multiplet (fig. 4.10(b)), the cut between the two spectral windows falls in the left wing of the two lines at 1335.66 Å and 1335.71 Å, so the integrated intensities of these two C II lines may be still acceptable at least for forward checking analysis.

A complete list of lines observed by SUMER is provided in Table 4.4. The line identifications have been compared with the work of (60). Further checks have been done looking at the relative intensities of the lines and at the centroid positions along the slit. Also, the transitions have been specified for each line and the identified blends have been marked with the letter "*b*" as a prefix of the ion symbol. This first line analysis will help to select the lines suitable for the differential emission measure and line ratio investigation. In addition, table 4.4 gives the order at which the identified lines are observed. Only two SUMER lines are in the second order, He I 584.33 Å and O V 629.73 Å, which are essential for co-alignment mainly with CDS and eventually with EIS.

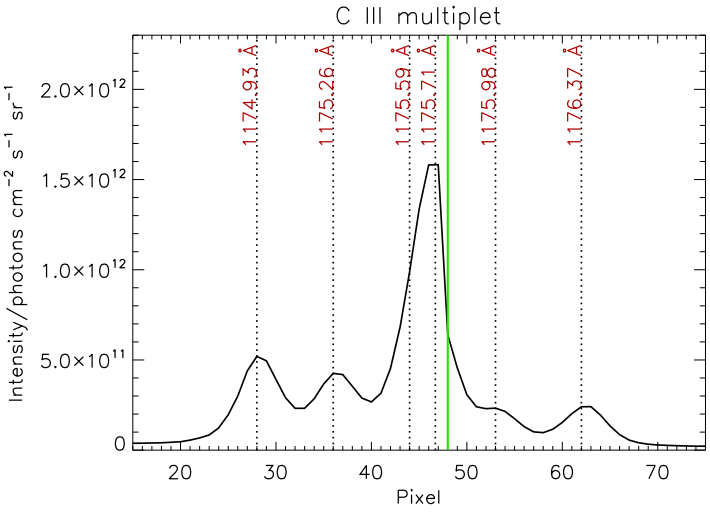


(a)

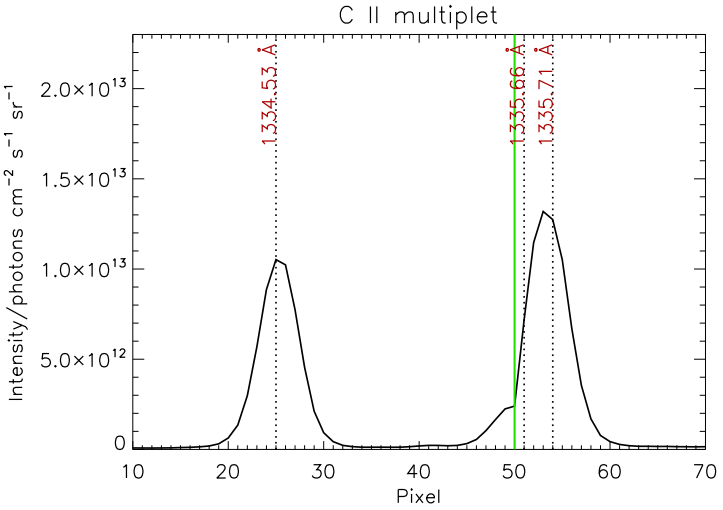


(b)

Figure 4.10: **(a)** Spectral interval spanning the C III $2s2p\,^3P - 2p^2\,^3P$ multiplet with component identification. The ordinate scale records the integrated intensity along the line of sight. The multiplet has been built up putting together the two windows band_11748 and band_11770. The vertical green line shows the end of the band_11748 and the beginning of the next band (band_11770). **(b)** Spectral interval spanning the C II $2s^2 2p\,^2P - 2s2p^2\,^2D$ multiplet with component identification. The multiplet has been built up putting together the two windows band_13345 and band_13357. Again, the ordinate scale records the integrated intensity along the line of sight and the green line shows where the first band finishes and the second one starts.

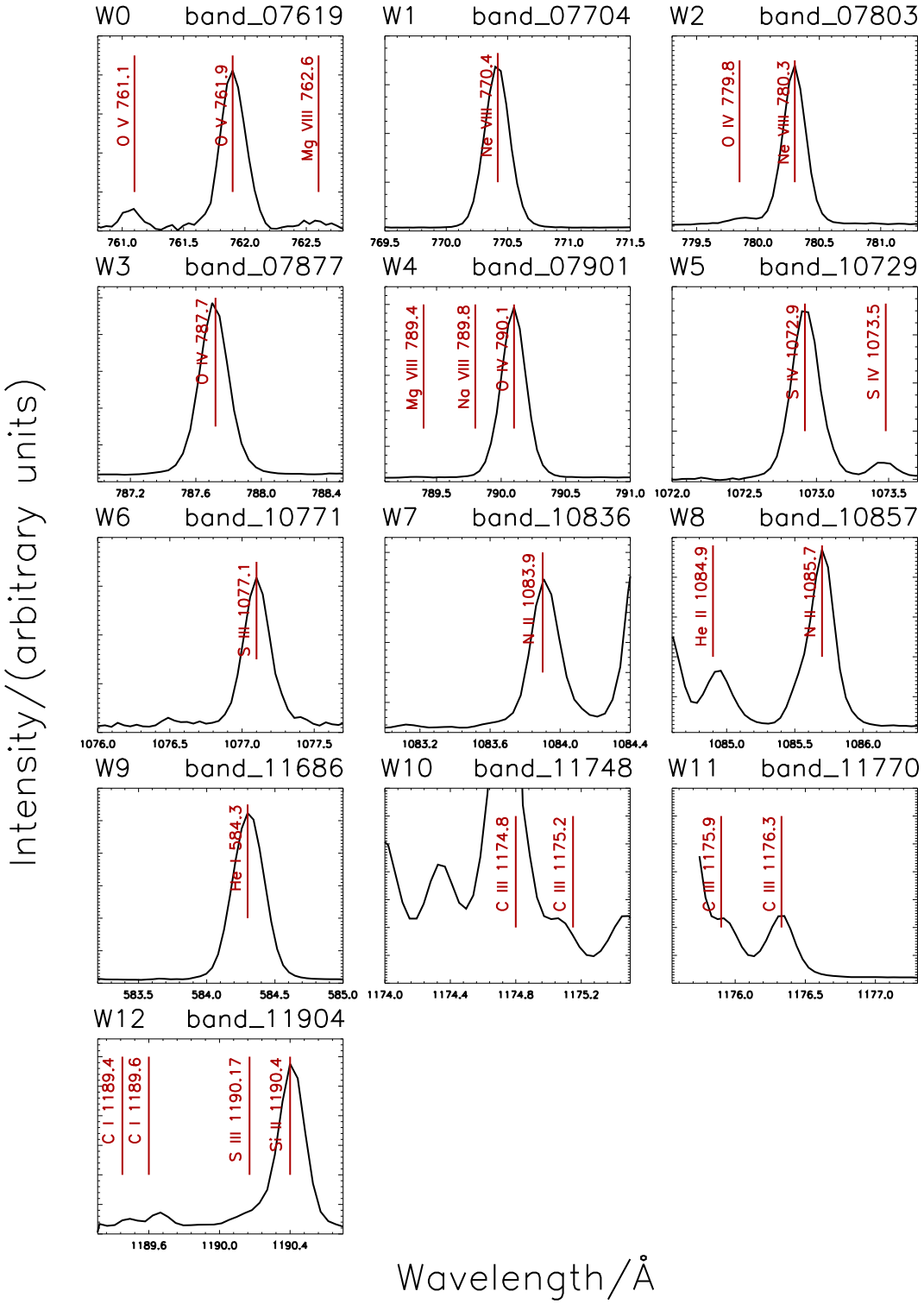


Figure 4.11: Average line profiles as a function of wavelength for the first SUMER raster ($\lambda < \lambda_{Ly-\alpha}$). The intensity along the Y-axis is in arbitrary units, while the wavelength along the X-axis is given in Angstrom. The red vertical lines with labels are the line identified for each spectral windows.

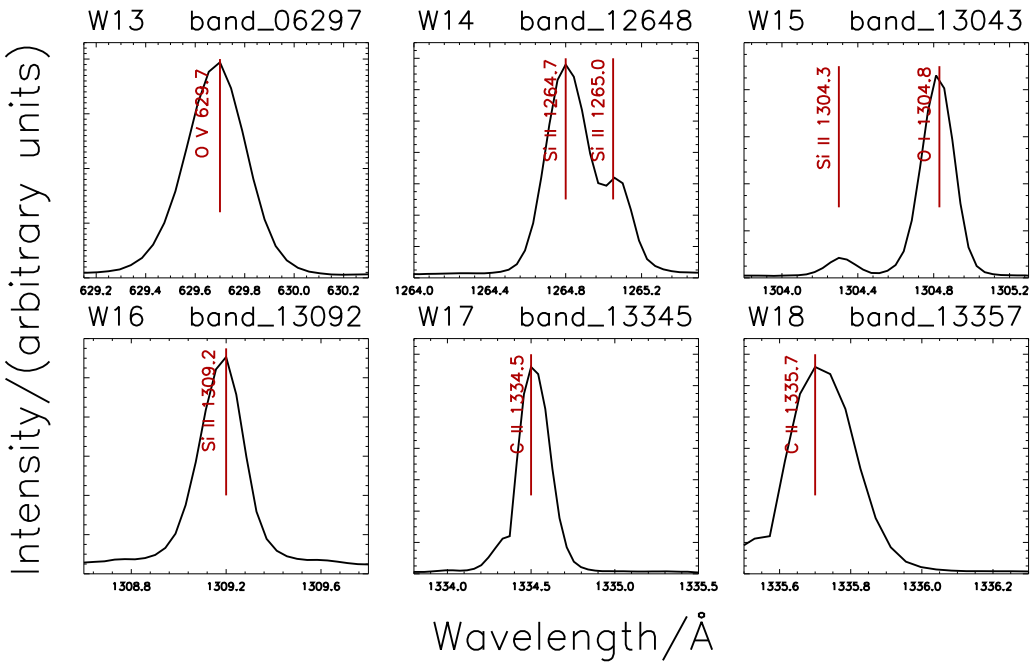


Figure 4.12: Average line profiles as a function of wavelength for the second SUMER raster ($\lambda > \lambda_{Ly-\alpha}$). Same comments as for fig. 4.11 can be done.

Table 4.4: List of the selected lines observed by SoHO/SUMER. Ions, wavelengths and atomic transitions are provided to allow the selection of ions of which the atomic data will be reviewed in chapter 5. Additionally, the order is given. Blends are indicaded by the letter "b"which is put just before the ion.

| Ion | Wavelength/Å | Transition | Order |
|---|---|---|---|
| $O^{+4}$ | 761.13 | $2s2p\,^3P_1 - 2p^2\,^3P_0$ | First |
| $O^{+4}$ | 761.99 | $2s2p\,^3P_2 - 2p^2\,^3P_1$ | First |
| $Mg^{+7}$ | 762.65 | $2s^22p\,^2P_{1/2} - 2s2p^2\,^4P_{3/2}$ | First |
| $Ne^{+7}$ | 770.42 | $1s^22s\,^2S_{1/2} - 1s^22p\,^2P_{3/2}$ | First |
| $bO^{+3}$ | 779.73 | $2s2p^2\,^2D_{5/2} - 2p^3\,^2D_{3/2}$ | First |
| $bO^{+3}$ | 779.82 | $2s2p^2\,^2D_{3/2} - 2p^3\,^2D_{3/2}$ | First |
| $bO^{+3}$ | 779.91 | $2s2p^2\,^2D_{5/2} - 2p^3\,^2D_{5/2}$ | First |
| $bO^{+3}$ | 780.00 | $2s2p^2\,^2D_{3/2} - 2p^3\,^2D_{5/2}$ | First |
| $Ne^{+7}$ | 780.30 | $1s^22s\,^2S_{1/2} - 1s^22p\,^2P_{1/2}$ | First |
| $O^{+3}$ | 787.72 | $2s^22p\,^2P_{1/2} - 2s2p^2\,^2D_{3/2}$ | First |
| $Mg^{+7}$ | 789.43 | $2s^22p\,^2P_{3/2} - 2s2p^2\,^4P_{1/2}$ | First |
| $Na^{+7}$ | 789.78 | $2s^2\,^1S_0 - 2s2p\,^3P_1$ | First |
| $bO^{+3}$ | 790.11 | $2s^22p\,^2P_{3/2} - 2s2p^2\,^2D_{3/2}$ | First |
| $bO^{+3}$ | 790.19 | $2s^22p\,^2P_{3/2} - 2s2p^2\,^2D_{5/2}$ | First |
| $S^{+3}$ | 1072.99 | $3s^23p\,^2P_{3/2} - 3s3p^2\,^2D_{5/2}$ | First |
| $S^{+3}$ | 1073.53 | $3s^23p\,^2P_{3/2} - 3s3p^2\,^2D_{3/2}$ | First |
| $S^{+2}$ | 1077.14 | $3s^23p^2\,^1D_2 - 3s^23p3d\,^1D_2$ | First |
| $N^{+1}$ | 1083.99 | $2s^22p^2\,^3P_0 - 2s2p^3\,^3D_1$ | First |
| $bHe^{+1}$ | 1084.91 | $2p\,^2P_{1/2} - 5d\,^2D_{3/2}$ | First |
| $bHe^{+1}$ | 1084.91 | $2p\,^2P_{1/2} - 5s\,^2S_{1/2}$ | First |
| $bHe^{+1}$ | 1084.91 | $2s\,^2S_{1/2} - 5p\,^2P_{3/2}$ | First |
| $bHe^{+1}$ | 1084.92 | $2s\,^2S_{1/2} - 5p\,^2P_{1/2}$ | First |
| $bHe^{+1}$ | 1084.97 | $2p\,^2P_{3/2} - 5d\,^2D_{5/2}$ | First |
| $bHe^{+1}$ | 1084.98 | $2p\,^2P_{3/2} - 5d\,^2D_{3/2}$ | First |
| $bHe^{+1}$ | 1084.98 | $2p\,^2P_{3/2} - 5s\,^2S_{1/2}$ | First |
| $bN^{+1}$ | 1085.54 | $2s^22p^2\,^3P_2 - 2s2p^3\,^3D_2$ | First |
| $bN^{+1}$ | 1085.70 | $2s^22p^2\,^3P_2 - 2s2p^3\,^3D_3$ | First |
| $He^{+0}$ | 584.33 | $1s^2\,^1S_0 - 1s2p\,^1P_1$ | Second |
| $C^{+2}$ | 1174.93 | $2s2p\,^3P_1 - 2p^2\,^3P_2$ | First |
| $C^{+2}$ | 1175.26 | $2s2p\,^3P_0 - 2p^2\,^3P_1$ | First |
| $bC^{+2}$ | 1175.59 | $2s2p\,^3P_1 - 2p^2\,^3P_1$ | First |
| $bC^{+2}$ | 1175.71 | $2s2p\,^3P_2 - 2p^2\,^3P_2$ | First |
| $C^{+2}$ | 1175.99 | $2s2p\,^3P_1 - 2p^2\,^3P_0$ | First |
| $C^{+2}$ | 1176.37 | $2s2p\,^3P_2 - 2p^2\,^3P_1$ | First |
| $C^{+0}$ | 1189.45 | $2s^22p^2\,^3P_2 - 2s^22p4d\,^3P_1$ | First |
| $C^{+0}$ | 1189.63 | $2s^22p^2\,^3P_2 - 2s^22p4d\,^3P_2$ | First |
| $S^{+2}$ | 1190.17 | $3s^23p^2\,^3P_0 - 3s3p^3\,^3D_1$ | First |

Table 4.4: – continued

| Ion | Wavelength/Å | Transition | Order |
|---|---|---|---|
| $Si^{+1}$ | 1190.42 | $3s^2 3p\,^2P_{1/2} - 3s3p^2\,^2P_{3/2}$ | First |
| $O^{+4}$ | 629.73 | $2s^2\,^1S_0 - 2s2p\,^1P_1$ | Second |
| $Si^{+1}$ | 1264.74 | $3s^2 3p\,^2P_{3/2} - 3s^2 3d\,^2D_{5/2}$ | First |
| $Si^{+1}$ | 1265.00 | $3s^2 3p\,^2P_{3/2} - 3s^2 3d\,^2D_{3/2}$ | First |
| $Si^{+1}$ | 1304.37 | $3s^2 3p\,^2P_{1/2} - 3s3p^2\,^2S_{1/2}$ | First |
| $O^{+0}$ | 1304.86 | $2s^2 2p^4\,^3P_1 - 2s^2 2p^3 3s\,^3S_1$ | First |
| $Si^{+1}$ | 1309.28 | $3s^2 3p\,^2P_{3/2} - 3s3p^2\,^2S_{1/2}$ | First |
| $C^{+1}$ | 1334.53 | $2s^2 2p\,^2P_{1/2} - 2s2p^2\,^2D_{3/2}$ | First |
| $C^{+1}$ | 1335.66 | $2s^2 2p\,^2P_{3/2} - 2s2p^2\,^2D_{3/2}$ | First |
| $C^{+1}$ | 1335.71 | $2s^2 2p\,^2P_{3/2} - 2s2p^2\,^2D_{5/2}$ | First |

**CDS**

The CDS data employed in this work have been taken using the HELI80N (ID 122 var. 8/9) observing sequence. This takes all the resonance lines of neutral helium which fall in the wavelength range of NIS2 and includes the intercombination lines at 591.41 Å and the doublet of He II at 303.78 Å at the second order. These are the main lines for helium line intensity prediction, together with the He II 256.32 Å doublet observed by EIS. In addition, lines which cover a wide temperature range are observed to allow a complete analysis of the different layers of the solar upper atmosphere. A full list of lines observed by CDS is given in table 4.5, which shows, as table 4.4 for SUMER, the line identification and the order at which they are observed.

The 14 spectral windows as a function of wavelength, used in this thesis, are displayed in figure 4.13. Regarding window 5, specified by `AL_11_549_96`, it should display a line at 550.03 Å, which was identified as Al XI by (18), and a blend of two lines of the Si VII multiplet at the second order. However, their intensities and shapes are significantly affected by the much stronger O IV multiplet, shown in window 6 (`O_4_554_40`).

The HELI80N var. 8 sequence builds up a raster using the $2 \times 240$ arcsec$^2$ slit by moving it to 40 adjacent locations to give an area of the Sun of $80 \times 240$ arcsec$^2$, ignoring the contribution of solar rotation. For the HELI80N var. 9 sequence, instead of the $2 \times 240$ arcsec$^2$ slit, the reduced $2 \times 150$ arcsec$^2$ slit was chosen. The exposure time at each raster step was 55 s and the whole sequence took 46 minutes and 50 seconds using variation 8 and 41 minutes and 40 second using variation 9. The HELI80N var. 8 sequence run four times, then the HELI80N var. 9 once and finally the HELI80N var. 8 sequence once again. In total, the following six observational studies have been done: `s40676r00`, `s40676r01`, `s40676r02`, `s40676r03`, `s40677r00`, `s40678r00`. However, the last sequence run from 15:50 to 16:37 UT, outside of the time covered by both SUMER and EIS (fig. 4.9 and table 4.2). Hence, it will not be included in subsequent analysis. Only the first five CDS scans will be considered.

Table 4.5: List of the selected lines observed by SoHO/CDS. Ions, wavelengths and atomic transitions are provided to allow the selection of ions of which the atomic data will be reviewed in chapter 5. Additionally, the order is given. Blends are indicaded by the letter "*b*"which is put just before the ion.

| Ion | Wavelength/Å | Transition | Order |
|---|---|---|---|
| $He^{+0}$ | 515.62 | $1s^2\,^1S_0 - 1s5p\,^1P_1$ | First |
| $Si^{+11}$ | 520.66 | $2s\,^2S_{1/2} - 2p\,^2P_{1/2}$ | First |
| $He^{+0}$ | 522.21 | $1s^2\,^1S_0 - 1s4p\,^1P_1$ | First |
| $O^{+2}$ | 525.80 | $2s^22p^2\,^1D_2 - 2s2p^3\,^1P_1$ | First |
| $Ar^{+7}$ | 526.49 | $3p\,^2P_{3/2} - 3d\,^2D_{5/2}$ | First |
| $He^{+0}$ | 537.03 | $1s^2\,^1S_0 - 1s3p\,^1P_1$ | First |
| $bC^{+2}$ | 538.08 | $2s2p\,^3P_0 - 2s3s\,^3S_1$ | First |
| $bC^{+2}$ | 538.15 | $2s2p\,^3P_1 - 2s3s\,^3S_1$ | First |
| $bC^{+2}$ | 538.31 | $2s2p\,^3P_2 - 2s3s\,^3S_1$ | First |
| $bO^{+1}$ | 537.83 | $2s^22p^3\,^2D_{3/2} - 2s2p^4\,^2P_{1/2}$ | First |
| $bO^{+1}$ | 538.26 | $2s^22p^3\,^2D_{5/2} - 2s2p^4\,^2P_{3/2}$ | First |
| $bO^{+1}$ | 538.32 | $2s^22p^3\,^2D_{3/2} - 2s2p^4\,^2P_{3/2}$ | First |
| $Ne^{+3}$ | 542.07 | $2s^22p^3\,^4S_{3/2} - 2s2p^4\,^4P_{3/2}$ | First |
| $Ne^{+3}$ | 543.88 | $2s^22p^3\,^4S_{3/2} - 2s2p^4\,^4P_{5/2}$ | First |
| $Al^{+10}$ | 550.03 | $2s\,^2S_{1/2} - 2p\,^2P_{3/2}$ | First |
| $bSi^{+6}$ | 275.35 | $2s^22p^4\,^3P_2 - 2s2p^5\,^3P_2$ | Second |
| $bSi^{+6}$ | 275.67 | $2s^22p^4\,^3P_1 - 2s2p^5\,^3P_1$ | Second |
| $O^{+3}$ | 553.33 | $2s^22p\,^2P_{1/2} - 2s2p^2\,^2P_{3/2}$ | First |
| $O^{+3}$ | 554.08 | $2s^22p\,^2P_{1/2} - 2s2p^2\,^2P_{1/2}$ | First |
| $O^{+3}$ | 554.51 | $2s^22p\,^2P_{3/2} - 2s2p^2\,^2P_{3/2}$ | First |
| $O^{+3}$ | 555.76 | $2s^22p\,^2P_{3/2} - 2s2p^2\,^2P_{1/2}$ | First |
| $bNe^{+4}$ | 572.11 | $2s^22p^2\,^3P_2 - 2s2p^3\,^3D_2$ | First |
| $bNe^{+4}$ | 572.33 | $2s^22p^2\,^3P_2 - 2s2p^3\,^3D_3$ | First |
| $Ca^{+9}$ | 574.01 | $3s\,^2S_{1/2} - 3p\,^2P_{1/2}$ | First |
| $Ca^{+7}$ | 582.84 | $3s^23p\,^2P_{1/2} - 3s3p^2\,^2D_{3/2}$ | First |
| $He^{+0}$ | 584.33 | $1s^2\,^1S_0 - 1s2p\,^1P_1$ | First |
| $Ar^{+6}$ | 585.75 | $3s^2\,^1S_0 - 3s3p\,^1P_1$ | First |
| $bHe^{+0}$ | 591.41 | $1s^2\,^1S_0 - 1s2p\,^3P_1$ | First |
| $bHe^{+0}$ | 591.41 | $1s^2\,^1S_0 - 1s2p\,^3P_2$ | First |
| $O^{+2}$ | 597.82 | $2s^22p^2\,^1S_0 - 2s2p^3\,^1P_1$ | First |
| $O^{+2}$ | 599.60 | $2s^22p^2\,^1D_2 - 2s2p^3\,^1D_2$ | First |
| $Si^{+10}$ | 303.33 | $2s^2\,^1S_0 - 2s2p\,^1P_1$ | Second |
| $bHe^{+1}$ | 303.78 | $1s\,^2S_{1/2} - 2p\,^2P_{3/2}$ | Second |
| $bHe^{+1}$ | 303.79 | $1s\,^2S_{1/2} - 2p\,^2P_{1/2}$ | Second |
| $O^{+3}$ | 608.40 | $2s^22p\,^2P_{1/2} - 2s2p^2\,^2S_{1/2}$ | First |
| $bMg^{+9}$ | 609.79 | $2s\,^2S_{1/2} - 2p\,^2P_{3/2}$ | First |
| $bO^{+3}$ | 609.83 | $2s^22p\,^2P_{3/2} - 2s2p^2\,^2S_{1/2}$ | First |

Table 4.5: – continued

| Ion | Wavelength/Å | Transition | Order |
|---|---|---|---|
| $O^{+4}$ | 629.73 | $2s^2\ ^1S_0 - 2s2p\ ^1P_1$ | First |

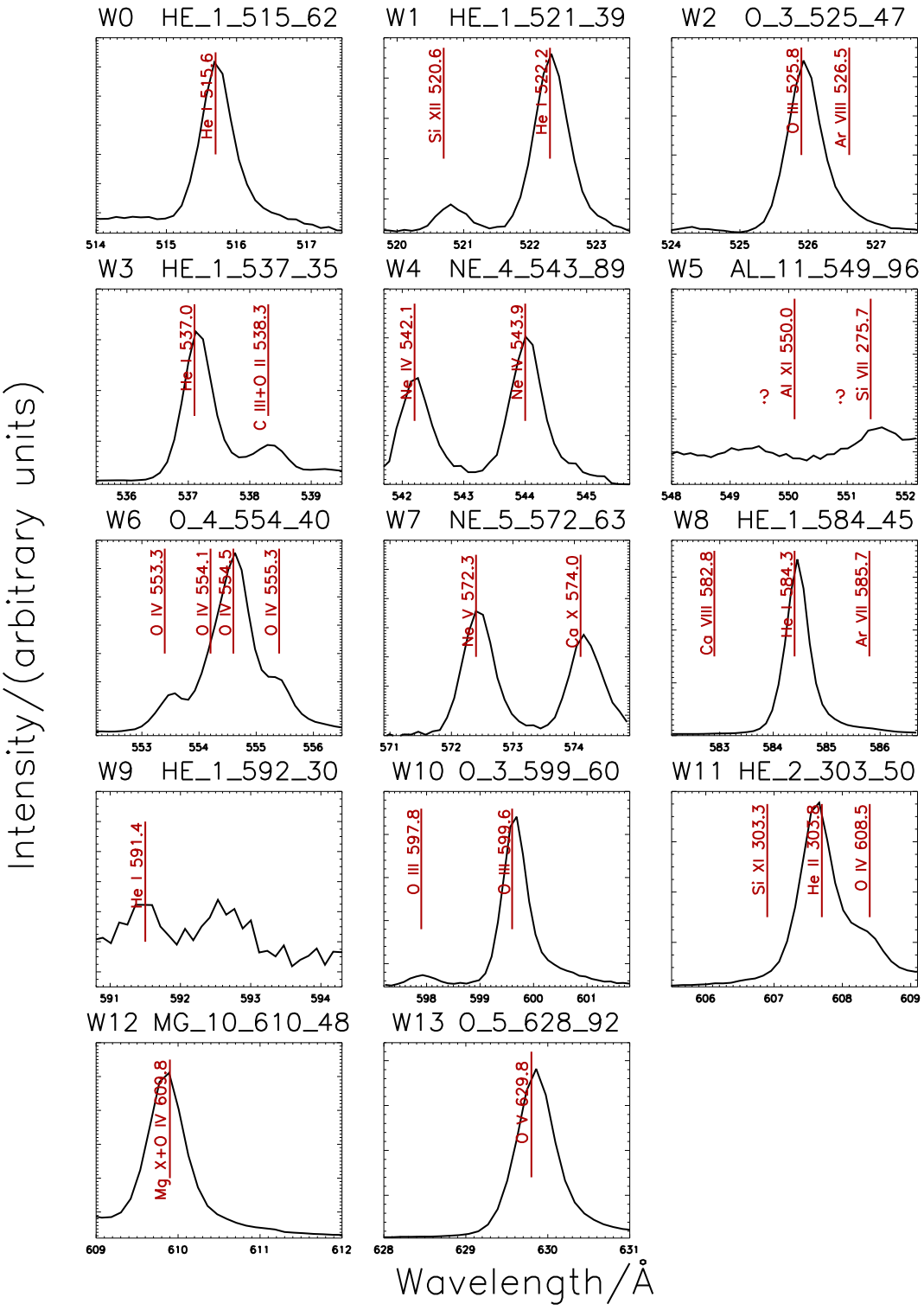


Figure 4.13: Average line profiles as a function of wavelength for the CDS study `s40676r00`. The intensity along the Y-axis is in arbitrary units, while the wavelength along the X-axis is given in Angstrom. The red vertical lines with labels are the lines identified for each spectral windows.

The raw NIS data require a number of corrections to remove effects due to the various spectrometer components and to convert counts to the same physical units adopted for SUMER and EIS. The reduction procedure has been thoroughly discussed by (18) and improved by (61) and (62). A semi-automatic procedure has been used to apply the standard reduction and calibration to the whole set of CDS observations. The correction path suitable for all data of the present set of studies can be grouped in the following three steps.

1. Since a bias voltage is added to the signal from the CCD, the NIS data in each observation require debias correction. This also takes care of the fact that the CCD is read out of four quadrants, so that it levels off them. Then the data have to be divided by the appropriate flat-field image and corrections for non-linearity in detector response has to be applied. Additionally, as expected, under exposure to radiation, the detector micro-channel plate suffers degradation, which increases where intensities increase, that is in line cores. This causes the responsivity to decline with photons detected, and so with time, and burn-in correction is needed. These corrections have been applied using the routine **nis_calib.pro**, within SolarSoft[6]. Also, the conversion into physical units - that are, as for SUMER, $photons\, cm^{-2}\, s^{-1}\, sr^{-1}$ - has been done.

2. Another problem arises from the fact that the dispersion plane from the grating is not exactly parallel to the edges of detector. Hence, the whole NIS images are slanted relative to the CCD and the individual spectrum lines within the images are tilted. The SolarSoft routine **nis_rotate.pro** gives the appropriate slant and tilt corrections to all the spectral windows.

3. Finally, random cosmic ray strikes can locally corrupt the NIS spectra. In order to locate and remove cosmic ray strikes, the routine **cds_new_spike.pro**, available within SolarSoft, has been used. This routine marks the pixels with values significantly larger compared to the adjacent pixels and replaces the aberrant values with a mean of values from the adjacent pixels.

Taking into account all these corrections, the uncertainty budget in the observed intensity has been estimated between 15% and 30%, essentially due to the burn-in uncertainty and the uncertainties for the wavelength-dependent count to photon conversion, as given by (61; 62). Also, an additional 10% error has been introduced for observations taken after SoHO's loss in 1998.

Recently, the burn-in corrections, discussed in the first step above, have been revised by (63), providing new long term wavelength-dependent correction factors which give significant changes in the calibrated intensity, especially for the strongest lines, such as He I 584.33 Å and O V 629.73 Å. In the context of this thesis, such lines are very important for the co-alignment and cross-calibration between CDS and SUMER. Therefore, a correct estimate of their absolute and relative intensity is vital to allow a reliable comparison of line intensity from the two instruments. Here these new correction factors have been adopted and a comparison with the previous intensity calibration is given in figure 4.14 for the two lines, He I 584.33 Å and O V 629.73 Å, which will be used for the cross-calibration in subsection 4.2.4. A large discrepancy has been found for He I 584.33 Å (plot 4.14(a)). The intensity was, in fact, overestimated by more than a factor 2, when the previous standard long-time correction was adopted. Regarding the O V 629.73 Å intensity, plot 4.14(b) shows an underestimate of about 14% compared with the new calibrated intensity.

As mentioned before, the wavelength range chosen for SUMER observations is split into two raster scans taken at different times. By contrast, both for CDS and EIS, the required wavelength ranges are covered by each raster scan (fig. 4.9). This implies that the temporal co-alignment between SUMER and the couple CDS-EIS is not valid for each scan. As a consequence, it has been decided to take an average of the five CDS raster scans taken while the first and the second SUMER rasters run. The same consideration will be done for EIS. In order to check the validity of this approach, the change of integrated intensity along the five rasters has been examined for each spectral band. As an example, figure 4.15 shows the averaged line intensity profiles for the window 1 (plot 4.15(a)), specified by `HE_1_521_39` in fig. 4.13, and window 7 (plot 4.15(b)), specified by `NE_5_572_63` in fig. 4.13. Window 1 includes Si XII 520.66 Å and He I 522.21 Å, while window 7 includes a blend of two Ne V lines observed at 572.30 Å and Ca X 574.01 Å. The four lines have been selected to cover a large temperature range in order to investigate the possible intensity change due to different plasma conditions through the atmosphere layers, from the upper chromosphere (He I) to the corona (Si XII). The third plot (4.15(c)) displayes the integrated line intensities of each raster scan relative to the first one. Due to the quiet Sun plasma condition, the integrated intensities of the four lines along the five CDS rasters do not show a variability more than 6.8%.

[6] SolarSoft IDL distribution is a set of integrated software libraries, databases and system utilities that provide a common programming and data analysis environment for solar physics (http://www.lmsal.com/solarsoft/).

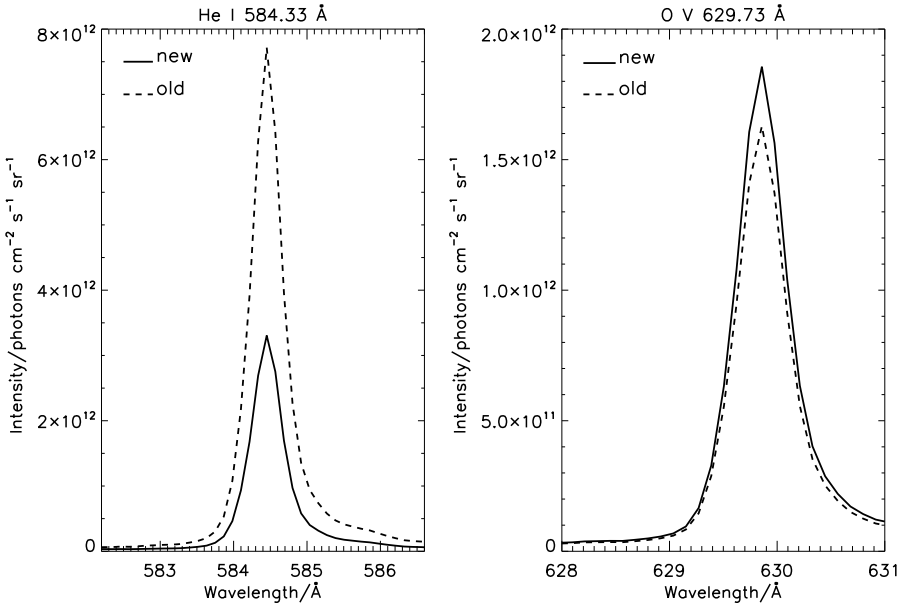


(a) (b)

Figure 4.14: Comparison between the new calibration (solid line) of (63) and the previous calibration (dashed line). Plot **(a)** shows the He I 584.33 Å line profile while plot **(b)** shows the O V 629.73 Å line profile.

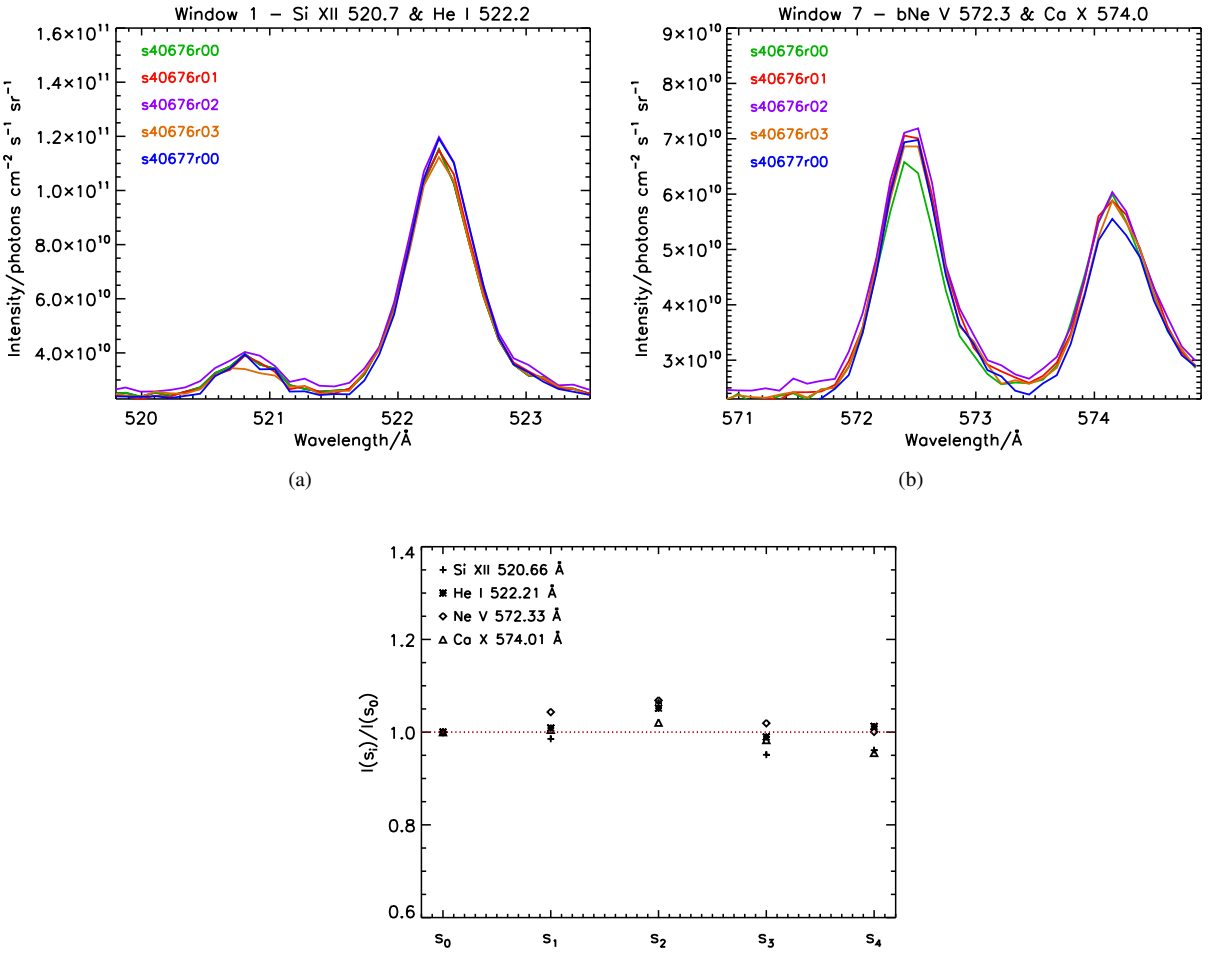


(a)

(b)

(c)

Figure 4.15: Variation of intensity in the Si XII 520.66 Å and He I 522.21 Å lines (plot **(a)**) and in the Ne V 572.30 Å and Ca X 574.01 Å lines ((**b**)), along the five CDS raster scans. Each color represents the respective scan. The letter "*b*" in front of Ne V indicates a blend of two Ne V lines, as shown in tab 4.5. Finally, plot **(c)** shows the integrated line intensities of each raster $s_i$ with respect the first one, $s_0$=`s40676r00`.

**EIS**

As for CDS, the basic unit of observation for EIS is a consecutive set of exposures which scans a spatial region on the Sun from west to east, i.e. a raster. The collection of a set of rasters is called, in the EIS context, "study" and is used to identify the particular science planning purpose. Two new studies have been written for this thesis: RAL_HE_INT_1SLIT and RAL_HE_INT_2SLIT. Both the observing sequences consist of 7 spectral windows, as illustrated in fig. 4.16. They were designed to be used both for quiet Sun and active region targets. Due to the quiet Sun conditions of the present observations, the window specified by `FE XVI 262.980` only shows a flat background. Lines which arises from an ion such as Fe XVI cannot be observed in quiet Sun, but become much more intense in active regions. Other lines included in this set of observations come essentially from oxygen, silicon and iron ions, while the fourth window contains the He II 256.32 Å doublet. Again, as for SUMER and CDS, table 4.6 gives a full list of the lines included in the EIS observations. The sequence RAL_HE_INT_1SLIT consisted of a 1 arcsec slit raster covering a region $60 \times 256$ arcsec$^2$ and with a duration of ∼41 minutes, while the RAL_HE_INT_2SLIT used the wider 2 arcsec slit, with a duration of ∼11 minutes to complete the raster scan. The 1 arcsec slit study was repeated four times, then the 2 arcsec slit study run five times, giving the following observing sequence, as also illustrated in table 4.2: `eis_l0_20090417_120241`, `eis_l0_20090417_124423`, `eis_l0_20090417_132605`, `eis_l0_20090417_140748`, `eis_l0_20090417_145842`, `eis_l0_20090417_150933`, `eis_l0_20090417_152025`, `eis_l0_20090417_154209`. The last three scans run from 15:20 to 15:52 UT, outside the time covered by the two SUMER rasters, but contemporaneous with the fifth CDS scan. Hence, the whole set of EIS observations has been included in the analysis.

The reduction and calibration for the EIS datasets follow a procedure similar to CDS. Such a procedure is automated using the EIS_PREP routine available in the SolarSoft distribution, as described by (64). The raw data are collected in the *level-0* FITS files, while the outputs of EIS_PREP are called *level-1* FITS files and contain calibrated intensities at each pixel and error bars. Firstly, the bad data points, due to pixel saturation or defective pixels on the CCD, have been flagged and the CCD bias and dark current subtracted. Futhermore, anomalously bright pixels can be found on the EIS CCD images. They arise from cosmic rays and single pixels, that have counts above a threshold specified by the CCD manufacturer (hot pixel) or that fall below this threshold but are still clearly identified as anomalous compared to the data (warm pixel).

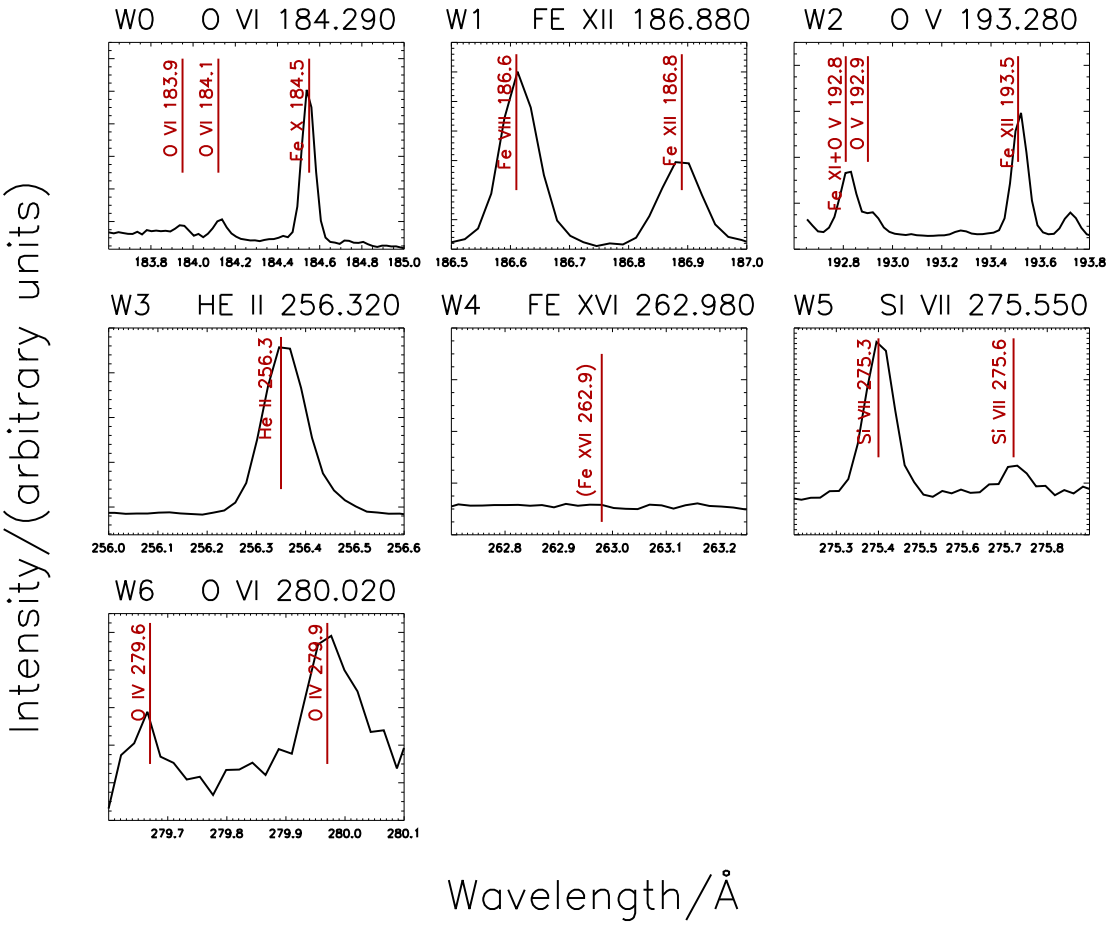


Figure 4.16: Average line profiles as a function of wavelength for the EIS study `eis_l0_20090417_145842`. The intensity along the Y-axis is in arbitrary units, while the wavelength along the X-axis is given in Angstrom. The red vertical lines with labels are the lines identified for each spectral windows.

Table 4.6: List of the selected lines observed by Hinode/EIS. Ions, wavelengths and atomic transitions are provided to allow the selection of ions of which the atomic data will be reviewed in chapter 5. Additionally, the order is given. Blends are indicaded by the letter "*b*"which is put just before the ion.

| Ion | Wavelength/Å | Transition | Order |
|---|---|---|---|
| $O^{+5}$ | 183.94 | $2p\,^2P_{1/2} - 3s\,^2S_{1/2}$ | First |
| $O^{+5}$ | 184.12 | $2p\,^2P_{3/2} - 3s\,^2S_{1/2}$ | First |
| $Fe^{+9}$ | 184.54 | $3s^2 3p^5\,^2P_{3/2} - 3s^2 3p^4 3d\,^2S_{1/2}$ | First |
| $Fe^{+7}$ | 186.60 | $3p^6 3d\,^2D_{3/2} - 3p^5 3d^2\,^2F_{5/2}$ | First |
| $b\,Fe^{+11}$ | 186.85 | $3s^2 3p^3\,^2D_{3/2} - 3s^2 3p^2 3d\,^2F_{5/2}$ | First |
| $b\,Fe^{+11}$ | 186.88 | $3s^2 3p^3\,^2D_{5/2} - 3s^2 3p^2 3d\,^2F_{7/2}$ | First |
| $b\,O^{+3}$ | 186.86 | $2s2p^2\,^4P_{1/2} - 2p^2 3p\,^4P_{3/2}$ | First |
| $b\,O^{+3}$ | 186.88 | $2s2p^2\,^4P_{1/2} - 2p^2 3p\,^4P_{1/2}$ | First |
| $b\,Fe^{+10}$ | 192.83 | $3s^2 3p^4\,^3P_1 - 3s^2 3p^3 3d\,^3P_2$ | First |
| $b\,O^{+4}$ | 192.75 | $2s2p\,^3P_0 - 2s3d\,^3D_1$ | First |
| $b\,O^{+4}$ | 192.80 | $2s2p\,^3P_1 - 2s3d\,^3D_2$ | First |
| $b\,O^{+4}$ | 192.80 | $2s2p\,^3P_1 - 2s3d\,^3D_1$ | First |
| $b\,O^{+4}$ | 192.91 | $2s2p\,^3P_2 - 2s3d\,^3D_3$ | First |
| $b\,O^{+4}$ | 192.91 | $2s2p\,^3P_2 - 2s3d\,^3D_2$ | First |
| $b\,O^{+4}$ | 192.92 | $2s2p\,^3P_2 - 2s3d\,^3D_1$ | First |
| $Fe^{+11}$ | 193.51 | $3s^2 3p^3\,^4S_{3/2} - 3s^2 3p^2 3d\,^4P_{3/2}$ | First |
| $b\,He^{+1}$ | 256.32 | $1s\,^2S_{1/2} - 3p\,^2P_{1/2}$ | First |
| $b\,He^{+1}$ | 256.32 | $1s\,^2S_{1/2} - 3p\,^2P_{3/2}$ | First |
| $b\,Si^{+9}$ | 256.37 | $2s^2 2p\,^2P_{1/2} - 2s2p^2\,^2P_{1/2}$ | First |
| $b\,Fe^{+12}$ | 256.42 | $3s^2 3p^2\,^1D_2 - 3s3p^3\,^1P_1$ | First |
| $b\,Fe^{+9}$ | 256.41 | $3s^2 3p^5\,^2P_{3/2} - 3s^2 3p^4 3d\,^4D_{3/2}$ | First |
| $Si^{+6}$ | 275.35 | $2s^2 2p^4\,^3P_2 - 2s2p^5\,^3P_2$ | First |
| $Si^{+6}$ | 275.67 | $2s^2 2p^4\,^3P_1 - 2s2p^5\,^3P_1$ | First |
| $O^{+3}$ | 279.63 | $2s^2 2p\,^2P_{1/2} - 2s^2 3s\,^2S_{1/2}$ | First |
| $O^{+3}$ | 279.93 | $2s^2 2p\,^2P_{3/2} - 2s^2 3s\,^2S_{1/2}$ | First |

The cosmic ray removal is performed by **eis_despike.pro**, which calls the same routine that remove cosmic ray strikes for CDS. Hot and warm pixels are usually removed with the help of a map of their location generated every 2-4 weeks and stored in SolarSoft. Finally, radiometric calibration has been performed to convert the count values into intensity units. **eis_prep.pro** provides calibration in *DN* (data number), *photon* − *events* and $ergs\,cm^{-2}\,s^{-1}\,sr^{-1}$ Å$^{-1}$. To be consistent with the units adopted for SUMER and CDS, calibration in $photons\,cm^{-2}\,s^{-1}\,sr^{-1}$ is needed. Firstly, EIS_PREP has been set up to give the calibrated intensity in $ergs\,cm^{-2}\,s^{-1}\,sr^{-1}$ Å$^{-1}$. Then the intensity has been converted to $photons\,cm^{-2}\,s^{-1}\,sr^{-1}$ Å$^{-1}$, using the conversion factor $(hc)/\lambda$, where $h$ is the Planck constant in $ergs\,s$, $c$ is the light speed in $cm\,s^{-1}$ and $\lambda$ is the wavelength in $cm$. Finally, the intensity has been multiplied by the width of a pixel in Å, that is ∼0.0223 to give the requested units $photons\,cm^{-2}\,s^{-1}\,sr^{-1}$. The accuracy of the EIS absolute intensity calibration was estimated to be around 20% before the launch (65), while the relative calibration is provided by the **eis_prep.pro** routine together with the calibrated data and depends on wavelength. Two further instrumental corrections should be applied to the calibrated data. They arise from a spatial offset between different wavelengths due to a misalignment of the EIS slits relative to the CCD (tilt correction) and the thermal changes occurring across the instrument during the orbit (orbit correction). For intensity measurements, these corrections are not important, but they become essential when multiple emissions from the same feature of the Sun have to be compared. The routine **eis_wave_corr.pro** provides the wavelength offset of each spatial pixel, which can be subtracted from the line centroids to remove the tilt and orbit effects.

Once the calibration procedure has been completed, the variation of integrated line intensities along the nine EIS rasters has been analysed, as has been done for CDS (fig. 4.15). Figure 4.17 displays, as an example, the line profiles for the window 2 (plot 4.17(a)), specified by `O V 193.280` in fig 4.16. The spectral window includes three identified lines: Fe XI 193.3 Å (blended with three lines of the O V multiplet), O V 192.91 Å (which is a self-blend of other three lines of the O V multiplet) and Fe XII 192.51 Å. The integrated line intensities of each scan relative to the first scan, $s_0$=`eis_l1_20090417_120241`[7], are plotted in fig. 4.17(b), showing a maximum deviation of 16% . This allows averaging of line intensities derived from the nine EIS scans for the joint analysis with SUMER and CDS line intensities.

[7]Note the notation `eis_l1_20090417_120241` instead of `eis_l0_20090417_120241` for the calibrated data.

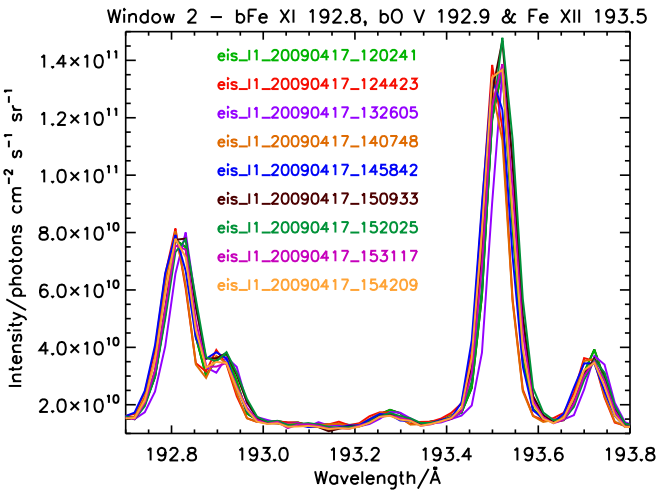


(a)

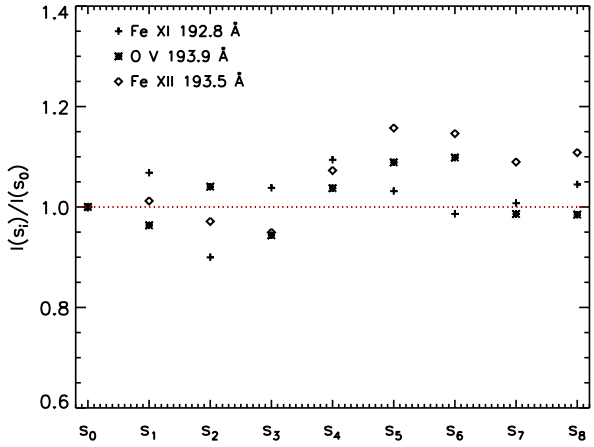


(b)

Figure 4.17: Variation of intensity in the Fe XII 192.83 Å, O V 192.91 Å and Fe XII 193.51 Å lines (plot **(a)**) along the nine EIS raster scans. Each color represents the respective scan. The letter "*b*" in front of Fe XI and O V indicates two blends (table 4.6). Plot **(b)** shows the integrated line intensities of each raster $s_i$ with respect the first one $s_0$=`eis_l1_20090417_120241`.

### 4.2.2 Spatial co-alignment

The SUMER, CDS and EIS observations were nominally pointed at the same location of the Sun (0,-40) in heliospheric coordinates. However, the actual pointings of the three instruments were not exactly at this location (table 4.3). Additionally, the uncertainties in the pointing of each instrument should be taken into account. The pointing accuracy of SUMER and CDS is within 5 arcsec, while typical values of EIS uncertainty pointing are 5-10 arcsec. However, the field of view covered by the three spectrometers are wide enough to allow a good overlap (fig. 4.6). Several steps have been followed to perform the co-alignment: (1) resize the images; (2) identify resolved solar structures; (3) align the two SUMER rasters; (4) align the five CDS rasters; (5) align the nine EIS rasters; (6) align SUMER, CDS and EIS rasters and crop the images.

1. *Resize the images*: The first problem which has been encountered during the co-alignment procedure is related to the fact that the images gathered by the three instruments are characterised by different spatial resolution along both X and Y axis. Table 4.7 displays the dimension in arcseconds covered by 1 pixel along X and Y directions on the solar surface for each SUMER, CDS and EIS scan. In order to quantitatively compare the

| **SUMER** | | |
|---|---|---|
| Scan | Solar-X/arcsec | Solar-Y/arcsec |
| raster_1 | 1.500 | 1.000 |
| raster_2 | 1.500 | 1.000 |
| **CDS** | | |
| Scan | Solar-X/arcsec | Solar-Y/arcsec |
| s40676r00 | 2.032 | 3.360 |
| s40676r01 | 2.032 | 3.360 |
| s40676r02 | 2.032 | 3.360 |
| s40676r03 | 2.032 | 3.360 |
| s40677r00 | 2.032 | 1.680 |
| **EIS** | | |
| Scan | Solar-X/arcsec | Solar-Y/arcsec |
| eis_l1_20090417_120241 | 1.000 | 1.000 |
| eis_l1_20090417_124423 | 1.000 | 1.000 |
| eis_l1_20090417_132605 | 1.000 | 1.000 |
| eis_l1_20090417_140748 | 1.000 | 1.000 |
| eis_l1_20090417_145842 | 2.000 | 1.000 |
| eis_l1_20090417_150933 | 2.000 | 1.000 |
| eis_l1_20090417_152025 | 2.000 | 1.000 |
| eis_l1_20090417_153117 | 2.000 | 1.000 |
| eis_l1_20090417_154209 | 2.000 | 1.000 |

Table 4.7: Distance on the solar surface covered by 1 pixel along the X and Y directions for SUMER, CDS and EIS.

images recontructed by the three spectrometers, it is necessary that each spatial pixel covers the same distance on the solar surface. Since the present analysis deals with averages along the two spatial dimensions of each raster, the spatial resolution is not a concern. Each image has been resized such that it is comparable with the images recorded at lowest resolution in the set (which are the images included in the first four CDS scans). That is to say, the $60 \times 256$ pixel arrays of the first four EIS scans and $30 \times 256$ arrays of the last five EIS scans have been resampled to $30 \times 76$ arrays, the SUMER $60 \times 120$ arrays to $44 \times 36$ and the $40 \times 89$ array of the fifth CDS scan to a $40 \times 45$ array. For the new resampled arrays each X-pixel corresponds to ~2 arcsec and each Y-pixel corresponds to ~3.36 arcsec. It should be noted that for CDS and EIS the solar tracking was off. As a consequence, the images gathered from them require a further resample. This gives the arrays $43 \times 89$ and $43 \times 45$ for the CDS scans. Regarding EIS, same consideration has been done for the first four scans, providing new $33 \times 256$ arrays, while no further correction was applied to the last five scans. This is because each of these last five EIS rasters took a time short enough (~11 minutes each) not to require correction for the solar rotation.

2. *Identify resolved solar structures*: Once the spatial arrays have been rescaled, several spectral lines have been selected to look for some particular feature in their intensity distribution. This is required to allow co-alignment

along north-south and east-west directions. Lines (or multiplets) which originate from same ions or which have a close temperature of formation have been chosen:

- He I 583.33 Å (second order), O V 629.73 Å (second order) and Si II 1309.28 Å for SUMER;
- He I 583.33 Å, O V 629.73 Å and He II 304.78 Å, (second order) for CDS;
- He II 256.32 Å for EIS.

The figure 4.18 shows the intensity distribution for the selected lines. Fortunately, a horseshoe-shaped feature

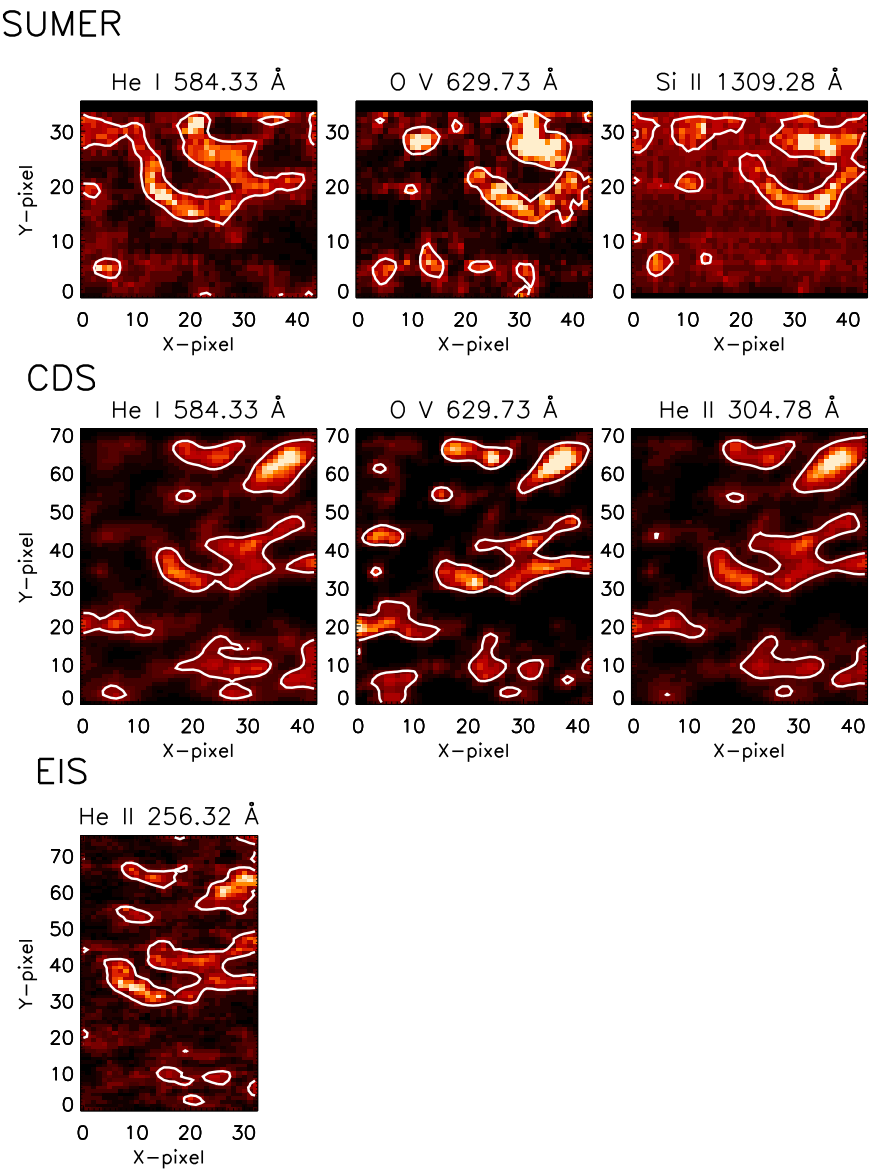


Figure 4.18: Intensity distribution of the lines/doublets which have been selected to perform the co-alignment amongst SUMER, CDS and EIS instruments. He I 584.33 Å and O V 629.73 Å lines are observed by both SUMER and CDS. Si II 1309.28 Å, observed by SUMER, is formed at a temperature close to the temperature of He I line formation. As a consequence, it shows an intensity distribution similar to the He I distribution. Finally, He II 303.78 Å and 256.32 Å doublets are observed by CDS and EIS respectively.

is visible, especially for the lines formed at the low temperature in the range $\log(T/\mathrm{K}) \sim 4.2 - 4.9$, including lines of Si II, He I and He II, but also O V. This particular feature, together with the other little features, are very useful in giving a first qualitative estimate of how much each image should be shifted to be aligned to the other images.

3. *Align the two SUMER rasters*: In order to do a proper co-alignment of SUMER, CDS and EIS, first of all, the alignment of the rasters gathered by each single instrument have to be done. SUMER observations consist of two rasters, which contain different wavelength bands. However, as seen in fig. 4.18, lines formed at similar temperature show a comparable intensity distribution. The alignment of the two SUMER rasters has been done using He I 584.33 Å and Si II 1309.28 Å. The first line is observed in the first raster scan at the second order, because its wavelength is shorter than the Lyman-$\alpha$ limit, while the second line is within the second raster, being $\lambda_{SiII} > \lambda_{Ly-\alpha}$. The co-alignment of the two images has been performed using the **cross_corr2.pro** routine, available within SolarSoft. Such program uses the standard cross-correlation method for estimating the degree of which two-dimensional image arrays are correlated. The cross-correlation is defined by the following expression:

$$corr = \frac{\sigma_{x_1 x_2}}{\sigma_{x_1}\sigma_{x_2}} = \frac{\sum_{i=1}^{n}(x_1^i - \overline{x_1})\,(x_2^i - \overline{x_2})}{\sqrt{\sum_{i=1}^{n}(x_1^i - \overline{x_1})^2 \;\sum_{i=1}^{n}(x_2^i - \overline{x_2})^2}} \tag{4.5}$$

where $\sigma$ is the standard deviation, $\overline{x_1}$ and $\overline{x_2}$ the means of the corresponding series, $x_1^i$ and $x_2^i$, and $n$ the dimension of each series. The same equation is applied to Y-directions. The relation 4.5 implies that the two image arrays must have the same dimensions and calculates the cross-correlation by shifting the second array $(x_2^i, y_2^i)$ relative to the first array $(x_1^i, y_1^i)$. The maximum correlation value has been found when the second SUMER raster was shifted by 10 pixels along X-direction and 2 pixels along Y-directions. Overplotting the shifted Si II contour (from the second raster) on the He I image (first raster), a satisfactory agreement between the two aligned horseshoe-shaped features is found (fig. 4.19).

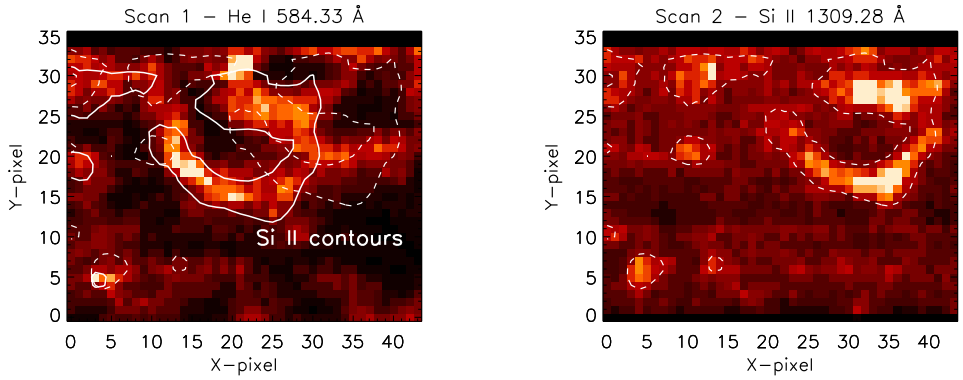


(a) (b)

Figure 4.19: Alignment between the two SUMER rasters. Image **(a)** shows the intensity distribution in the He I 584.33 Å spectral band, while image **(b)** displays the intensity distribution of Si II 1309.28 Å. The overplotted contours of both the images are the Si II contours: the dashed contours are Si II contours without shift, the solid contour is Si II contour shifted by 10 pixels along X-axis and 2 pixels along Y-axis.

4. *Align the five CDS rasters*: The same procedure has been applied for co-aligning the five CDS raster scans. He I 584.33 Å has been used to determine the relative shift in the east-west direction. Again the cross-correlation has been computed, giving maximum value when each raster is shifted with respect the next one by 3 pixels along the X-direction. The study `s40677r00` has been treated separately, because of the different dimension along the Y-direction. Figure 4.20 displays, as example, the first three CDS rasters. The overplotted dashed feature belongs to the third scan. The solid contour is the same feature shifted by the values calculated using **cross_corr2.pro**. As further check, the O V 629.73 Å has been used, providing same results.

5. *Align the nine EIS rasters*: EIS scans can be divided into two sets to be examined separately: (1) the first four rasters; (2) the last five rasters. For the second group, the cross-correlation function gives a relative shift of ±1 pixel along the X-direction. Regarding the first group, the relative shifts along X-direction are the following:

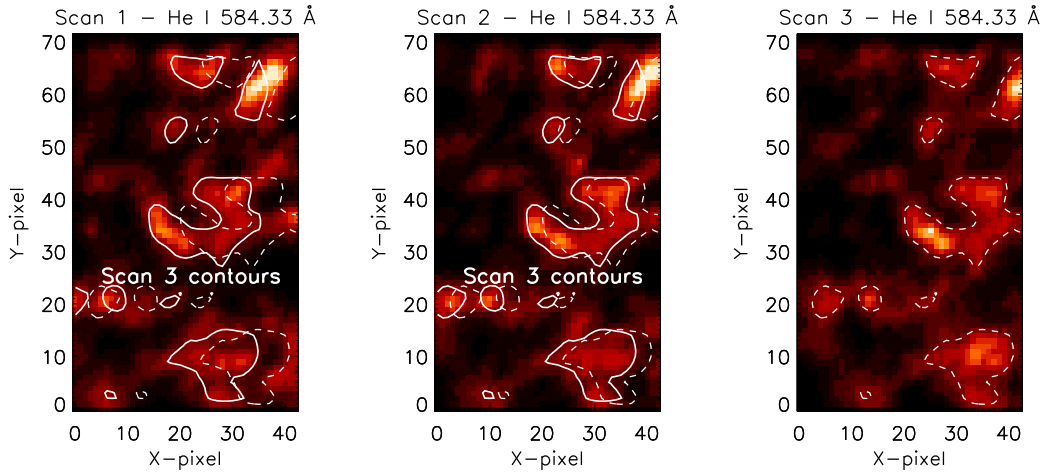


(a) (b) (c)

Figure 4.20: Alignment of CDS rasters. Figures **(a)**, **(b)**, **(c)** show the first three scans, as example. The dashed contours represent the overplotted scan 3 feature shifted by the values discussed in the text.

- `eis_l1_20090417_120241` – `eis_l1_20090417_124423` 2 pixels
- `eis_l1_20090417_124423` – `eis_l1_20090417_132605` 5 pixels
- `eis_l1_20090417_132605` – `eis_l1_20090417_140748` 2 pixels

Then the images from the second set have been cut in order to have the same dimension as the first set of images and the relative shift between the two sets has been estimated. The EIS raster alignment is shown in figure 4.21, providing, as an example, the He II 256.32 Å intensity distribution for the first three rasters.

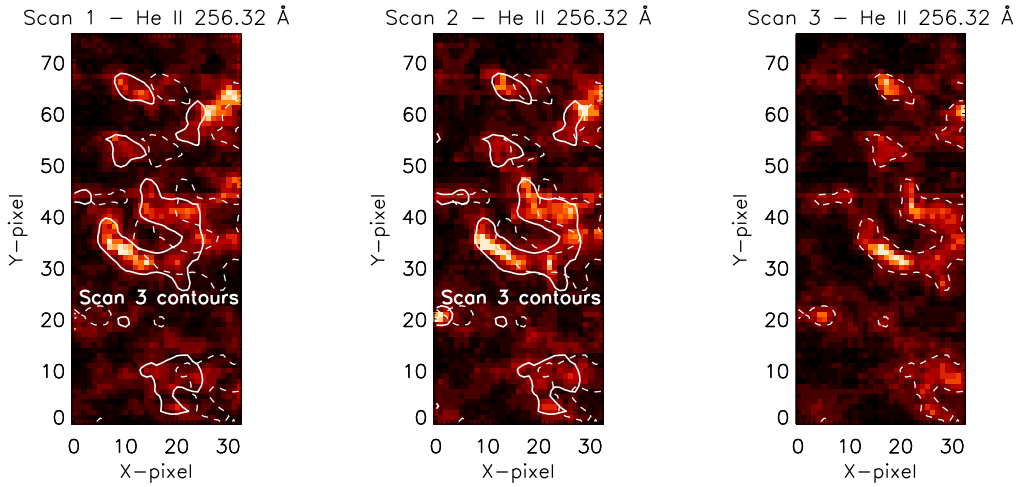


(a) (b) (c)

Figure 4.21: Alignment of EIS rasters. Figures **(a)**, **(b)**, **(c)** show the first three scans, as example. The dashed contours represent the overplotted scan 3 feature shifted by the values discussed in the text.

Finally, it should be noted that for both CDS and EIS rasters there is no shift along the Y-direction and the shift provided for the X-direction is essentially due to the solar rotation.

6. *Align SUMER, CDS and EIS rasters and crop the images*: Once the rasters belonging to each of the three observational sets have been aligned, the common feature observed in He I and He II line intensity distributions has been used to co-align SUMER, CDS and EIS. As last step, all the images have been cropped to $16 \times 32$

pixel arrays in order to have same dimensions along the X and Y directions. Figure 4.22 shows the final rasters, which will be examined in the analysis that follows (sec. 4.2.3, 4.2.4 and chapter 6).

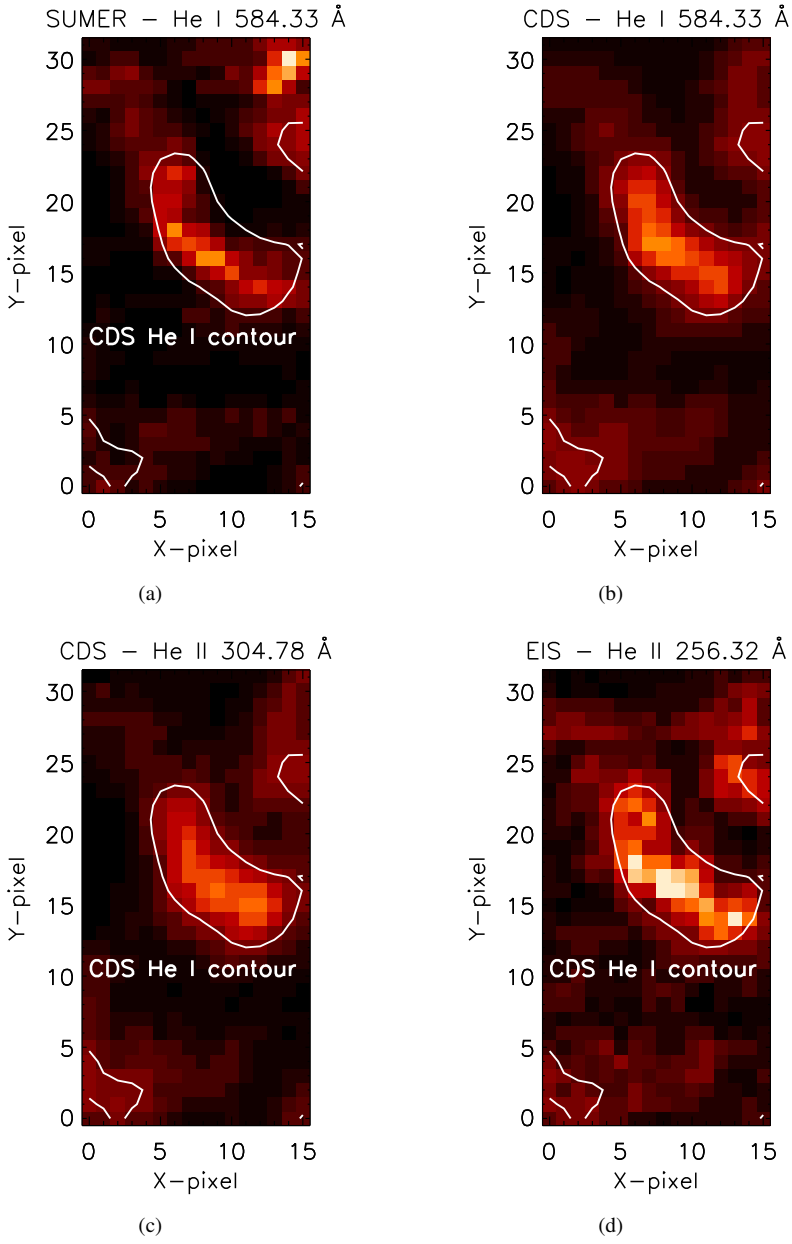


Figure 4.22: Final cropped rasters of SUMER, CDS and EIS. He I 584.33 Å line intensity distribution is shown for SUMER ans CDS (fig. **(a)** and **(b)**). He II 304.78 Å and He II 256.32 Å doublet intensity distributions are displayed in fig. **(c)** and **(d)** respectively. The first one is observed by CDS, the second one by EIS. The white solid line overplotted on each image is the contour of CDS He I 584.33 Å feature in order to show the good agreement in co-aligning the three instrument scans.

### 4.2.3 Profile fitting procedure

One of the central goals of this work is the study of spectral line intensities. This requires an appropriate fitting procedure to obtain the observed fluxes in the lines. The method used in this thesis to fit a theoretical spectrum to the observed one is based on a program developed by (66) and implemented as code ADAS602 within ADAS, as

described by (18). Given the observed spectra, the ADAS602 program gives positions, widths, integrated intensities of the observed lines and background parameters. It also provides an estimate of standard error in the integrated intensities, which has to be added to the calibration uncertainty, and in the individual output quantities.

Before applying the fitting procedure, the spatial average of each observed line intensity has been done using the new spatial cropped arrays. In addition, following the considerations discussed in section 4.2.1 (see figures 4.15 and 4.17), the line intensities derived from the five CDS scans and the nine EIS scans, have been, in turn, averaged. The final data to be analysed consist, now, of a one-dimension array for each spectral window. Each array contains the spectrum with intensity calibrated in $photons\, cm^{-2} s^{-1} sr^{-1}$ as a function of spectral pixels. The conversion from pixel to wavelength is not used to perform the fitting, but it has been discussed previously.

The spectra are fitted with a multi-Gaussian line profiles and a constant, linear or quadratic background using a maximum likehood method to calculate the total integrated counts under line profiles. The observed data are fitted to an equation represented by the following form:

$$I_k = b_0 + b_1 x_k + b_2 x_k^2 + \sum_{i=1}^{L} h_i G_i(x_k) \tag{4.6}$$

where $G_i(x_k)$ is the Gaussian term, defined as:

$$G_i(x_k) = e^{-\left(\frac{x_k - xo_i}{w_i}\right)^2} \tag{4.7}$$

while $I_k$ is the observed counts; $b_0$, $b_1$ and $b_2$ are respectively constant, linear and quadratic components of the background; $x_k$ gives the pixel positions; $L$ is the number of lines; $h_i$ gives the peak of each line, $xo_i$ gives the fitted positions of the lines; finally $w_i$ is the width to fit each line. Such fitting program has been tested extensively on SUMER and CDS spectra. Here, it is used successfully for fitting EIS spectra too. The SUMER and EIS integrated intensities have been obtained by fitting Gaussian functions and linear background to the profiles, as stated by equation 4.6. The capability to separate the semi-overlapped components of multiplets is shown, for instance, in figure 4.23, where two SUMER lines originate from the $3s^2 3p\,^2P - 3s^2 3d\,^2D$ multiplet are resolved. By contrast, a fit of two

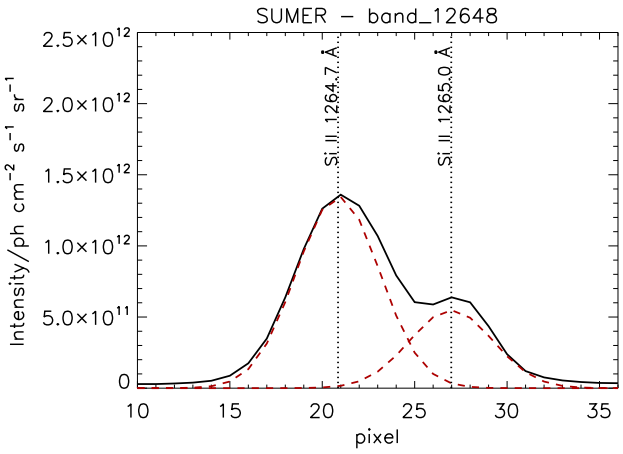


Figure 4.23: Example of SUMER line profile fitting using ADAS602 fitting routine. Two Gaussian shapes have been used to fit the two component of Si II multiplet.

completely resolved lines is displayed for EIS in figure 4.24. For CDS/NIS, the line profile is not described simply by a Gaussian. After the SoHO satellite loss in 1998 the line profiles in both NIS1 and NIS2 had changed. The post-recovery lines exhibit wings of different strength on each side, due to an irreversible distortion in the instrument caused by the prolonged heating suffered by CDS. In this work, only NIS2 has been used. The wings in the NIS2 spectrum mostly affect the red sides of the lines. (67) developed special fitting routines to account for the changed profiles. He modelled the line profiles as a combination of a Gaussian term, to which a component describing the wings is added. The Gaussian term has been already specified by equation 4.7, whereas the wings are defined by the following function:

$$W(x_k) = \frac{1}{(\frac{x_k - xo_i}{w'})^2 + 1} \tag{4.8}$$

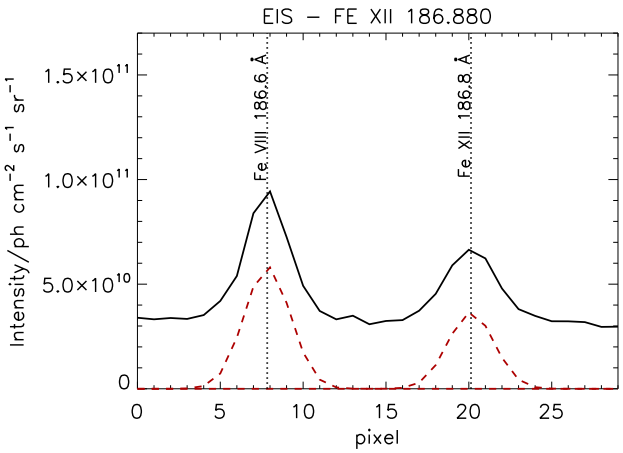


Figure 4.24: Example of EIS line profile fitting using ADAS602 fitting routine. As for SUMER, the two lines present in the spectral window here displayed, have been fitted using two Gaussian profiles and a linear background.

where $w' = 2w_i\sqrt{2ln2}$. Then, the combined line profile is described by the expression:

$$B(x_k) = h_i[(1-\alpha)G_i(x_k) + \alpha W(x_k)] \tag{4.9}$$

where $\alpha$ has different values for the left and right wings. For NIS2, a good fit is achieved when $\alpha_{right} = 0.317$ and $\alpha_{left} = 0.088$. This broadened Gaussian profile has been added in the ADAS602 routine allowing to take into account the CDS line profile distorsion. Figure 4.25 shows an example of the new line shape. It is visible especially in the right wing of the strongest He II lines, overlapping the less intense line of O IV. Another weak line has been fitted in the left wing on He II. It has been identified by (18) as Si XI 303.3 Å at the second order.

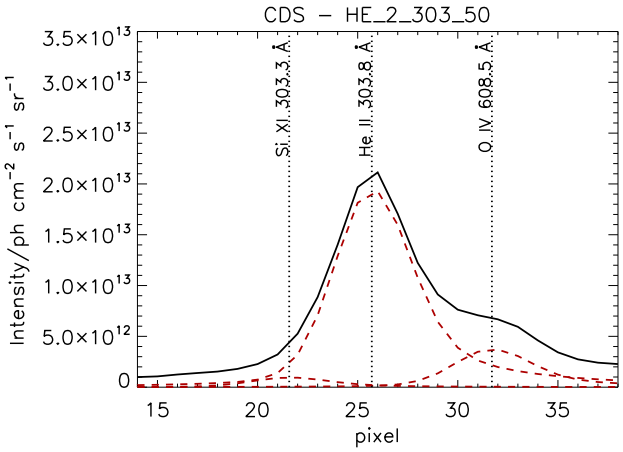


Figure 4.25: Example of CDS line profile fitting using ADAS602 fitting routine. The combined $B(x_k)$ profile has been applied to fit the three lines included in the spectral window `HE_2_303_50`.

### 4.2.4 Cross-calibration

Since the intensities that will be used in this thesis were measured by three different instruments, it is essential that their relative intensity calibration is accurate, to avoid systematic error in their comparison. As discussed in previous sections, each instrument is well calibrated within its own wavelength range. However, the wavelength ranges covered by the three instruments are very different: SUMER works at longer wavelengths between approximately 600 and 1600 Å, CDS at intermediate wavelengths in the range of ~300-630 Å and EIS at very short wavelengths between about 170 and 290 Å. This implies that the direct comparison of common emission lines is not always possible and the

SUMER/CDS/EIS inter-calibration has to be checked with the further help of spectroscopic diagnostic methods. In the context of this work, three approaches have been followed. Firstly, a direct comparison of common emission lines has been done whenever possible. Secondly, spectroscopic diagnostics have been used to compare line intensities emitted by ions belonging to the same element. Finally, the physical properties of the solar plasma have been determined with each instrument independently and the results have been compared.

Before going into details and showing the results of the three methods employed for the cross-calibration, it is important to focus on the SUMER raster construction and its effect on observed line intensities. As mentioned in subsection 4.2.1, each SUMER raster was built up repeating the stated sequence of a spectral band set followed by a slit step of 1.5 arcsec along east-west direction. The slit used for the present SUMER observations was 1 arcsec wide. Therefore, in order to take into account the 0.5 arcsec gap between a slit position and the next one, SUMER line intensities have been multiplied by a factor 1.5. This estimated correction factor will be verified using the following inter-calibration procedures.

**Direct line comparison**

In the present joint observations, only SUMER and CDS cover wavelength ranges which overlap in the He I 584.33 Å and O V 629.73 Å spectral bands. This allows a direct comparison of the integrated intensities arising from those two lines. The inter-calibration between SUMER and CDS/NIS was introduced and thoroughly discussed by (68; 69). They examined the intensities measured by the two instruments before and after the SoHO's attitude loss, including He I 584.33 Å, Mg X 609.79 Å and Mg X 629.94 Å lines in the pre-loss datasets and adding O V 629.73 Å line in the post-loss datasets. They found that in the He I line at 584.33 Å the CDS instrument measured 33-38 % higher values than SUMER for the pre-loss period, while for the post-loss period the relative differences of the average intensity amounted to 43 % for He I 584 Å and -4 % for O V 629.73 Å. In this thesis, the new burn-in correction of (63) has been applied for the absolute calibration of CDS. As a result, the radiometric calibration of CDS has been modified with respect to the previous one and a new comparison between the average intensity of SUMER and CDS in given in table 4.8. The He I line intensity observed by CDS shows a value 10.1 % higher than the SUMER value, while

| Line | | SUMER $I/ph\,cm^{-2}s^{-1}sr^{-1}$ | CDS $I/ph\,cm^{-2}s^{-1}sr^{-1}$ | Ratio |
|---|---|---|---|---|
| He I | 584.33 Å | 1.689e+13 | 1.879e+13 | 0.899 |
| O V | 629.73 Å | 1.453e+13 | 1.273e+13 | 1.141 |

Table 4.8: Spatial averaged intensity in the He I 584.33 Å and O V 629.73 Å measured by SUMER and CDS. Additionally, the ratio between SUMER and CDS intensity for each line in shown.

in the O V line the CDS instrument measures 14.1 % lower value than SUMER. In conclusion, the inter-calibration between SUMER and CDS is correct within the standard error, when the new CDS radiometric calibration is used and the SUMER line intensities is corrected by the factor 1.5, above specified.

**Oxygen line comparison**

Once the relative calibration between SUMER and CDS has been established, it has to be compared with the EIS calibration to extend the cross-calibration to the whole set of instruments used for this work. Unfortunately, the wavelength bands covered by the EIS observations do not overlap SUMER or CDS ranges. However, several spectral lines observed by the three instruments are emitted by different ions of oxygen. Assuming that the relative line intensities of SUMER and CDS is correct and the absolute calibration of each spectrometer is reliable, this enables diagnostic techniques to predict the oxygen ion intensities and compare them to the observed intensities. The technique used is differential emission measure, which will be extensively described and applied to the present observations in chapter 6. Here, the technique is used as means to check the relative intensity between EIS and SUMER-CDS. Furthermore, the relative intensity calibration between SUMER and EIS has been analysed and determined recently by (70). They concluded that a good agreement between the intensities observed by the two spetrometers is found when SUMER line intensities are multiplied by the 1.28 ± 0.17 correction factor, which was obtained to account for the residual east-west misalignment of the two fields of view. The 1.5 correction factor here estimated from

different considerations provides similar conclusion. The SUMER-CDS-EIS cross-calibration is tested calculating the differential emission measure using four oxygen lines formed at different temperatures. Two of these lines are from

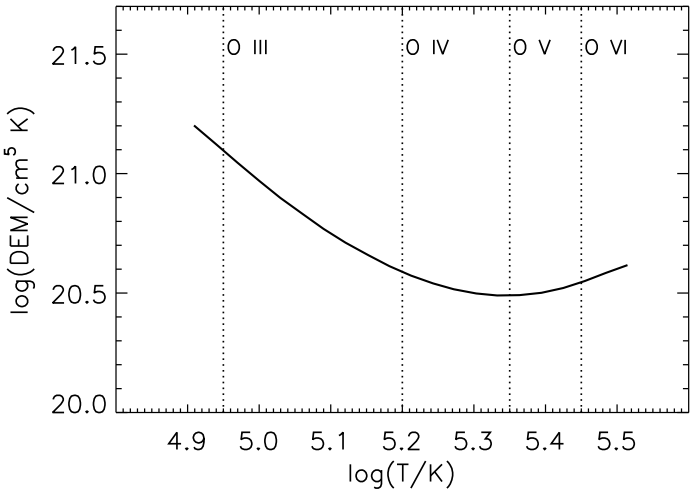


Figure 4.26: Differential emission measure obtained using the following oxygen lines: O III 599.598 Å from CDS, O IV 787.711 Å from SUMER, O V 629.732 Å from CDS and O VI 184.117 Å from EIS. The dotted vertical lines indicate the formation temperature of each ion. For the inversion, a constant electron pressure of $10^{15}$ cm$^{-3}$ K has been used.

CDS (O III 599.598 Å and O V 629.732 Å), one line is from SUMER (O IV 787.711 Å) and the last line is from EIS (O VI 184.117 Å). Fig. 4.26 illustrates the differential emission measure curve reconstructed using the four oxygen lines, which cover the narrow temperature interval log($T$/K)=4.95-5.45. The advantage of using lines from the same element

| | Line | | log(T/K) | Obs.Intensity $ph\,cm^{-2}s^{-1}sr^{-1}$ | Rec.Intensity $ph\,cm^{-2}s^{-1}sr^{-1}$ | Ratio |
|---|---|---|---|---|---|---|
| (i) | O III | 599.598 Å | 4.95 | 1.289e+12 | 1.289e+12 | 1.000 |
| (i) | O IV | 787.711 Å | 5.20 | 2.989e+12 | 3.761e+12 | 0.833 |
| (i) | cO V | 629.732 Å | 5.35 | 1.273e+13 | 1.248e+13 | 1.019 |
| (i) | O VI | 184.117 Å | 5.45 | 7.506e+10 | 7.682e+10 | 0.978 |
| (f) | O III | 597.818 Å | 4.95 | 8.404e+10 | 7.808e+10 | 1.076 |
| (f) | O IV | 279.933 Å | 5.25 | 5.009e+10 | 5.308e+10 | 0.943 |
| (f) | *b*O IV | 790.109 Å | 5.15 | | 4.828e+11 | |
| (f) | *b*O IV | 790.199 Å | 5.15 | | 4.538e+12 | |
| (f) | b-sum | | | 5.852e+12 | 5.020e+12 | 1.165 |
| (f) | O V | 762.004 Å | 5.30 | 3.389e+11 | 2.555e+11 | 1.326 |
| (f) | sO V | 629.732 Å | 5.30 | 1.453e+13 | 1.248e+13 | 1.164 |
| (f) | O VI | 183.937 Å | 5.45 | 3.966e+10 | 3.841e+10 | 1.033 |

Table 4.9: Oxygen lines used for checking the SUMER-CDS-EIS cross-calibration. The temperatures listed represent the peak temperature of line formation. The letter "(i)" indicates the lines used in the inversion for obtaining the differential emission measure, while the letter "(f)" specifies the lines compared with observations in the forward sense. The letters "c" and "s" before the O V line at 629.73 Å indicate if the line is observed by CDS ("c") or SUMER ("s"). Finally, the letter "*b*" indicates an observed blend. For this O IV blend the intensity is reconstructed for each line independently, then summed and compared to the observed intensity.

is that every error which arises from abundance values can be neglected. Also, the atomic data have been accurately checked and revised, as will be described in detail in chapter 5. Table 4.9 lists the four lines selected for the inversion with their relative formation temperatures and the other oxygen lines, included in the present observations, which have been used as a forward intensity check. In addition, the table shows the observed intensities, the reconstructed values and their ratios. A good agreement is found for all the oxygen lines displayed in the table, confirming that the current

calibrations adopted for this work are consistent within uncertainties.

### Structure of the emitting plasma comparison

Finally, the last approach for testing the cross-correlation is to perform a differential emission measure analysis independently for each instrument and compare the results. Since the differential emission measure depends directly on the absolute calibration of the instrument, a comparison between the values obtained with each instrument shows whether they are relatively well calibrated or if a relative correction is needed. The main problem for the set of observations here used is that only a few lines suitable for the integral inversion from the three different spectrometers overlap in temperature. Moreover, a minimum number of lines is needed to provide a reliable integral inversion. However, the lines selected as shown in table 4.10 allow the overlap of the differential emission measure curve in the small temperature range $\log(T/\mathrm{K})\simeq 5.24\text{-}5.76$.

The graphic output is displayed in figure 4.27. Each curve, specified by a color, represents the differential emission measure calculated with a single instrument.

Although the various uncertainty sources in such an analysis (e.g. choice of abundance values, extrapolation of the curve due to the limited number of lines used, value of electron pressure adopted and so on), a consistent overall behaviour is observed. Table 4.11 shows the differential emission measure values for each instrument in the overlapping temperature region. The ratio SUMER/CDS increases for value higher than $\log(T/\mathrm{K})=5.54$. This is due to the fact that the SUMER differential emission measure curve is less constrained at high temperature than the CDS and EIS curves. Also, the similarity in shape of the CDS and EIS curves in the common temperature region ensures that the present results are consistent and can be used as further test to verify the relative calibration among the three instruments.

| log(T/K) | SUMER | | CDS | | EIS | |
|---|---|---|---|---|---|---|
| 4.30 | Si II | 1309.28 Å | | | | |
| 4.85 | C III | 1174.93 Å | | | | |
| 5.00 | | | O III | 525.80 Å | | |
| 5.20 | O IV | 787.71 Å | Ne IV | 543.89 Å | | |
| 5.25 | | | | | O IV | 279.63 Å |
| 5.35 | O V | 629.73 Å | O V | 629.73 Å | | |
| 5.45 | | | | | O VI | 184.12 Å |
| 5.75 | Ne VIII | 770.41 Å | | | Si VII | 275.35 Å |
| 6.00 | | | | | Fe X | 184.54 Å |
| 6.15 | | | | | Fe XII | 193.51 Å |
| 6.25 | | | Si XII | 520.66 Å | | |

Table 4.10: Lines used to perform the differential emission measure independently for SUMER, CDS and EIS. Each line is related to its formation temperature.

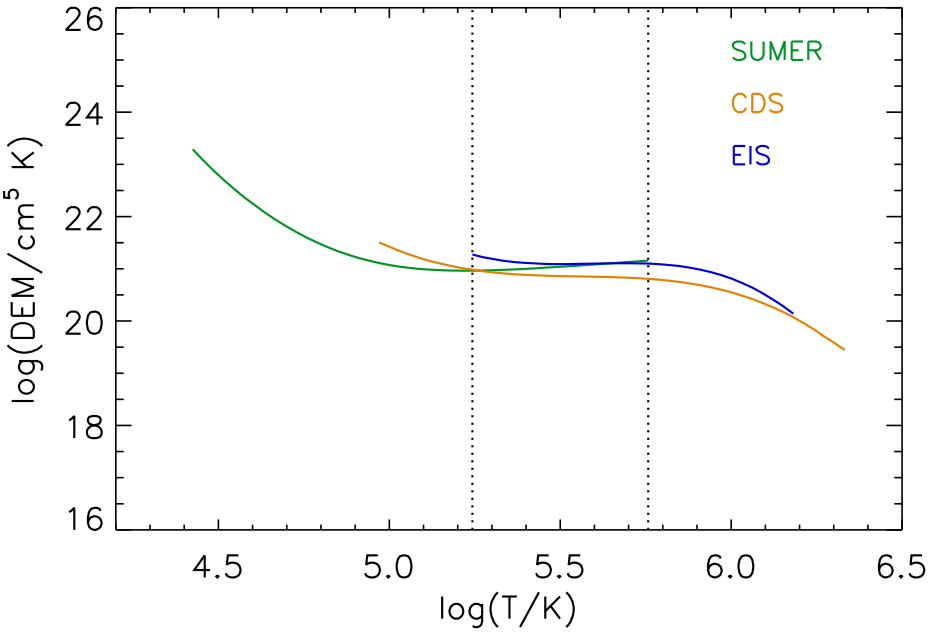


Figure 4.27: Differential emission measure determined independently for SUMER, CDS and EIS as further cross-calibration check. The two dotted vertical lines delimit the overlapping temperature region. A constant electron pressure of $10^{15}$ cm$^{-3}$ K has been used.The abundance values come from (71).

| log(T/K) | log(DEM) SUMER | log(DEM) CDS | log(DEM) EIS | SUMER/CDS | SUMER/EIS |
|---|---|---|---|---|---|
| 5.2430 | 20.9643 | 20.9823 | 21.2742 | 0.9593 | 0.4898 |
| 5.2718 | 20.9675 | 20.9547 | 21.2253 | 1.0299 | 0.5523 |
| 5.3032 | 20.9727 | 20.9315 | 21.1875 | 1.0995 | 0.6097 |
| 5.3324 | 20.9795 | 20.9128 | 21.1553 | 1.1662 | 0.6671 |
| 5.3636 | 20.9881 | 20.8976 | 21.1303 | 1.2316 | 0.7207 |
| 5.3944 | 20.9974 | 20.8854 | 21.1139 | 1.2942 | 0.7646 |
| 5.4248 | 21.0086 | 20.8756 | 21.1038 | 1.3581 | 0.8031 |
| 5.4548 | 21.0212 | 20.8686 | 21.0934 | 1.4208 | 0.8467 |
| 5.4843 | 21.0334 | 20.8627 | 21.0899 | 1.4814 | 0.8780 |
| 5.5145 | 21.0453 | 20.8585 | 21.0899 | 1.5374 | 0.9024 |
| 5.5453 | 21.0569 | 20.8549 | 21.0934 | 1.5921 | 0.9193 |
| 5.5751 | 21.0719 | 20.8513 | 21.0969 | 1.6619 | 0.9440 |
| 5.6063 | 21.0864 | 20.8476 | 21.1004 | 1.7329 | 0.9682 |
| 5.6364 | 21.1004 | 20.8432 | 21.1038 | 1.8077 | 0.9921 |
| 5.6665 | 21.1139 | 20.8370 | 21.1072 | 1.8922 | 1.0156 |
| 5.6972 | 21.1303 | 20.8299 | 21.1072 | 1.9970 | 1.0546 |
| 5.7275 | 21.1430 | 20.8195 | 21.1038 | 2.1060 | 1.0944 |
| 5.7574 | 21.1584 | 20.8075 | 21.1004 | 2.2429 | 1.1428 |

Table 4.11: List of the differential emission measure values for SUMER, CDS and EIS as a function of temperature, calculated using a $\Delta(\log T)$~0.03 interval. The differential emission measure (DEM) is in cm$^5$ K. In addition, the ratio between SUMER DEM and CDS DEM and the ratio between SUMER DEM and EIS DEM are shown in the last two columns.

# Chapter 5

# Atomic physics and data developments

As described in chapter 2 (par. 2.2) and in chapter 4 in more detail, SUMER, CDS and EIS instruments complement each other very well, covering all together a very wide spectral range from 150 Å to 1610 Å. They allow observations of lines which enable determination and study of the physical parameters of the solar atmosphere from the chromosphere and transition region to the hot corona. It is convenient to divide the type of analysis of spectral lines, gathered by this instrumentation, into two main aspects, the spectral line profiles on one hand and the line intensities on the other hand. The former is related to line shifts and broadenings, which return information on the local plasma conditions, such as flow velocities, and give evidence of the dynamic nature of the atmosphere. This work however focusses, instead, on the examination of line intensities as means of understanding solar measurements. To interpret observational data and to relate them to plasma conditions, it is necessary to model and analyse the radiative behaviour of atomic species in the plasma. This implies knowledge of the fundamental properties of the atoms, ions and electrons in interaction which contribute to the spectral emission. In general, the study of spectral emission requires also that account is taken of the transport of the radiation through the plasma. In fact, inside the plasma, the radiation is subjected to processes such as emission, absorption and scattering. As a consequence, when the radiation travels through a layer of thickness $ds$ and mass density $\rho$, its intensity $I_\nu$ increases, because of the emission of photons, by the amount $j_\nu \rho ds$, where $j_\nu$ is the emissivity coefficient and represents the power radiated by unit of mass per unit frequency interval per unit solid angle. At the same time, the absorption of the photons causes the intensity to decrease by the amount $-I_\nu \chi_\nu \rho ds$, where $\chi_\nu$ is the absorption coefficient. Hence the change of intensity, along the line of sight, can be described as following:

$$dI_\nu = -I_\nu \chi_\nu \rho ds + j_\nu \rho ds \tag{5.1}$$

if scattering processes are neglected. It is common to write the eq. 5.1 in terms of $d\tau_\nu$ instead of $ds$, where $\tau_\nu = \int \chi_\nu \rho ds$ is called optical depth:

$$\frac{dI_\nu}{d\tau_\nu} = -I_\nu + \frac{j_\nu}{\chi_\nu} \tag{5.2}$$

The general solution of the relation 5.2, called the equation of radiative transfer, is very complex because, even if the scattering is ignored, it requires solution of a large number of coupled integro-differential equations with coefficients which vary in space and time and depend on frequency too. However, assuming a uniform plasma in a plane parallel atmosphere and neglecting any spatial dependence of the processes, the resulting approximate solution can be written as follows:

$$I_\nu = \frac{j_\nu}{\chi_\nu}\left(1 - e^{-\chi_\nu \rho D}\right) = \begin{cases} j_\nu \rho D & \text{for } \tau_\nu \ll 1 \\ j_\nu / \chi_\nu & \text{for } \tau_\nu \gg 1 \end{cases} \tag{5.3}$$

where $D$ is the thickness in the direction in which the plasma is viewed and $j_\nu/\chi_\nu$ is called the source function. This simplified form shows an interesting feature. Since $\chi_\nu \rho$ has the dimension of inverse of length, $(\chi_\nu \rho)^{-1}$ can be interpreted as a mean free path governed by the probability that the particles interact leading to absorption processes. Hence, when $\tau_\nu = \chi_\nu \rho D \ll 1$, the mean free path $\chi_\nu \rho$ is much larger than the source size $D$ and the absorption is not very effective. In this case, the plasma is said to be optically thin and the observed intensity is given simply by $j_\nu \rho D$. In the other extreme limit, when $\tau_\nu = \chi_\nu \rho D \gg 1$, the plasma is optically thick and the observed intensity is the ratio between the emissivity and the absorption coefficient of the source. In particular, if the emission arises from a plasma in thermal equilibrium, the source function is given by the Planck function and the plasma radiates like a black body.

In the solar context, the high temperature and low density conditions of the upper atmosphere is such that, under most circumstances, the plasma is optically thin. Therefore, the radiation is one of the main energy loss mechanisms and it is potentially the only means to obtain any diagnostic information. In general, the intensity of radiation, emitted by the Sun or any other astrophysical and laboratory source, depends on the probability that the atoms within the observed plasma are in a condition to make transitions and on the probability that the photons produced by these transitions escape from the volume of the plasma without being reabsorbed. The first aspect is related to the distribution of atomic population among the various energy levels, which is established by collisions with other particles and by radiative processes, and to the atomic probability of the transitions. The second issue concerns the effect of the interaction of radiation with the plasma and in the optically thin case may be neglected, reducing significantly the complexity of the problem. In the optically thin regime, in fact, the intensity of a spectral line arising from a transition between the bound levels $j$ and $i$, derived by eq. 5.3, is simply:

$$I_\nu = j_\nu \rho D = \frac{1}{4\pi} A_{j\to i} N_j \psi_\nu D \ \ [\text{photons cm}^{-2}\text{s}^{-1}\text{sr}^{-1}\text{Hz}^{-1}] \tag{5.4}$$

with

$$j_\nu = \frac{1}{4\pi\rho} A_{j\to i} N_j \psi_\nu \tag{5.5}$$

where $A_{j\to i}$ is the Einstein coefficient for spontaneous emission, $N_j$ the population density of the level $j$ and $\psi_\nu$ is the emission profile, normalised to unity when integrated over the frequencies. Concentrating on the total emissivity in the transition, the eq. 5.5 becomes:

$$j_{j\to i} = \frac{1}{4\pi\rho} A_{j\to i} N_j = \frac{1}{4\pi\rho} \varepsilon_{j\to i} \tag{5.6}$$

The quantity $\varepsilon_{j\to i} = A_{j\to i} N_j$ is called *photon emissivity* for a transition between the upper level $j$ and the lower level $i$. Thus, generalizing, the radiative transfer equation can be reduced to the expression for the frequency-integrated line intensity from a column of plasma of cross-sectional area $A$:

$$I_{j\to i} = \frac{1}{4\pi A} \int \varepsilon_{j\to i} dV \ \ [\text{photons cm}^{-2}\text{s}^{-1}\text{sr}^{-1}] \tag{5.7}$$

where the integral is taken over the volume of the plasma viewed. In these circumstances, to know the observed intensity $I_{j\to i}$ attention must be given to the component quantities making up the photon emissivity. $A_{j\to i}$, the spontaneous transition probability, can usually be obtained by reference to the atomic physics literature or collected within database such as NIST (National Institute of Standards and Technology)[1]. The more difficult factor is the population density $N_j$ of an ion in the excited level $j$. It can be expressed in terms of other parameters of the solar plasma through the following relation:

$$N_j = \frac{N_j}{N_Z^{+z}} \frac{N_Z^{+z}}{N_Z} \frac{N_Z}{N_H} \frac{N_H}{N_e} N_e \tag{5.8}$$

where:

- $N_j/N_Z^{+z}$ is the relative population density of the excited level $j$ with respect to the total density of the ion of charge $z$ and nuclear charge $Z$;
- $N_Z^{+z}/N_Z$ is the *fractional abundance*, which is the relative abundance with respect to the total density of ions with nuclear charge $Z$;
- $N_Z/N_H = A(Z)$ is the abundance of element of nuclear charge $Z$;
- $N_H/N_e$ is the density of hydrogen relative to the density of electrons, which is $\sim 0.8$ for a totally ionised gas of elemental cosmic abundances;
- $N_e$, finally, is the electron density.

Using the expression 5.8, the emissivity for the spectral line between the levels $j$ and $i$ can be written as:

$$\varepsilon_{j\to i} = A(Z) \frac{N_H}{N_e} \left( \frac{1}{N_e} A_{j\to i} \frac{N_j}{N_Z^{+z}} \right) \left( \frac{N_Z^{+z}}{N_Z} \right) N_e^2 = A(Z) G(T_e, N_e) N_e^2 \tag{5.9}$$

where the quantity $G(T_e, N_e)$ is called *contribution function*. Because $N_H/N_e$ is a generally known value, the contribution function in essentially formed by two main terms:

[1] http://www.nist.gov/pml/data/asd.cfm

- a contribution due to the distribution of atomic population amongst excited levels:

$$\frac{1}{N_e} A_{j\to i} \frac{N_j}{N_Z^{+z}} \tag{5.10}$$

- a contribution relative to the fractional abundance for the ionisation state which includes the levels involved in the considered transition:

$$\frac{N_Z^{+z}}{N_Z} \tag{5.11}$$

These two contributions are both essential to predict spectrum lines and analyse them, using a diagnostic method such as the Differential Emission Measure (DEM) approach, that will be described properly in the next chapter. To establish them, it is necessary to take into account all the rate coefficients of every participating atomic process which contributes to the formation of the individual level population. However, the atomic structure of atoms and ions is in principle an infinite assembly of levels with an infinite number of reactions between them. This makes the problem complex to handle. Therefore, simplifying assumptions about the nature of the plasma, its dynamic character and the relative importance of the various reactions have to be made. In the sections that follow, some of the common models are described and it is shown that the *Generalised Collisional-Radiative theory* (GCR) is the most suitable approach within the perspective of this thesis and its concentration on its application especially to helium ions. Nevertheless, a realistic examination of helium line behaviour requires an accurate model of population not only of helium ions but also of other ions which will be included in the DEM analysis. Particular attention will be given to silicon ions. SUMER can observe, in fact, some Si II multiplets (chapter 4), that arise at the low temperatures ($\log(T/\mathrm{K}) \leq 4.5$) at which the helium lines are formed. So refined atomic data for silicon, together with a high quality set of observations, are important and come within the scope of this work. In the following sections, in order to assemble precise and updated contribution functions, fundamental and derived atomic data have been revised, incorporating recent calculations presented in the general literature and atomic databases and including execution of new calculations using the full GCR approach, which in principle treats all the atomic processes with the required accuracy.

## 5.1 The collisional-radiative modelling environment

This development is in the context of the ADAS project, which is designed to apply to all densities of plasma up to and exceeding that of magnetic confinement fusion devices. Also it is oriented to dynamic plasma that is in which the ionisation state and possibly excited population state is not relaxed to local thermal conditions. It is of course a core assumption of differential emission measure analysis that contribution functions are calculated in ionisation equilibrium. So the development here exceeds the immediate requirements. A further departure from usual solar analysis is the independent treatment of metastable states. These are handled on the same footing as ground states, that is allowing for slowly relaxing populations. This is termed generalised collisional radiative (GCR) modelling. ADAS has extensive derived data for applications in the GCR approximation for the light elements up to neon. For the present work it will be necessary to extend the GCR calculations up to silicon. Also it will be appropriate to re-examine the precision of the earlier calculations for the light elements and revise them where necessary. It is also noted that spectral emission from silicon ions of as low charge state as 1 is used. From a collisional-radiative point of view and at chromospheric densities, this places the problem in the "finite density" regime. This has two consequences. Firstly, the excited population structure of $Si^{+1}$ is modified by collisional redistribution amongst excited states, including quantum shells above the emitting levels. Secondly, effective recombination, particularly the dielectronic recombination component of it, is reduced by collisional re-ionisation of excited states. These issues cannot be ignored for precise calculations. In the following subsections, the mathematical/matrix representation of collisional-radiative modelling is briefly repeated for completeness, but then the work moves rapidly on to specific detail of the calculations. Although the results made available here are general, illustration of the importance of the various effects will be drawn from the key ions, such as $Si^{+1}$.

### 5.1.1 Solving the collisional-radiative equations

Consider the populations of ionisation stage $z$, separated into the metastable populations $N_\rho^{+z}$, indexed by the Greek letter $\rho$, and ordinary excited populations $N_i^{+z}$, indexed by the Roman letter $i$. The stage $z$ has adjacent stages $z-1$ and

$z+1$, its *child* and *parent*, with metastable populations labelled as $N_\mu^{+z-1}$ and $N_\nu^{+z+1}$ respectively. The time-dependent equations 5.12 of the populations are written in matrix/suffix form[5], where coupling to more distant ionisation stages has been omitted.

$$\frac{d}{dt}\begin{bmatrix} N_\mu^{+z-1} \\ N_\rho^{+z} \\ N_i^{+z} \\ N_\nu^{+z+1} \end{bmatrix} = \begin{bmatrix} \mathcal{C}_{\mu\mu'} & N_e\mathcal{R}_{\mu\sigma} & 0 & 0 \\ N_e\mathcal{S}_{\rho\mu'} & C_{\rho\sigma} & C_{\rho j} & N_e r_{\rho\nu'} \\ 0 & C_{i\sigma} & C_{ij} & N_e r_{i\nu'} \\ 0 & N_e S_{\nu\sigma} & N_e S_{\nu j} & \mathcal{C}_{\nu\nu'} \end{bmatrix} \begin{bmatrix} N_{\mu'}^{+z-1} \\ N_\sigma^{+z} \\ N_j^{+z} \\ N_{\nu'}^{+z+1} \end{bmatrix} \tag{5.12}$$

This means that these equations are actually complete only for the stage $z$. Note that the ordinary populations of stages $z-1$ and $z+1$ are not shown explicitly and that some of the sub-matrices are shown as script letters (eg. $\mathcal{C}_{\mu\mu'}$ and $\mathcal{R}_{\mu\sigma}$) whereas others are shown as standard letters (eg. $C_{\rho\sigma}$ and $S_{\nu j}$). Technically, this is because a 'quasi-static' assumption has been made about the ordinary populations of the stages $z-1$ and $z+1$ and the influence of their ordinary populations has been condensed onto their metastable populations. Note that the on-diagonal elements of $C$ and $\mathcal{C}$ are -ve quantities. $C$ and $\mathcal{C}$ are linear in the electron density $N_e$. This procedure is demonstrated for the ordinary populations of the stage $z$.

The quasi-static assumption is that $dN_i^{+z}/dt = 0$ which means that these ordinary populations are assumed in instantaneous statistical equilibrium with the various metastable populations[6]. This implies that

$$\begin{bmatrix} N_{\mu'}^{+z-1} \\ N_\sigma^{+z} \\ N_j^{+z} \\ N_{\nu'}^{+z+1} \end{bmatrix} = \begin{bmatrix} 1 & 0 & 0 \\ 0 & 1 & 0 \\ 0 & -C_{ji}^{-1}C_{i\rho} & -N_e C_{ji}^{-1} r_{i\nu} \\ 0 & 0 & 1 \end{bmatrix} \begin{bmatrix} N_\mu^{+z-1} \\ N_\rho^{+z} \\ N_\nu^{+z+1} \end{bmatrix} \tag{5.13}$$

and then

$$\frac{d}{dt}\begin{bmatrix} N_\mu^{+z-1} \\ N_\rho^{+z} \\ N_\nu^{+z+1} \end{bmatrix} = \begin{bmatrix} \mathcal{C}_{\mu\mu'} & N_e\mathcal{R}_{\mu\sigma} & 0 \\ N_e\mathcal{S}_{\rho\mu'} & \mathcal{C}_{\rho\sigma} & N_e\mathcal{R}_{\rho\nu'} \\ 0 & N_e\mathcal{S}_{\nu\sigma} & \mathcal{C}_{\nu\nu'} \end{bmatrix} \begin{bmatrix} N_{\mu'}^{+z-1} \\ N_\sigma^{+z} \\ N_{\nu'}^{+z+1} \end{bmatrix} \tag{5.14}$$

where we have the definitions of the effective metastable cross-coupling coefficient, effective recombination coefficient and effective ionisation coefficients between the various metastables of stages $z$, $z-1$ and $z+1$

$$\begin{aligned} Q_{\sigma\to\rho}^{cd} &\equiv \mathcal{C}_{\rho\sigma}/N_e &&= (C_{\rho\sigma} - C_{\rho j}C_{ji}^{-1}C_{i\sigma})/N_e \\ A_{\nu'\to\rho}^{cd} &\equiv \mathcal{R}_{\rho\nu'} &&= r_{\rho\nu'} - C_{\rho j}C_{ji}^{-1}r_{i\nu'} \\ S_{\sigma\to\nu}^{cd} &\equiv \mathcal{S}_{\nu\sigma} &&= S_{\nu\sigma} - S_{\nu j}C_{ji}^{-1}C_{i\sigma}. \end{aligned} \tag{5.15}$$

Also there is formally an addition to the $\mathcal{C}_{\nu\nu'}$ term called the parent metastable cross-coupling coefficient

$$X_{\nu'\to\nu}^{cd} \equiv -(S_{\nu j}C_{ji}^{-1}r_{i\nu'})/N_e \tag{5.16}$$

which had already been incorporated as assumption. The superscript 'CD' denotes 'collisional-dielectronic' - a historic synonym for 'collisional-radiative' and parallels the naming conventions in the ADAS data format *adf11* used for such data.

The matrix algebra and description above is the most complete formulation within the collisional-radiative framework. The collisional-radiative matrix $C_{ij}$ is composed of collisional and radiative terms and is infinite (having an infinite number of levels) in general. The matrix is truncated in practice and the completeness of inclusion of the collisional terms may be restricted according to the particular type of plasma application. In this thesis, the simplifying approximations typically used in solar upper atmosphere spectroscopy are examined and the error introduced by these assessed. In this section, the algebraic quantities which correspond to these omissions are identified so that they can be evaluated in specific cases later. The simplifications of concern are (1) truncation; (2) zero-density assumptions; (3) ionisation from excited states and top-up; (4) bundling and resolution level; (5) metastable correction (which spans essentially three main aspects: (i) large metastable fractional populations with respect to the ground, (ii) recombination contributions to metastable populations, (iii) unrelaxed metastable populations).

[5] In the following equations summation convention over repeated indices is adopted.

[6] No direct populating mechanism from stage $z-1$ to ordinary excited state of stage $z$ has been assumed.

1. *Truncation*: It used to be common to assume that each ordinary excited state is coupled independently only to the ground state and that there are no metastables. Thus the matrix $C_{ij}$ has only non-zero diagonal elements $C_{ii} = N_e q^{(e)}_{i\to 1} + A_{i\to 1}$. Also $C_{i1} = N_e q^{(e)}_{1\to i}$. So in equation 5.13 $-C^{-1}_{ji} C_{i\rho} = N_e q^{(e)}_{1\to j}/(N_e q^{(e)}_{j\to 1} + A_{j\to 1})$. This is a severe oversimplification, justified only if the lowest resonance line is under consideration for observation. Radiative transitions may take place between other levels besides the ground. Also cascade from higher levels above the level $j$ is ignored. This truncation error may be substantial depending on whether the level $j$ is in the same principal quantum shell as the ground. For higher $n$-shells the cascade correction is of order $n_0/2$ where $n_0$ is the upper n-shell of the transition. The correction for these omissions is

$$- C^{-1}_{ji} C_{i1} - N_e q^{(e)}_{1\to j}/(N_e q^{(e)}_{j\to 1} + A_{j\to 1}) \tag{5.17}$$

   where $C_{ij}$ is the full unabbreviated collisional-radiative matrix, and we are assuming only a ground state $\rho = 1$ (no metastables).

2. *Zero-density assumptions:* The collisional-radiative matrix element $C_{ij}$ is of the form $N_e q^{(e)}_{j\to i} + A_{j\to i}$ for $i < j$ and of the form $N_e q^{(e)}_{j\to i}$ for $i > j$. In the zero-density limit, collisional de-excitation is usually neglected for all excited levels, because the electron density times the rate coefficient is small, that is $A_{j\to i} >> N_e q^{(e)}_{j\to i}$ or more precisely for the population structure $\sum_i A_{j\to i} >> N_e \sum_i q^{(e)}_{j\to i}$. The collisional excitation rate coefficient $q^{(e)}_{i\to j} = \omega_j \exp((I_j - I_i)/kT_e) q^{(e)}_{j\to i}/\omega_i$, where the $\omega_i$, $\omega_j$ are statistical weights and $I_i$, $I_j$ are ionisation potentials. The excitation rate coefficient is generally smaller than the excitation energy apart from the statistical weight and so the collisional excitation rates are ignored except for the ground state, since it has no radiative decay. This is the coronal picture for excitation, namely excitation from the ground followed by radiative decay. The solution for the excited populations with purely radiative decays, for the general atom or ion, was done by Seaton (1959) and called the *cascade matrix*. An element $C^{(cas)}_{ij}$ of the cascade matrix is the probability of making a transition to the level $i$ from the level $j$ by any route. It is analogous to a 'propagator'. The name 'propagator' is used hereafter as the theory is extended to the collisional-radiative case. In the collisional-radiative case, collisional rate coefficients cannot be ignored and the collisional-radiative matrix $C_{ij}$ includes both radiative and collisional parts as shown in 1. above. Considering equation 5.17, it is evident that $C^{-1}_{ji}$ is effectively the propagator. Thus the left-hand-side of this equation (see also equations 5.13) can be interpreted as the contribution to the population of the level $j$ by excitation from the ground state to a level $i$ and then propagation to the level $j$ by any route, summed over all $i$. Note the implicit summation over repeated indices in the notation of this thesis. Accepting $C^{-1}_{ji}$ as the definition of the propagator from $i$ to $j$, then

$$C^{-1}_{ji}(N_e \to 0) = \frac{1}{A_{(i)}} C^{(cas)}_{ij} \tag{5.18}$$

   where $A_{(i)} = \sum_{k,k<i} A_{i\to k}$. The () indicates that there is no sum over the index $i$ in equation 5.18. Seaton (1959) was concerned with recombination on to highly excited n-shell followed by cascade, corresponding to the (3,3) element in the equation 5.13. Here we are concerned with the excitation part from the ground only corresponding to the (3,2) element. Finally the correction for the zero density assumption for the extended level set is

$$- C^{-1}_{ji} C_{i1} - C^{-1}_{ji}(N_e \to 0) C_{i1} \tag{5.19}$$

3. *Ionisation from excited states and top-up:* If one continues to increase the extended level set to high levels then a point is reached at which collisional ionisation must become important. However, when collisional ionisation becomes important then collisional transitions upwards and downwards to neighbouring n-shells must also be important. Ionisation from highly excited states is unlikely to proceed stepwise through n-shell to the continuum as directly to the continuum. So ionisation from excited states is properly treated as a top-up coming from a study of the very high population structure above the extended truncated set. Because for those very high levels the collisional de-excitation rate can exceed the radiative transition probability, they can satisfy the condition of Local Thermodynamic Equilibrium (LTE) as the continuum. There is, therefore, a particular state in the ion, called collision limit, above which the distributions of atomic population approximate to the thermal and the population is given by the Saha-Boltzmann and Boltzmann equations. An electron in the collision limit is equally likely to be ionised or to cascade downward. So the bound levels above this limit behave, in certain respects, as the continuum. In fact, any transition to lower levels is equivalent to recombination, because the hole that is left is immediately populated by a collisional transition from the continuum, and any excitation from

lower levels to those upper levels is equivalent to ionisation. The principal quantum number $n_{cl}$, representing the collision limit in a hydrogen-like ion has been defined by (72) as following:

$$n_{cl} = \left[ 5.57 \times 10^{17} \frac{z_1^6}{N_e} \left( \frac{kT_e}{I_H} \right)^{1/2} \right]^{1/7} \tag{5.20}$$

where $I_H$ is the ionisation potential of hydrogen and $k$ the Boltzmann constant. The dependence on electron density of the collision limit represents the finite density collisional-radiative effects. For low electron densities, the collision limit is very close to the ionisation limit and the coronal approximation is adequate, but as $N_e$ increases, the collision limit becomes lower and the coronal approach is not valid. To take into account these effects on the very high populations, the diagonal elements of the collisional radiative matrix $C_{ij}$ become $C_{ii} = \sum_{j<i} A_{i\to j} + N_e q^{(e)}_{i\to j} + N_e q^{(I)}_i$. They include one more term, $N_e q^{(I)}_i$, which describes the loss from the excited level $i$ due to the electron-impact ionisation. Note that in the solar atmosphere the most important processes which contribute to ionisation are collisions driven by electrons. Collisional interaction involving atoms or ions, rather than electrons, are often omitted from models, because of the much smaller relative velocities. However for multi-electron ions and when the plasma temperature increases, especially collisions driven by protons can be quite effective in populating and depopulating the excited levels and ionising them. Also, (73) showed that collision excitation rates from proton-ion collisions increase when the energy separation between the levels involved in the transition decreases. In that case, proton collisions become important and may affect the level population. Ionisation due to heavy particle collisions is generally negligible except in very weakly ionised plasma or in some other cases (e.g. (74), (75)) far from solar atmosphere conditions. Coming back to the extended truncated set, if it spans levels up as far as the collision limit, from which an electron is equally likely to be ionised or to cascade downward, then an approximation to the ionisation + top-up can be made by lowering the threshold energy of the cross section for ionisation to the n-shell above the last included level. This is a somewhat crude approximation. If collisional cross sections between neighbouring n-shells are large then collisional redistribution cross sections between l-shells of the same n must be much larger again. In this situation it is sufficient to treat the population of whole n-shells. This requires consideration of resolution, that is item 4.

4. *Bundling and resolution level:* In ADAS generalised collisional-radiative model is implemented as so called *ls* resolution, that is to say the population structure is evaluated for LS terms. This is appropriate for light element ions for which the fine structure separation of levels is small. Although fine structure separation may be observable through distinct components in high resolution spectroscopy. The levels are in relative statistical proportion. As one moves to heavier species and more highly ionised ions, the relativistic terms in the hamiltonian become larger, the fine structure separations become larger and the relative population become to deviate from relative statistical. Here this is called *ic* resolution. On the other hand, in finite density plasma, as one moves to higher quantum shells collisional redistribution becomes more efficient and populations move progressively towards the LTE regime. Firstly, terms of the same nl-shell move into relative statistical proportions. This is called *ca* resolution. Finally l-subshells of the same n-shell move into relative statistical populations. This is referred to as *bn* resolution. This mnemonics indicate that at *bn* resolution it is only necessary to work with whole n-shell population whereas at *ic* resolution it is necessary to work with individual level population. A high precision study must deal with all the levels of an atom, but it is only required to treat the low levels, particularly which are observed spectroscopically in high resolution, higher level population may be treated in coarser resolution. Returning to the collisional-radiative matrix, it is helpful to consider sub-divisions of the ordinary excited states spanned by $C_{ij}$. For the ionisation stage $z$, let $n^{(ic)}_{cf}$ be the number of configurations which one needs to include in structure calculations at *ic* resolution for spectroscopy (subject also to the constraint of computational resources). Let $n^{(ca)}_{cf}$ be the number of configurations which one needs to include in structure calculations at *ca* resolution to ensure the excitation line power is sufficiently complete. One expects $n^{(ca)}_{cf}$ to include configurations up to some principal quantum n-shell $n^{(ca)}_{ns}$ of the valence electron. Finally let $n^{(bn)}_{ns}$ be number of principal quantum shells of the valence electron which must be considered to ensure dielectronic recombination is sufficiently complete (*bn* stands for 'bundle-*n*'). Evidently the $n^{(ic)}_{cf}$ should be contained in the set $n^{(ca)}_{cf}$. Also $n^{(ca)}_{ns}$ should be contained in $n^{(bn)}_{ns}$. It is of course unrealistic computationally to evaluate fully-coupled *ic*-populations over all configurations $n^{(ca)}_{cf}$ and to evaluate fully-coupled *ca*-populations over all n-shells $n^{(bn)}_{ns}$. It is equally unrealistic from a physics point-of-view, since collisional processes in finite density plasmas ensure that sub-shell populations of high-enough configurations approach statistical within each configuration and also that *l*-sub-shell populations of high-enough n-shells approach statistical within each n-shell. This treatment is

illustrated through three manageable collisional-radiative matrices, of progressively greater excited level span but of progressively coarser resolution.

$$\left[\ C^{(ic)}_{ij}\ \right], \left[\begin{array}{cc} C^{(ca)}_{\bar{i}\,\bar{j}} & C^{(ca)}_{\bar{i}\,j'} \\ C^{(ca)}_{i'\,\bar{j}} & C^{(ca)}_{i'\,j'} \end{array}\right], \left[\begin{array}{ccc} C^{(bn)}_{\bar{\bar{i}}\,\bar{\bar{j}}} & C^{(bn)}_{\bar{\bar{i}}\,\bar{j}'} & C^{(bn)}_{\bar{\bar{i}}\,j''} \\ C^{(bn)}_{\bar{i}'\,\bar{\bar{j}}} & C^{(bn)}_{\bar{i}'\,\bar{j}'} & C^{(bn)}_{\bar{i}'\,j''} \\ C^{(bn)}_{i''\,\bar{\bar{j}}} & C^{(bn)}_{i''\,\bar{j}'} & C^{(bn)}_{i''\,j''} \end{array}\right] \tag{5.21}$$

where partitioning delimits the progressively extending ranges. The notation means that $C^{(ca)}_{\bar{i}\,\bar{j}}$ spans the same range of levels as $C^{(ic)}_{ij}$, but in the former case the components are bundled-up for whole configurations, while in the latter the levels are fully resolved. Again $C^{(ca)}_{i'\,j'}$ and $C^{(bn)}_{\bar{i}'\,\bar{j}'}$ span the same range of configurations, but in the latter case are bundled-up into principal quantum shells. Sophisticated population modelling, as is done in *GCR* modelling of light elements, carries out a sequence of condensations (analogous to that of equations 5.12 → 5.14) and expansions from the three-by-three partition matrix to the two-by-two partition matrix and finally to the one-by-one partition matrix. In illustration, the step from the two-by-two *ca* matrix is as follows: Eliminate the direct couplings in the $C^{(ca)}_{\bar{i}\,\bar{j}}$ partition of the two-by-two matrix and call it $\bar{C}^{(ca)}_{\bar{i}\,\bar{j}}$. Then replace it with $\bar{\bar{C}}^{(ca)}_{\bar{i}\,\bar{j}} = \bar{C}^{(ca)}_{\bar{i}\,\bar{j}} - C^{(ca)}_{\bar{i}j'}(C^{(ca)}_{j'i'})^{-1}C^{(ca)}_{i'\,\bar{j}}$. Expand the matrix $\bar{\bar{C}}^{(ca)}_{ij}$ over the resolved manifold of $C^{(ic)}_{ij}$ through replacing $C^{(ic)}_{ij}$ by $C^{(ic)}_{ij} + W_{i\bar{i}}\,\bar{\bar{C}}^{(ca)}_{\bar{i}\,\bar{j}}U_{\bar{j}\,j}$ The pre-multiplier $W_{i\bar{i}}$ is $\omega_i/\omega_{\bar{i}}$ if $i \in \bar{i}$ otherwise 0. The $\omega$s are statistical weights. The post-multiplier $U_{\bar{j}\,j}$ is 1 if $j \in \bar{j}$ otherwise 0. This prescription will be followed in this thesis for silicon, with condensation and projection extended down to the low levels in *ls* resolution. As one progresses to heavier atoms and ions up to iron, it becomes appropriate to condense and project down to the low levels in *ic* resolution. So, the basic correction arising from the projection is an addition to the collisional radiative matrix for the low set of levels in *ic* coupling, that is to $C^{(ic)}_{ij}$, namely $W_{i\bar{i}}\,\bar{\bar{C}}^{(ca)}_{\bar{i}\,\bar{j}}U_{\bar{j}\,j}$. The correction to the populations and emissivity must be evaluated by following through the matrix inversion. However some clarification is required about the low level target collisional radiative matrix and the high level projected matrices.

The target here remains silicon, but the prescription and expert system will be set up for extension to iron. In the above general discussion, the identifiers *ca* and *bn* have been used as though they apply to all the levels, but in practice it is the valence electron whose character is a concern. Thus from the collisionality it may be appropriate to treat the valence electrons as in bundled *nl*- or *n*-shells, but the parent core should still be represented in a resolved form - that is *ls* or *ic*, for example $(S_pL_p)nl$ or $(J_p)n$. For a light element in a low state of ionisation the parent is appropriately in the $(S_pL_p)$ form with a valence n-shell, separately for each spin system S of the whole ion. This is because provided one does not go to too high n-shell, there is good spin system separation. For highly ionised heavy systems, it is appropriate to have $(J_P)$ coupled parent and an uncoupled valence n-shell electron. Silicon ions tend to the first situation while tungsten ions are strongly in the second situation. Some of the ions of iron are between these two extremes. It is appropriate to consider the various forms of coupling for the high valence shells, the parent and the targeted low levels and the projection between them in more detail. The table 5.1 summarises the situation and the methods which are open to be used in this thesis or which should be developed in the future.

| Parent \ Valence | *ca* | *bn* | *bnl* |
|---|---|---|---|
| *ls* | *ls-ca* | *ls-bn* | *ls-bnl* |
| *ic* | *ic-ca* | *ic-bn* | *ic-bnl* |

Table 5.1: Scheme of different resolutions for a parent and a valence shell and forms of coupling between them. Note that for the *bnl* model the coupling arises from a partial *ca* resolution, so that *ic-ca* coupled to *bn* gives *ic-bnl* and *ls-ca* coupled to *bn* gives *ls-bnl*.

For this table some extension to resolution mnemonics is appropriate. The form *ls-ca* is used to denote the core parent ion in *ls* resolution and the valence electron in *ca* resolution. There are many variants such as *ic-bn*, some of which are useful and some of which are not. Then there are various options for projecting from these combinations onto low levels. Clearly, the resolution of the targeted low level system must be consistent with the resolution of the high level system shown in the table 5.1. A second table (table 5.2) summarises the useful projection paths.

| Low levels / Parent+Valence | $C_{ij}^{(ls)}$ | $C_{ij}^{(ic)}$ |
|---|---|---|
| *ls-ca* | *ls-ca* $\rightarrow C_{ij}^{(ls)}$ | *ls-ca* $\rightarrow C_{ij}^{(ic)}$ |
| *ls-bn* | *ls-bn* $\rightarrow C_{ij}^{(ls)}$ * | *ls-bn* $\rightarrow C_{ij}^{(ic)}$ ◇ |
| *ls-bnl* | *ls-bnl* $\rightarrow C_{ij}^{(ls)}$ | *ls-bnl* $\rightarrow C_{ij}^{(ic)}$ |
| *ic-ca* | *ic-ca* $\rightarrow C_{ij}^{(ls)}$ | *ic-ca* $\rightarrow C_{ij}^{(ic)}$ |
| *ic-bn* | *ic-bn* $\rightarrow C_{ij}^{(ls)}$ | *ic-bn* $\rightarrow C_{ij}^{(ic)}$ ◇ |
| *ic-bnl* | *ic-bnl* $\rightarrow C_{ij}^{(ls)}$ | *ic-bnl* $\rightarrow C_{ij}^{(ic)}$ ◇ |

Table 5.2: Scheme of the various options of coupling of parent and high valence shells and projection onto low levels. The symbol * indicates that the model exists. It is good for light and low charge elements, so it is a quite save approach until silicon. The symbol ◇ indicates that those models almost exist. In particular, *ic-bn* and *ic-bnl* projected onto $C_{ij}^{(ic)}$ already exist for hydrogen and they are good for heavy species and high charge elements. This thesis is dealing with *ls-bn* projected onto $C_{ij}^{(ic)}$, using the statistical weight. The other models do not exist.

5. *Metastable correction:* Low lying metastable states have been a source of confusion and error in population modelling for many years. This is because such a metastable in a plasma can have a population of the same order as the true ground population. It is often assumed that the whole population of an ionisation stage of an element is the ground state. However, for an ion such as $C^{+2}$ the $2s2p\,^3P$ may exceed that of $2s^2\,^1S$ ground state. So the population count for the stage must include that metastable. Note that the true excited populations normally give a negligible contribution (of order $10^{-4}$) to the population count. Equilibrium emissivity coefficients coming from simple collisional-radiative calculations are often refered to the ground population, leading to potential error when combined with ionisation balance fractions. The problem is more severe. A metastable ion, because of its abundance, may be a target system for free electron recombination, but dielectronic recombination with a metastable opens quite different Auger pathways from recombination with the ground. Naive calculation can omit recombination with the metastable entirely. Other calculations treat the availability of target recombining ions as the whole population of the ionisation stage with dramatically different result. Clearly the metastable should be treated fully as an independent target system similar to the ground. This is the approach of generalised collisional-radiative theory used here. A ion, in a metastable state, is such because it has a long radiative lifetime. That is to say, it has a relaxation time which is long compared with true excited states, a lifetime which may be of the order of that of the ground state. Evidently a dynamic plasma evolving in space or time with scale length or characteristic time of order the relaxation time of ground and/or metastable population cannot be treated as in ionisation equilibrium. The ionisation state and the dynamics are coupled. Generalised collisional-radiative theory treats ground states and metastable states on the same footing and distinguish them from ordinary excited states of fast (relatively) relaxation time. As has been described earlier, this validates quasi-static approximations. The error arising from incomplete treatment of metastables are more severe in dynamic plasma. Properly the dynamic time scale must be evaluated in association with the atomic time scales and metastable identified and handled appropriately. Although the study in this thesis examines equilibrium models this is with a view to establishing where they break down. So generalised collisional-radiative model is a prerequisite here ((76), (77)).

   Returning to the two-by-two submatrix partition of the full collisional-radiative matrix (equation 5.12), from the quasi-static assumption and equations 5.13, the ordinary level populations of the stage $z$ are given by

$$\begin{aligned} N_j^{+z} &= -C_{ji}^{-1} C_{i\sigma} N_\sigma^{+z} - C_{ji}^{-1} r_{i\nu} N_e N_\nu^{+z+1} \\ &= F_{j\sigma}^{(exc)} N_e N_\sigma^{+z} + F_{j\nu}^{(rec)} N_e N_\nu^{+z+1} \end{aligned} \tag{5.22}$$

   where $F_{j\sigma}^{(exc)} = -(1/N_e) C_{ji}^{-1} C_{i\sigma}$ and $F_{j\nu}^{(rec)} = -C_{ji}^{-1} r_{i\nu}$. The above expression shows that the ordinary level populations are made up of two parts, driven by excitation from the metastables of the stage $z$ and by recombination from the metastables of the stage $z+1$ respectively. The equation 5.22 has a general character being valid for both light and heavy elements. However, for heavy species with typically small energy differences between true ground and populated metastables, the metastable-ground collisional coupling in $C_{\rho\sigma}$ would be large and move the relative populations to Boltzmann. Forcing the metastable relative populations of the stages $z-1$ and $z+1$

to Boltzmann, the metastable populations become:

$$\left[N_{\mu}^{+z-1}\right] = \left[f_{\mu}^{Boltz}\right] N^{+z-1}$$
$$\left[N_{\nu}^{+z+1}\right] = \left[f_{\nu}^{Boltz}\right] N^{+z-1} \tag{5.23}$$

where $f_{\mu}^{(z-1)Boltz} = \omega_{\mu} exp(I_{\mu}/kT_e)/\sum_{\mu'} \omega_{\mu'} exp(I_{\mu'}/kT_e)$ and $N^{+z-1} = \sum_{\mu} N_{\mu}^{+z-1}$. This manipulation has the same effect as introducing artificial strong collisional coupling rates between the metastables, creating local thermodynamic equilibrium within the metastable set. Since the sum of the populations of the ordinary levels is very small compared with the sum of the metastable populations, $N^{+z-1}$ is the effectively the whole population of the stage $z-1$. Similarly for $f_{\nu}^{(z+1)Boltz}$ and $N^{+z+1}$. The $I_{\mu}$ denote ionisation potentials. Then adding up equations 5.16 over $\mu$ and $\nu$ and substituting from equations 5.23

$$\frac{d}{dt}\begin{bmatrix} N^{+z-1} \\ N_{\rho}^{+z} \\ N^{+z+1} \end{bmatrix} = \begin{bmatrix} \mathcal{C}^{(z-1)} & N_e \mathcal{R}_{\sigma}^{(z-1\leftarrow z)} & 0 \\ N_e \mathcal{S}_{\rho}^{(z-1\rightarrow z)} & \mathcal{C}_{\rho\sigma} & N_e \mathcal{R}_{\rho}^{(z\leftarrow z+1)} \\ 0 & N_e \mathcal{S}_{\sigma}^{(z\rightarrow z+1)} & \mathcal{C}^{(z+1)} \end{bmatrix} \begin{bmatrix} N^{+z-1} \\ N_{\sigma}^{+z} \\ N^{+z+1} \end{bmatrix} \tag{5.24}$$

where $\mathcal{C}^{(z-1)} = \sum_{\mu} \mathcal{C}_{\mu\mu'} f_{\mu'}^{Boltz}$, $\mathcal{R}_{\sigma}^{(z-1\leftarrow z)} = \sum_{\mu} \mathcal{R}_{\mu\sigma}$ , $\mathcal{S}_{\rho}^{(z-1\rightarrow z)} = \mathcal{S}_{\rho\mu'} f_{\mu'}^{Boltz}$ and so on. Evidently, it is possible to do the same for the metastables of ionisation stage $z$ so returning completely to the collisional-radiative (*CR*) picture. But equations 5.24 demonstrate how to mix *GCR* and *CR* data selectively. Using this simplification, the equation 5.22 may be expressed as:

$$N_j^{+z} = F_{j\sigma}^{(exc)} f_{\sigma}^{(z)Boltz} N_e N^{+z} + F_{j\nu}^{(rec)} f_{\nu}^{(z+1)Boltz} N_e N^{+z+1}. \tag{5.25}$$

Sometimes it is preferred to refer the ordinary populations to the ground state (lowest metastable) of the stage. Putting $f_{\sigma 1}^{(z)Boltz} = f_{\sigma}^{(z)Boltz}/f_1^{(z)Boltz}$, then equation 5.25 is replaced by

$$N_j^{+z} = F_{j\sigma}^{(exc)} f_{\sigma 1}^{(z)Boltz} N_e N_1^{+z} + F_{j\nu}^{(rec)} f_{\nu 1}^{(z+1)Boltz} N_e N_1^{+z+1}. \tag{5.26}$$

This treatment gives a complete picture of the simplifications that can be applied to the calculations for the level populations of an ion, showing how the corrections provided by a full GCR approach allow a more accurate description of the real condition of the examined plasma.

## 5.2 Data status and the solar requirements

A large amount of fundamental and derived atomic data is necessary to model the plasma in typical solar upper atmosphere conditions. Its precision combines with the accuracy of observation and calibration to determine the reliability of the diagnostic techniques. The precision of atomic physics calculations has improved considerably over the past decades. Theoretical and experimental results are becoming available and more reliable for many ions, both light and heavy. However, in previous studies, interpretation of data has sometimes been confused by uncertainties in the appropriateness of simplifying assumptions in excited ion population and ionisation state models. An example is the O IV line theoretical ratio examined by (78), which shows a significant deviation from the observed ratio due to the fact that only transitions which involve the first five levels (as lower level) have been considered. This example will be discussed in the next chapter, sec. 6.2. As mentioned, although the goal of this thesis is the study of the EUV helium line intensities observed by CDS and EIS, the DEM analysis which is used as diagnostic technique requires the revision and upgrade of atomic data for all the ions which give rise to the transitions listed in tables 4.4, 4.5 and 4.6. The main source for this work is the ADAS database. Some other sources of fundamental and derived atomic data have been selected and reviewed. Also they have been compared with the data collection currently present in ADAS. The main other databases with which the thesis is concerned, apart from ADAS, are NIST and CHIANTI ((79) and references therein). Furthermore, the most recent calculations from literature have been included in the review. Finally, a recommendation has been provided, suggesting the preferred values of energy levels, transition probabilities, collision strengths/effective collision strengths for collisional excitation and ionisation/recombination rates that can be used to produce updated contribution functions.

This update is performed within the ADAS framework (8). The ADAS package consists of an archive of atomic data and a set of codes. The atomic data are stored as ADAS data format files, called *adf* and followed by a two digit number,

| Data file | Content |
|---|---|
| *adf00* | Ground and metastable configuration and ionisation potentials |
| *adf04* | Specific ion data collections |
| *adf07* | Electron impact ionisation coefficients |
| *adf09* | Dielectronic recombination coefficients |
| *adf10* | Iso-electronic master files for GCR coefficients |
| *adf11* | Iso-nuclear master files for GCR coefficients |
| *adf17* | Condensed projection coefficients |
| *adf18* | Cross-referencing data |
| *adf20* | Contribution functions |
| *adf23* | State selective electron impact ionisation coefficients |
| *adf25* | Driver datasets for ADAS204 calculation |
| *adf32* | Driver datasets for ADAS802 calculation |
| *adf56* | Promotional rules |

Table 5.3: Key ADAS data formats used in this work.

which indicates the data class. The key *adf*s used in this work are listed in table 5.3. The *adf* data files are designed such that they can be accessed by the ADAS codes. They are of two types, those which contain the calculated values of a particular quantity on a grid of temperatures, densities or appropriate factors and those which are driver files for the codes within ADAS. An example of the first type is the *adf04* data file which provides the list of specified low levels with their energies, the radiative atomic probabilities related to the transitions amongst them and the associated rate coefficients as a function of temperature for an ion. An example of the second *adf* type is *adf32*, which is a driver file containing configurations and other control parameters for distorted wave cross-section calculation using ADAS802. The first type of ADAS data files with their associated reading routines are available online at http://open.adas.ac.uk. The ADAS codes consists of eight series. Each series is identified by the first digit. For example, series 6 codes are

| Series | Code | Description |
|---|---|---|
| ADAS2 | ADAS204 | Bundle-*nS* GCR recombination and ionisation coefficient calculation |
| | ADAS208 | Production of GCR coefficients and line emissivities |
| | ADAS209 | Change of resolution level by bundling |
| | ADAS211 | Addition of extra data lines for radiative recombination |
| | ADAS212 | Addition of extra data lines for dielectronic recombination |
| | ADAS215 | Change of the temperatures at which the specific ion file is tabulated |
| ADAS4 | ADAS403 | Iso-electronic tabulation of GCR coefficients |
| | ADAS404 | Conversion from iso-electronic to iso-nuclear collection of GCR coefficients |
| | ADAS407 | Preparation of iso-nuclear parameter sets |
| | ADAS412 | Contribution function calculation |
| ADAS6 | ADAS601 | Differential emission measure analysis |
| | ADAS602 | Gaussian spectral line fit |
| ADAS7 | ADAS701 | AUTOSTRUCTURE |
| | ADAS704 | Production of *adf04*, *adf09* and *adf18* by post-processing the output from ADAS701 |
| ADAS8 | ADAS801 | Cowan structure code |
| | ADAS802 | CADW ionisation cross-section calculation |
| | ADAS807 | Preparation of extra data lines for ionisation and cross-reference and template files for GCR modelling |

Table 5.4: ADAS codes used in this work.

concerned with analysis of spectral data. Two key codes of these series are ADAS601 and ADAS602, which will be extensively used in this thesis. Alternatively, if there is no atomic data present for a given calculation, it is possible to generate them, often of basic/lower quality, using various ADAS routines. For instance, ADAS211 generates radiative recombination data following the approach of (80), ADAS701 runs AUTOSTRUCTURE code of (81) and ADAS801 runs the Cowan code (82). Table 5.4 lists the ADAS codes used in this thesis with their general description.

As shown in table 5.3, the contribution functions are collected in the *adf20* data files. A contribution function is formed by two main terms (eq. 5.10 and 5.11), which take into account the atomic population of excited levels and the ionisation fraction. Using the equation 5.22 for the excited level populations, the *excitation* and *recombination Photon Emissivity Coefficients* (*PEC*) for a spectral line can be defined as following (11):

$$PEC^{(exc)}_{\sigma,j\to i} = A_{j\to i}F^{(exc)}_{j\sigma} \tag{5.27}$$

$$PEC^{(rec)}_{\nu',j\to i} = A_{j\to i}F^{(rec)}_{j\nu'} \tag{5.28}$$

where $A_{j\to i}$ and the coefficients $F^{(exc)}_{j\sigma}$ and $F^{(rec)}_{j\nu'}$ have been already specified. So the contribution function can be written as:

$$G^{[z]}_{j\to i}(T_e, N_e) = \sum_{\sigma} PEC^{[z](exc)}_{\sigma,j\to i}\left(\frac{N^{+z}_{\sigma}}{N^{tot}}\right)_{eq} + \sum_{\nu'} PEC^{[z](rec)}_{\nu',j\to i}\left(\frac{N^{+z+1}_{\nu'}}{N^{tot}}\right)_{eq} \tag{5.29}$$

where the fractional abundances, $N^{+z}_{\sigma}/N^{tot}$ and $N^{+z+1}_{\nu'}/N^{tot}$, are calculated in equilibrium - that is when the plasma is in the steady-state of ionisation balance - and $N^{tot} = \sum_z \sum_{\sigma} N^{+z}_{\sigma}$ is the ion density of the considered element in the whole set of ionisation stages. All information about the structure of excited level populations comes inside the *PEC*s, while the processes responsible to ionisation and recombination come inside the ionisation balance terms. In order to update the contribution functions, both contributions have to be reviewed. Within ADAS, the structure of excited population is provided by the *adf04* data files, which contain all required energy levels, radiative data and rate coefficient data for specified low levels of an ion, while the ionisation balance calculations are supplied by the means of the *adf11* data files, which provide the collisional-dielectronic ionisation and recombination coefficients. The *adf20* collection is built up using the *adf04* and *adf11* data files through the ADAS412 routine, which gives the contribution functions as a function of electron temperature for a specific ion when the value of electron density or electron pressure are fixed (for common assumptions on electron density and pressure used in astrophysics see chapter 6).

In the following sections the update of *adf04*s (sec. 5.2.1) and *adf11*s (sec. 5.2.2 and 5.3) are discussed. In addition, a final table (table 5.6) shows a summary of recommended data for *adf04* and *adf11* data files and the *adf20* status.

### 5.2.1 Energy levels, radiative data and collision strengths

In this section, the *adf04* data files for the ions included in the DEM analysis are revised along the iso-electronic sequences. An example of *adf04* for neutral helium is shown in fig. 5.1. This ADAS data file consists of three main parts: (1) energy levels; (2) radiative data (A-value); (3) collisional data (Y-value).

1. *Energy levels*: Accurate energy levels, and so accurate wavelengths, are very important in the solar context, where the only means to examine the plasma is the observed spectrum. Precise theoretical wavelengths can be extremely helpful to identify from which transitions the observed lines originate. However, the measured energy levels for some of the coronal ions (such as iron and silicon ions) are not well known. The most notable tabulation is the NIST database and is used as the main source in this work, but for many systems the number of observed energy levels is too small or non-existent. Therefore, it has been necessary to supplement these data with other laboratory measurements or theoretical values (e.g. Cowan calculations).

2. *Radiative data*: The radiative transition probabilities have been introduced with the eq. 5.4 to define the intensity for an optically thin plasma and denoted by $A_{j\to i}$ or simply by the word A-value. Also, in place of the A-value the oscillator strength can be used. The latter is equivalent to the A-value and does not need further data to be calculated except for a conversion factor. Details used in the calculation of such radiative data are provided by (82), (83) (SUPERSTRUCTURE) and (81) (AUTOSTRUCTURE). As for the energy levels, the main source adopted here is the NIST database, supplemented by preferred data from literature and from Cowan calculations where necessary.

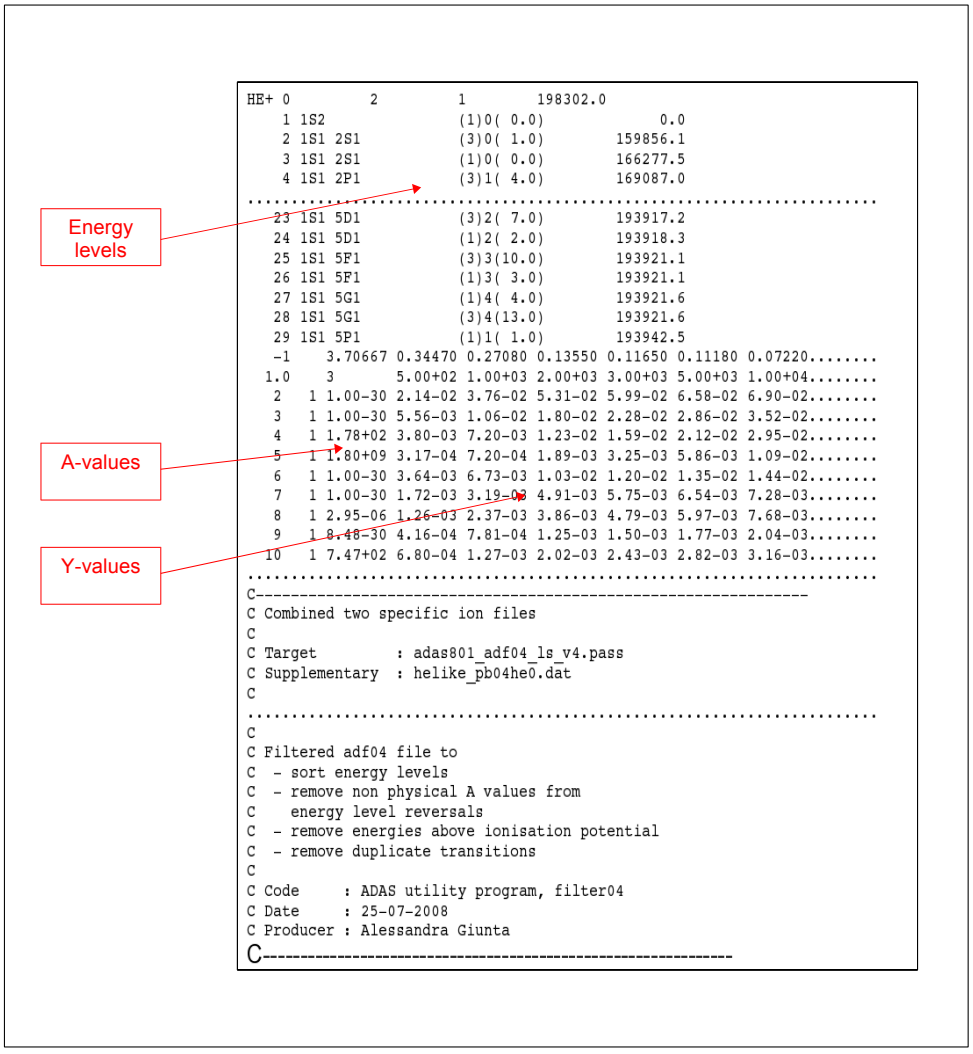


Figure 5.1: Example of *adf04* data file for neutral helium. This dataset contains a list of energy levels, specified by configuration, weight and energy (in $cm^{-1}$), followed by electron impact excitation rate coefficients (Y-values) as a function of electron temperature. For each transition, the radiative transition probability (A-values) is provided.

3. *Collisional data*: The collisional data revised in the following subsections are those related to electron impact excitation. An electron impact excitation reaction can be described by a cross-section denoted by $\sigma_{i\rightarrow j}(\epsilon_i)$ or $\sigma_{j\rightarrow i}(\epsilon_j)$ for the de-excitation, where $\epsilon_i$ is the energy of the incident electron and $\epsilon_j$ the energy of the scattered electron. Denoting by $E_i$ and $E_j$ the energies of the lower and upper level respectively for an ion $X^{+z}$, in order to excite an electron from the level $i$ to the level $j$ it is required that $\epsilon_i \geq E_j - E_i = \Delta E_{ij}$. It is common to write the collisional cross-section in terms of a dimensionless quantity called collision strength, $\Omega_{ij}(\epsilon)$, which is usually tabulated as function of the kinetic energy of the exciting electron. The relationship between collision strength and cross-section is:

$$\Omega_{ij}(\epsilon) = \omega_i \left(\frac{\epsilon_i}{I_H}\right)\left(\frac{\sigma_{i\rightarrow j}(\epsilon_i)}{\pi a_0^2}\right) = \omega_j \left(\frac{\epsilon_j}{I_H}\right)\left(\frac{\sigma_{j\rightarrow i}(\epsilon_j)}{\pi a_0^2}\right) \tag{5.30}$$

where again $\omega_i$ and $\omega_j$ are the statistical weights, $I_H$ is the ionisation potential of hydrogen and $a_0$ is the Bohr radius. For a thermal plasma where the free electrons can be described by a Maxwellian distribution, it is useful to introduce the effective collision strength $\Upsilon_{ij}$, which is function of the electron temperature, defined by:

$$\Upsilon_{ij} = \int_0^\infty \Omega_{ij}(\epsilon) e^{-\epsilon/kT_e} d\left(\frac{\epsilon}{kT_e}\right) \tag{5.31}$$

The effective collision strength is related to the excitation and de-excitation rate coefficients as follows:

$$q^{(e)}_{i\rightarrow j}(T_e) = 2\sqrt{\pi}\alpha c a_0^2 \frac{1}{\omega_i} e^{-\Delta E_{ij}/kT_e}\left(\frac{I_H}{kT_e}\right)\Upsilon_{ij} \tag{5.32}$$

$$q^{(e)}_{j\rightarrow i}(T_e) = 2\sqrt{\pi}\alpha c a_0^2 \frac{1}{\omega_j}\left(\frac{I_H}{kT_e}\right)\Upsilon_{ij} = \frac{\omega_i}{\omega_j} e^{\Delta E_{ij}/kT_e} q^{(e)}_{i\rightarrow j}(T_e) \tag{5.33}$$

where $\alpha$ is the fine structure constant and the relationship between the excitation and de-excitation rate coefficients has been already mentioned in the previous section.

### Electron impact calculation methods

The electron impact excitation cross-section (and hence the collision strength and effective collision strength) calculations can be provided by a variety of different sources. Several codes available for obtaining cross-sections are summarised in table 5.5. The solution of the electron-ion scattering problem is notably complex. The accuracy of a specific calculation depends mainly on the representation used for the target wavefunctions, which should take into account of configuration interaction and allow intermediate coupling for higher ionisation stages, and on the choice of scattering approximation type. Very accurate - real - results are given by Time Dependant Schrödinger Equation (TDSE) measurements, but unfortunately this method is limited in terms of computational resources because it is very slow. As it will be seen for the ionisation case, apart from the TDSE method, cross-section calculations can be grouped into two sets: perturbative and non-perturbative types. The first type includes the plane wave Born (PWD) approach and the distorted wave (DW) approximation. The PWD approach, as implemented for instance within the Cowan code (82), does not take into account resonance structure and the coupling between different spin systems, but it requires rapid computations and is generally applicable especially as top up - that is to add missed transitions between higher levels where the interaction between spin systems is less important. The DW approximation, which has been developed in the Hebrew University Lawrence Livermore Atomic Code (HULLAC) (84) and the Flexible Atomic Code (FAC) (85), neglects the coupling of the target + scattering electron channels and give more reliable results for systems which are a few times ionised.

Table 5.5: Main codes available for calculation of electron impact cross-sections.

| Code | Method | Usual application | Precision | Comments |
|---|---|---|---|---|
| AUTOSTRUCTURE/ COWAN | Plane Wave Born: Multi-config, Breit-Pauli, Thomas-Fermi and Slater-type parametric potential (for AUTOSTRUCTURE), Multi-config, Breit-Pauli and Hartree-Fock potential (for COWAN) | Low to medium/ high $z$ | < 40% | Very general and stable. *ls* and *ic* coupling. No spin change. No resonances. Baseline data. |

Table 5.5: – continued

| Code | Method | Usual application | Precision | Comments |
|---|---|---|---|---|
| HULLAC/ FAC | Distorted Wave: Multi-config, Dirac Hamiltonian, *j-j* coupled basis | Medium to high $z$ | ~ 20% | *ic* coupling. Includes spin changes. No resonances. |
| CCC | Convergent Close-Coupling | Low to medium/ high $z$, 1-2 valence electrons | < 5% | Highest precision, inefficient for very many energies and delimiting resonances. Limited ion scope. |
| RM-RMPS | R-matrix with pseudo-states | Low to medium $z$ | ~ 5 – 10% | High precision. *ls* coupling. Tuned to AUTOSTRUCTURE and shared algebra. Resonances included. Use also for ionisation and implemented for iso-electronic sequences. |
| RM-ICFT | R-matrix with *ic* frame transformation | Medium/ high $z$ | ~ 5 – 10% | As for RM but extends to higher $z$ ions in *ic* coupling. |
| DARC | R-matrix close-coupling with radiation damping | Medium to high $z$ | ~ 5 – 10% | As for RM but extends to high $z$ ions with significant radiative/Auger branching of resonances. |

The second type includes the convergent close-coupling (CCC) (86) and R-matrix methods, which are more accurate, but more expensive in terms of computing resources. The non-perturbative methods have the advantage to generate consistently the complex target + projectile resonance structure in their collision strengths. Using this approach, in fact, the scattering electron sees individuals target electrons and the channels are coupled. The R-matrix theory has been implemented by means of different techniques and codes, such as R-Matrix with Pseudo-States (RMPS) (87), IC Frame Transformation (ICFT) (88) and Dirac Atomic R-matrix Code (DARC) (89), which have been appropriately described in the respective references. Commonly, the R-matrix calculations give rapid resonance resolution but they are not valid at all energies, in contrast with the CCC computations. However they are computationally more feasible than the CCC approach. In order to give a general estimate, the non-perturbative methods are accurate to better than 10%, while the perturbative approximations to about 25%. The preferred electron impact data in the following update are those obtained from the most accurate CCC and R-matrix methods, when available. Alternatively, data from DW are considered. Supplementation with Cowan code calculations are also made when appropriate.

The recommended data are discussed below and a comparison with other data sources is provided. A summary of the main sources for energy levels, radiative and collisional data included in the revised *adf04* data files will be listed in table 5.6.

Moreover, it has to be noted that proton impact data are not included in the following review and analysis. Although the role of proton impact may be relevant especially for Be-like an B-like ions, it is not essential for the purpose of this thesis.

### H-like ions

For $He^{+1}$ the energy values of terms up to $5g$ are taken from NIST, as well as the radiative transition probabilities for transitions between the terms $1s\,^2S - 2p\,^2P$, $1s\,^2S - 3p\,^2P$ and $2p\,^2P - 5d\,^2D$. The most recent collision strength data included in the ADAS database come from the RMPS calculations of (90) and are adopted here. However, because of the degeneracy, terms with the same principal quantum number $n$ have been grouped (*bn* resolution). The data from (90) have been incorporated in CHIANTI v.6 database too, but only transitions which involve the first two configurations ($1s$ and $2s$) are included in CHIANTI computations. This affects the *PEC* values and, as a consequence, the ratio of the two resonance doublets between the terms $1s\,^2S - 2p\,^2P$ and $1s\,^2S - 3p\,^2P$, observed by CDS and EIS. The plot in figure 5.2 shows an illustrative comparison between the *PEC*s derived by the data of (90) using the complete set of transitions (black line) and neglecting some of them (red line). This results in overestimated *PEC* values by CHIANTI for the set of transitions between $n = 1$ and $n = 3$, while the *PEC* related to transitions $n = 1 \rightarrow n = 2$ are underestimated. This emphasises that the inclusion of all relevant transitions in the excitation coefficient calculation is important, to avoid unnecessary truncation errors in the derived line emissivities. In the specific case of the EUV resonance lines which arise from the $He^{+1}$ ion, further details about their ratio and the implications in the comparison with observations will be provided in chapter 6, sec. 6.2.

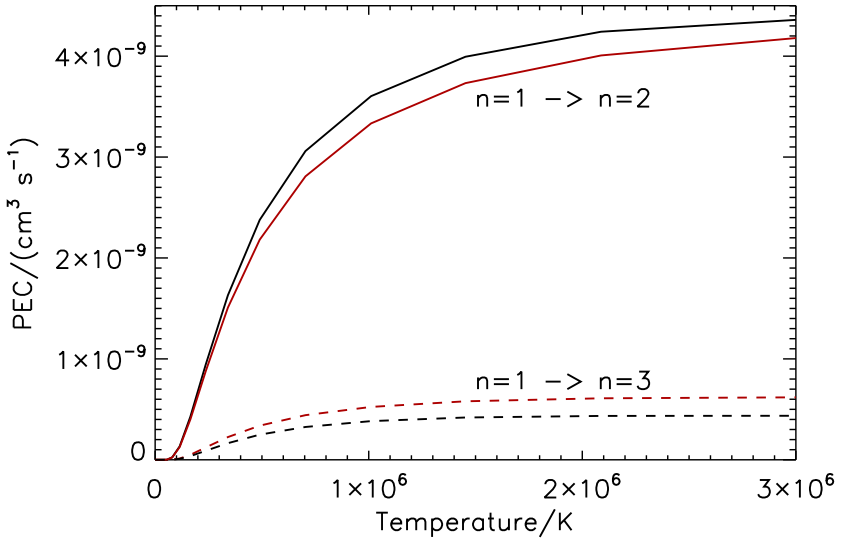


Figure 5.2: Comparison between the *PEC*, for two selected sets of transitions for $He^{+1}$, derived from the R-matrix calculation of (90). The main difference between the black and red lines comes from the inclusion or exclusion of the transitions which involve configurations above $2s$. The electron density has been fixed at $10^{10}$ cm$^{-3}$.

**He-like ions**

Along the He-like iso-electronic sequence, only lines from neutral helium are selected for the present work. These lines are all the EUV resonance lines between the ground term $1s^2\,{}^1S$ and the excited terms $1snp\,{}^1P$, with $n = 2, 3, 4, 5$. In addition, the intercombination line between the $1s^2\,{}^1S$ in the singlet state and the $1s2p\,{}^3P$ term in the triplet state is observed by CDS. The *ls* resolution is a good approximation for $He^{+0}$, because levels belonging to the same term are closer to degenerate. The first 29 energy terms up to $5p\,{}^1P$ have been included in the model. Energy levels come from the NIST database. The A-value for the transition $1s^2\,{}^1S - 1s2p\,{}^3P$ has been modified using the values from (91) and performing the *ls* average. For the configurations up to $1s4f$ recently assessed data are available in the ADAS database. These data were assembled by (92), including earlier surveys of (93) and R-matrix calculation of Ballance (2003). Cowan calculations have been performed to add transitions which involve $n = 5$ configurations and then merged with the more accurate R-matrix calculations. Ionisation and recombination contributions have been added following ADAS prescription. These revised data will be used to estimate theoretical ratios in the optically thin approximation and compare them with observations in next chaper. It is important to remember that the EUV resonance lines as observed in the Sun are affected by opacity effects, which causes deviation from the optically thin behaviour.

**Li-like ions**

The lines observed during the April 2009 campaign, which belong to the Li-like sequence, arise from transitions between the ground level $1s^22s\,{}^2S_{1/2}$ and the fine-structure levels $1s^22p\,{}^2P_{1/2,3/2}$ of the ions $Ne^{+7}$, $Mg^{+9}$ and $Si^{+11}$ (SUMER and CDS) and from transitions between these latter excited levels and the level $1s^23s\,{}^2S_{1/2}$ of the ion $O^{+5}$ (EIS). For $O^{+5}$, $Ne^{+7}$ and $Mg^{+9}$, the energy levels, A-values and collision strengths of (94) are adopted, as collected in ADAS database (see also (95)). The data include fine structure resolved levels up to $5g\,{}^2G_{9/2}$. The relativistic DW effective collision strengths of (94) were modified to correct the data for the effect of resonances and to increase or decrease their values to bring them into closer agreement with the close-coupling data, as reviewed by (96). For $Si^{+11}$ more details will be given in sec. 5.3.2.

### Be-like ions

The required ions of Be-like system are $O^{+4}$, $C^{+2}$, $Na^{+7}$ and $Si^{+10}$. $Si^{+10}$ will be discussed in further detail later (sec. 5.3.2). The most important transitions arising from $O^{+4}$ are $2s^2\,^1S_0 - 2s2p\,^1P_1$, which gives rise to the resonance line at 629.73 Å (observed both by SUMER in second order and by CDS), and $2s2p\,^3P_1 - 2p^2\,^3P_2$, which gives rise to the line at 762.00 Å (observed by SUMER). Their ratio will be used as a density diagnostic in next chapter, sec 6.1.3. Also, the $2s2p\,^3P - 2s3d\,^3D$ multiplet is observed by EIS. Transitions between the terms $2s2p\,^3P - 2p^2\,^3P$ from $C^{+2}$ are also relevant. For $Na^{+7}$, only the intercombination line between the level $2s^2\,^1S_0 - 2s2p\,^3P_1$ is present in the current observations. It is a very faint line which lies in the wing of the more intense line of $O^{+3}$ at around 790 Å. For these Be-like ions, the first 20 levels up to $2s3d\,^1D_2$ have been included in the data. For $O^{+4}$ and $C^{+2}$ the energy levels come from (97). Radiative transition probabilities from (98) have been adopted for $O^{+4}$, while the main source for $C^{+2}$ is (99). For $Na^{+7}$ both the energy levels and A-values have been taken from (100), except for the forbidden transitions, which come from (101). The electron impact excitation data have been taken following the recommendations of (102), who reviewed and assessed the state of the fundamental atomic collision data for Be-like ions.

### B-like ions

For $C^{+1}$ and $Mg^{+7}$, the first 18 and 15 fine-structure energy levels up to $2p^3\,^2P_{3/2}$ are included. The energy levels adopted for these two ions are from (103). The radiative transition probabilities between 1/2 and 3/2 levels of the ground terms have been derived from the multi-configuration Hartree-Fock results of (104), while for the other transitions the A-values of (105) have been used. The collision strengths have been taken from the review of (106). More care has to be given to the $O^{+3}$ ion. A recent assessment is provided by CHIANTI v.6, where 125 energy levels up to $2p^23d\,^2D_{3/2}$ have been included in the model. The observed energy levels come from NIST, while the theoretical values come from the work of (107). However, only transitions which involve the first five levels belonging to the $2s^22p$ and $2s2p^2$ configurations have been taken into account. Hence, the CHIANTI data have been merged with the Sampson data collected in the ADAS database. This means that the radiative and collisional data for transitions involving the first five levels come from CHIANTI, while the data for transitions amongst all the other levels included in the model are taken from the Sampson collection. As for $He^{+1}$, the omission of transitions can lead to interpretation errors when comparing with observations. In particular, it affects the line ratio between the lines at 787.72 Å and 279.93 Å. Comparison with previous works will be given in chapter 6, sec. 6.2. Here the *PEC*s obtained from the

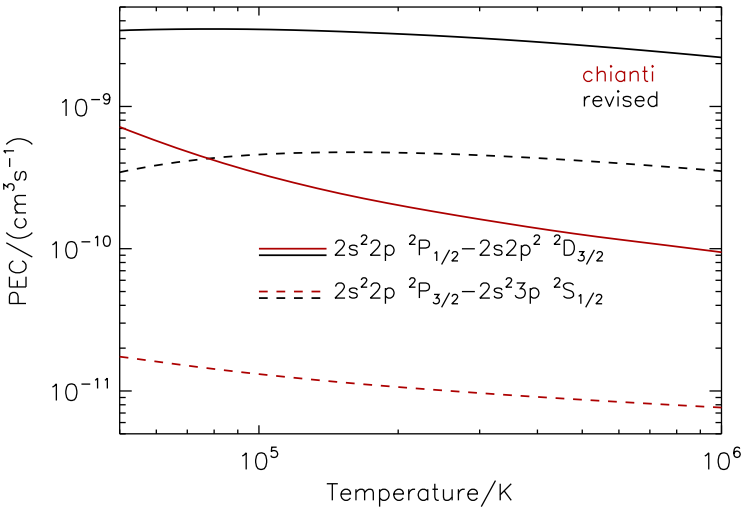


Figure 5.3: Comparison between the *PEC* for the two transitions $2s^22p\,^2P_{1/2} - 2s2p^2\,^2D_{3/2}$ and $2s^22p\,^2P_{3/2} - 2s^23s\,^2S_{1/2}$ arising from the $O^{+3}$ ion. The solid and dashed red lines represent the data from "pure" CHIANTI, while the solid and dashed black lines are derived from the CHIANTI data supplemented with the Sampson calculations.

original CHIANTI data and the ones supplemented with the Sampson data are displayed (fig. 5.3). The transitions involved are $2s^22p\,^2P_{1/2} - 2s2p^2\,^2D_{3/2}$ and $2s^22p\,^2P_{3/2} - 2s^23s\,^2S_{1/2}$ and the electron density has been fixed at $10^{10}$

cm$^{-3}$. Finally, EIS observes the line at 256.38 Å which arises from the transition $2s^2 2p\,^2P_{1/2} - 2s2p^2\,^2P_{1/2}$ of the $Si^{+9}$ ion. It is blended with the much more intense resonance line from the $He^{+1}$ ion. Atomic data recommended for this ion will be discussed with other silicon ions in sec. 5.3.2.

#### C-like ions

The C-like ions, from which lines included in the current observation sequences, are $C^{+0}$, $N^{+1}$, $O^{+2}$ and $Ne^{+4}$. For $O^{+2}$ and $Ne^{+4}$, the data used are collected in the ADAS database. The first 46 fine-structure resolved energy levels (belonging to the configurations $2s^2 2p^2$, $2s^2 2p^3$ and $2s^2 2p\,ls$ with $l = s, p, d$) have been included in the model for $O^{+2}$. The energy levels come from NIST while the transition probabilities come from the critical compilation of (108). The effective collision strengths have been computed by (109), using the R-matrix method. For $Ne^{+4}$, the ICFT R-matrix calculations of (110) are the main source of electron impact data. These data have been merged with Cowan code calculations and data from (111; 112; 113). The energy levels up to $n = 3$ have been taken from NIST. The other values come from Cowan calculations and (110). The A-value are those of (110) supplemented by those of (111; 112; 113), and (114). For neutral carbon, only Cowan calculations with *ls* resolution are available within ADAS. However, SUMER resolves the two lines at 1189.45 Å and 1189.63 Å, which arise from the transitions $2s^2 2p^2\,^3P_2 - 2s^2 2p4d\,^3P_1$ and $2s^2 2p^2\,^3P_2 - 2s^2 2p4d\,^3P_2$. This requires the *ic* resolution. Hence, *ic* PWB calculations have been performed through ADAS801 for this ion. The energy levels and radiative data have been replaced by values from NIST where available. Finally, for $N^{+1}$, the R-matrix computations of (115) have been used. They have been supplemented with Cowan calculation to include transitions between fine-structure levels belonging to the configurations $2s^2 2p3d$, $2s^2 2p4l$ with $l = s, p, d, f$ and $2p^4$.

#### N-like ions

CDS observes the multiplet which arises from transitions between the terms $2s^2 2p^3\,^2D - 2s2p^4\,^2P$ of $O^{+1}$ blended with the multiplet $2s2p\,^3P - 2s3s\,^3S$ of $C^{+2}$ and two resolved lines (at 542.07 Å and 543.89 Å) of the multiplet $2s^2 2p^3\,^4S - 2s2p^4\,^4P$ of $Ne^{+3}$. For $O^{+1}$ *ls* resolution is appropriate while for $Ne^{+3}$ *ic* resolution is required. Data for $O^{+1}$ have been taken from the review of (116) and supplemented with Cowan calculations. The main source for effective collision strengths is (117). For $Ne^{+3}$, the energy levels from NIST have been taken where available. The other values come from Cowan. Oscillator strengths of (118) have been adopted. The collision strengths are from (119), calculated in the close-coupling approximation using the multichannel R-matrix method.

#### O-like ions

Along the O-like sequence, the two lines which arise from $Si^{+6}$, observed by EIS, are very important in the context of this work because their ratio will be used as density diagnostics. As for the other silicon ions, data available and recommended for $Si^{+6}$ will be reviewed in section 5.3.2. The other ion of such isoelectronic sequence included in the present observations is neutral oxygen. The observed line originates from the transition between the fine-structure levels $2s^2 2p^4\,^3P_1$ and $2s^2 2p^3 3s\,^3S_1$. Since *ic* resolution is required, Cowan calculations have been performed. However, this line should be formed at temperature lower than $10^4$ K, typical of the lower chromosphere, and so in plasma conditions which depart from the optically thin regime. Therefore, any result that can be obtained by a DEM analysis may not be reliable.

#### Na-like ions

For Na-like $Ar^{+7}$, $Ca^{+9}$ and $Fe^{+15}$ ions, the first 21 fine-structure resolved levels up to $5g\,^2G_{9/2}$ are included in the model. The data for this sequence have been taken from the work of (120), who calculated collision data in the distorted wave approximation. The energy levels and A-values have been replaced by NIST values where possible.

### Mg-like ions

The most recent data for $Ar^{+6}$, and here adopted, come from the ICFT R-matrix close-coupling calculations of (121). The calculations include 25 terms and 45 levels belonging to the configurations $3l^2$, $3s3l$ and $3s4l$ with $l = s, p, d$, $l = p, d$ and $l = s, p, d$. The line at 585.75 Å from this ion, observed by CDS, lies in the wing of the strong resonance line at 584.32 Å, which arises from neutral helium. Hence, the evaluation of its intensity is important so as not to overestimate the helium line intensity.

### Al-like ions

Data from $Si^{+1}$ ion will be discussed in section 5.3.2. The other two Al-like ions with which this work is concerned are $S^{+3}$ and $Ca^{+7}$. The line at 584.84 Å originated from $Ca^{+7}$ is in the wing of the resonance line at 584.32 Å of neutral helium. Again, as for the line arising from $Ar^{+6}$, the knowledge of its intensity is relevant in the reconstruction of the helium line intensity. The main source from which $Ca^{+7}$ data have been taken is the CHIANTI v.6 database. The ion model includes 47 levels belonging to the configurations $3s^23p$, $3s3p^2$, $3s^23d$, $3p^3$ and $3s3p3d$. The energy levels of (122) have been adopted. The radiative data and the effective collision strengths come from the work of (123), who performed their calculations using the R-matrix approach. These data have been supplemented with PWB calculations to add the $3s^24l$ with $l = s, p$, $3s3d^2$ amd $3d^3$ configurations and transitions among higher levels. Regarding $S^{+3}$, SUMER allows observations of two lines which arise from the transitions $3s^23p\,^2P_{3/2}-3s3p^2\,^2D_{5/2,3/2}$. Calculations using the PWB approach in *ls* resolution are collected in the ADAS database. However, due to the need for *ic* resolution, new Cowan calculations have been performed for $S^{+3}$. Another data source for $S^{+3}$ is the CHIANTI v.6 database, which includes electron impact calculations of (124). The *PEC*s for the two transitions observed by SUMER have been examined, comparing Cowan calculations with those of (124) and the behaviour of data from the two different sources for the transition $3s^23p\,^2P_{3/2} - 3s3p^2\,^2D_{5/2}$ is shown in figure 5.4. Due to the unexpected

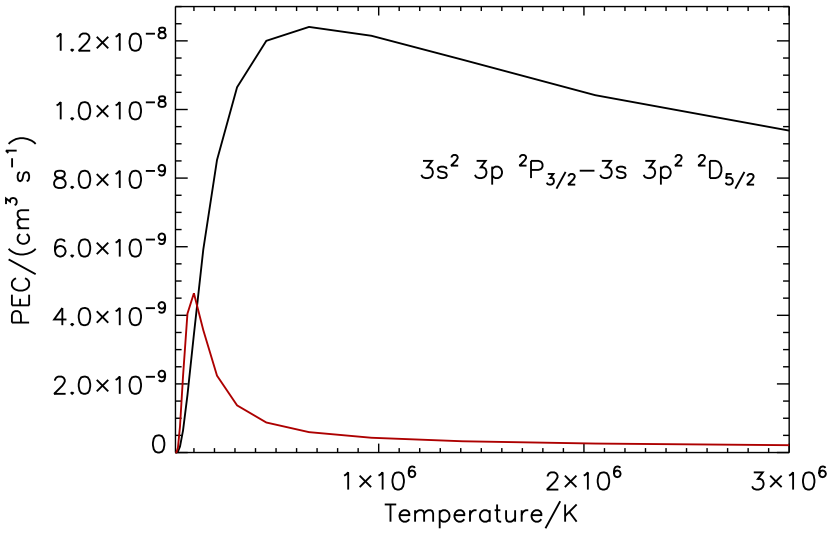


Figure 5.4: Comparison between the *PEC* for the transition $3s^23p\,^2P_{3/2} - 3s3p^2\,^2D_{5/2}$ arising from the $S^{+3}$ ion. The red line represent the data from (124), while the black line are derived from the Cowan calculations performed using the ADAS801 routine. The electron density is equal to $10^{10}$ cm$^{-3}$.

behaviour of the *PEC* from (124) data for electron temperature higher than around $10^5$ K, the data from Cowan have been preferred.

### Si-like ions

As for the case of $S^{+3}$, the main sources of electron impact data for $S^{+2}$ are Cowan calculations or the data from (125) collected in CHIANTI. Again, the uncommon behaviour of *PEC* derived from the (125) data leads to prefer the collision strengths calculated in the PWB approximation. For $Fe^{+12}$, the data come from the optimisation technique developed by (126). The line at 256.42 Å from this ion is observed in a blend with the much stronger resonance line arising from $He^{+1}$, together with the line at 256.32 Å from $Si^{+9}$, discussed later. Obviously, the contribution of an ion such $Fe^{+12}$ is negligible in quiet Sun conditions, but it may become significant in active regions.

### P-like, S-like, Cl-like, K-like, and Ca-like iron ions

Lines which arises from $Fe^{+11}$, $Fe^{+10}$, $Fe^{+9}$, $Fe^{+7}$ and $Fe^{+6}$ are at the shorter wavelength range which is covered by EIS. The most recent data for the first three iron ions are collected in the CHIANTI v.6 database. For $Fe^{+11}$, the scattering calculation, performed by (127) using the R-matrix method, includes the lowest 58 *ls* terms which give rise to 143 fine-structure levels. The energy levels and A-values come essentially from (128). These data have been merged with Cowan calculation to add missing levels belonging to the $3s^2 3p 3d^2$ and $3s 3p^3 3d$ configurations and the respective transitions. Here this supplemented set of data is used. A comparison between the data from CHIANTI and the merged set is illustrated in figure 5.5 for the three observed transitions which give the wavelengths 193.51 Å, 186.89Å and 186.85Å. For $Fe^{+10}$, the collision strengths have been taken from (129), while both energy levels and

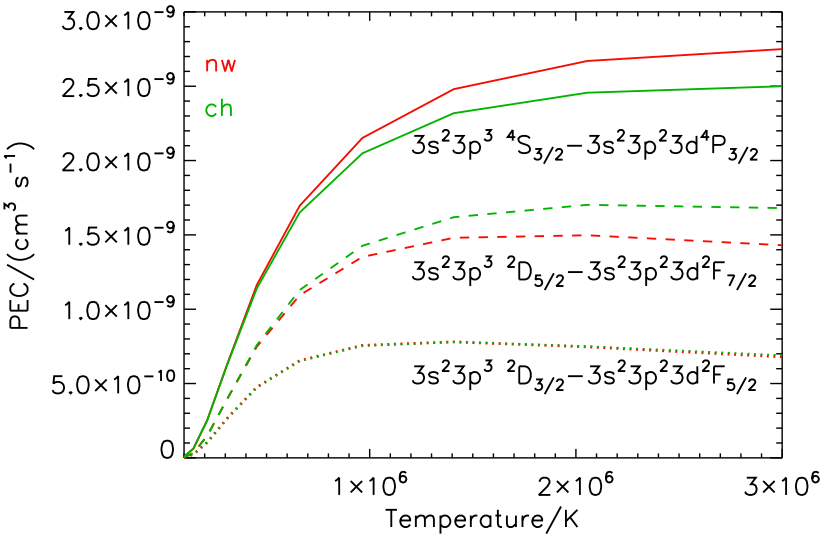


Figure 5.5: Comparison of *PEC*s for the three transitions $3s^2 3p^3\ ^4S_{3/2} - 3s^2 3p^2 3d\ ^4P_{3/2}$, $3s^2 3p^3\ ^2D_{5/2} - 3s^2 3p^2 3d\ ^2F_{7/2}$ and $3s^2 3p^3\ ^2D_{3/2} - 3s^2 3p^2 3d\ ^2F_{5/2}$ arising from the $Fe^{+11}$ ion and corresponding to the wavelengths 193.51 Å, 186.89Å and 186.85Å respectively. The solid, dashed and dotted green lines represent the data from CHIANTI, while the solid, dashed and dotted orange lines are derived from the CHIANTI data supplemented with Cowan calculations. An electron density of $10^{10}$ $cm^{-3}$ has been chosen, as for the other *PEC* examples.

radiative data come essentially from NIST. For $Fe^{+9}$, energy levels, A-values and effective collision strengths up to 54 levels are from the review of (130). For the other 118 levels the DW approximation from the work of (131) is adopted. As for $Fe^{+11}$, the CHIANTI data have been supplemented with PWB calculations to fill the gap left by the missing transitions. For the last two iron ions more accurate R-matrix calculations are collected within the ADAS database. The ICTF R-matrix close-coupling calculations of (132), that include 33 terms and 77 levels belonging to the configurations $3p^6 3d$, $3p^5 3d^2$, $3p^5 3d 4s$, $3p^6 4s$, $3p^6 4l$ with $l = p, d, f$ in the close-coupling expansion, have been used for $Fe^{+7}$. Finally, for $Fe^{+6}$ the calculations of (133) have been adopted.

### 5.2.2 Ionisation and recombination data

Methods to derive ionisation balance from ionisation and recombination rates and new atomic calculations related to them will be discussed in the next section. Here the ionisation/recombination coefficients used for the DEM analysis and currently within the ADAS database are mentioned. Ionisation and recombination data for all the ions of hydrogen, helium, carbon, nitrogen, oxygen and neon have been obtained following the GCR approach, as described in (11). They are specified by the date mnemonic "96" within the ADAS database. For the ions of magnesium, sodium, calcium, argon and sulphur the ionisation balance of (134) has been used, while for iron ions the (135) results have been adopted. The calculation of (134) and (135) have been scaled in $N_e$, to take into account the effect of finite electron density (136). Finally, for the silicon ions new calculations have been done, as will be illustrated in detail in next section.

A summary of the updated data to build up the contribution functions used in this thesis are listed in tab 5.6. Only the main sources have been included in the table. The ionisation balance is denoted by the date mnemonic "96" for calculations from (11), "85" for calculations from (134), "92" for calculations from (135) and by the word *new* for calculations performed in this thesis. Regarding the silicon ions, only those present in the observation sequences are taken into account here. A detailed revision of all silicon ions will be done in section 5.3.2.

Table 5.6: Recommended data sources. Note that this table simply shows the principal source. For more information on each individual ion see sub-sections 5.2.1 and 5.2.2 and section 5.3.

| **Iso-electronic sequence** | **Ion** | *adf04* **sources** | | | *adf11* **sources** | *adf20* **status** |
|---|---|---|---|---|---|---|
| | | Energy levels | A-value | $\Upsilon$-value | | |
| H-like | $He^{+1}$ | NIST | NIST | (90) | 96 | updated |
| He-like | $He^{+0}$ | NIST | NIST | Ballance (2003) | 96 | updated |
| Li-like | $O^{+5}$ | (94) | (94) | (94) | 96 | updated |
| | $Ne^{+7}$ | (94) | (94) | (94) | 96 | updated |
| | $Mg^{+9}$ | (94) | (94) | (94) | 85 | not updated |
| | $Si^{+11}$ | NIST | NIST | (94) | *new* | updated |
| Be-like | $C^{+2}$ | (97) | (98) | (102) | 96 | updated |
| | $O^{+4}$ | (97) | (99) | (102) | 96 | updated |
| | $Na^{+7}$ | (100) | (100) | (102) | 85 | not updated |
| | $Si^{+10}$ | NIST | NIST | (137) | *new* | |
| B-like | $C^{+1}$ | (103) | (104) | (106) | 96 | updated |
| | $O^{+3}$ | NIST | NIST | (107) | 96 | updated |
| | $Mg^{+7}$ | (103) | (104) | (106) | 85 | not updated |
| | $Si^{+9}$ | NIST | NIST | (13) | *new* | updated |
| C-like | $C^{+0}$ | NIST | NIST | Cowan | 96 | updated |
| | $O^{+2}$ | NIST | (108) | (109) | 96 | updated |
| | $N^{+1}$ | NIST | NIST | (115) | 96 | updated |
| | $Ne^{+4}$ | NIST | NIST | (110) | 96 | updated |
| N-like | $O^{+1}$ | NIST | (116) | (116) | 96 | updated |
| | $Ne^{+3}$ | NIST | (118) | (119) | 96 | updated |
| O-like | $O^{+0}$ | Cowan | Cowan | Cowan | 96 | updated |
| | $Si^{+6}$ | NIST | NIST | (138) | *new* | updated |
| Na-like | $Ar^{+7}$ | NIST | NIST | (120) | 85 | updated |
| | $Ca^{+9}$ | NIST | NIST | (120) | 85 | updated |
| | $Fe^{+15}$ | NIST | NIST | (120) | 92 | updated |
| Mg-like | $Ar^{+6}$ | (121) | (121) | (121) | 85 | updated |
| Al-like | $Si^{+1}$ | NIST | NIST | (139) | *new* | updated |
| | $S^{+3}$ | Cowan | Cowan | Cowan | 85 | updated |
| | $Ca^{+7}$ | (122) | (123) | (123) | 85 | updated |
| Si-like | $S^{+2}$ | Cowan | Cowan | Cowan | 85 | updated |
| | $Fe^{+12}$ | NIST | SUPERSTRUCTURE | (126) | 92 | updated |
| P-like | $Fe^{+11}$ | (128) | (128) | (127) | 92 | updated |
| S-like | $Fe^{+10}$ | NIST | NIST | (129) | 92 | updated |
| Cl-like | $Fe^{+9}$ | (130) | (130) | (130) | 92 | updated |
| K-like | $Fe^{+7}$ | (132) | (132) | (132) | 92 | updated |
| Ca-like | $Fe^{+6}$ | (133) | (133) | (133) | 92 | updated |

## 5.3 New atomic calculations

In this section the computational procedures for implementing the collisional-radiative modelling of section 5.1 are described. There are several steps which are shown schematically in figure 5.6. In previous ADAS GCR studies a number of these steps were performed as *ad hoc* hand manipulations. An objective of this thesis is to set up a basis for implementing all of these steps automatically so that the work can be extended easily to further elements. At each step, it is necessary to access and examine preferred data from the literature and also to perform computations which extend or top-up these data. Extension or top-up data are inevitably at lower precision. In general for automatic processing, it is a more efficient and easier practice to perform a complete data generation automatically, at as high a precision as is feasible, and then to substitute these data from the preferred sources where available. In the following sub-sections, the automatic generation procedures and then substitution procedures are described. In the next section a critique of the quality of the automatically generated data is given, compared with other sources and choices of preferred substitution data.

### 5.3.1 Step 1 - state selective ionisation rate coefficients

Electron impact ionisation rate coefficients from ordinary excited states in GCR modelling adopt the Exchange Classical Impact Parameter (ECIP) procedure of (140). This technique applies to any Rydberg level and is used in both *bn* and *bnl* methods. It has been possible to examine the precision of this approximation in recent work by Loch in the both Configuration Average Distorted Wave approximation (CADW) and in Monte Carlo approaches (141). The energy behaviour of the ECIP approach is substantiated but multiplicative discrepancies ~2 are found with some systematic character according to n-shell and target charge. A full assessment, as a correction to ECIP, has not yet been provided by Loch. The potential error from use of ECIP at all astrophysical and fusion plasma densities is small, since it concerns only the stepwise addition to the direct ionisation from the ground and/or metastable states. ECIP continues to be used for the present work from ordinary Rydberg states. Ionisation from ground and metastables states is the principal concern. There have been many studies from the early sixties (142; 143), up to present times (144), which

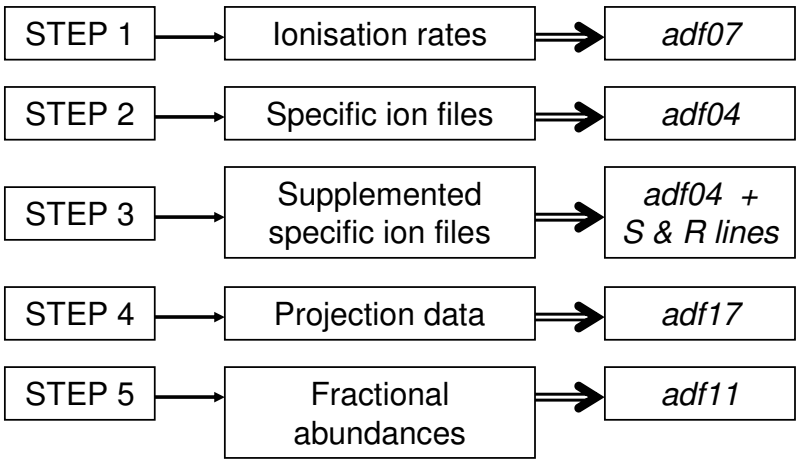


Figure 5.6: Schematic of GCR processing steps. This is a summary of the main steps necessary to calculate the GCR coefficients which are collected in the final *adf11* data files. For each step the key output data file is shown.

have examined experimental cross sections and compared them with relatively simple empirical or semi-empirical expressions. The intention has been to use these expressions universally. There has been no one fully theoretical approach which has been of sufficient precision or computability to be used universally. However the CADW method including proper Auger branching of excitation-autoionisation channels now comes close to fulfilling these requirements. Also CADW extended to resolved *ls* or *ic* fine structures is now available for a few systems including H-like and He-like and this range is increasing. Here CADW is used for ground to ground state ionisation and some detail comparison are given in section 5.4. For GCR studies, ionisation resolved into ground and metastable initial and final states is required and at this time semi-empirical formulae must be used to assist this. The semi-empirical method adopted here comes from the work of (145) as extended to a greater range of ions by (146) and to metastable resolution by (147). The expression for the electron impact rate coefficient, viewed as a formula for the direct ionisation of an ion of charge $z$ from a quantum shell (*shell direct* ionisation, with generic name $S_{shd}$) of ionisation potential $\chi$ and number of equivalent electrons in the shell, $\zeta$, is

$$\begin{aligned} S^{bchid}_{shd} &= 2\sqrt{\pi}\alpha c a_0^2\, C\, \zeta (I_H/\chi)^{3/2} (\chi/kT_e)^{1/2} \times \\ &\quad E_1(\chi/kT_e) w \end{aligned} \tag{5.34}$$

where $w = \{\ln(1 + kT_e/\chi)\}^{\beta(1+kT_e/\chi)}$ and $\beta = [\{(100z + 91)/(4z + 3)\}^{1/2} - 5]/4$. The constant $2\sqrt{\pi}\alpha c a_0^2 = 2.17 \times 10^{-8}$ cm$^3$ $s^{-1}$ and the multiplier $C = 2.3$ (as recommended by (146)). Since $S^{bchid}_{shd}(z, \chi, \zeta, T_e)$ gives the direct ionisation rate coefficient out of one *nl* shell, the total direct ionisation rate out of all the shells of a complex atom or ion in its ground configuration (state), which is called the *configuration shell direct* ionisation, is

$$S^{bchid}_{cfg-shd} = \sum_{i=1}^{N_s} S^{bchid}_{shd}(z, \chi_i, \zeta_i, T_e) \tag{5.35}$$

Here the ground configuration is $n_1 l_1^{q_1} \cdots n_i l_i^{q_i} \cdots n_{N_s} l_{N_s}^{q_{N_s}}$, $\zeta_i \equiv q_i$ and $\chi_i$ is the binding energy of an electron in the shell $i$. It is to be noted that such an expression is really only intended to apply to ionisation from the ground state or possibly metastable states of an ion. Ionisation out of highly excited states is completely dominated by valence electron loss alone to an adequate approximation. Also it has not been specified if the ionisation energy of the valence shell electron is the ionisation potential of the ground state or the configuration average valence electron orbital binding energy. Since the threshold region in temperature of the ionisation rate coefficient is important for ionisation balance, in fact the ionisation potential is to be preferred for the valence electron shell, but the above formulation still has a major omission, namely the contribution of *excitation-autoionisation*. The excitation-autoionisation contribution from the ground state of an ion for promotion from a particular shell (generic name $S_{ea}$) can be written as

$$S_{ea} = \sum_{k=1}^{N_r} q_k(T_e) \frac{A^a_k}{A^a_k + A^r_k} = \sum_{k=1}^{N_r} q_k(T_e) B_k \tag{5.36}$$

where the sum is over resonance states $k$, with $q_k$ the excitation rate coefficient to resonance $k$ from the ground state and $B_k$ is the branching ratio for autoionisation, assembled from $A_k^a$ the autoionisation probability and $A_k^r$ the radiative stabilisation probability. For most ions, the details of equation 5.36 for all the contributing resonances are not available or feasible to evaluate. It was a prescription for the inclusion of excitation/autoionisation in expressions of the same form as equation 5.35 which allowed simple semi-empirical expressions to match higher quality results with significantly lower standard error. This is especially important for heavy species ions for which the $S_{ea}$ contribution often dominates shell direct ionisation. The use of this semi-empirical method for modern GCR is outlined in (11). Since that work must be extended now to silicon and it is useful to have a prescription through to at least iron, the method is reiterated here and developed as a automatic procedure (section 5.3.1).

Consider CADW and its links to other pure theoretical methods. These can essentially be divided into two categories: non-perturbative (e.g. R-matrix or close coupling) and perturbative (e.g. DW approach) methods. The more elaborate non-perturbative methods are normally required for neutral and near neutral systems, where the effects of all exchange and coupling terms are not negligible. However, these effects become less important with increasing the ion charge and orbital angular momentum. This allows the use of the distorted wave approximation, which performs well for ionisation from ground or metastable states of systems more than a few times ionised. In such a context, the CADW approach (148) allows evaluation of the direct ionisation and excitation to highly excited resonance states followed by autoionisation or competing radiative decay. That is to say it is able to evaluate the four key constituent reactions, namely:

- *shell direct ionisation*

  $(n_1 l_1)^{q_1} k_i l_i \rightarrow (n_1 l_1)^{q_1} k_e l_e k_f l_f$,

  with differential (in ejected electron energy) cross-section

$$\frac{d\sigma_{ion}}{d\epsilon} = \frac{32}{k_i^3 k_e k_f}(q_1 + 1) \sum_{l_i, l_e, l_f} (2l_i + 1)(2l_e + 1)(2l_f + 1) M(ef; 1i); \tag{5.37}$$

- *shell excitation*

  $(n_1 l_1)^{q_1+1} (n_2 l_2)^{q_2-1} k_i l_i \rightarrow (n_1 l_1)^{q_1} (n_2 l_2)^{q_2} k_f l_f$,

  with cross-section

$$\sigma_{excit} = \frac{8\pi}{k_i^3 k_f}(q_1 + 1)(4l_2 + 3 - q_2) \sum_{l_i, l_f} (2l_i + 1)(2l_f + 1) M(2f; 1i); \tag{5.38}$$

- *Auger breakup*

  $(n_1 l_1)^{q_1} (n_2 l_2)^{q_2} (n_3 l_3)^{q_3} \rightarrow (n_1 l_1)^{q_1+1} (n_2 l_2)^{q_2-1} (n_3 l_3)^{q_3-1} k_e l_e$,

  with autoionisation rate coefficient

$$A^a = q_2 q_3 \frac{(4l_1 + 2 - q_1)(4l_2 + 2) M(1e; 23)}{k_e}; \tag{5.39}$$

- *radiative damping*

  $(n_1 l_1)^{q_1-1} (n_2 l_2)^{q_2} \rightarrow (n_1 l_1)^{q_1} (n_2 l_2)^{q_2-1}$,

  with spontaneous emission coefficient

$$A^r = \frac{8\nu^3}{3c^2} \frac{q_2(4l_2 + 3 - q_2) D(12)}{(4l_1 + 2)(4l_2 + 2)}. \tag{5.40}$$

These reactions are assembled to yield expressions for $S_{cfg-shd}$ and $S_{cfg-ea}$ (see equations 5.35 and 5.36) with appropriate integration over ejected electron and final colliding electron energies and Maxwellian averaging over initial

projectile electron energy. In the above $k_i$, $k_f$ and $k_e$ denote initial and final projectile wave numbers and ejected electron wave number respectively. $M(14;23)$ denotes the squared two-body Coulomb matrix element and $D(12)$ the one-body dipole matrix element. Other notation is conventional.

The scheme in figure 5.7 shows the procedures here employed.

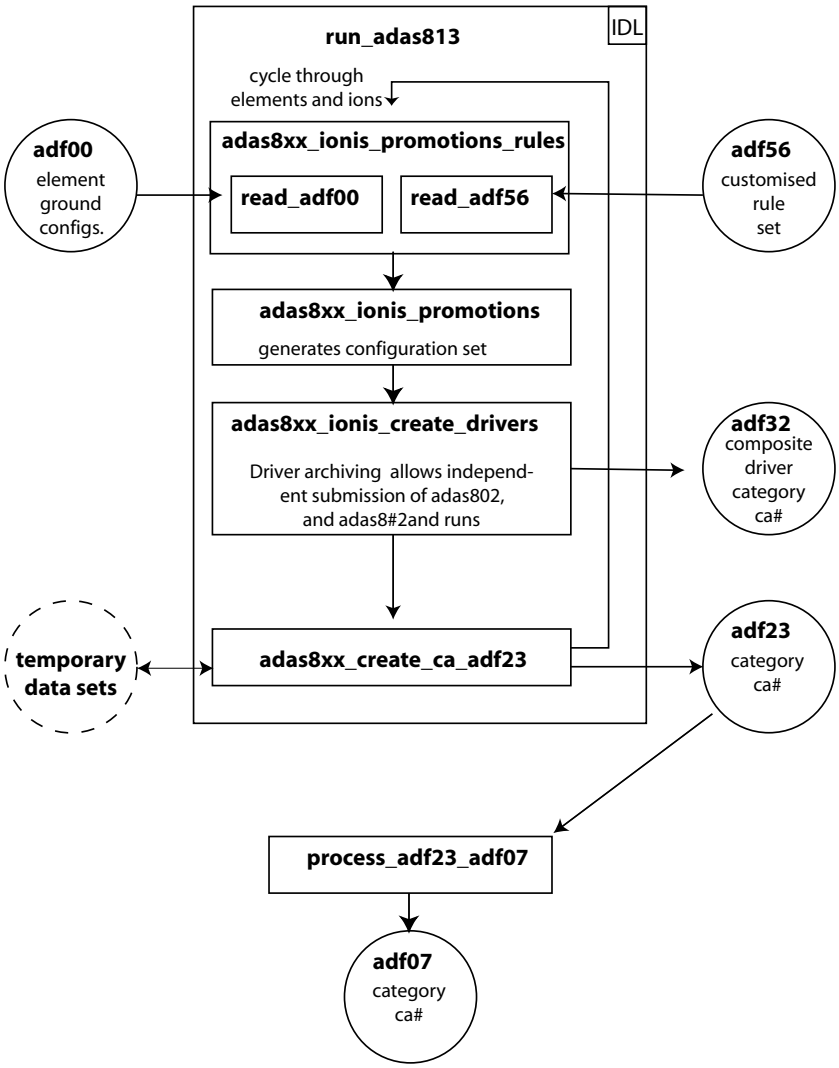


Figure 5.7: Scheme for step 1, showing offline version of ADAS8#2 (**run_adas802.pro**) program flow for complete ionisation rate coefficient calculations. This schematic example illustrates the various temporary and permanent datasets created. The final *adf07*, which contains the ionisation rate coefficients, is created from the *adf23* dataset obtained as output of the procedure illustrated. Note that the programs are shown as rectangles while archived and driver datasets are represented by circles.

The ionisation cross-section computations through the configuration average distorted wave code is performed by the online version of ADAS802 and the offline version ADAS8#2. The starting point is to create the driver files for the ionisation cross-section calculations. They are derived from the dataset *adf56*, which contains the promotional rules for ionisation and excitation-autoionisation for all possible ground states of ions of an elements. The ground configurations and ionisation potentials for the required ions are provided by the *adf00* data files. This *adf00* for silicon is shown in figure 5.8.

In addition, there is a second category of *adf00* data files, which include metastable configurations and excitation energies between metastables as well as ionisation energies (metastable resolved *ls* type). A sample for $Si^{+2}$-$Si^{+7}$, shown in figure 5.9, illustrates the metastable term choices and their energies. The original principal data source for

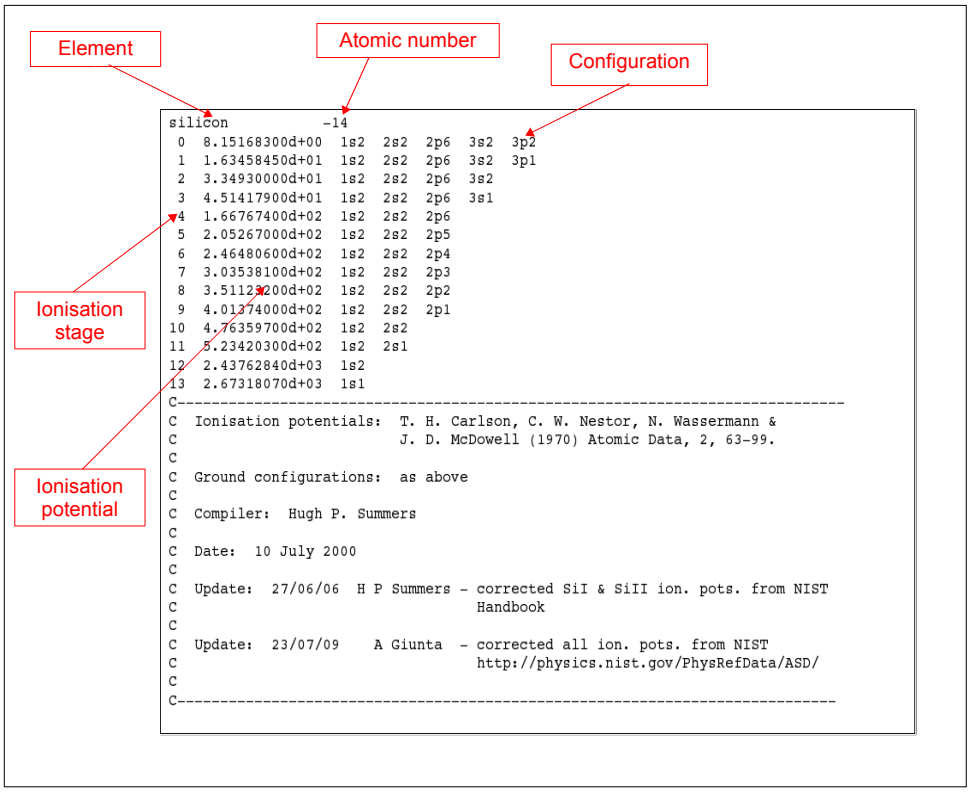


Figure 5.8: Example of *adf00* data file for silicon. This is a basic dataset which provides ground configurations and ionisation potentials for each silicon ion. The ionisation potentials are given in eV. The dataset is followed by comments which give information about the data sources.

ionisation potentials is the NIST database, but it is incomplete especially on progression towards heavier species. The gaps can be filled from some literature sources but mostly through calculations of the required atomic energy levels using the Cowan code in the form available in the ADAS project as ADAS801. The Cowan calculations do not have the spectroscopic precision of the NIST tabulations, but for the current purpose energy differences are sufficiently accurate. The driver files for ionisation cross-section calculations belong to ADAS data format *adf32*. They provide configurations and other control parameters for distorted wave electron impact collisional ionisation rate coefficient calculations. An example of a driver file for $Si^{+11}$ is shown in figure 5.10.

As shown in the flow diagram of fig. 5.7, the specific rules for an element are extracted from the *adf56* data files by the routine **adas8xx_ionis_promotion_rules.pro**. Then, the procedure **adas8xx_ionis_promotion.pro** establishes the actual configurations for both direct ionisation and excitation-autoionisation and the drivers are created by **adas8xx_ionis_write_drivers.pro**. Finally, the *adf23* dataset is generated using the *adf32* drivers, through the **adas8xx_create_ca_adf23.pro** routine. The *adf23* datasets provide tabular selective ionisation rate coefficients between initial ionising and final ionised states at *ca* resolution. The data also may include electron impact excitation rate coefficients to autoionising states and Auger yields allowing detailed evaluation of excitation-autoionisation channels, as shown for $Si^{+11}$ in figure 5.11.

The final *adf07* collection, which provides electron impact ionisation rate coefficients for all the ions of an element, is built up from the *adf23* dataset. A sample of the *adf07* data file for three silicon ions ($Si^{+1}$, $Si^{+}2$ and $Si^{+}3$) is illustrated in figure 5.12.

### Using $S^{bchid}$ for metastable resolution of ionisation rates

As for CADW, electron removal from shells of electronic configurations is considered along with the flexible attribution of shell ionisation potentials (I) and numbers of equivalent electrons ($\zeta$). Also, the division of ionisation between

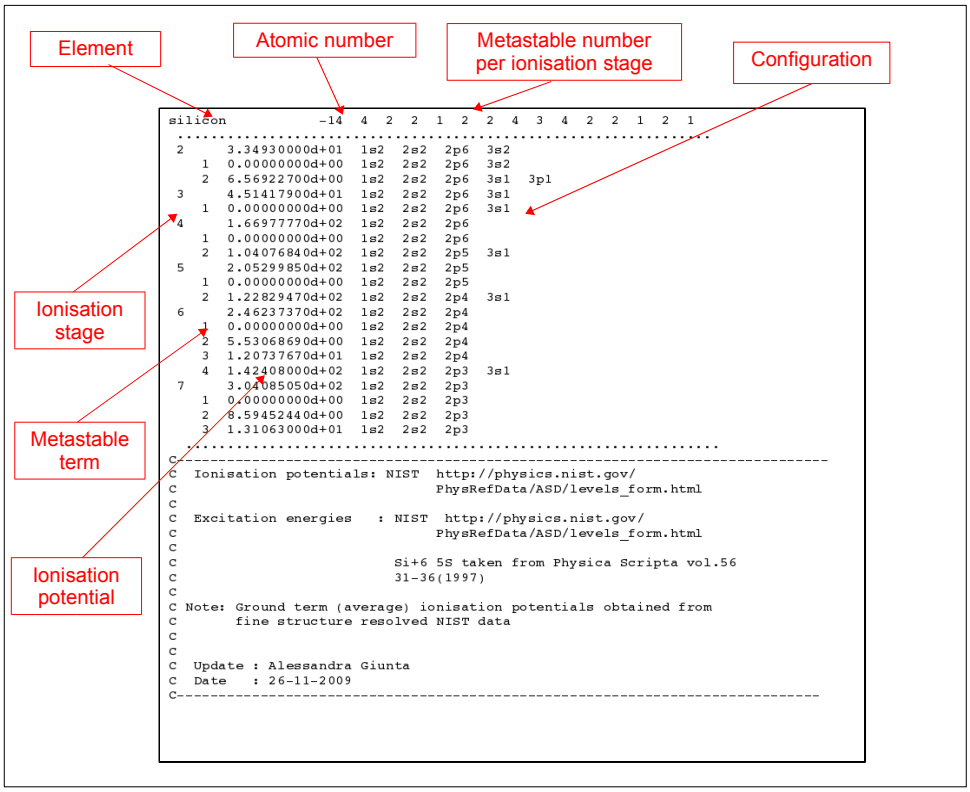


Figure 5.9: Example of *ls* resolved *adf00* data file for silicon. This is a second category of *adf00* dataset, which includes metastable configurations and excitation energies as well as ionisation potentials. The energy values are given in eV.

shell-direct and excitation-autoionisation is treated flexibly. Firstly two illustrations are given and on the basis of these an expert system is developed. This is then used to create a computational procedure. The two ions used as examples are $Si^{+8}$ and $Si^{+1}$ ionising to $Si^{+9}$ and $Si^{+2}$ respectively, illustrating first period and second period systems.

- *$Si^{+8}$ ionising to $Si^{+9}$*: As a C-like system, the ion $Si^{+8}$ includes four metastable terms, which are highlighted in red in tables 5.7 and 5.8. The former table lists the metastable levels (including the ground level) for both $Si^{+8}$ and $Si^{+9}$ and the levels to which the electron can be promoted. Of concern is the lowest autoionising levels. The level energy values come from NIST database or, if not available, from Cowan calculations.The latter calculations also give the orbital energy values.

Table 5.7: List of energy levels for $Si^{+8}$ and $Si^{+9}$. The first three columns contain configurations, terms and J values for the metastables (indicated in red) of each ion and for the levels to which the electron can be promoted. The fourth and fifth columns show respectively level and term energy values. The term energies (Eav) have been obtained by the weighted average of the level energies. In the last two columns, the orbitals and their energies in Rydberg are listed. They have been taken from *adf04* data files derived from ADAS801. The ionisation potentials (I.P.) for both the ions are also given.

| $Si^{+9}$ | | | | I.P. ($cm^{-1}$) 3237300.0 | $Si^{+9}$ | |
|---|---|---|---|---|---|---|
| Config | Term | J | E($cm^{-1}$) | Eav($cm^{-1}$) | Orbital | Energy (Ryd) |
| 2s2 2p1 | 2P | 0.50 | 0.0 | 4660.4 | 1s | 165.27 |
| | | 1.50 | 6990.6 | | 2s | 32.21 |
| 2s1 2p2 | 2D | 2.50 | 287880.0 | 287868.0 | 2p | 29.10 |
| | | 1.50 | 287850.0 | | 3s | 12.87 |
| 2s1 2p2 | 4P | 0.50 | 161010.0 | 164861.7 | 3s | 12.87 |
| | | 1.50 | 163490.0 | | 3d | 11.47 |
| | | 2.50 | 167060.0 | | | |
| 2s0 2p3 | 4S | 1.50 | 509330.0 | 509330.0 | | |
| 2s1 2p2 | 2P | 0.50 | 390040.0 | 392700.0 | | |

Table 5.7: – continued

| Config | Term | J | E($cm^{-1}$) | Eav($cm^{-1}$) | Orbital | Energy (Ryd) |
|---|---|---|---|---|---|---|
| | | 1.50 | 394030.0 | | | |
| 2s1 2p2 | 2S | 0.50 | 367670.0 | 367670.0 | | |
| $Si^{+8}$ | | | | I.P. ($cm^{-1}$) 2832000.0 | $Si^{+8}$ | |
| Config | Term | J | E($cm^{-1}$) | Eav($cm^{-1}$) | Orbital | Energy (Ryd) |
| 2s2 2p2 | 3P | 0.00 | 0.0 | 4411.7 | 1s | 160.19 |
| | | 1.00 | 2545.0 | | 2s | 28.87 |
| | | 2.00 | 6414.0 | | 2p | 26.50 |
| 2s2 2p2 | 1D | 2.00 | 52925.9 | 52925.9 | 3s | 10.99 |
| 2s2 2p2 | 1S | 0.00 | 107799.0 | 107799.0 | 3p | 10.17 |
| 2s1 2p3 | 5S | 2.00 | 150770.0 | 150770.0 | 3d | 9.38 |
| 2s1 2p3 | 3D | 3.00 | 292232.0 | 292295.1 | | |
| | | 2.00 | 292296.0 | | | |
| | | 1.00 | 292441.0 | | | |
| 2s1 2p3 | 3P | 2.00 | 344118.0 | 344076.9 | | |
| | | 1.00 | 344009.0 | | | |
| | | 0.00 | 344075.0 | | | |
| 2s1 2p3 | 1D | 2.00 | 440403.0 | 440403.0 | | |
| 2s1 2p3 | 1P | 1.00 | 492755.0 | 492755.0 | | |
| 2s1 2p3 | 3S | 1.00 | 446942.0 | 446942.0 | | |

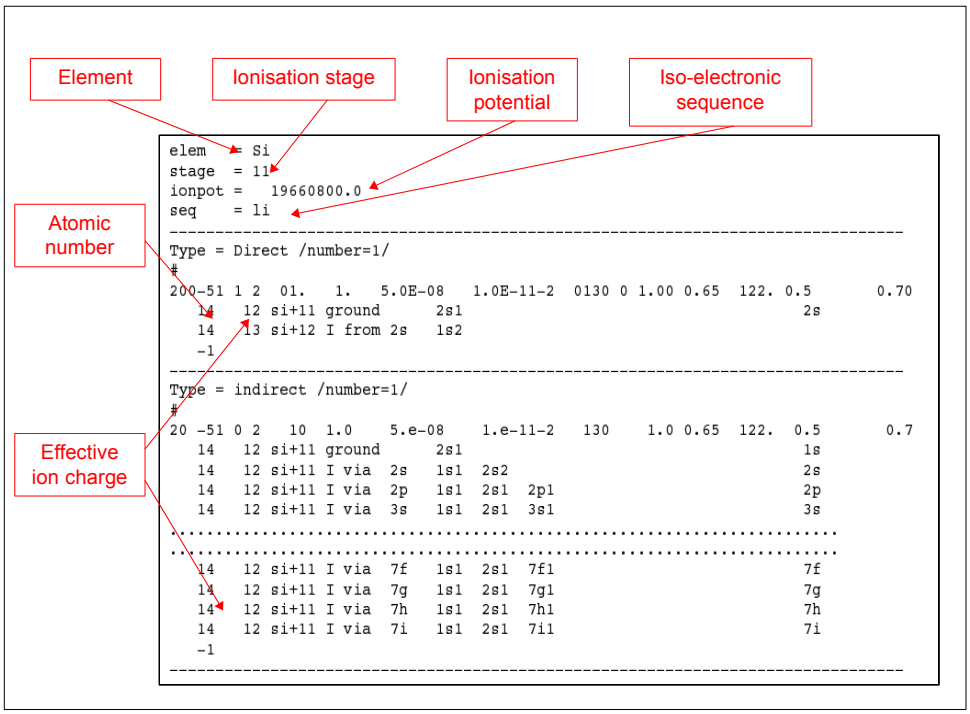


Figure 5.10: Example of *adf32* data file for $Si^{+11}$. This is a driver file created by the IDL routine **adas8xx_ionis_create_drivers.pro**, as illustrated in the schematic of fig. 5.7. It provides all the parameters needed for distorted wave electron impact collisional ionisation rate coefficient calculations.

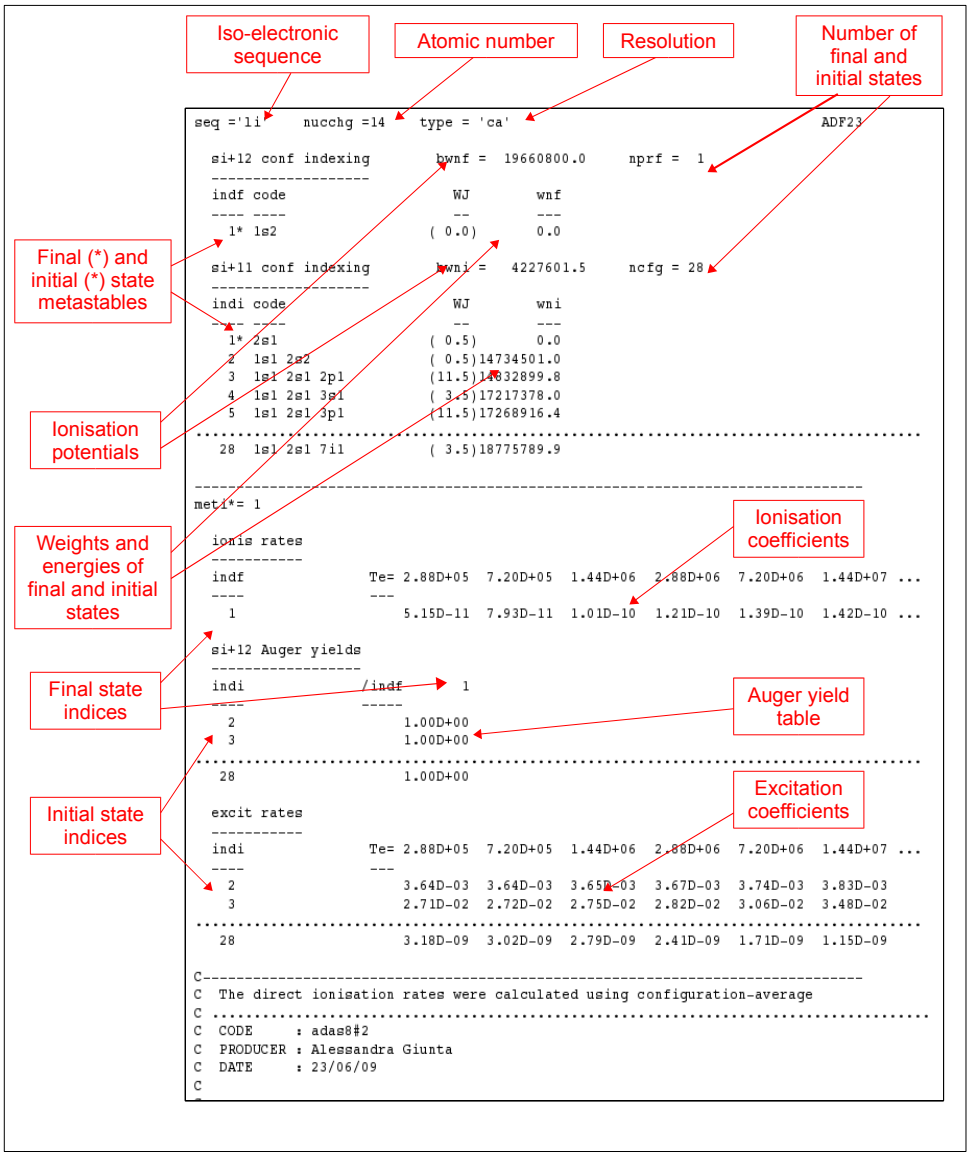


Figure 5.11: Example of *adf23* data file for $Si^{+11}$. Both ionising and ionised ionisation stages are specified in the dataset together with configurations and energy values (given in $cm^{-1}$). This dataset contains tabular selective ionisation rate coefficients needed to build up the final *adf07* data files. It includes also Auger yields and electron impact excitation rate coefficients to evaluate the contributions due to excitation-autoionisation.

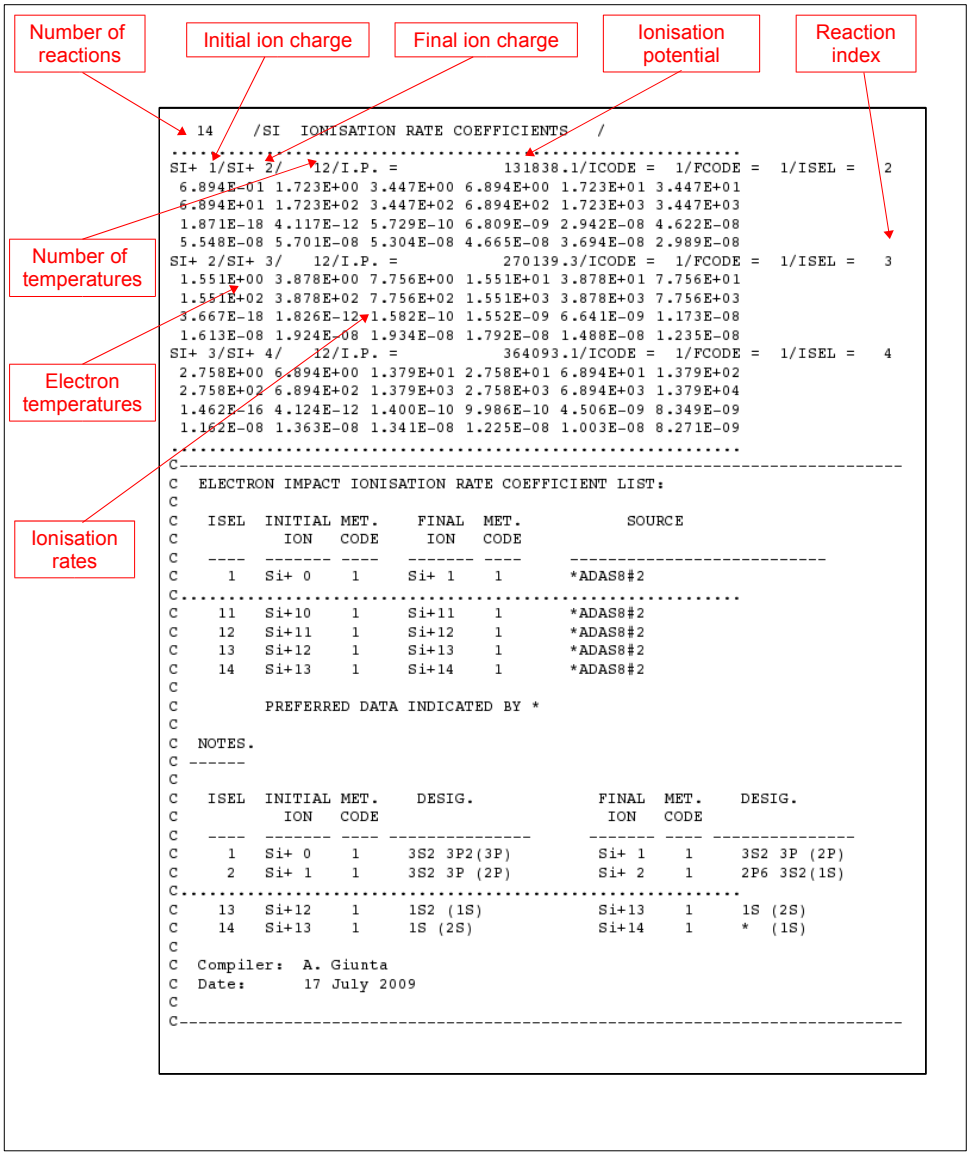


```
 14    /SI  IONISATION RATE COEFFICIENTS    /
.....................................................................
SI+ 1/SI+ 2/    12/I.P. =           131838.1/ICODE =  1/FCODE =  1/ISEL =   2
 6.894E-01 1.723E+00 3.447E+00 6.894E+00 1.723E+01 3.447E+01
 6.894E+01 1.723E+02 3.447E+02 6.894E+02 1.723E+03 3.447E+03
 1.871E-18 4.117E-12 5.729E-10 6.809E-09 2.942E-08 4.622E-08
 5.548E-08 5.701E-08 5.304E-08 4.665E-08 3.694E-08 2.989E-08
SI+ 2/SI+ 3/    12/I.P. =           270139.3/ICODE =  1/FCODE =  1/ISEL =   3
 1.551E+00 3.878E+00 7.756E+00 1.551E+01 3.878E+01 7.756E+01
 1.551E+02 3.878E+02 7.756E+02 1.551E+03 3.878E+03 7.756E+03
 3.667E-18 1.826E-12 1.582E-10 1.552E-09 6.641E-09 1.173E-08
 1.613E-08 1.924E-08 1.934E-08 1.792E-08 1.488E-08 1.235E-08
SI+ 3/SI+ 4/    12/I.P. =           364093.1/ICODE =  1/FCODE =  1/ISEL =   4
 2.758E+00 6.894E+00 1.379E+01 2.758E+01 6.894E+01 1.379E+02
 2.758E+02 6.894E+02 1.379E+03 2.758E+03 6.894E+03 1.379E+04
 1.462E-16 4.124E-12 1.400E-10 9.986E-10 4.506E-09 8.349E-09
 1.162E-08 1.363E-08 1.341E-08 1.225E-08 1.003E-08 8.271E-09
.....................................................................
C-----------------------------------------------------------------------------
C  ELECTRON IMPACT IONISATION RATE COEFFICIENT LIST:
C
C   ISEL  INITIAL MET.    FINAL  MET.           SOURCE
C           ION   CODE     ION   CODE
C   ----  ------- ----   ------- ----     ---------------------------
C     1   Si+ 0    1     Si+ 1    1       *ADAS8#2
C.....................................................
C    11   Si+10    1     Si+11    1       *ADAS8#2
C    12   Si+11    1     Si+12    1       *ADAS8#2
C    13   Si+12    1     Si+13    1       *ADAS8#2
C    14   Si+13    1     Si+14    1       *ADAS8#2
C
C         PREFERRED DATA INDICATED BY *
C
C  NOTES.
C ------
C
C   ISEL  INITIAL MET.    DESIG.             FINAL  MET.    DESIG.
C           ION   CODE                        ION   CODE
C   ----  ------- ---- ---------------      ------- ---- ---------------
C     1   Si+ 0    1     3S2 3P2(3P)         Si+ 1    1     3S2 3P (2P)
C     2   Si+ 1    1     3S2 3P (2P)         Si+ 2    1     2P6 3S2(1S)
C.....................................................
C    13   Si+12    1     1S2 (1S)            Si+13    1     1S (2S)
C    14   Si+13    1     1S (2S)             Si+14    1     *  (1S)
C
C  Compiler:  A. Giunta
C  Date:      17 July 2009
C
C-----------------------------------------------------------------------------
```

Figure 5.12: Example of *adf07* data file for silicon, containing the final stage-to-stage CADW ionisation rate coefficients. The figure shows only a sample of the dataset including three silicon ions ($Si^{+1}$, $Si^{+2}$ and $Si^{+3}$ ionising to $Si^{+2}$, $Si^{+3}$ and $Si^{+4}$). The temperature values are given in eV, while the rate coefficients are in $cm^3\ s^{-1}$. Final comments are provided at the bottom of the file.

The ionisation potentials, corrected for the shift of the average are shown in table 5.8. Also, the possible pathways promoting an electron from 2p and then from 2s are illustrated for each metastable. Consider, as example, the term $2s^2 2p^2\,{}^3P$ of $Si^{+8}$. Removing a 2p electron, the only possible pathway for ionisation is $2s^2 2p\,{}^2P$. Calling $I_{(Si^{+8})}$=2832000.0 $cm^{-1}$ the ionisation potential of $Si^{+8}$, $I_{(2s^2 2p^2\,{}^3P)}$=4411.7 $cm^{-1}$ the energy of the term $2s^2 2p^2\,{}^3P$ of $Si^{+8}$ and $I_{(2s^2 2p\,{}^2P)}$=4660.4 $cm^{-1}$ the energy of the term $2s^2 2p^1\ {}^2P$ of $Si^{+9}$, the corrected ionisation potential, $I_{corr}$, is given by $I_{corr}=I_{(Si^{+8})}-I_{(2s^2 2p^2\,{}^3P)}+I_{(2s^2 2p\,{}^2P)}$=2832248.7 $cm^{-1}$.

| $Si^{+8} \rightarrow Si^{+9}$ | | | | | | |
|---|---|---|---|---|---|---|
| Pathway | | | | | I.P. ($cm^{-1}$) | I.P. (Ryd) |
| 2s2 2p2 | 3P | → | 2s2 2p1 | 2P | 2832248.7 | 25.80936 |
| | | → | 2s1 2p2 | 2P | 3220288.3 | 29.34544 |
| | | → | 2s1 2p2 | 4P | 2992450.0 | 27.26922 |
| 2s2 2p2 | 1D | → | 2s2 2p1 | 2P | 2783734.5 | 25.36727 |
| | | → | 2s1 2p2 | 2D | 3066942.1 | 27.94805 |
| 2s2 2p2 | 1S | → | 2s2 2p1 | 2P | 2728861.4 | 24.86723 |
| | | → | 2s1 2p2 | 2S | 3091871.0 | 28.17522 |
| 2s1 2p3 | 5S | → | 2s1 2p2 | 4P | 2846091.7 | 25.93551 |
| | | → | 2s0 2p3 | 4S | 3190560.0 | 29.07454 |

Table 5.8: Ionisation potentials corrected for the shift of the average, relative to every possible pathway.

Table 5.9 establishes in detail how to use different pathways for ionisation and how to make up the $S^{bchid}$ formulae and finally correct them using CADW calculations performed for ground to ground state ionisation. For $Si^{+8}$, the ground state has the outer electron configuration $2s^2 2p^2$. The ionisation potential for a $2p$ electron is denoted by I($2p$) and for a $2s$ electron is denoted by I($2s$). The initial shell direct equivalent electron assignments are $\zeta(2p)$=2 and $\zeta(2s)$=2 at these ionisation potentials respectively. The autoionising levels of the form $2s2p^2nl$ lie densely through the threshold for $2p$ shell-direct ionisation and on into the $2s^2 2p + e^-$ continuum. Excitation of a $2s$ electron to such levels leads to autoionisation into the continuum with probability near to the unity. (145) calls this case (b). In this case the autoionising states lie well above the lowest excited inner-shell electron state. So there are many of these states near to the outer-shell ionisation electron state and they lie densely up to the inner-shell direct ionisation threshold. In the case of $Si^{+8}$, the $2s2p^2 3p$ states, for example, are closely packed between the $2p$ and $2s$ ionisation thresholds. Furthermore, all of the states arising from these configurations have a very high probability to be autoionising, because they lie in the continuum. These excitation-autoionisation effects can be included in the shell direct part by lowering the effective ionisation potential for the $2s$ electron to I($2p$). This is illustrated in table 5.9 along the first row, where the total contribution to ionisation from ground level is considered. Then it is compared with the CADW calculations to adjust the formula employed. Same consideration has been done for each metastable term. Each formula (indicated by the indices f1, f2, f3 and so on) is a combination of ionisation potentials $I_i$ and number of equivalent electrons $\zeta_i$, following the semi-empirical approach of (146), as described in eq. 5.34. The scale factors, by which the formulae are multiplied, take into account the statistical weights of the terms involved in the computation.

| Transition | Metastable | Index | Purpose | Formula | Shell 1 I(1s) (Ryd) | ζ(1s) | Shell 2 I(2s) (Ryd) | ζ(2s) | Shell 3 I(2p) (Ryd) | ζ(2p) | Shell 4 I(3s) (Ryd) | ζ(3s) | Scale factor |
|---|---|---|---|---|---|---|---|---|---|---|---|---|---|
| $Si^{+8} \rightarrow Si^{+9}$ | | f1 | Total | | 131.32000 | 2.000 | 25.80936 | 2.000 | 25.80936 | 2.000 | | | 1.000 |
| | | | CADW comparison | ratio=CADW/f1 | | | | | | | | | |
| | 2s2 2p2 (3P) | f2 | 2p direct | | | | | | 25.80936 | 2.000 | | | 1.000 |
| | | f3 | 2s via 2P + auto | | | | 25.80936 | 2.000 | | | | | 0.333 |
| | | f4 | 2s via 4P + auto | | | | 25.80936 | 2.000 | | | | | 0.667 |
| | | f5 | 2s via 4P direct | | | | 27.26922 | 2.000 | | | | | 0.667 |
| | | f6 | 1s + auto | | 131.32000 | 2.000 | | | | | | | 1.000 |
| | | f7 | 1s direct | | 160.19000 | 2.000 | | | | | | | 1.000 |
| | | | 2s2 2p2 (3P) total | (f2+f3+f4+f6)*ratio | | | | | | | | | |
| | # | | 2s2 2p2 (3P) → 2s2 2p1 (2P) | (f2+f3+f4+0.333*f6-f5)*ratio | | | | | | | | | |
| | # | | 2s2 2p2 (3P) → 2s1 2p2 (4P) | (f5+0.667*f6)*ratio | | | | | | | | | |
| | 2s2 2p2 (1D) | f8 | 2p direct | | | | | | 25.36727 | 2.000 | | | 1.000 |
| | | f9 | 2s via 2D + auto | | | | 25.36727 | 2.000 | | | | | 1.000 |
| | | f10 | 2s via 2D direct | | | | 27.94805 | 2.000 | | | | | 1.000 |
| | | f11 | 1s + auto | | 131.32000 | 2.000 | | | | | | | 1.000 |
| | | f12 | 1s direct | | 160.19000 | 2.000 | | | | | | | 1.000 |
| | | | 2s2 2p2 (1D) total | (f8+f9+f11)*ratio | | | | | | | | | |
| | # | | 2s2 2p2 (1D) → 2s2 2p1 (2P) | (f8+f9+f11)*ratio | | | | | | | | | |
| | 2s2 2p2 (1S) | f13 | 2p direct | | | | | | 24.86723 | 2.000 | | | 1.000 |
| | | f14 | 2s via 2S + auto | | | | 24.86723 | 2.000 | | | | | 1.000 |
| | | f15 | 2s via 2S direct | | | | 28.17522 | 2.000 | | | | | 1.000 |
| | | f16 | 1s + auto | | 131.32000 | 2.000 | | | | | | | 1.000 |
| | | f17 | 1s direct | | 160.19000 | 2.000 | | | | | | | 1.000 |
| | | | 2s2 2p2 (1S) total | (f13+f14+f16)*ratio | | | | | | | | | |
| | # | | 2s2 2p2 (1S) → 2s2 2p1 (2P) | (f13+f14+f16)*ratio | | | | | | | | | |
| | 2s1 2p3 (5S) | f18 | 2p direct | | | | | | 25.93551 | 3.000 | | | 1.000 |
| | | f19 | 2s via 4S + auto | | | | 25.93551 | 1.000 | | | | | 1.000 |
| | | f20 | 2s via 4S direct | | | | 29.07454 | 1.000 | | | | | 1.000 |
| | | f21 | 1s + auto | | 131.32000 | 2.000 | | | | | | | 1.000 |
| | | f22 | 1s direct | | 160.19000 | 2.000 | | | | | | | 1.000 |
| | | | 2s1 2p3 (5S) total | (f18+f19+f21)*ratio | | | | | | | | | |
| | # | | 2s1 2p3 (5S) → 2s1 2p2 (4P) | (f18+f19+f21)*ratio | | | | | | | | | |

Table 5.9: Details concerning the different direct ionisation and excitation-autoionisation pathways. The second column shows the metastable configurations and terms. The third, fourth and fifth columns illustrate the formula indeces, the associated paths and how to make up the final formula considering all contribution for ionisation of the examined term. Columns six to thirteen use ionisation potentials and energy values from tables 5.7 and 5.8, following the case (a) and/or (b), as discussed by (145). The last column collects the scale factors by which the formulae have to be multiplied. Note that the sum of the total formula f1 must be equal to the sum of the separate direct and indirect contributions to the ionisation from ground level (described by f2, f3, f4 and f6), multiplied by the scale factors.

- *$Si^{+1}$ ionising to $Si^{+2}$*: The same consideration, as the previous example, can be done for tables 5.10 and 5.11. The ion $Si^{+1}$, more complex than $Si^{+8}$, belongs to Al-like system. Hence, it is characterised by two metastable terms (again shown in red in tables 5.10 and 5.11). The comment "cowan" in table 5.10 indicates that the level energy values for the configurations in which a $2p$ or $2s$ electron has been promoted to higher n-shell come from Cowan calculations. All these levels show energy values larger than the ionisation potential for $Si^{+1}$ I.P.=270139.3 $cm^{-1}$. So they may be autoionised.

  Again, the detailed use of different ionisation pathways, as identified in table 5.11, is illustrated in table 5.12. For this ion, the ground state outer electron configuration is $3s^2 3p$. As for the first example, because the autoionising levels $3s3pnl$ lie densely through the $3s^2$ ionisation threshold, the case (b) of (145) can be applied, lowering the effective ionisation potential for the 3s electron to I($3p$). However, the complete shell structure is $1s^2 2s^2 2p^6 3s^2 3p$. The shell direct part from inner shell $2p^6$ has a large $\zeta$ weighting and must be included. The first autoionising configuration from promotion of a $2p$ electron is $2p^5 3s^2 3p^2$ and it lies considerably above the $3s^2$ ionisation threshold. As a consequence, such excitation-autoionisation effect is included by reducing the ionisation potential of the $2p$ electron from I($2p$) to I($2p$)-I($3p$). (145) calls this situation case (a). In practice, since the real first resonant state is not precisely known, it is a reasonable approximation to take such inner shell contribution into account by setting the ionisation potential of the $2p$ electron equal to the energy needed to remove such electron from the $2p$ orbital. This is done in the table 5.12 both for the $2p$ and $2s$ inner shells. Regarding the metastable terms, concentrate, along this second example, on how the separate contributions to ionisation are built up. As discussed, $Si^{+1}$ has two metastables, as well as $Si^{+2}$. The first $Si^{+1}$ metastable term, $3s^2 3p\,^2P$ can be ionised both to $3s^2\,^1S$ and $3s3p\,^3P$. Other possible pathways are provided by the state $3s3p\,^1P$ and all states obtained by the promotion of a 2p electron (see table 5.11). However, these latter states are not metastables and the electron tends to decay to lower energy states. The separate contributions for ionisation due to the first $Si^{+1}$ metastable to $3s^2\,^1S$ and $3s3p\,^3P$ of $Si^{+2}$ are given by the combinations of $S^{bchid}$ formulae, as shown in table 5.12, considering the statistical weights of the final states. For $3s^2 3p\,^2P \rightarrow 3s^2\,^1S$, it has been taken into account the following processes:

  1. direct ionisation of the $3p$ via $^1S$, described by the formula index f2;
  2. ionisation of a $3s$ electron via $^1P$ including autoionisation, described by the formula index f3;
  3. ionisation of a $3s$ electron via $^3P$ including autoionisation, described by the formula index f4;
  4. ionisation of a $2p$ via $^1S$, $^1P$ and $^1D$, described respectively by the formula indices f9, f10 and f11;
  5. ionisation of a 2s and a 1s electron including autoionisation, which have been multiplied by 0.25 to consider the statistical weight of $3s^2\,^1S$ state. They are described by the formula indices f12 and f14.

  These five contributions have been summed and the direct ionisation of a 3s electron via $^3P$ (described by the formula index f5) has been subtracted. By contrast, for $3s^2 3p\,^2P \rightarrow 3s3p\,^3P$ the pathways included to calculate the total ionisation contribution relative to the second metastable only are the following:

  1. direct ionisation of the $3s$ via $^3P$, described by the formula index f5;
  2. ionisation of a $2p$ via $^3S$, $^3P$ and $^3D$, described respectively by the formula indices f6, f7 and f8;
  3. ionisation of a $2s$ and a $1s$ electron including autoionisation, which have been multiplied by 0.75 to consider the statistical weight of $3s3p\,^3P$ state. They are described by the formula indices f12 and f14.

  Again, these three contributions have been summed together. The second $Si^{+1}$ metastable term, $3s3p^2\,^4P$ can be ionised to $3s3p\,^3P$. As before, the appropriate contributions for ionisation have been summed together, giving the final formula for $3s3p^2\,^4P \rightarrow 3s3p\,^3P$.

Table 5.10: List of energy levels for $Si^{+1}$ and $Si^{+2}$. See table 5.7 for more explanation.

| $Si^{+2}$ | | | | I.P. ($cm^{-1}$) | 270139.3 | $Si^{+2}$ | |
|---|---|---|---|---|---|---|---|
| Config | Term | J | E($cm^{-1}$) | Eav($cm^{-1}$) | Comment | Orbital | En.(Ryd) |
| 2s2 2p6 3s2 | 1S | 0.00 | 0.0 | 0.0 | | 1s | 140.15 |
| 2s2 2p6 3s1 3p1 | 3P | 0.00 | 52724.7 | 52984.4 | | 2s | 14.42 |
| | | 1.00 | 52853.3 | | | 2p | 10.58 |
| | | 2.00 | 53115.0 | | | | |
| 2s2 2p6 3s1 3p1 | 1P | 1.00 | 82884.4 | 82884.4 | | 3s | 2.76 |
| 2s2 2p6 3p2 (3P) | 3P | 0.00 | 129708.5 | 129970.8 | | 3p | 1.92 |
| | | 1.00 | 129842.0 | | | 3d | 1.20 |
| | | 2.00 | 130100.5 | | | | |
| 2s2 2p5 (2P) 3s2 3p1(2P) | 3S | 1.00 | 833382.1 | 833382.1 | cowan | | |
| 2s2 2p5 (2P) 3s2 3p1(2P) | 3P | 0.00 | 846731.5 | 845281.9 | cowan | | |
| | | 1.00 | 847563.6 | | cowan | | |
| | | 2.00 | 843623.0 | | cowan | | |
| 2s2 2p5 (2P) 3s2 3p1(2P) | 3D | 1.00 | 842136.4 | 840461.5 | cowan | | |
| | | 2.00 | 840547.8 | | cowan | | |
| | | 3.00 | 839682.1 | | cowan | | |
| 2s2 2p5 (2P) 3s2 3p1(2P) | 1S | 0.00 | 884086.1 | 884086.1 | cowan | | |
| 2s2 2p5 (2P) 3s2 3p1(2P) | 1P | 1.00 | 845909.2 | 845909.2 | cowan | | |
| 2s2 2p5 (2P) 3s2 3p1(2P) | 1D | 2.00 | 847150.9 | 847150.9 | cowan | | |
| 2s2 2p5(2P) 3s1 3p2 (4P) | 5S | 2.00 | 887446.1 | 887446.1 | cowan | | |
| 2s2 2p5(2P) 3s1 3p2 (4P) | 5P | 1.00 | 876131.7 | 874991.7 | cowan | | |
| | | 2.00 | 875231.0 | | cowan | | |
| | | 3.00 | 874332.1 | | cowan | | |
| 2s2 2p5(2P) 3s1 3p2 (4P) | 5D | 0.00 | 882367.3 | 880133.5 | cowan | | |
| | | 1.00 | 881889.8 | | cowan | | |
| | | 2.00 | 881073.5 | | cowan | | |
| | | 3.00 | 880053.5 | | cowan | | |
| | | 4.00 | 878840.0 | | cowan | | |
| 2s2 2p5(2P) 3s1 3p2 (4P) | 3S | 1.00 | 891400.1 | 891400.1 | cowan | | |
| 2s2 2p5(2P) 3s1 3p2 (4P) | 3P | 0.00 | 891658.7 | 893035.5 | cowan | | |
| | | 1.00 | 892853.9 | | cowan | | |
| | | 2.00 | 893419.8 | | cowan | | |
| 2s2 2p5(2P) 3s1 3p2 (4P) | 3D | 1.00 | 887134.2 | 888887.3 | cowan | | |
| | | 2.00 | 888513.5 | | cowan | | |
| | | 3.00 | 889905.7 | | cowan | | |
| 2s1 2p6 (2S) 3s1 3p2 (4P) | 5P | 1.00 | 1305905.8 | 1306116.7 | cowan | | |
| | | 2.00 | 1306047.1 | | cowan | | |
| | | 3.00 | 1306256.8 | | cowan | | |
| 2s1 2p6 (2S) 3s1 3p2 (4P) | 3P | 0.00 | 1321869.5 | 1322088.9 | cowan | | |
| | | 1.00 | 1321979.6 | | cowan | | |
| | | 2.00 | 1322198.4 | | cowan | | |

| $Si^{+1}$ | | | | I.P. ($cm^{-1)}$ | 131838.1 | $Si^{+1}$ | |
|---|---|---|---|---|---|---|---|
| Config | Term | J | E($cm^{-1}$) | Eav($cm^{-1}$) | Comment | Orbital | En.(Ryd) |
| 2s2 2p6 3s2 3p1 | 2P | 0.50 | 0.0 | 191.5 | | 1s | 139.21 |
| | | 1.50 | 287.2 | | | 2s | 13.51 |
| 2s2 2p6 3s1 3p2 | 4P | 0.50 | 42824.3 | 43002.2 | | 2p | 9.67 |
| | | 1.50 | 42932.6 | | | 3s | 1.94 |
| | | 2.50 | 43107.9 | | | 3p | 1.27 |
| 2s2 2p6 3s1 3p2 | 2P | 0.50 | 83802.0 | 83936.8 | | 3d | 0.62 |
| | | 1.50 | 84004.3 | | | | |
| 2s2 2p6 3s1 3p2 | 2S | 0.50 | 76665.4 | 76665.4 | | | |
| 2s2 2p6 3s1 3p2 | 2D | 1.50 | 55309.4 | 55318.8 | | | |
| | | 2.50 | 55325.2 | | | | |
| 2s2 2p5 (2P) 3s2 3p2 (3P) | 4D | 0.50 | 812238.2 | 808961.5 | cowan | | |
| | | 1.50 | 809697.1 | | cowan | | |
| | | 2.50 | 808835.5 | | cowan | | |
| | | 3.50 | 807869.0 | | cowan | | |
| 2s2 2p5 (2P) 3s2 3p2 (3P) | 4P | 0.50 | 805772.6 | 804586.0 | cowan | | |
| | | 1.50 | 804916.0 | | cowan | | |
| | | 2.50 | 803970.4 | | cowan | | |
| 2s2 2p5 (2P) 3s2 3p2 (3P) | 4S | 1.50 | 816394.1 | 816394.1 | cowan | | |
| 2s2 2p5 (2P) 3s2 3p2 (3P) | 2D | 1.50 | 813646.1 | 814319.6 | cowan | | |
| | | 2.50 | 814768.6 | | cowan | | |
| 2s2 2p5 (2P) 3s2 3p2 (3P) | 2P | 0.50 | 809397.4 | 810247.7 | cowan | | |
| | | 1.50 | 810672.9 | | cowan | | |
| 2s2 2p5 (2P) 3s2 3p2 (3P) | 2S | 0.50 | 816312.1 | 816312.1 | cowan | | |
| 2s1 2p6 (2S) 3s2 3p2 (3P) | 4P | 0.50 | 1239576.3 | 1239771.2 | cowan | | |
| | | 1.50 | 1239694.1 | | cowan | | |

| $Si^{+1} \rightarrow Si^{+2}$ | | | | | | |
|---|---|---|---|---|---|---|
| Pathway | | | | | I.P. ($cm^{-1}$) | I.P. (Ryd) |
| 2s2 2p6 3s2 3p1 | 2P | → | 2s2 2p6 3s2 | 1S | 131646.6 | 1.19965 |
| | | → | 2s2 2p6 3s1 3p1 | 3P | 184631.0 | 1.68248 |
| | | → | 2s2 2p6 3s1 3p1 | 1P | 214531.1 | 1.95495 |
| | | → | 2s2 2p5 (2P) 3s2 3p1(2P) | 3S | 965028.7 | 8.79399 |
| | | → | 2s2 2p5 (2P) 3s2 3p1(2P) | 3P | 976928.6 | 8.90243 |
| | | → | 2s2 2p5 (2P) 3s2 3p1(2P) | 3D | 972108.2 | 8.85851 |
| | | → | 2s2 2p5 (2P) 3s2 3p1(2P) | 1S | 977555.8 | 8.90815 |
| | | → | 2s2 2p5 (2P) 3s2 3p1(2P) | 1P | 977555.8 | 8.90815 |
| | | → | 2s2 2p5 (2P) 3s2 3p1(2P) | 1D | 978797.5 | 8.91946 |
| 2s2 2p6 3s1 3p2 | 4P | → | 2s2 2p6 3s1 3p1 | 3P | 141820.3 | 1.29236 |
| | | → | 2s2 2p6 3p2 (3P) | 3P | 218806.7 | 1.99391 |
| | | → | 2s2 2p5(2P) 3s1 3p2 (4P) | 5S | 976282.0 | 8.89654 |
| | | → | 2s2 2p5(2P) 3s1 3p2 (4P) | 5P | 963827.6 | 8.78305 |
| | | → | 2s2 2p5(2P) 3s1 3p2 (4P) | 5D | 968969.5 | 8.82990 |
| | | → | 2s2 2p5(2P) 3s1 3p2 (4P) | 3S | 980236.0 | 8.93257 |
| | | → | 2s2 2p5(2P) 3s1 3p2 (4P) | 3P | 981871.4 | 8.94748 |
| | | → | 2s2 2p5(2P) 3s1 3p2 (4P) | 3D | 977723.3 | 8.90967 |
| | | → | 2s1 2p6 (2S) 3s1 3p2 (4P) | 5P | 1394952.6 | 12.71175 |
| | | → | 2s1 2p6 (2S) 3s1 3p2 (4P) | 3P | 1410924.8 | 12.85730 |

Table 5.11: Ionisation potentials corrected for the shift of the average, relative to every possible pathway.

Table 5.10: – continued

| | | | | | | |
|---|---|---|---|---|---|---|
| | | 2.50 | 1239887.5 | | cowan | |
| 2s1 2p6 (2S) 3s2 3p2 (3P) | 2P | 0.50 | 1245004.7 | 1245159.1 | cowan | |
| | | 1.50 | 1245236.3 | | cowan | |
| 2s2 2p5 (2P) 3s2 3p2 (1D) | 2P | 0.50 | 838236.9 | 836367.4 | cowan | |
| | | 1.50 | 835432.6 | | cowan | |
| 2s2 2p5 (2P) 3s2 3p2 (1D) | 2D | 1.50 | 825390.2 | 825235.8 | cowan | |
| | | 2.50 | 825132.9 | | cowan | |
| 2s2 2p5 (2P) 3s2 3p2 (1D) | 2F | 2.50 | 820249.2 | 818695.4 | cowan | |
| | | 3.50 | 817530.0 | | cowan | |
| 2s1 2p6 (2S) 3s2 3p2 (1D) | 2D | 1.50 | 1251877.7 | 1251876.7 | cowan | |
| | | 2.50 | 1251876.1 | | cowan | |
| 2s2 2p5 (2P) 3s2 3p2 (1S) | 2P | 0.50 | 845415.4 | 845450.1 | cowan | |
| | | 1.50 | 845467.5 | | cowan | |
| 2s1 2p6 (2S) 3s2 3p2 (1S) | 2S | 0.50 | 1267343.7 | 1267343.7 | cowan | |

| Transition | Metastable | Index | Purpose | Formula | Shell 1 I(1s) (Ryd) | $\zeta$(1s) | Shell 2 I(2s) (Ryd) | $\zeta$(2s) | Shell 3 I(2p) (Ryd) | $\zeta$(2p) | Shell 4 I(3s) (Ryd) | $\zeta$(3s) | Shell 5 I(3p) (Ryd) | $\zeta$(3p) | Scale factor |
|---|---|---|---|---|---|---|---|---|---|---|---|---|---|---|---|
| $Si^{+1} \rightarrow Si^{+2}$ | | f1 | Total | | 125.70000 | 2.000 | 13.51000 | 2.000 | 9.67000 | 6.000 | 1.19965 | 2.000 | 1.19965 | 1.000 | 1.000 |
| | | | CADW comparison | ratio=CADW/f1 | | | | | | | | | | | |
| | 3s2 3p1 (2P) | f2 | 3p via 1S direct | | | | | | | | | | 1.19965 | 1.000 | 1.000 |
| | | f3 | 3s via 1P + auto | | | | | | | | 1.19965 | 2.000 | | | 0.250 |
| | | f4 | 3s via 3P + auto | | | | | | | | 1.19965 | 2.000 | | | 0.750 |
| | | f5 | 3s via 3P direct | | | | | | | | 1.68248 | 2.000 | | | 0.750 |
| | | f6 | 2p via 2s2 2p5 3s2 3p1 (3S) | | | | | | 9.67000 | 6.000 | | | | | 0.083 |
| | | f7 | 2p via 2s2 2p5 3s2 3p1 (3P) | | | | | | 9.67000 | 6.000 | | | | | 0.250 |
| | | f8 | 2p via 2s2 2p5 3s2 3p1 (3D) | | | | | | 9.67000 | 6.000 | | | | | 0.417 |
| | | f9 | 2p via 2s2 2p5 3s2 3p1 (1S) | | | | | | 9.67000 | 6.000 | | | | | 0.028 |
| | | f10 | 2p via 2s2 2p5 3s2 3p1 (1P) | | | | | | 9.67000 | 6.000 | | | | | 0.083 |
| | | f11 | 2p via 2s2 2p5 3s2 3p1 (1D) | | | | | | 9.67000 | 6.000 | | | | | 0.139 |
| | | f12 | 2s + auto | | | | 13.51000 | 2.000 | | | | | | | 1.000 |
| | | f13 | 2s direct | | | | 13.51000 | 2.000 | | | | | | | 1.000 |
| | | f14 | 1s + auto | | 125.70000 | 2.000 | | | | | | | | | 1.000 |
| | | f15 | 1s direct | | 139.21000 | 2.000 | | | | | | | | | 1.000 |
| | | | 3s2 3p1 (2P) total | (f2+f3+f4+f6+f7+f8+f9+ f10+f11+f12+f14)*ratio | | | | | | | | | | | |
| | # | | 3s2 3p1 (2P) → 3s2 (1S) | (f2+f3+f4+f9+f10+f11+ 0.25*f12+0.25*f14-f5)*ratio | | | | | | | | | | | |
| | # | | 3s2 3p1 (2P) → 3s1 3p1 (3P) | (f5+f6+f7+f8+0.75*f12+ 0.75*f14)*ratio | | | | | | | | | | | |
| | 3s1 3p2 (4P) | f16 | 3p direct | | | | | | | | | | 1.29236 | 2.000 | 1.000 |
| | | f17 | 3s via 3P + auto | | | | | | | | 1.29236 | 1.000 | | | 1.000 |
| | | f18 | 3s via 3P direct | | | | | | | | 1.99391 | 1.000 | | | 1.000 |
| | | f19 | 2p via 2s2 2p5 3s1 3p2 (5S) | | | | | | 9.67000 | 6.000 | | | | | 0.069 |
| | | f20 | 2p via 2s2 2p5 3s1 3p2 (5P) | | | | | | 9.67000 | 6.000 | | | | | 0.208 |
| | | f21 | 2p via 2s2 2p5 3s1 3p2 (5D) | | | | | | 9.67000 | 6.000 | | | | | 0.347 |
| | | f22 | 2p via 2s2 2p5 3s1 3p2 (3S) | | | | | | 9.67000 | 6.000 | | | | | 0.042 |
| | | f23 | 2p via 2s2 2p5 3s1 3p2 (3P) | | | | | | 9.67000 | 6.000 | | | | | 0.125 |
| | | f24 | 2p via 2s2 2p5 3s1 3p2 (3D) | | | | | | 9.67000 | 6.000 | | | | | 0.208 |
| | | f25 | 2s via 2s1 2p6 3s1 3p2 (5P) | | | | 13.51000 | 2.000 | | | | | | | 0.625 |
| | | f26 | 2s via 2s1 2p6 3s1 3p2 (3P) | | | | 13.51000 | 2.000 | | | | | | | 0.375 |
| | | f27 | 1s+auto | | 125.70000 | 2.000 | | | | | | | | | 1.000 |
| | | f28 | 1s direct | | 139.21000 | 2.000 | | | | | | | | | 1.000 |
| | | | 3s1 3p2 (4P) total | (f16+f17+f19+f20+f21+f22+ f23+f24+f25+f26+f27)*ratio | | | | | | | | | | | |
| | # | | 3s1 3p2 (4P) → 3s1 3p1 (3P) | (f16+f17+f19+f20+f21+f22+ f23+f24+f25+f26+f27)*ratio | | | | | | | | | | | |

Table 5.12: Details concerning the different direct ionisation and excitation-autoionisation pathways. Same consideration as the table 5.9 can be done. Other two columns have been added to take into account the $3p$ shell.

Following these procedures and considerations, a new metastable resolved *adf07* data file has been produced. An example of such a set for the two ions discussed above is shown in figure 5.13.

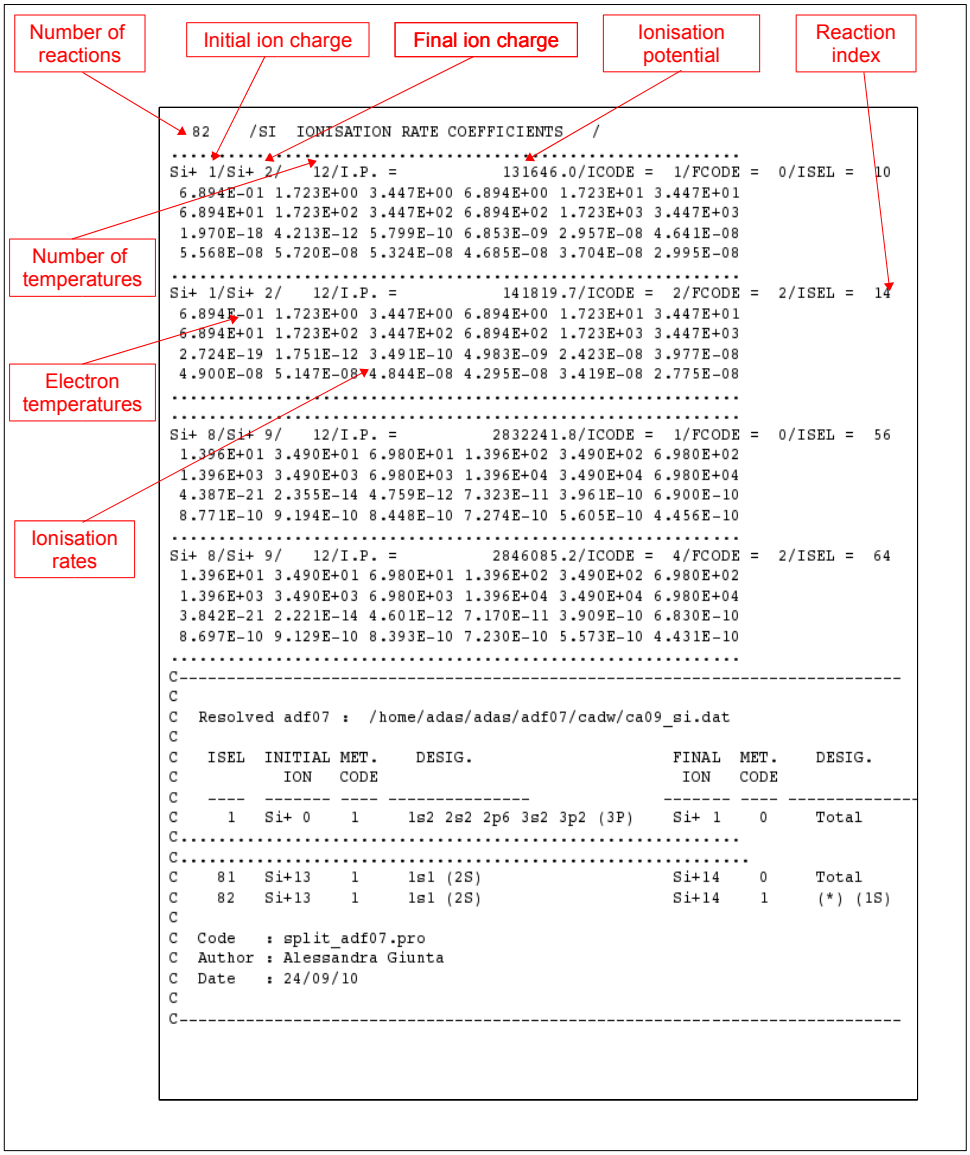


Figure 5.13: Example of *adf07* data file for silicon, containing the resolved ionisation rate coefficients. The figure shows a sample of the dataset including $Si^{+1}$ ionising to $Si^{+2}$ and $Si^{+8}$ ionising to $Si^{+9}$. As for figure 5.12, the temperature values are in eV and the ionisation rate coefficients are in $cm^3\ s^{-1}$.

It illustrates the total contribution to ionisation rate due to ionisation from each metastable term of the ion in the ionising state to the ion in the ionised state and the single contribution of each metastable term of the ion in the ionising state to each metastable of the ion in the ionised state. Finally the figure 5.14 shows the comparison between the unresolved ground to ground ionisation rates and the split by metastable set. Also, the ratio between the unresolved ionisation rate and the resolved rates is displayed in order to examine the partial contribution of each metastable with respect to the total ionisation rates.

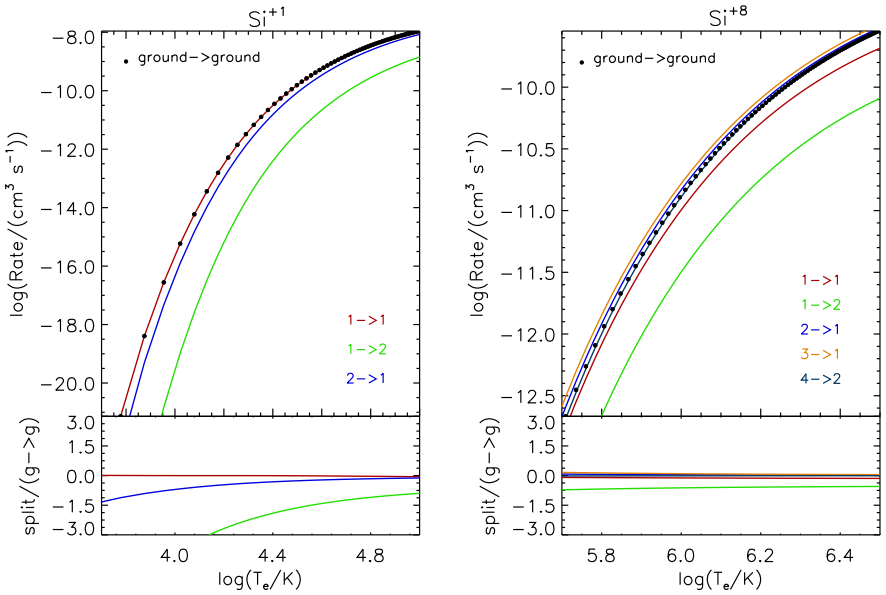


Figure 5.14: Comparison between the ground to ground ionisation rates, calculated using the CADW approach and the contributions due to the single metastable terms, calculated following the semi-empirical approach of (146) and adjusting the results using the ground to ground ionisation rates.

### 5.3.2 Step 2 - specific ion files for low levels

The second step is to revise the *adf04* data files collected in ADAS, from literature selection and eventually merging the data already existing with the Cowan code calculations to add missed transitions. Lists of main sources for the silicon ions are shown in table 5.13 to 5.26.

Only plane wave Born calculations are available for neutral silicon (tab. 5.13). The ADAS801 routine has been used to compute the energy levels, A-values and effective collision strengths, using the configurations $3s^2 3p^2$, $3s3p^3$, $3s^2 3p4s$, $3s^2 3p4p$, $3s^2 3p3d$, $3s^2 3p4f$, $3s^2 3p4d$ and $3p^4$. Then, energy levels have been replaced with the more accurate values

| *Ion* | $Si^{+0}$ |
|---|---|
| *Energy levels* | NIST |
| *A-value* | Cowan |
| *ϒ-value* | Cowan |

Table 5.13: Recommended data for $Si^{+0}$.

from NIST.

The $Si^{+1}$ ion is of fundamental importance for this work. In fact, lines which arise from such an ion are formed at a temperature as low as that of neutral helium. Furthermore, as suggested by (149), they may be slightly affected by opacity, which makes this analysis more complicated. The role of opacity in the silicon lines will be discussed in the next chapter, sec. 6.1.4. Hence, the precision and reliability of atomic data for this ion are essential. The only calculations included in the ADAS database for $Si^{+1}$ have been derived using the PWB approach. More accurate calculations have been done by (139). They included in their model 15 fine-structure levels up to $3s3p^2\,{}^2P_{3/2}$ and calculated collision strengths using the R-matrix approach for transitions amongts the lowest 7 levels and for transitions from the ground state $3s^2 3p\,{}^2P_j$ (with $j = 1/2, 3/2$) to all the other levels. These collision strengths have been included in the CHIANTI v.6 database, together with energy levels from NIST and radiative data from (150) and (151). Here these data have been supplemented with Cowan calculations to add the higher levels belonging to the configurations $3s3p3d$ and $3p^3$ and transitions amongst them. A comparison of the *PEC*s from CHIANTI (dashed lines) e those supplemented with Cowan (solid lines) have been displayed in figure 5.15. The five transitions, $3s^2 3p\,{}^2P_{3/2} - 3s^2 3d\,{}^2D_{5/2}$, $3s^2 3p\,{}^2P_{3/2} - 3s^2 3d\,{}^2D_{3/2}$ (plot 5.15(a)) and $3s^2 3p\,{}^2P_{3/2} - 3s3p^2\,{}^2S_{1/2}$,

| *Ion* | $Si^{+1}$ |
|---|---|
| *Energy levels* | NIST<br>SUPERSTRUCTURE |
| *A-value* | NIST<br>(150)<br>(151) |
| $\Upsilon$-*value* | (139)<br>Cowan |

Table 5.14: Recommended data for $Si^{+1}$.

$3s^2 3p\,^2P_{1/2} - 3s3p^2\,^2P_{3/2}$, $3s^2 3p\,^2P_{1/2} - 3s3p^2\,^2S_{1/2}$ (plot 5.15(b)), which are shown in the figure, give rise to the five lines observed by SUMER at the wavelengths 1264.74 Å, 1265.00 Å and 1309.28 Å, 1190.42 Å, 1304.37 Å respectively.

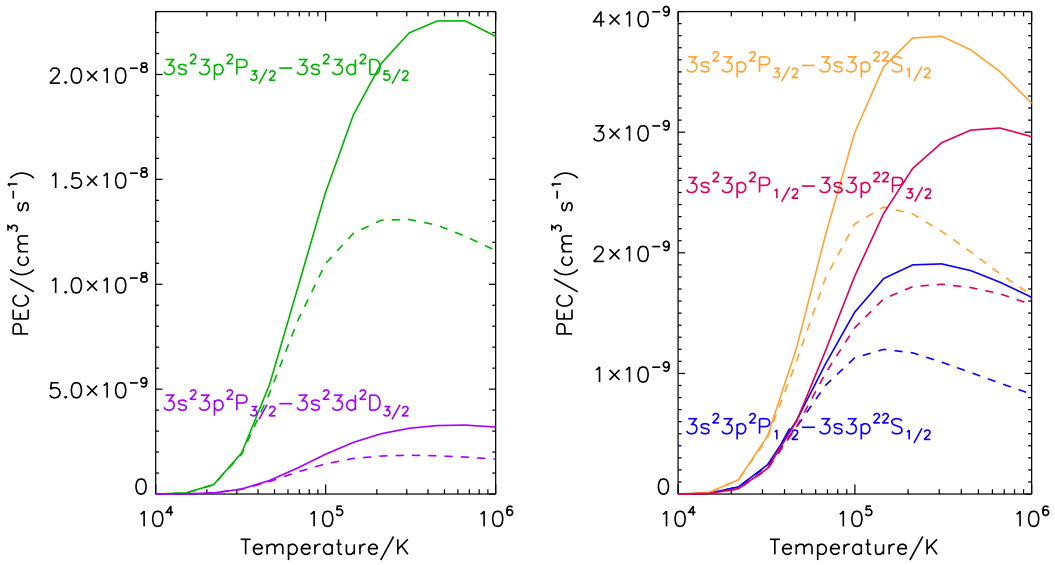


(a) (b)

Figure 5.15: Comparison between *PEC*s of $Si^{+1}$. The dashed lines are the data from CHIANTI, while the solid lines represent the data from CHIANTI supplemented with Cowan calculations. Each color indicates a particular transitions. In the plot 5.15(a): $3s^2 3p\,^2P_{3/2} - 3s^2 3d\,^2D_{5/2}$ at 1264.74 Å and $3s^2 3p\,^2P_{3/2} - 3s^2 3d\,^2D_{3/2}$ at 1265.00 Å. In the plot 5.15(b): $3s^2 3p\,^2P_{3/2} - 3s3p^2\,^2S_{1/2}$ at 1309.28 Å, $3s^2 3p\,^2P_{1/2} - 3s3p^2\,^2P_{3/2}$ at 1190.42 Å and $3s^2 3p\,^2P_{1/2} - 3s3p^2\,^2S_{1/2}$ at 1304.37 Å. The electron density has been fixed at $10^{10}$ $cm^{-3}$.

For $Si^{+2}$, the most recent calculations are from the work of (121), as for the other ion of Mg-like iso-electronic sequence ($Ar^{+6}$), previously discussed (5.2.1). They are collected within the ADAS database and adopted here.

| *Ion* | $Si^{+2}$ |
|---|---|
| *Energy levels* | NIST |
| *A-value* | (121) |
| $\Upsilon$-*value* | (121) |

Table 5.15: Recommended data for $Si^{+2}$.

Excitation data for $Si^{+3}$ come essentially from two sources within the ADAS database: *ic* and *ls* PWB calculations and the relativistic DW collision strengths of outer-shell excitations with $n \leq 5$ of (120). The latter has been also

in the CHIANTI v.6 database, but considering only transitions among the lowest 5 levels and from them to all the higher levels. New calculations have been done by (152). They computed the outer-shell electron impact excitation of Na-like iso-electronic sequence from $Mg^{+1}$ to $Kr^{+25}$, using the ICFT R-matrix approach. The first 32 fine-structure resolved energy levels up to $6h\,^2H_{11/2}$ have been included in their model. Their values have been obtained from AUTOSTRUCTURE, as well as the radiative data, and compared with the NIST values, providing an agreement within 1%. Here these data have been used, as shown in tab. 5.16.

| *Ion* | $Si^{+3}$ |
|---|---|
| *Energy levels* | NIST |
| *A-value* | (152) |
| *ϒ-value* | (152) |

Table 5.16: Recommended data for $Si^{+3}$.

As for $Si^{+1}$, only Cowan calculations for $Si^{+4}$ are available within ADAS. DW calculations have been performed by (153) to provide collision strengths in *ic* coupling. They included 27 levels belonging to the $2p^6$ and $2p^5 3l$ with $l = s, p, d$ configurations and transitions amonst them. Such data are included in the ADAS database and used for this thesis. Energy levels and transition probabilities have been replaced with the NIST values where possible. Table 5.17 shows the suggested data.

| *Ion* | $Si^{+4}$ |
|---|---|
| *Energy levels* | NIST (153) |
| *A-value* | NIST (153) |
| *ϒ-value* | (153) |

Table 5.17: Recommended data for $Si^{+4}$.

For $Si^{+5}$, data from Cowan code calculations are collected within the ADAS database. In addition, it provides the results of R-matrix calculations using the ICFT method. They have been performed by (154) and automated by offline ADAS code ADAS8#3. Previous calculations using R-matrix approach have been done by (155) and (156). Such data were collected in CHIANTI v.5.2.1, but they did not include transitions between levels related to configurations $2s^2 2p^4 3s$, $2s^2 2p^4 3p$ and $2s^2 2p^4 3d$. By contrast, the last CHIANTI version (v.6) includes the data of (154), but again only transitions between the lowest two levels and amongst them and all the other 193 levels are considered. For an astrophysical point of view, there are some lines observed by SUMER - but not used for this thesis - (such as $2p^4 3s\ ^4P_{5/2}$-$2p^4 3p\ ^4D_{3/2}$ at 1131.01 Åand $2p^4 3s\ ^4P_{3/2}$-$2p^4 3p\ ^4D_{5/2}$ at 1148.69 Å), which involve those levels. Hence, because of the accuracy of ICFT R-matrix method and the larger number of levels included with respect to the previous R-matrix calculations, the computations of (154) are recommended, as shown in table 5.18.

| *Ion* | $Si^{+5}$ |
|---|---|
| *Energy levels* | (154) |
| *A-value* | (154) |
| *ϒ-value* | (154) |

Table 5.18: Recommended data for $Si^{+5}$.

Two lines which rise from $Si^{+6}$ are observed by EIS and their ratio will be used as density diagnostics in chapter 6 sec. 6.1.3. So, appropriate atomic data for this ions are important to provide a reliable estimate of electron density. Besides the baseline PWB calculations, excitation data available in ADAS for $Si^{+6}$ have been taken from CHIANTI v.1. They include 10 energy levels related to the configurations $2p^4$, $2s2p^5$ and $2p^6$. The experimental energy level come from NIST, while theoretical calculations for energy levels, oscillator strengths and collision strengths are from (157). The data have been updated in CHIANTI v.6, giving rise to 86 fine-structure energy levels up to $2s^2 2p^3 3d\ ^1P_1$ in intermediate-coupling. The calculations have been performed by (138), using the distorted wave approximation.

However, CHIANTI v.6 takes into account effective collision strengths only for transitions among the first five levels and from them to the other higher levels. This requires Cowan calculations to add the missing transitions. Such supplemented data are adopted here (tab. 5.19). Also a comparison of the *PEC*s from the three sources discussed above

| *Ion* | $Si^{+6}$ |
|---|---|
| *Energy levels* | NIST (138) |
| *A-value* | NIST (138) Cowan |
| *ϒ-value* | (138) Cowan |

Table 5.19: Recommended data for $Si^{+6}$.

is given in fig. 5.16 for the two transitions of interest ($2s^2 2p^4\ ^3P_2 - 2s2p^5\ ^3P_2$ at 275.35 Å and $2s^2 2p^4\ ^3P_1 - 2s2p^5\ ^3P_1$ at 275.67 Å). For the illustration, the electron density has been fixed at $10^{10}$ $cm^{-3}$, although the ratio between the *PEC*s derived by the two transitions depends on the density.

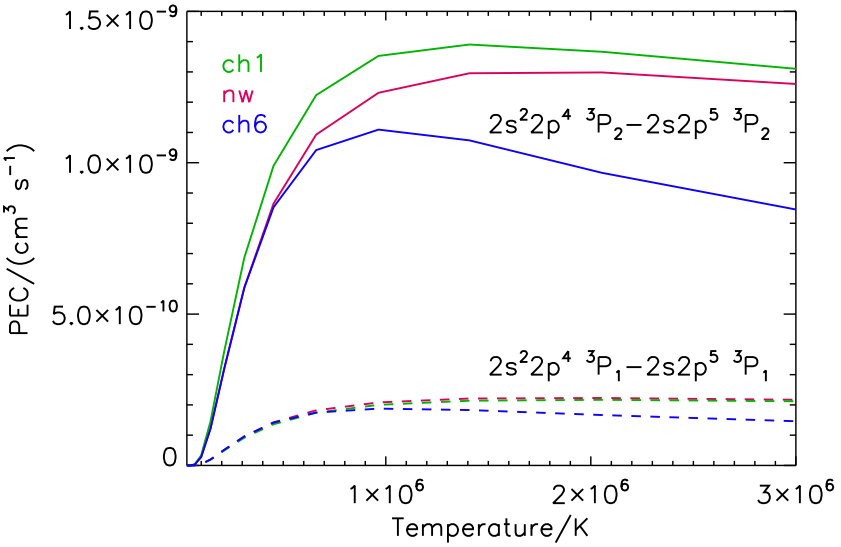


Figure 5.16: Comparison of the *PEC*s for the two transitions $2s^2 2p^4\ ^3P_2 - 2s2p^5\ ^3P_2$ and $2s^2 2p^4\ ^3P_1 - 2s2p^5\ ^3P_1$ arising from the $Si^{+6}$ ion and corresponding to the wavelengths 275.35 Å and 275.67 Å respectively. The solid and dashed green lines are the data from CHIANTI v.1; the solid and dashed red lines are derived from the CHIANTI v.6 data supplemented with Cowan calculations; finally the solid and dashed blue lines represent data from CHIANTI v. 6.

As for the previous silicon ions, Cowan calculations for $Si^{+7}$ are provided by ADAS. The other source included in the database is the work of (158), which includes intermediate-coupling energy levels, oscillator strengths and collision strengths for transitions which involve the configurations $2s^2 2p^3$ and $2s2p^4$. An improvement of these data can be found in CHIANTI v.6.0. More configurations have been included, considering 72 fine-structure levels in intermediate-coupling. Effective collision strengths within ground configuration have been calculated by (159) in the close-coupling approximation using the *ab initio* R-matrix method. For all other transitions, the scattering problem has been carried out using distorted wave calculations performed by (160) and (161). These data have been supplemented with Cowan calculations to add all missing transitions. Table 5.20 shows the suggested sources for energy levels, A-values and collision strengths.

Apart from the *ic* and *ls* Cowan calculations, the other *adf04* for $Si^{+8}$ provides oscillator strengths and collision strengths taken from the work of (163). In the last version of CHIANTI database (v.6), 46 levels, belonging to the

| *Ion* | $Si^{+7}$ |
|---|---|
| *Energy levels* | NIST |
| | (162) |
| | (160) |
| | (161) |
| *A-value* | NIST |
| | (162) |
| | (160) |
| | (161) |
| | Cowan |
| $\Upsilon$-*value* | (159) |
| | (160) |
| | (161) |
| | Cowan |

Table 5.20: Recommended data for $Si^{+7}$.

configurations $2s^2 2p^2$, $2s2p^3$, $2p^4$, $2s^2 2p3s$, $2s^2 2p3p$ and $2s^2 2p3d$, are available and the excitation data have been taken again from the work of (163). Additionally, the work of (164) has been included. He used the more accurate R-matrix approach, but only calculations for the transitions arising within the configuration $2s^2 2p^2$ have been performed. However, only transitions among the first six levels and from them to the other 40 levels are considered. To fill the gap, Cowan calculations have been performed. The sources of data here adopted are listed in table 5.21.

| *Ion* | $Si^{+8}$ |
|---|---|
| *Energy levels* | NIST |
| | (163) |
| *A-value* | NIST |
| | (163) |
| | Cowan |
| $\Upsilon$-*value* | (164) |
| | (163) |
| | Cowan |

Table 5.21: Recommended data for $Si^{+8}$.

As discussed in section 5.2.1, for $Si^{+9}$, only the line which arises from the transition between the ground level $2s^2 2p\,^2P_{1/2}$ and the excited level $2s2p^2\,^2P_{1/2}$ is present in the observations analysed in this thesis. This line is observed in a blend with the strong resonance line of $He^{+1}$ at 256.32 Å. Hence, a correct estimate of its absolute intensity is important to evaluate how much it contributes to the blend. The ADAS database includes Cowan calculations and data both from (165) and from (107). The first source gives relativistic distorted wave collision strengths and oscillator strengths respectively for transitions between 15 levels with n=2 and for transitions between 125 levels with n=2,3. The second source provides collision strengths which have been derived using the R-matrix method and including fine structure and relativistic effects. These calculations take into account 105 transitions among 15 fine-structure levels with n=2. CHIANTI v.6 collects such latter calculations for the first 15 levels and the results from (165) for the other 110 levels. However, it only includes transitions among the first five levels and transitions from them to the higher 120 levels. New electron impact collision strength results have been reported by (13). Their calculations have been performed using ICFT R-matrix calculation and are included in the ADAS database. Here, the collision strengths from (13) have been adopted, while the energy levels have been taken from NIST when possible. Table 5.22 summarises the recommended sources. Also a comparison of the *PEC*s derived from the available data is shown in the plot in figure 5.17.

Data for $Si^{+10}$ collected in the ADAS database come from different sources. The baseline *adf04* in *ic* and *ls* resolutions have been calculated using PWB approach. More accurate calculations have been taken from (100). They gives the transition energies, electric dipole oscillator strengths and relativistic distorted wave collision strengths for 45 transitions among 10 levels belonging to the configurations $2s^2$, $2s2p$ and $2p^2$. Further data has been created from a general z excitation file of type *adf05* for the Be-like sequence, using the ADAS203 routine. The collision strengths

| *Ion* | $Si^{+9}$ |
|---|---|
| *Energy levels* | NIST (13) |
| *A-value* | NIST (13) |
| $\Upsilon$-*value* | (13) |

Table 5.22: Recommended data for $Si^{+9}$.

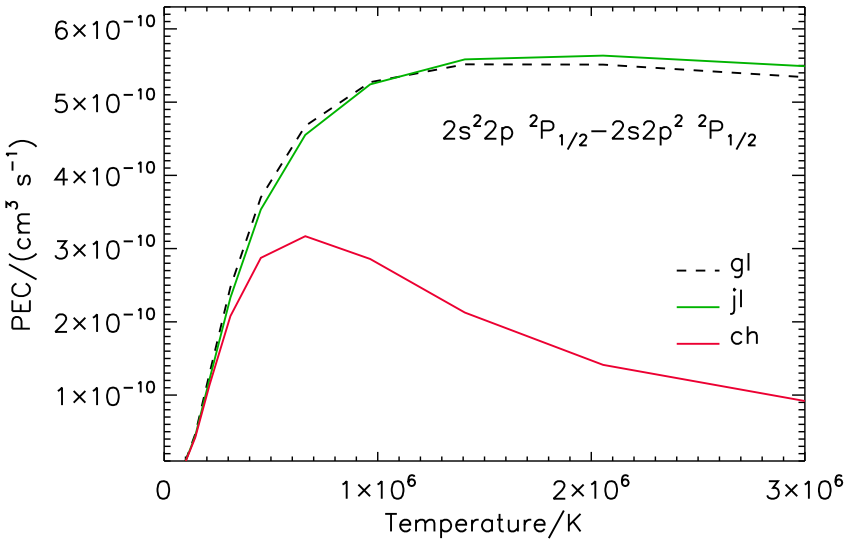


Figure 5.17: A comparison of *PEC* for $Si^{+9}$ derived from the following sources: (1) (13) (gl); (2) (107) (jl); (3) CHIANTI v.6 (ch). The transition which has been selected gives rise to the line at 256.38 Å, observed by EIS. The electron density has been fixed at $10^{10}$ $cm^{-3}$.

have been calculated by (166) using R-matrix method for the first 10 levels, while A-values come from (101). Data for more levels are included in CHIANTI v.6 database. Collision strengths from (166) are still used for the 10 first levels. For the other 82 levels, belonging to the configurations $2l3l'$, $2l4l'$ and $2s5l'$ with $l = s, p$ and $l' = s, p.d$, the data have been derived by (137), using the distorted wave approximation. These data have been adopted here and supplemented with Cowan code calculations to add missing transitions. Figure 5.18 provides a comparison of the data available and above discussed. The transition which is shown give rise to the line at 303.33 Å observed by CDS in the second order. Table 5.23 lists the suggested data for energy levels, radiative transition probabilities and effective collision strengths.

| *Ion* | $Si^{+10}$ |
|---|---|
| *Energy levels* | NIST (137) |
| *A-value* | NIST (137) |
| $\Upsilon$-*value* | (166) (137) Cowan |

Table 5.23: Recommended data for $Si^{+10}$.

The *adf04* data files present in ADAS for $Si^{+11}$ include the Cowan code calculations, as for the other silicon ions. Also, more accurate relativistic distorted wave calculations for the 3 transitions amongst the $2s\ ^2S_{1/2}$, $2p\ ^2P_{1/2}$ and $2p\ ^2P_{3/2}$ levels and the 63 transitions from these levels to the excited levels with $n = 3, 4, 5$ are collected in the database. In

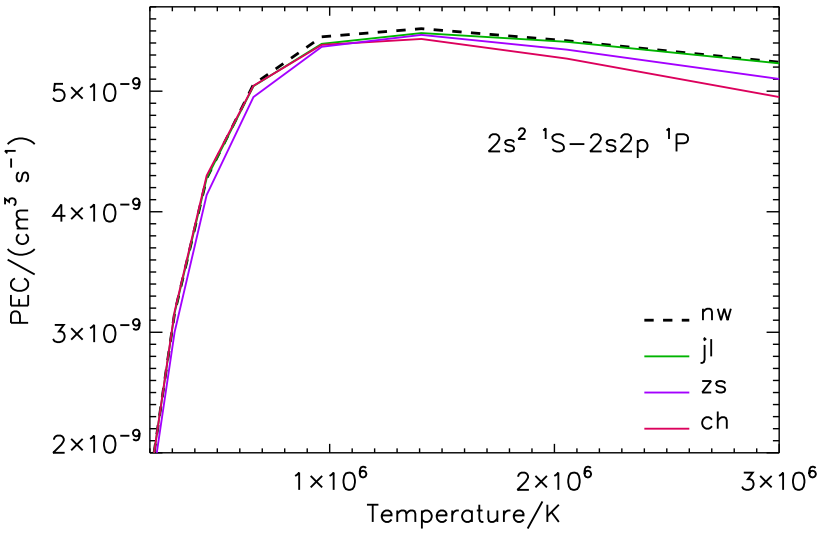


Figure 5.18: A comparison of *PEC* for $Si^{+10}$ derived from the following sources: (1) (100) (zs); (2) data created using ADAS203 (jl); (3) CHIANTI v.6 (ch); (4) CHIANTI v.6 supplemented with Cowan calculations (nw). The transition which has been selected gives rise to the line at 303.33 Å, observed by CDS at the secpnd order. The electron density has been fixed at $10^{10}$ $cm^{-3}$.

addition, the energy values and the electric dipole oscillator strengths are given. Such data have been taken from (94) and extended with impact parameter data for transitions between higher levels, as for the other Li-like ions. Again, some modifications have been done to correct the data accorging to the (96) approach. The data have been updated in CHIANTI v.6, including the calculations performed by (167). Collision strengths have been obtained using Coulomb-Born-Exchange method for inner-shell excitation from levels of the $1s^2 2s$ and $1s^2 2p$ configurations to all fine-structure levels of the $1s2l2l'$ configurations. However, transitions which involve configurations above $1s^2 2p$ have been omitted. This entails the need to merge the CHIANTI data with the (94) or the Cowan calculations. Recommended data have been listed in table 5.24.

| *Ion* | $Si^{+11}$ |
|---|---|
| *Energy levels* | NIST<br>(94)<br>(167) |
| *A-value* | NIST |
| $\Upsilon$*-value* | (94)<br>(167) |

Table 5.24: Recommended data for $Si^{+11}$.

Only the baseline PWB *ic* and *ls* calculations are present in the ADAS database for $Si^{+12}$. Collision strengths using a Coulomb-Born-Exchange method have been computed by (168). They included in their ion model 49 fine-structure energy levels and calculated intermediate-coupling collision strengths for transitions of the kind $1s2p\ ^{2S+1}P_j - 1snl'\ ^{2S'+1}L'_{j'}$, with $n = 3, 4, 5$ and $l' \geq 1$ (i.e. $p, d, f, g$). This work has been improved by (169), who considered all components $1s^2\ ^1S_0 - 1s2l'\ ^{2S'+1}L'_{j'}$ and $1s2l\ ^{2S+1}L_j - 1s2l'\ ^{2S'+1}L'_{j'}$ and concentrated on their resonance contribution. These data have been assembled within the CHIANTI v.6 database and used here. In addition, since only the transitions among the first 6 levels and among them and the other 43 higher levels have been included, new Cowan calculations have been performed to fill the gap. Table 5.25 illustrates the suggested data sources for $Si^{+12}$.

For $Si^{+13}$ ion, apart from Cowan calculations, both in *ic* and *ls* resolution, the ADAS database contains data from (170). They are scaled hydrogenic collision strengths, obtained following the Coulomb-Born-Oppenheimer method

| *Ion* | $Si^{+12}$ |
|---|---|
| *Energy levels* | NIST (168) |
| *A-value* | NIST (168) Cowan |
| $\Upsilon$-*value* | (169) (168) Cowan |

Table 5.25: Recommended data for $Si^{+12}$.

for all transitions of the type $nl - n'l'$ with $n' \geq 5$. More recent calculation can be found in the CHIANTI v.6 database, where collision strengths have been taken from (171) and the fine structure is derived assuming distribution according to statistical weights. These data have been computed in *ls* coupling scheme using R-matrix approach. However, since transitions which involve the first two configurations ($1s$ and $2s$) only have been included, CHIANTI data have been merged with the (170) calculations to give a more complete set of values (tab. 5.26).

| *Ion* | $Si^{+13}$ |
|---|---|
| *Energy levels* | NIST |
| *A-value* | NIST (172) |
| $\Upsilon$-*value* | (171) (170) |

Table 5.26: Recommended data for $Si^{+13}$.

The revised *adf04* for all silicon ions are provided in *ic* resolution. The need of these J-resolved datasets is motivated by the available spectral resolution of the instruments involved in the present analysis. As seen in Tab. 4.1, the spectral resolutions of SUMER, CDS and EIS are in the range of 0.02-0.14 Å depending of the wavelength. Therefore, these spectrometers actually see J-resolved subcomponents of emission lines and may require appropriate data for analysis. However, *ic* resolution of all transitions does not necessarily imply the need for a full *ic* treatment of ionisation balance. As discussed in section 5.1.1, *ls* resolution is required for silicon ionisation calculations. Therefore, the *adf04* data files obtained above have been processed using the ADAS209 routine. This program allows conversion of the *adf04* to a smaller file by bundling together J-resolved levels of the same term. Hence, in this case the *ls* resolution is derived from the *ic* resolution according to the following prescription for the "bundled" energy levels, "bundled" A-values and the "bundled" effective collision strengths respectively:

$$\mathbf{E}_{J\to I} = \frac{\sum_{i\in I}\sum_{j\in J}\omega_j E_{j\to i}}{\sum_{j\in J}\omega_j} \tag{5.41}$$

$$\mathbf{A}_{J\to I} = \frac{\sum_{i\in I}\sum_{j\in J}\omega_j A_{j\to i}}{\sum_{j\in J}\omega_j} \tag{5.42}$$

$$\mathbf{\Upsilon}_{IJ} = \sum_{i\in I}\sum_{j\in J}\Upsilon_{ij} \tag{5.43}$$

where the index $I$ and $J$ refer to a transition in *ls* coupling and $\omega_i$, $\omega_j$ are again the statistical weights.

### 5.3.3 Step 3 - specific ion file supplementation with s- and r-lines

The third step is to add the ionisation and recombination data lines to the *adf04* data files. The input data are the *adf04*, the resolved *adf07* as produced in sec. 5.3.1, and the *adf09*, which includes the dielectronic processes. This step is concerned with the state selective low level data for *adf04* file. Regarding the DR part, there are substantial contributions via highly excited levels, as will be described in sec. 5.3.4. These contributions will be handled by the ADAS204 routine.

The *adf04* and resolved *adf07* files have been illustrated in figures 5.1 and 5.13. An example of *adf09* is shown in fig. 5.19. The *adf09* data file archives state selective dielectronic recombination coefficients in *ls* and *ic* resolution.

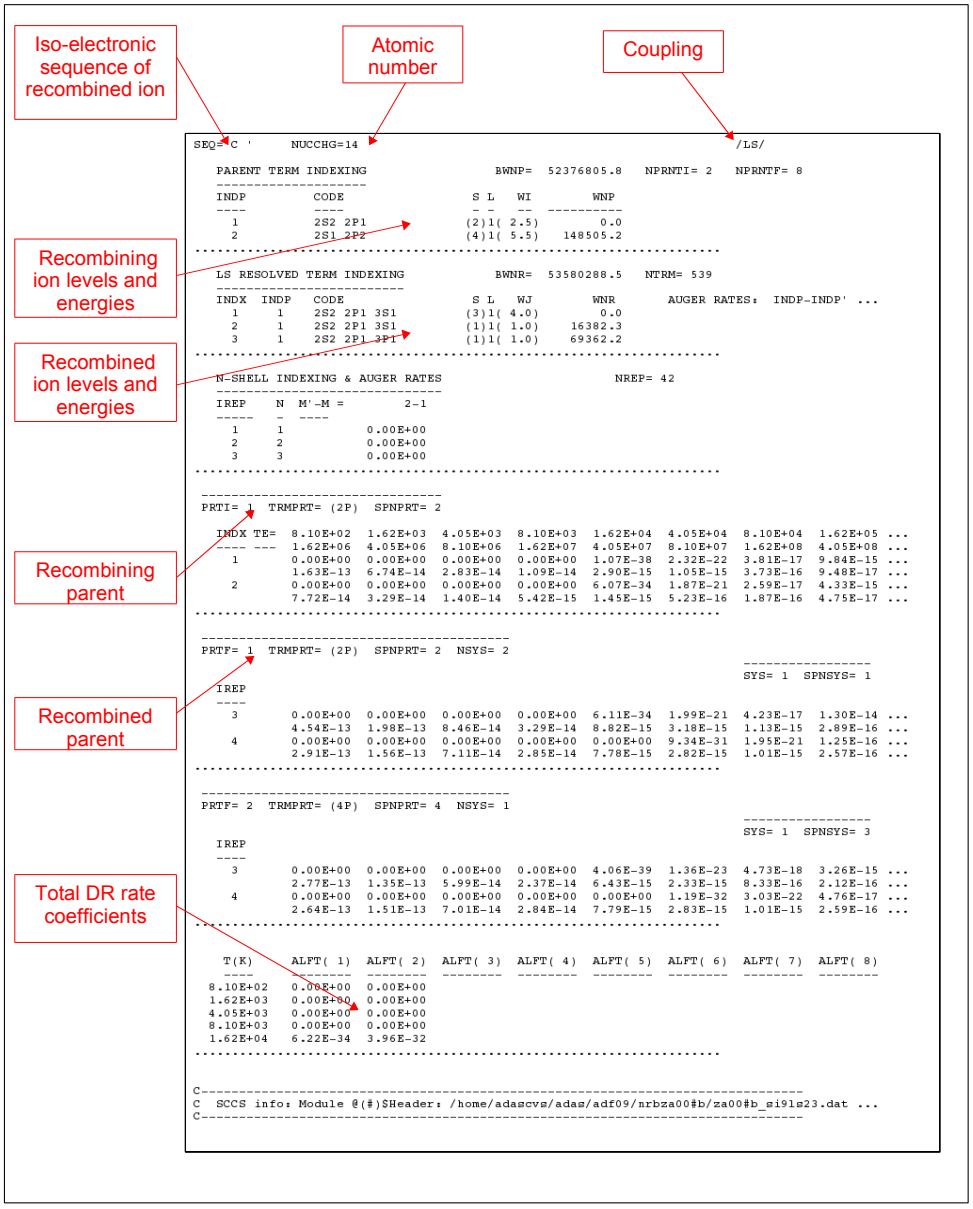


Figure 5.19: Example of *adf09* data file for the recombining ion $Si^{+9}$. This dataset includes high precision dielectronic recombination data, which have been produced using the multi-electron, multi-configuration structure and radiative transition code AUTOSTRUCTURE (10). The initial (recombining) and final (recombined) parents are specified as well as the $n$-shell indexing and Auger rates and the resolved DR coefficients as a function of electron temperature. A final sum of all contributions are given for each initial parent. The dataset is in *ls* resolution and refers to parent $n = 2 - 3$ transition type.

For the present purpose the *ls* coupling has been used. The data are resolved by initial and final parent metastable and includes captures to *ls* or *ic* resolved low levels, *nl*- and $n$-shells to very high $n$. Each dataset is distinguished according the recombining ion iso-electronic sequence, element, coupling and parent principal quantum shell, for example $n = 2 \rightarrow n = 3$ transition group "23" (e.g. for the file "za00#b_si9ls23.dat", shown in fig. 5.19, "b" is the recombining iso-electronic sequence, "si" is the elements, "ls" is the coupling and "23" is $n = 2 \rightarrow n = 3$ transition group). The *adf09* data files used for the present work are those obtained by AUTOSTRUCTURE code calculations of (10) (and references therein), as implemented within ADAS through the ADAS701 routine. Such

files include high precision dielectronic recombination data for iso-electronic sequences up to Mg-like. For Al-like sequence, dielectronic recombination data produced using an extension of the Burgess General Formula (173), called Burgess-Bethe General Program (BBGP) has been employed. A comparison between the two methods is provided by (10), showing a good convergence of BBGP to AUTOSTRUCTURE. The consistency between these two approaches justifies the use of BBGP to complete the set of DR data needed for this thesis.

The three input files above discussed (*adf04*, *adf07* and *adf09*) are handled by the ADAS807 routine, as illustrate schematically in figure 5.20. This program gives the ionisation coefficients as a function of electron temperature,

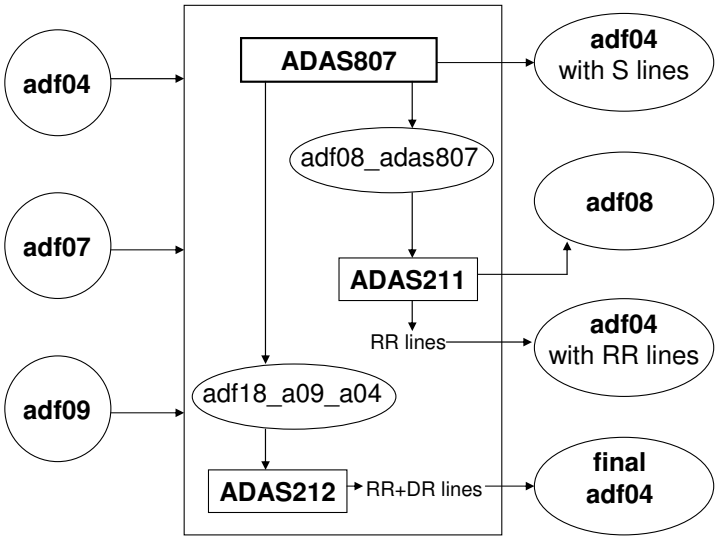


Figure 5.20: Scheme of step 3, showing a program flow for supplementing the *adf04* data files with ionisation and recombination contributions. The routines are represented by rectangles, whilst the datasets are specified by circles or ellipses.

specified as S lines, to add to the target *adf04*. Moreover, it prepares the set of template and driver files which are required for a complete GCR modelling, using the ADAS211 and ADAS212 codes. ADAS211 produces the radiative recombination data, called RR lines, which are used to supplement the target *adf04* file. State selective radiative recombination coefficients to *ls*-coupled terms are calculated using a one-electron Slater type model potential adjusted to observed energies (see (80) for detail). In addition, the program provides a further output, in the *adf08* format, which includes the energy level lists, the requested temperature values and the line coefficients. This file is suitable for archiving. ADAS807 prepares also cross-reference files to the bundled-*nl* and bundled-*n* data which are required for the very high level population calculations and evaluation of the projection matrices by ADAS204 (step 4). The final R lines are given by ADAS212, adding the dielectronic recombination contribution (as specified by the selected *adf09*s) to the RR lines.

### 5.3.4 Step 4 - projection data

Although the exclusion of collisional-radiative effects has been often justified for solar coronal density by suggesting that zero density calculations only are necessary, in reality this is not so (sec. 5.1). At finite density, in fact, the effective contributions to the evolution of the dominant populations include not only direct transitions to the dominant states, but also transitions via indirect pathways. Examples are stepwise excitation which leads to ionisation via highly excited states and recombination into highly excited states followed by recombination cascade. Dielectronic recombination particularly is strongly mediated by highly excited states, yet the low level character of the recombining system, including its metastables cannot be ignored. Differential Auger behaviour markedly distinguishes different metastables in recombination. High levels, but within a GCR framework, are essential. The vulnerability of dielectronic recombination to secondary collisions causing redistribution before stabilisation and causing re-ionisation from

highly excited states after stabilisation is well known. Dielectronic recombination occurs when an incident electron excites an electron in a target parent ion while simultaneously losing sufficient energy to be captured into a bound state *nl* with large *n* and *l*. As a consequence, dielectronic recombination is efficient in populating very excited states. This implies that detailed calculation for those highly excited states is required for a proper theoretical treatment of dielectronic recombination. However, at the same time, the main interest in the context of this thesis is in transitions involving low lying states (including metastables), so that it is important to focus attention on the transitions in question but attempting to maintain the effect of highly excited states. Step 4 approaches this issue by providing the condensed influence on the low *n*-shells as projection matrices in the *adf17* format. The condensation and projection method used for light elements has been fully described by (11) and mentioned in section 5.1.1. A schematic view is shown in figure 5.21.

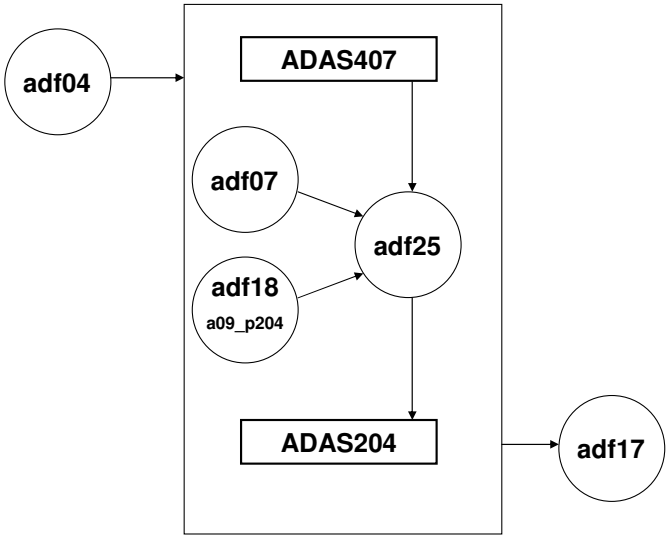


Figure 5.21: Scheme of step 4, illustrating a program flow for projection data calculations. Note that the *adf25* driver file, required for bundle-*nS* calculations through ADAS204, is linked to the *adf07* built up in step 1 (sec. 5.3.1) and the *adf18/a09_p208* driver produced by ADAS807 in step 2 (sec. 5.3.2). Again, the programs are shown as rectangles and the data files as circles.

Firstly, ADAS407 produces the driver files in the *adf25* format for ADAS204 bundle-*n* population calculation. Then, the *adf25* drivers are edited to access to zero density metastable resolved ionisation rate coefficients data, collected in the *adf07* format and to recombination rate coefficients through the cross-referencing file *adf18*. The routine ADAS204 is designed to deal with very many *n*-shells in order to guarantee a correct and consistent treatment of dielectronic recombination and the effect of finite plasma density on it. The bundle-*n* approach is justified by the fact that collisional processes fully mix sub-levels of the same principal quantum shell (because of their virtual degeneracy), so that the highly excited level populations may be considered for whole principal quantum shells. However, the program does not handle low level individual line emission and power with sufficient accuracy for spectroscopy. The solution generates a condensed projection matrix, which can be expanded using statistical weight factors over the resolved low level group separated into terms and combined with the detailed direct couplings, using the high precision low level population code ADAS208 (step 5).

Particular attention has to be given to the cross-referencing file *adf18/a09_p204*. It provides a parent cross-reference list for the dielectronic recombination *adf09* data files, which take into account the relevant Auger rates for transitions allowed by *ls*-coupling selection rules. However, Auger break-up can occur from *n*-shells built up on a parent metastable to another metastable via a different spin system. These supplementary *ls*-breakdown autoionisation rates are also provided by the *adf18/a09_p204* driver. They are obtained from an intermediate coupling AUTOSTRUCTURE run using ADAS701 and by extracting the required Auger transition probabilities using the ADAS704 post-processor.

### 5.3.5 Step 5 - fractional abundances

The final step, as shown schematically by figure 5.22, provides the generalised collisional-radiative (or collisional-dielectronic) coefficients for ionisation and recombination, as defined by equations 5.15. The projection matrices produced in the previous step are picked up, through the cross-reference driver files *adf18/a17_p208*, by the ADAS208 routine. This code is based on the low-level resolved population model, which draws its key data from the fundamental energy levels and rate coefficients collected in the fully configured *adf04* (which has been prepared by the step 3, sec. 5.3.3) and supplements these with projection data (which has been prepared by the step 4, sec. 5.3.4). Three-body recombination is included consistently as the inverse process to ionisation in the population equations, together with the radiative and dielectronic recombinations, already discussed. The primary GCR output from ADAS208 provides the evaluation of the population structure at an extended set of $z$-scaled electron temperatures and densities[2] suitable for interpolation along the iso-electronic sequences. Such initial tabulation of GCR coefficients is handled by the ADAS403 routine, which supplies the full iso-electronic datasets in the *adf10* format. The subsequent conversion to iso-nuclear collections for a specific element, silicon in this case, is done by the ADAS404 program. The iso-electronic

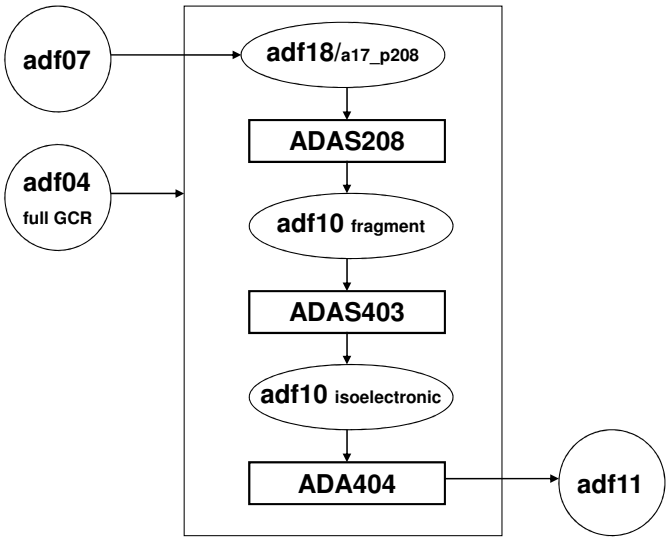


Figure 5.22: Scheme of step 5, showing the final program flow for the GCR rate coefficient production in the *adf11* ADAS data format. The *adf07* (step 1) and the full GCR *adf04* (step 2) data files are combined together with the projection data provided by the *adf17* data file (step 3). The projection data are supplied by the means of the *adf18/a17_p208* driver file. As for the previous schemes, the programs are represented by rectangles while the datasets by circles or ellipses.

master files *adf10* for silicon contain the generalised metastable resolved collisional-radiative coefficients, which are handled by ADAS404 to provide both stage to stage (called *Standard*) and metastable to metastable (called *Partial*) forms in the *adf11* output datasets. These files collect the final data needed for the ionisation balance calculation at equilibrium, that is when $dN_\sigma^{+z}/dt = 0$. Once defined the GCR coefficients by equations 5.14, 5.15 and 5.16, the fractional abundances, $N_\sigma^{+z}/N^{tot}$, are derived solving the following equation:

$$\begin{aligned}\frac{dN_\sigma^{+z}}{dt} &= N_{\mu'}^{(+z-1)} N_e S_{\mu'\to\sigma}^{cd,(+z-1)\to+z} + N_{\nu'}^{(+z+1)} N_e A_{\nu'\to\sigma}^{cd,(+z+1)\to+z} \\ &+ N_\sigma^{+z}\left(N_e Q_{\tau\to\sigma}^{cd,+z\to+z} + N_e X_{\tau\to\sigma}^{cd,+z\to+z}\right) \\ &- N_\sigma^{+z}\left(N_e S_{\sigma\to\nu'}^{cd,+z\to(+z+1)} + N_e A_{\sigma\to\mu'}^{cd,+z\to(+z+1)}\right) \\ &+ N_\sigma^{+z}\left(N_e Q_{\sigma\to\tau}^{cd,+z\to+z} + N_e X_{\sigma\to\tau}^{cd,+z\to+z}\right) = 0\end{aligned} \tag{5.44}$$

[2]Scaled (or reduced) temperatures and densities of the form $\theta_e \propto T_e/z_1^2$ and $\rho_e \propto N_e/z_1^7$, with $z_1 = z + 1$, are introduced to make the calculation suitable for interpolation within an iso-electronic sequence.

which describes the population evolution of each metastable $\sigma$ of each ionisation stage $+z$. As before, the symbols $\mu'$ and $\nu'$ index the metastables of the $(+z-1)$th and $(+z+1)$th ionisation stages respectively, while $\sigma$ and $\tau$, with $\sigma \neq \tau$, are the metastables of the $z$th ionisation stage. Again, summation over repeated indices is adopted.

## 5.4 Comparison of data sources, methods and data precision

The data for fractional abundances used in solar physics and in astrophysics have gone through numerous updates over the years as more precise atomic data have become available from theoretical calculations or laboratory measurements. As thoroughly illustrated in previous sections, reliable DEM estimate requires accurate fractional abundances for all the ionisation stages of the elements observed in the plasma. In turn, fractional abundance calculations need comprehensive knowledge of the rate coefficients for all the relevant ionisation and recombination processes. The most longstanding reliable analysis of fractional abundances was performed by (134) and (135) (for iron). In their ionisation balance calculations, as well as in the subsequent work of (174) and the most recent papers of (175; 176), ionisation is a result of electron impact ionisation with the additional contribution of excitation-autoionisation processes. Recombination is due to radiative recombination (RR) and dielectronic recombination (DR). Also, the zero density assumption is made. However, it has been pointed out that, although it is common to assume that the observed solar upper atmosphere plasma is optically thin, low-density and in steady or quasi-steady state, the effects of finite density and population redistribution cannot be ignored. Furthermore, three-body collisions may become important when higher density regions are approached, that is when the observations are extended in order to include lines formed in the upper chromosphere.

Considering the ionisation contribution, there have been recent attempts to improve the state of the electron impact ionisation rate coefficients, due to the development of new atomic codes (such as the Flexible Atomic Code, FAC), to enable calculations of ionisation cross sections, as well as new experimental measurements. (177) gave an update of the ionisation data proposed in the previous review papers of (174) and (178). Their work provides electron impact ionisation cross sections for all elements from hydrogen to germanium, but they did not take into account all ionisation stages of every elements. The most complete study is that of (144), who produced recommended ground level ionisation cross sections and rate coefficients for all ionisation stages of the elements from hydrogen through zinc. He combined the analysis of measurements of ionisation cross sections with theoretical calculations, which have been performed using FAC. Scaling laws, such as those developed by (179) for collisional excitation, have been used to facilitate his analysis. Here, the electron impact ionisation rates for the silicon ions, obtained by the CADW approximation as described in the subsection 5.3.1 for ionisation from ground states, are compared with the (144) ionisation rates. Table 5.27 gives an average estimate in percentage of how much the ionisation rates for each ion calculated by the CADW approach move away from the (144) calculations. As expected, the largest discrepancy between the two

| Ion | Difference | Ion | Difference |
|---|---|---|---|
| $Si^{+0}$ | 78.8% | $Si^{+7}$ | 23.9% |
| $Si^{+1}$ | 10.3% | $Si^{+8}$ | 12.3% |
| $Si^{+2}$ | 28.9% | $Si^{+9}$ | 4.5% |
| $Si^{+3}$ | 19.6% | $Si^{+10}$ | 6.6% |
| $Si^{+4}$ | 33.3% | $Si^{+11}$ | 5.6% |
| $Si^{+5}$ | 6.6% | $Si^{+12}$ | 6.0% |
| $Si^{+6}$ | 22.6% | $Si^{+13}$ | 6.7% |

Table 5.27: Averaged difference in percentage between the electron impact ionisation rates from ground states obtained by CADW and (144) calulations. For each ion, the averaged difference has been estimated within the temperature ranges shown in figures. 5.23 and 5.24.

ionisation rates is found for the neutral silicon, while for the other ions the differences in their ratio do not exceed about 30%. The ionisation rate coefficients for all silicon ions developed here through the CADW approach (red lines) are plotted as function of temperature together with the rates from (144) (black lines) in figures 5.23 and 5.24. Also the ratios between them are plotted. The temperature ranges for each ion have been selected by taking into account their temperature of formation.

Regarding the contribution due to the recombination, the most recent RR and DR coefficients have been calulated by

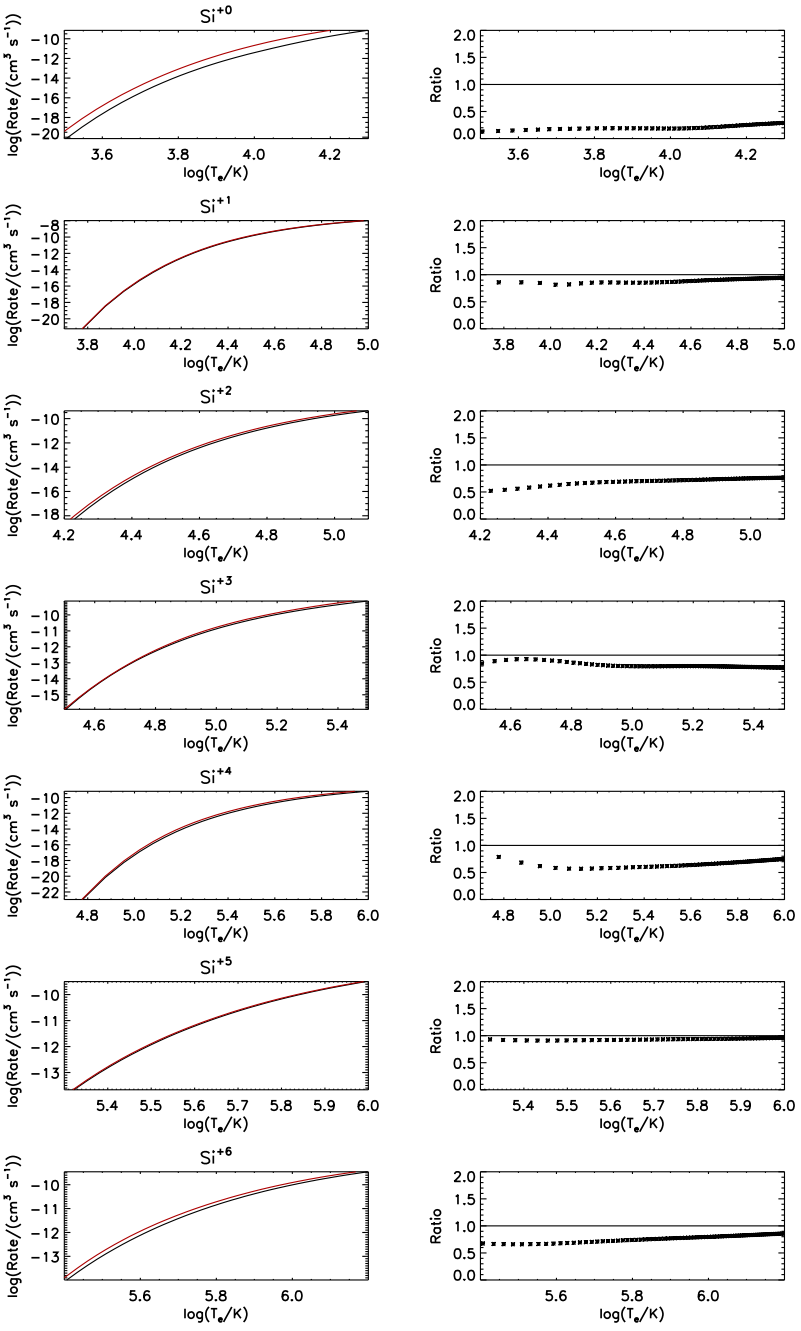


Figure 5.23: Comparison between ionisation rate coefficients for silicon ions from $Si^{+0}$ to $Si^{+6}$. The plots on the left show the ionisation rates calculated by CADW with the red lines, while the ionisation rates from (144) are indicated by the black lines. The plots on the right show the ratio between the (144) and CADW rates with respect to unity (solid line).

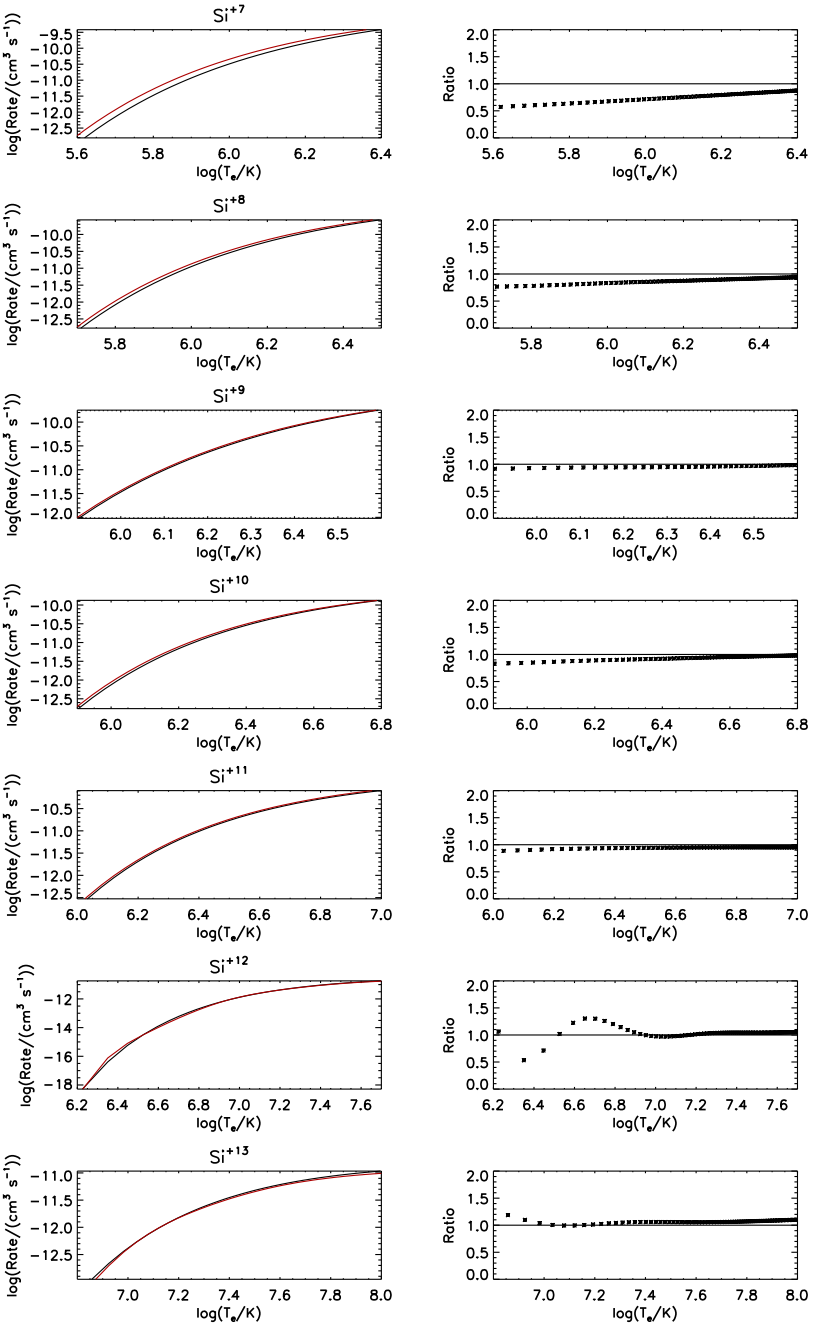


Figure 5.24: Comparison between ionisation rate coefficients for silicon ions from $Si^{+7}$ to $Si^{+13}$ as for figure 5.23.

(85) and (180; 181; 182), using the relativistic FAC and the semirelativistic AUTOSTRUCTURE code respectively, for H-like through Mg-like isolectronic sequences of all elements from hydrogen up to zinc. A review and comparison between them and with the recombination rate coefficients recommended by (174) has been extensively done by (175). In the context of this work, the new fully GCR recombination coefficients are compared with the summed RR+DR data of Badnell in the zero density approximation for five key ions, $Si^{+1}$, $Si^{+6}$, $Si^{+9}$, $Si^{+10}$ and $Si^{+11}$. The comparison has been done including a large range of temperature from $10^3$ K to $10^8$ K for all silicon ions. However, it is important to concentrate on the temperature region where the fractional abundances assume significant values, which is called the ionisation equilibrium formation zone. Following the definition of (175), such a region covers the temperature range where the fractional abundance of an ion is greater than 0.01 and so where the specific ion is most likely to be formed. Table 5.28 shows that an agreement within 30% is found for the recombined ions $Si^{+6}$, $Si^{+10}$ and $Si^{+11}$. The agreement is significantly poorer for the other two recombined ions, $Si^{+1}$ and $Si^{+9}$. The deviation

| Ion | Difference |
|---|---|
| $Si^{+2} \rightarrow Si^{+1}$ | 110.7% |
| $Si^{+7} \rightarrow Si^{+6}$ | 28.0% |
| $Si^{+10} \rightarrow Si^{+9}$ | 66.6% |
| $Si^{+11} \rightarrow Si^{+10}$ | 28.7% |
| $Si^{+12} \rightarrow Si^{+11}$ | 26.0% |

Table 5.28: Averaged difference in percentage between the total GCR recombination rate coefficients close to zero density and the RR+DR Badnell calculations.

in percentage in tab. 5.28 is referred to an average estimate along the whole range of temperature ($10^3$ K-$10^8$ K). Considering the ionisation equilibrium formation zone only, an agreement around 30% in found for $Si^{+9}$ too. A more detailed comparison is illustrated in the plots in figure 5.25. The GCR recombination rate coefficients are plotted as a function of electron temperature at three different densities (red lines) together with the summed RR+DR zero density coefficients of Badnell (black lines). The three density values are chosen in order to illustrate the effects of the finite density on the recombination rate coefficients. As said, the *adf10* master files collect the GCR coefficients as a function of reduced densities, as well as reduced temperatures. This implies that the lowest and highest densities, which have been chosen here, depend on the considered ionisation stage. An intermediate density, $N_e = 10^{10}$ cm$^{-3}$, has been chosen, because it reflects the solar plasma conditions of the observed regions selected for this thesis. Additionally, the ratios between recombination coefficients from Badnell and from GCR calculations close to the zero density limit are plotted in fig. 5.25. Approaching zero density, recombination is due primarily to DR and RR. At the temperature of the peak of fractional abundances, DR dominates over RR for most ions. At lower temperature, RR dominates over DR. Increasing the density (dotted red lines), the three body recombination contribution increases significantly leading to a large deviation from the Badnell rate coefficients. The biggest discrepancy in the recombination coefficients of $Si^{+1}$ is essentially due to the finite density effects. In fact, as shown in the first plot of fig. 5.25, the GCR recombination coefficients for this low ionisation stage, as well as for $Si^{+2}$ and $Si^{+3}$, depends drastically on density. This will affect the fractional abundance calculations in a finite density regime, even at the low coronal densities ($10^8$-$10^{10}$ cm$^{-3}$). This explains the need of a full GCR approach in the fractional abundance calculation in order to provide a consistent DEM analysis.

Finally, figure 5.26 shows the silicon fractional abundances calculated here compared to those of (176). These authors incorporated into their collection the ionisation rates of (144) and the RR+DR recombination rates of (183) up to Mg-like and those recommended by (174) for the two remaining ions. Moreover, they worked in the coronal approximation where each ionisation stage is represented by its ground population only (that is by assuming equals to zero the metastable populations). Also, they neclected the effects of three-body processes and electron density. The main differences can be attributed to the effect of the finite density (even if it is as low as $10^8$ cm$^{-3}$). The density effects affect especially the fractional abundances of the low ionisation stages up to $Si^{+3}$, leading to a shift of their peaks towards lower temperature values, as shown in tab. 5.29. The differences in the GCR fractional abundances relative to those of (176) are less than 15% at their peaks for $Si^{+4}$ up to $Si^{+13}$. For the first three silicon ions, peak abundance differences up to 84% are found.

In conclusion, the present results for silicon fractional abundances represent a significant improvement over both the past calculations (such as those of (174)) and the most recent calculations of (176). This impacts directly on the analysis of the plasma conditions inferred from the spectral observations employed for this thesis. The final results, which will be obtained using the DEM diagnostics method (chapter 6), will take the advantage of such a consistent

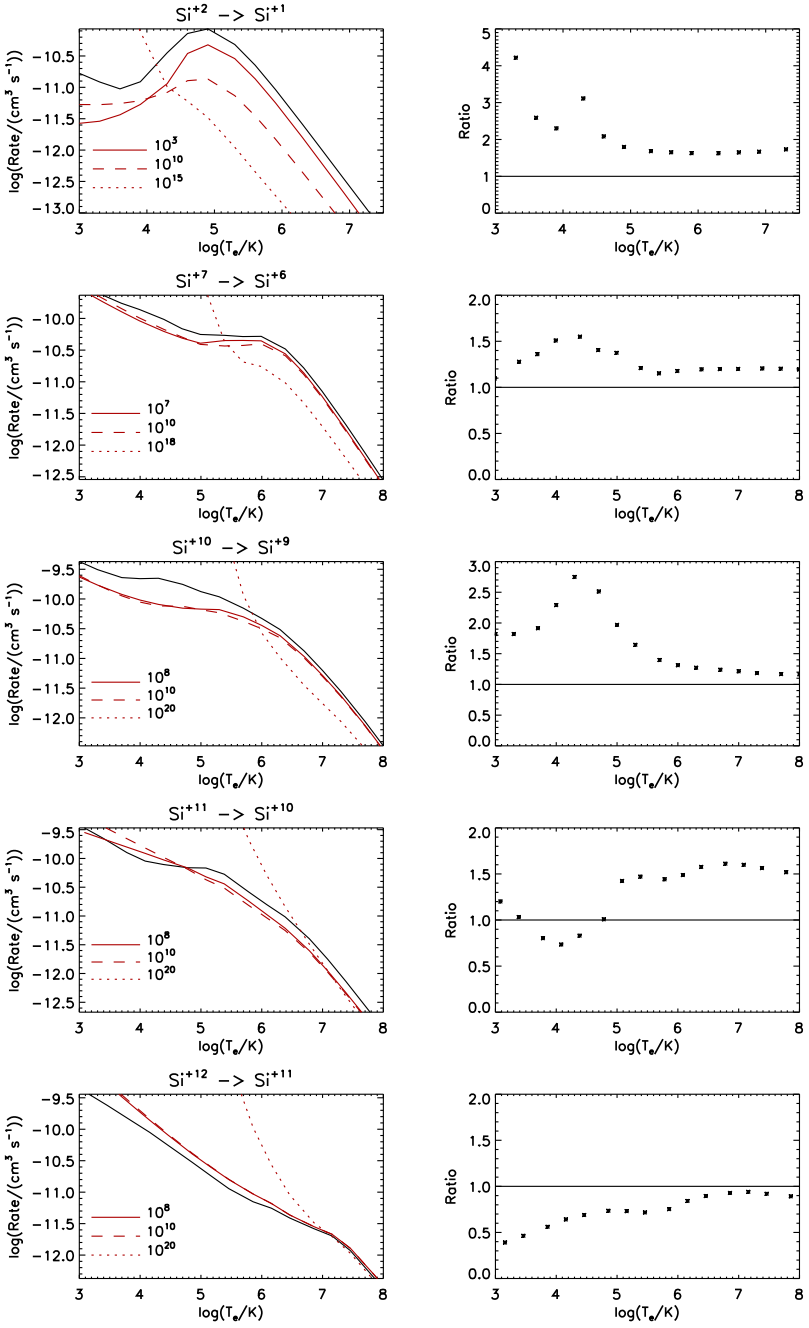


Figure 5.25: Comparison between recombination rate coefficientsfor the five key ions $Si^{+1}$, $Si^{+6}$, $Si^{+9}$, $Si^{+10}$ and $Si^{+11}$. The plots on the left show the full GCR recombination rates at three different densities (in $cm^{-3}$) with solid, dashed and dotted red lines, while the zero density summer RR+DR rate coefficients from Badnell are indicated by the black lines. The plots on the right show the ratios between recombination coefficients from Badnell and from GCR calculations using the lowest plotted density (solid red lines).

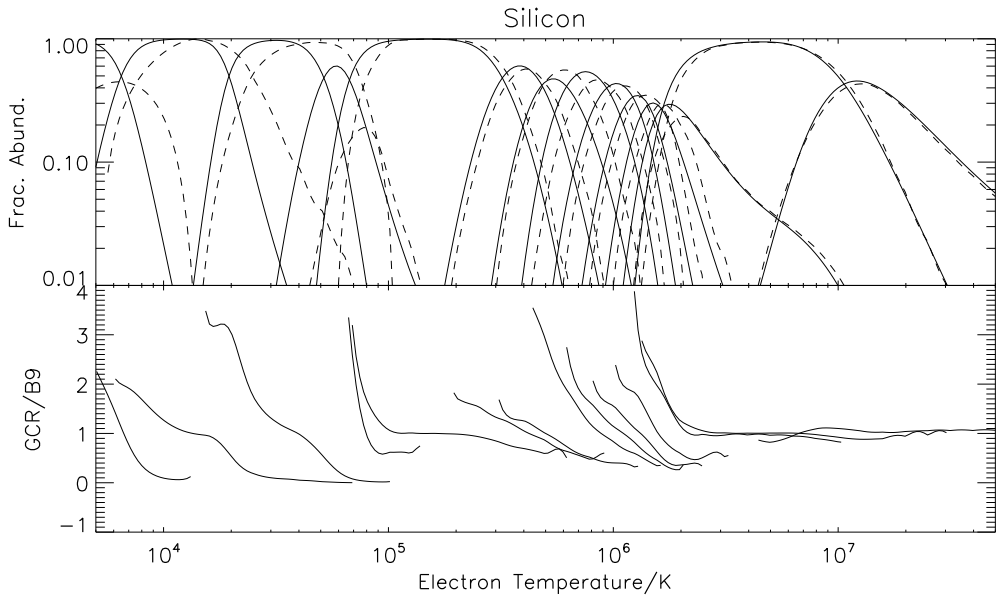


Figure 5.26: Fractional abundances versus electron temperature for all silicon ions. The upper plot shows the full GCR results approaching zero density ($N_e = 10^8$ cm$^{-8}$), represented by the solid curves and labeled GCR, and the (176) zero density results, represented by the dashed curves and labeled B9. The lower plot shows the ratios between them.

| Ion | log($T_e$) (GCR) | log($T_e$) (B9) | Diff./dex | Diff. |
|---|---|---|---|---|
| $Si^{+0}$ | 3.00 | 3.80 | 0.80 | 84.2% |
| $Si^{+1}$ | 4.09 | 4.15 | 0.07 | 14.3% |
| $Si^{+2}$ | 4.51 | 4.67 | 0.17 | 32.0% |
| $Si^{+3}$ | 4.77 | 4.89 | 0.12 | 23.6% |
| $Si^{+4}$ | 5.17 | 5.17 | 0.00 | 0.0% |
| $Si^{+5}$ | 5.59 | 5.61 | 0.02 | 3.8% |
| $Si^{+6}$ | 5.73 | 5.78 | 0.05 | 10.9% |
| $Si^{+7}$ | 5.88 | 5.93 | 0.05 | 10.9% |
| $Si^{+8}$ | 6.01 | 6.04 | 0.03 | 7.4% |
| $Si^{+9}$ | 6.11 | 6.14 | 0.03 | 7.4% |
| $Si^{+10}$ | 6.18 | 6.21 | 0.03 | 7.4% |
| $Si^{+11}$ | 6.24 | 6.31 | 0.07 | 14.3% |
| $Si^{+12}$ | 6.66 | 6.66 | 0.00 | 0.0% |
| $Si^{+13}$ | 7.08 | 7.11 | 0.03 | 7.4% |

Table 5.29: List of fractional abundance peak temperatures (in Kelvin) for the GCR calculations and those of (176) (B9). Also, for each silicon ion the differences in peak temperature both in dex and in percentage are shown.

and accurate approach for the GCR coefficient calculations, as described through the previous sections of this chapter.

# Chapter 6

# Revised integrated analysis

## 6.1 Differential emission measure

The derivation of the emission measure from spectra of the solar upper atmosphere is a first step in extracting physical quantities from observations and hence in understanding the morphology of these higher layers of the solar atmosphere. A further refinement is to determine the Differential Emission Measure (DEM), which describes the temperature and density structure of the solar atmosphere plasma and allows the reconstruction of the observed emission in terms of theory. It is derived from the inversion of the equation:

$$I_{j\to i} = \frac{1}{4\pi A}\int A(Z)G_{j\to i}(T_e, N_e)N_e^2 dV \tag{6.1}$$

obtained from equations 5.7 and 5.9 in chapter 5. The contribution function $G(T_e, N_e)$ has been already introduced in chapter 5 and specified by eq. 5.29, which take into account the structure of the atomic population of excited states through the *PEC*s and the fractional abundances calculated in equilibrium through the terms $N_\sigma^{+z}/N^{tot}$ and $N_{\nu'}^{+z+1}/N^{tot}$. Also, in solar physics, the abundance of hydrogen relative to electrons $N_H/N_e$ is often incorporated in the definition of the $G(T_e, N_e)$. It has been done in equation 6.1. Moreover, only a contribution due to excitation, described by $PEC_{\sigma,j\to i}^{[z](exc)}$ is usually considered, because the contribution due to the recombination is negligible for most of the ions in the solar upper atmosphere conditions. The measure of the amount of plasma at temperature $T_e$ and density $N_e$ is described by the quantity $N_e^2 dV$ in equation 6.1, the so-called *Differential Emission Measure* to which this chapter is mainly addressed. In principle, for a set of lines whose intensities $I$ have been observed and whose contribution functions $G(T_e, N_e)$ are known, it is possible to derive the DEM. However, there are three main sources of uncertainties involved in the inversion. The first source is the inversion process itself, which requires some assumptions about the nature of the solution, as reviewed thoroughly by (184), (185), (186) and references therein. The second source is related to the errors in the measured intensities, as described in chapter 4. Finally, the third source concerns the atomic physics underlying the calculation of the contribution functions. Firstly, the $G(T_e, N_e)$s are strongly peaked functions in temperature and weakly dependent on density, so the inverse problem is very poorly conditioned in the density dimension. Secondly, it is important to take into account the accuracy of the atomic data employed in the calculation of the *PEC* and the fractional abundances, as discussed in sections 5.2-5.4.

For the present analysis, it is convenient to transform the volume integral 6.1 to an integral over a corresponding temperature domain. Following the treatment of (184), the variable $dV$ is written as:

$$dV = |\bigtriangledown T|^{-1} dS_T dT \tag{6.2}$$

where $dS_T$ is an element of surface of constant temperature in some region. The volume increment enclosing material in the range $T$ to $T + dT$ associated with this surface is then:

$$dV_l = \left(\int_{S_T} |\bigtriangledown T|^{-1} dS\right)_l dT \tag{6.3}$$

where $l$ indicates each of the $N$ surfaces of constant $T$. Hence, the total volume of material between $T$ and $T + dT$ is

$$dV = \sum_{l=1}^{N} \left( \int_{S_T} | \bigtriangledown T|^{-1} dS \right)_l dT = \Psi(T) dT \tag{6.4}$$

where $\Psi(T) = \sum_{l=1}^{N} \left( \int_{S_T} | \bigtriangledown T|^{-1} dS \right)_l$. As a consequence, the equation 6.1 can be written in terms of $T$ as following:

$$I_{j \to i} = \frac{1}{4\pi A} \int_T A(Z) G_{j \to i}(T, N_e) \sum_{l=1}^{N} \left( \int_{S_T} N_e^2(V) | \bigtriangledown T|^{-1} dS \right)_l dT \tag{6.5}$$

The relation 6.5 allows the definition of the Differential Emission Measure in temperature, $\Phi(T)$, as:

$$\Phi(T) = \frac{1}{A} \sum_{l=1}^{N} \left( \int_{S_T} N_e^2(V) | \bigtriangledown T|^{-1} dS \right)_l \tag{6.6}$$

This definition implies that $\Phi(T)dT = \bar{N}_e^2(T)dV$, which is true when $\bar{N}_e^2(T)$ is interpreted as the mean square electron density over the $N$ surfaces at temperature $T$, weighted with respect to the inverse temperature gradients ($| \bigtriangledown T|^{-1}$) over these surfaces, that is:

$$\bar{N}_e^2(T) = \frac{\sum_{l=1}^{N} \left( \int_{S_T} N_e^2(V) | \bigtriangledown T|^{-1} dS \right)_l}{\sum_{l=1}^{N} \left( \int_{S_T} | \bigtriangledown T|^{-1} dS \right)_l} \tag{6.7}$$

Then, the intensity becomes:

$$I_{j \to i} = \frac{1}{4\pi} \int_{T_1}^{T_2} A(Z) G_{j \to i}(T, N_e) \Phi(T) dT \tag{6.8}$$

where the DEM, $\Phi(T)$, is the average value over the area covered by the spectrometers, while the limits $T_1$ and $T_2$ are the minimum and maximum electron temperatures in the part of the atmosphere which contribute to the spectrum. Regarding the $G(T_e, N_e)$ functions, they depend both on electron temperature and electron density, so some assumption about the relation between them must be done. Two assumptions are that the plasma electron density or pressure is constant over the relatively small range of temperature where the $G(T_e, N_e)$ assume significant values, that is the most probable region where the lines are formed. The constant pressure assumption implies a relation $N_e = N_e(T_e)$, so that $G = G(T_e, N_e(T_e))$ is effectively only function of $T_e$.

Summarising, in order to derive the DEM in temperature defined above, it is necessary to adopt a number of underlying assumptions (187):

1. the plasma should be optically thin to the radiation that can effect the level population of the ions which produce the observed lines;
2. statistical equilibrium has to be a good approximation (that is $dN_j/dt = 0$ for all $j$) (see chapter 5);
3. the distribution function of free electrons has to be Maxwellian, which allows the calculation of the GCR coefficients as used in this thesis;
4. emission sources of photons should be negligible except for those which come from the atomic transitions;
5. the plasma should be completely ionised, which allows use of the assuption of $N_H/N_e$=constant or use of the tabulated values of (188);
6. the elemental abundance does not change with the optical depth of the solar atmosphere, which justifies moving the term $A(Z)$ outside the integral, so that the intensity can be written as:

$$I_{j \to i} = \frac{A(Z)}{4\pi} \int_{T_1}^{T_2} G_{j \to i}(T, N_e) \Phi(T) dT \tag{6.9}$$

Despite doubts generated by the previous assumptions and limitations, the DEM method remains very powerful for providing the most information that can be learned about the structure of the solar atmosphere from the analysis of spectral intensities.

In the context of the helium problem, the main difficulty arises from the fact that the resonance lines of He I and He II are expected to be optically thick and, therefore, they are not usually included in the analysis of EUV line intensities from which models are made. As a consequence, it is important to focus on to what extent emission measure distribution can reproduce the observed flux of the EUV helium resonance lines, as observed by CDS and EIS. As support, the intercombination line of neutral helium observed by CDS at 591.41 Å can be used to examine the behaviour of helium line intensities without including opacity effects. In this environment, the form of equation 6.9 explains why such a study requires spatially and spectrally resolved observations in EUV range as well as sophisticated atomic modelling. This clarifies the need of the new joint observations described in chapter 4 and the revisit of atomic data to build up updated contribution functions (chapter 5).

The first approach in this analysis is to reconstruct the helium line intensities using the DEM as a diagnostic method to compare theoretical and observed intensities in the optically thin case. In order to achieve this purpose, an inversion technique is chosen, then electron density and pressure values are derived from observations and selected for this analysis. Finally, all these ingredients are put together to reconstruct the measured intensities of the lines included in the set of observations of the April 2009 campaign.

### 6.1.1 Review of different inversion techniques

Many mathematical procedures have been developed to deduce the DEM in temperature ($\Phi(T)$) by inverting systems of integral equations 6.9. However, the validity of most of the inversion methods is controversial and lots of problems are usually encountered in computing DEM models. From a mathematical point of view, the determination of DEM involves the inversion of a linear integral equation of the form:

$$g(x) = \int_a^b k(x,y) f(y) dy \tag{6.10}$$

where $a$ and $b$ are constants (the limits $T_1$ and $T_2$), $f(y)$ is termed the *source function* which is to be determined (the $\Phi(T)$), $g(x)$ the *data function* which is given (the $I$) and $k(x,y)$ is the *kernel* (the $G(T, N_e)$). The expression 6.10 is a Fredholm type integral equation of the first order, which is in general an ill-conditioned problem. This means that, as frequently happens, the solution may be not unique or may depend discontinuously on the data function (see (185) for details), producing instabilities in the deduced DEM. From a physical point of view, all the limitations have been already enumerated and discussed in the previous section.

A careful study of different integral inversion techniques to solve the DEM problem has been carried out by (189), who compared various methods using a known DEM distribution as a test case with specified values of contribution functions. Also, some more recent techniques have been listed and described by (190). The techniques most frequently used are an iterative procedure and a maximum entropy method. The first one is essentially based on a progressive iteration of a trial function (e.g. $\Phi_0(T)$) until the best agreement is reached between the observed and predicted line intensities. The second one is often needed to avoid non-unique and oscillatory solutions, by imposing the condition of the constancy of the quantity $S = \sum_i \Phi_i ln \Phi_i / w_i$, where $w_i$ is an appropriate weight and $S$ is called entropy of the function $\Phi_i$.

An iterative technique that starts from a mean value of $\Phi$ around the peak of $G(T)$ (assuming $N_e$ constant) has been developed by (191). Assuming $\Phi_i$ the initial estimate of $\Phi$, he obtained a new estimate for DEM of the form:

$$\Phi_{i+1}(T) = \Phi_i(T) \frac{\sum_l (I_l / I_{il}) W_l(T)}{\sum_l W_l(T)} \tag{6.11}$$

where $W_l(T)$ is a weighting function to ensure that the correction $I_l / I_{il}$ is applied most heavily to those values of $\Phi_i$ where the line is formed and is defined by:

$$W_l(T) = G_l(T) \Phi_i(T) \frac{\int_T G_l(T) \Phi_i(T) dT}{\int_T [G_l(T) \Phi_i(T)]^2 dT}. \tag{6.12}$$

This method was afterwards improved by (192) and tested by (193). Also, it was compared with the non-linear least squares procedure carried out by (194), to take into account the case of a model in which the number of temperature points is greater than the number of spectral lines (e.g. the number of equations) used. The main problem which arises from the (191) iterative technique is that it is very sensitive to errors in data. This implies that, in the presence of

errors, the method gives discontinuous DEM if it is not stopped after only a few iterations. An improvement of this procedure has been provided by (48). Their method is based on the observation that the dependence of contribution function on electron temperature and electron density is such that it is possible to express $G(T_e, N_e)$ as the product of a function $g(T)$, mainly due to the ionisation equilibrium, and a function $\omega(T, N_e)$, essentially determined by the population of the upper level from which the line is originated. Once defined the $\omega(T)$ correction function at a fixed density, they assumed that a trial $\Phi_0(T)$ is known and the true $\Phi(T)$ is given by

$$\Phi(T) = \omega(T)\Phi_0(T) \tag{6.13}$$

where

$$\omega(T) = \omega(T_0) + \left(\frac{\partial\omega}{\partial logT}\right)_{T_0}(logT - logT_0) \tag{6.14}$$

and

$$logT_0 = \frac{\int G(T)\Phi_0(T)logT\,dT}{\int G(T)\Phi_0(T)dT}. \tag{6.15}$$

Thus, the total observed intensity ca be expressed as

$$I = \frac{1}{4\pi}\omega(T_0)\int G(T)\Phi_0(T)dT \tag{6.16}$$

from which the correction $\omega(T_0)$ for each line can be computed and the first approximation of $\Phi(T)$ at $T = T_0$ evaluated. Then the procedure is repeated until the correction $\omega(T)$ reaches the unity within the uncertainties. The advantage of such method is that it gives a self-consistent definition of the temperature at which the corrections to an initial arbitrary DEM are applied. However, it requires an interpolation of the $\omega(T)$ values, which implies a smoothing of the corrections from those lines that provide $\omega(T_0)$ at similar values of $logT_0$ to avoid instabilities in the solution.

One of the main problems which was identified is how to specify the constraints on the method, whichever it is. In fact, it usually happens that the solution values are not "fine shaped", they may oscillate from one to the next and they may be not positive. Also, following the procedure of (195), more difficulty can arise from the choice of contribution functions that overlap. Their approach to the study of the equation 6.9 was to perform initially a discretisation of the variable interval ($T_1$, $T_2$,...,$T_n$). Then, they assumed that $\Phi(T)$ is constant (e.g. $\Phi(T) = \Phi_i$) within the interval $T_i - T_{i+1}$ and defined the *kernel* as

$$K_{si} = k\int G_s(T)dT \tag{6.17}$$

to get the intensity $I_s = \sum_i K_{si}\Phi_i$. Information on the $\Phi_i$ were obtained by inserting a trial set of values $\Phi_i$ in the sum and changing them until the evaluated intensities match the observed values $I_s$, within the errors $\sigma_s$. This procedure was carried out by minimising the quantity:

$$\chi^2 = \sum_s \frac{(I - Is)^2}{\sigma_s^2} \tag{6.18}$$

that means $d(\chi^2)/d\Phi_i = 0$ for every $i$, which can be put in matrix form as:

$$\mathbf{K}^T\mathbf{K}\mathbf{\Phi} = \mathbf{K}^T\mathbf{I}. \tag{6.19}$$

Therefore, if some $G_s(T)$ partially overlaps, some of the rows of the determinant which solves the system 6.19 have similar values and the determinant is near to zero. This entails that any small variation of the $I_s$ results in large changes in the solution. To avoid all the problems above discussed, (195) added some further condition using the entropy method. They found that such a method appears to be very efficient, because it doesn't put constraint on the shape of the DEM and gives always positive values of the solution. Furthermore, it allows the attainment of a good reproduction of the data from the fit to the DEM, with a reasonable $\chi^2$. However, the disadvantage of this method is that it is very sensitive to errors in atomic physics quantities affecting the *kernel* $K$. To address and overcome difficulties presented by uncertainties in atomic parameters, (196) developed a line ratio-like methodology to infer the DEM in temperature. He still used the maximum entropy approach to derive the solution $\Phi(T)$, but he introduced a revised $\chi^2$, which involve the observed and estimated line ratios, $R^l_{obs}$ and $R^l_{th}$ respectively. So, in this case, the inversion problem is addressed to solve a system of $N$ line pairs equations, with respective integrated intensities $I_i$ and $I_j$

$$R_{ij} = \frac{I_i}{I_j} = \frac{\int_T G_i(T)\Phi(T)dT}{\int_T G_j(T)\Phi(T)dT} \tag{6.20}$$

by seeking the form of $\Phi(T)$ which satisfy the least-square expression:

$$\chi^2 = \sum_{l=1}^{N} \left[ \frac{(R^l_{obs} - R^l_{th})^2}{(\sigma^2_{l_{obs}} + \sigma^2_{l_{th}})} \right] \sim 1 \tag{6.21}$$

including both the observed and theoretical errors $\sigma_{obs}$ and $\sigma_{th}$ for each ratio. He showed that their Ratio Inversion Technique (RIT) in not influenced seriously by large systematic errors in the atomic rate coefficients that could make the results of standard intensity inversions highly ambiguous. Another problem, which is likely to be encountered for the DEM curves derived from the solar atmosphere, is that the spectral inversion can involve data functions which span many decades in amplitude. Such a problem is often handled by means of regularising functions, including the maximum entropy. However, if the source function has a large dynamic range, the regularisation techniques tend to oversmooth the parts of it with large amplitudes and to undersmooth the parts of it with low amplitudes. In order to minimise this problem, (197) suggested a *data adaptive smoothing approach*, which as been implemented through the Glasgow code and automated within ADAS. In the context of this thesis, it is such technique that has been chosen as inversion method to derive the DEM and reconstruct the observed intensities. In addition to be fully automated, in fact, this method reduces the problem of uneven smoothing to more acceptable levels while still taking advantage of the use of the maximum entropy approach. The procedure will be summarised in the next section. Finally, for completeness, the Monte Carlo technique has to be mentioned. It has been developed by (198) to be applied to problems with a large set of unknown parameters, such as the abundances. Furthermore, this approach deals with the smoothing problem, reducing the common assumptions adopted by the other techniques (especially the iterative ones) by confining smoothing only to local scales which have the same order of the contribution function widths. However, although this method is suitable for situations where the number of parameters is large, in some cases convergence is slow.

### 6.1.2 The Glasgow code

In order to derive the differential emission measure, the integral equation 6.9 has to be solved for a set of $n$ lines. Considering the assumptions on the electron density and its relation with the electron temperature previously mentioned, the integral equation can be rewritten only in terms of $T$:

$$I_i = \frac{A(Z)}{4\pi} \int_{T_1}^{T_2} G_i(T)\Phi(T)dT \qquad i = 1, 2, ..., m \tag{6.22}$$

To obtain numerical solutions of such integral equations, it has to be reduced to a matrix form. Firstly the integral is discretised, using the product integration method of (199), so that from the form 6.22 the intensity becomes:

$$\begin{aligned} I_i &= \frac{A(Z)}{4\pi} \sum_{j=1}^{n} \int_{T_{j-1}}^{T_j} G_i(T)\Phi(T)dT \\ &= \frac{A(Z)}{4\pi} \sum_{j=1}^{n} \Phi^*_j \int_{T_{j-1}}^{T_j} G_i(T)\Phi_0(T)dT \end{aligned} \tag{6.23}$$

where $\Phi^*_j$ represents a weighted average of $\Phi(T)/\Phi_0(T)$ between $T_{j-1}$ and $T_j$, that is:

$$\Phi^*_j = \frac{\int_{T_{j-1}}^{T_j} G_i(T)\Phi(T)dT}{\int_{T_{j-1}}^{T_j} G_i(T)\Phi_0(T)dT} \tag{6.24}$$

and $\Phi_0(T)$ is an initial estimate of $\Phi(T)$. Although such a discretisation process introduces errors into the inversion process, it is possible to choose $T_j$ such that the discretisation errors are much smaller than the data noise. Following the product integration method described above, the integral can be reduce to discrete form:

$$g_i = \sum_{j=1}^{n} H_{ij} f_j + \varepsilon_i \tag{6.25}$$

and in the matrix form:

$$(\mathbf{H}^T\mathbf{H} + \lambda\mathbf{\Phi})\mathbf{f} = \mathbf{H}^T\mathbf{g} \tag{6.26}$$

These are the canonical forms for inverse problems. The variables in eq. 6.25 are listed below:

- $g_i$, with $i = 1, 2, ..., n$, is the data and is equal to $I_i/s_i$, where $I_i$ is the observed intensity of the ith line and $s_i$ is a weighting parameter or an estimate of the noise variance on each line;
- $H_{ij}$, with $j = 1, 2, ..., m$, contain the elemental abundances, the contribution functions and the first estimate of $\Phi(T)$ in the form

$$H_{ij} = \frac{A(Z)}{4\pi} \frac{\int_{T_{j-1}}^{T_j} G_i(T)\Phi_0(T)dT}{s_i}; \tag{6.27}$$

- $f_j$ is the quantity to be estimated, that is $\Phi_j^*$;
- $\varepsilon_i$ can be considered as a Gaussian error of constant variance so that the product $\varepsilon_i s_i$ is the data noise.

Although it is usually possible to solve the eq. 6.25 by evaluating the least squares solution, a regularisation approach is followed instead. This allows one to avoid that the solution is unstable to the errors in the data (which is a typical problem of the least squares method) and to stabilise the inversion. Following such procedure, a solution is derived by solving the optimisation problem

$$\min_{\hat{f}} \left[ \sum_{i=1}^{m} \left( g_i - \sum_{j=1}^{n} H_{ij}\hat{f}_j \right)^2 + \lambda\Phi(\hat{f}) \right] \tag{6.28}$$

where $\Phi(\hat{f})$ is a linear functional of $\hat{f}$, which is the estimate of $f$, and $\lambda$ is a smoothing parameter, to be determined. The regularising function $\Phi(\hat{f})$ contains the a priori information about the function $f$. A second order quadratic choice of the linear functional $\Phi(\hat{f})$ is adopted as solution of eq. 6.25 for this particular problem. It derives from the minimisation of the norm of the second derivative of the solution and can be expressed as:

$$\Phi(\hat{f}) = \sum_{j=1}^{n} \left( \hat{f}_{j+1} - 2\hat{f}_j + \hat{f}_{j-1} \right)^2 \tag{6.29}$$

which is obtained by representing the second order derivative through second order differences and with the conditions $\hat{f}_0 = \hat{f}_{n+1} = 0$. The smoothing parameter $\lambda$ is chosen using the method proposed by (200), as described by (197), according to:

$$\min_{\hat{f}} \left[ \frac{\|\mathbf{H}\hat{\mathbf{f}} - \mathbf{g}\|^2}{(trace[\mathbf{H}^T\mathbf{H} + \lambda\mathbf{C}])^2} \right] \tag{6.30}$$

where $\mathbf{C}$ is the Hessian matrix of $\Phi(\hat{f})$ (i.e. the square matrix of second-order partial derivatives of such function) and the matrix form 6.26 has been used. This method has the advantage that it is based purely on the data and does not require additional information such as the absolute value of the noise variance of the data points, but only their ratio. This means that the scaling factor $\sigma_0$ of the true standard deviation of the noise on the $i$th elements $\sigma_i = \sigma_0 s_i$ can be calculated a posteriori using the following relation:

$$\sigma_0^2 = \frac{\|\mathbf{H}\hat{\mathbf{f}} - \mathbf{g}\|^2}{(trace[\mathbf{H}^T\mathbf{H} + \lambda\mathbf{C}])}. \tag{6.31}$$

It now remains to evaluate the prior function $\Phi_0(T)$, in order to obtain a solution to the inverse problem from eq. 6.22. As mentioned in the previous subsection, in general, regularisation techniques tend to give an uneven smoothing when source functions span a large dynamic range. This explains the use of the alternative approach (*data adaptive smoothing*), proposed by (197), which would reduce the dynamic range of the underlying source function by transforming the kernel. Returning to the eq. 6.10, let $f^*(y)$ be a smooth function which corresponds to a data function $g^*(x)$ that fits the data crudely to, for instance, an order of magnitude, then:

$$g^*(x) = \int_a^b k(x, y) f^*(y) dy. \tag{6.32}$$

This parametric model can be used to reconstruct the source function. Using the eq. 6.32, it is possible to re-write the eq. 6.10 as follows:

$$\begin{aligned}
\frac{g(x)}{g^*(x)} g^*(x) &= \int_a^b k(x,y) \frac{f(y)}{f^*(y)} f^*(y) dy \quad \Rightarrow \\
g^+(x) g^*(x) &= \int_a^b k(x,y) f^+(y) f^*(y) dy \quad \Rightarrow \\
g^+(x) &= \int_a^b \frac{k(x,y)}{g^*(x)} f^*(y) f^+(y) dy \quad \Rightarrow \\
g^+(x) &= \int_a^b k^*(x,y) f^+(y) dy
\end{aligned} \tag{6.33}$$

where $g^+(x) = g(x)/g^*(x)$, $f^+(y) = f(y)/f^*(y)$ and $k^*(x,y) = (k(x,y)/g^*(x))f^*(y)$. The form 6.33 allows one to reduce the dynamic range of the source function $f(y)$ to the dynamic range of the new source function $f^+(y)$. Applying a standard regularisation techniques, such as a first or second order quadratic regularisation (e.g. eq. 6.29), to invert the eq. 6.33, the reconstruction of the $f(y)$ will no longer be smoothed towards a straight line but towards a function with a specific shape $f^*(y)$. Considering the discretised form, the eq. 6.33 becomes:

$$g_i^+ = \sum_{j=1}^{n} H_{ij}^* f_j^+. \tag{6.34}$$

If the kernel $G_i(T)$ is approximated by $\bar{G}_i \delta(T - T_i^{max})$, where

$$\bar{G}_i = \int_0^\infty G_i(T) dT \tag{6.35}$$

and using the notation of the relation 6.23, a rough estimate of $\Phi(T)$ is derived from eq. 6.34 as follows:

$$I_i = \frac{A(Z)}{4\pi} \bar{G}_i \bar{\Phi}(T_i^{max}) \quad \Rightarrow \quad \bar{\Phi}(T_i^{max}) = \frac{4\pi}{A(Z)} \frac{I_i}{\bar{G}_i} \tag{6.36}$$

where $T_i^{max}$ is the temperature corresponding to the maximum of the $G_i(T)$. In order to obtain a smooth representation of the $\Phi_0(T)$, the values $log(\bar{\Phi}(T_i^{max})$ are fitted using a cubic B-spline, following the procedure of (201) (see also (202) and (203)). This evaluation can only provide features with a width comparable to the typical kernel width, which is estimated to approximately 1/2 decade. Therefore, the knot points for the spline are selected around 1/2 decade apart. Denoting the B-spline fit (with interior knot points about 1/2 decade apart) with $S(log(T))$, one obtains:

$$log(\Phi_0(T)) = S(log(T)) \tag{6.37}$$

Such a B-spline fit gives an acceptable estimate of $\Phi_0(T)$ between the maximum and the minimum values of $T_i^{max}$ - which means between the temperature corresponding to the maximum of the $G_i(T)$ representing the *coldest* observed line and the temperature corresponding to the maximum of the $G_i(T)$ representing the *hottest* observed line. However, in order to evaluate the eq. 6.27, it is necessary to extrapolate the prior function $\Phi_0(T)$ beyond these boundaries. According to the prescription illustrated by (95), the following procedure to extrapolate $\Phi_0(T)$ is adopted:

- for $T < min(T_i^{max})$:

$$\begin{aligned}
&\text{if } \left(\frac{d\Phi_0}{dt}\right)_{min(T_i^{max})} > 0 \Rightarrow \Phi_0 \quad \text{is extrapolated linearly,} \\
&\text{if } \left(\frac{d\Phi_0}{dt}\right)_{min(T_i^{max})} < 0 \Rightarrow log(\Phi_0) \text{ is extrapolated linearly;}
\end{aligned}$$

- for $T > max(T_i^{max})$:

$$\begin{aligned}
&\text{if } \left(\frac{d\Phi_0}{dt}\right)_{max(T_i^{max})} > 0 \Rightarrow log(\Phi_0) \text{ is extrapolated linearly,} \\
&\text{if } \left(\frac{d\Phi_0}{dt}\right)_{max(T_i^{max})} < 0 \Rightarrow \Phi_0 \quad \text{is extrapolated linearly.}
\end{aligned}$$

The linear extrapolation of $log(\Phi_0(T))$ would allow the value of $\Phi_0(T)$ to decrease smoothly and ensure that it is always positive, while the linear extrapolation of $\Phi_0(T)$ is done because any rapid power-law variation in $\Phi_0(T)$ beyond the maximum and minimum of $T_i^{max}$ would give a large discrepancy between the values of $\bar{\Phi}(T_i^{max})$ and the corresponding average value of $\Phi_0(T)$. However, in the context of this thesis, the trend of the extrapolated function for $T < min(T_i^{max})$ is likely to lead to inconsistent interpretations. Since the study of this work is focussed on the analysis of the low temperature range (where helium ions are formed) a linear extrapolation of $\Phi_0(T)$ has been applied for $T < min(T_i^{max})$ both if $(d\Phi_0/dT)_{min(T_i^{max})} > 0$ and if $(d\Phi_0/dT)_{min(T_i^{max})} < 0$. A comparison between the extrapolation at low temperature used by (95) and the extrapolation here adopted is displayed in the plot in figure 6.1. The vertical

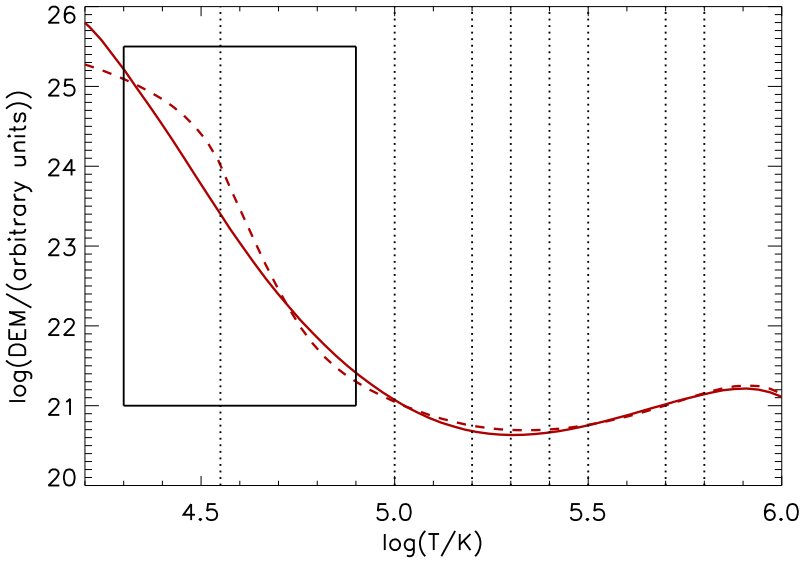


Figure 6.1: Illustrative plot of DEM as a function of temperature. The red dotted line is the DEM curve obtained using the extrapolation from (95), while the red solid line comes from the extrapolation adopted here. The box shows the region affected by the extrapolation.

dotted lines indicate the formation temperatures of the spectral lines employed for the inversion. Such a plot, only by way of illustration, shows that a linear extrapolation of $\Phi_0(T)$ at low temperatures allows one to avoid strange behaviour of the DEM curve. This can be useful, for instance, when only a few spectral lines are available in the lower temperature range (e.g.: in the plot in fig. 6.1 only two points are available between $log(T/K) = 4.5$ and $log(T/K) = 5.0$.

Once the three unknown quantities, $\lambda$, $\Phi(\hat{f})$ and $\Phi_0(T)$ have been determined, the eq. 6.28 can be solved to obtain an approximation to $\Phi(T)$ given by

$$\Phi\left(\frac{T_j + T_{j+1}}{2}\right) = \hat{f}_j \Phi_0\left(\frac{T_j + T_{j+1}}{2}\right) \tag{6.38}$$

In practice, the DEM is calculated by the ADAS601 routine, which evaluates an estimate of the DEM in temperature, using the Glasgow code. A schematic view of the program is shown in figure 6.2. The input data are the following:

- the elemental abundances, $A(Z)$,
- the set of observed intensities, $I_i$,
- the kernel, which collects the contribution functions $G_i(T)$.

The observed intensities have been derived and discussed thoroughly in chapter 4. The contributions functions have been updated and built up in chapter 5, sections 5.2-5.3. Regarding the elemental abundances, a dual analysis is done, as will be described in section 6.1.5. Firstly, known values are used from (204), (71), (190) and (205); secondly, once selected the observed lines to perform the integral inversion, the elemental abundances are adjusted to get the minimum

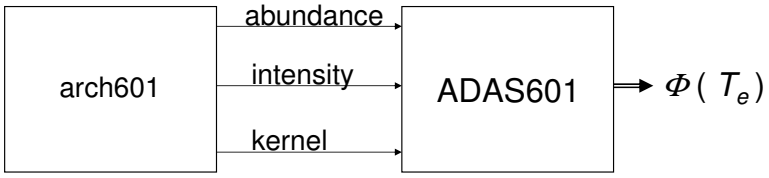


Figure 6.2: Scheme of the ADAS601 routine. The input data files (which include the elemental abundances, the observed intensities and the kernel) are collected in the directory **arch601**, within the ADAS database. The program evaluates an estimate of $\Phi(T)$, using the integral algorithm of (197), as described in the section.

deviation from observations. Such a procedure needs an estimate of electron density and/or electron pressure from the observations, in order to provide those kernel values which can give a satisfactory description of the plasma conditions of the observed solar region.

### 6.1.3 Electron density from line ratios

A preliminary study using intensity ratios of lines emitted by the same ion is performed for deducing the most likely electron density to be used in the evaluation of the kernel. Also, it is known that any spectral analysis based on the DEM requires caution in many aspects. Of fundamental importance is, in fact, the choice of lines used in the integral inversion. Not only accurate atomic data must be available, but also the lines employed for the inversion should be free from blend as much as possible. This initial analysis may help to select, for the integral inversion, lines not significantly affected by blending. Other methods are sometimes adopted to measure the electron density. For the solar upper atmosphere, reviews of early work have been provided by (206), while more recent assessments have been done by (207) and (190). However, diagnostics based on line ratios which are density sensitive remain a very accurate method. The power of such diagnostic techniques lies in the fact that, especially when the plasma is optically thin, the derived density depends purely on the atomic data for the emitting ion and is free of any physical assumptions about the volume, abundances or temperature structure within the plasma.

Considering the equation 6.8, the intensity ratio of two lines emitted by the same ion is given by the following relation:

$$\frac{I_1}{I_2} = \frac{\int G_1(T, N_e)\Phi(T)dT}{\int G_2(T, N_e)\Phi(T)dT}. \tag{6.39}$$

Because the density dependence is contained in the atomic data, the contribution functions are functions also of $N_e$. In this case, some assumption about the relation between density and temperature is made. As seen above, the most common assumptions are that the plasma density or pressure is constant over the relatively restricted range of temperature where the lines are emitted. This allows derivation of both $N_e$ and $P_e \simeq N_e T_e$ in the temperature region where contribution functions have their peaks (the G functions are predominantly peaked functions of the temperature). If the range of temperature $\Delta T$, where the contribution functions peak, is small enough to consider the DEM constant in that range, the equation 6.39 becomes:

$$\frac{I_1}{I_2} = \frac{\int_{\Delta T} G_1(T, N_e)dT}{\int_{\Delta T} G_2(T, N_e)dT}. \tag{6.40}$$

Since most of the emission of the lines originates at the temperature of the peaks of the contribution functions, a further simplification is that to estimate each $G(T, N_e)$ at the temperature of its peak. Because the ion is the same for the lines involved in the ratio, the fractional abundances, which are needed for the calculation of the two contribution functions at that fixed temperature ($T = T^{peak}$), show the same value when the density is fixed too. This allows one to write the intensity ratio as the PEC ratio only:

$$\frac{I_1}{I_2} = \frac{PEC_1(T^{peak}, N_e)}{PEC_2(T^{peak}, N_e)}. \tag{6.41}$$

Using such an approach, the density sensitive line ratio can be plotted as a function of electron density at the fixed temperature $T^{peak}$ and the density can be evaluated overplotting the ratios of observed line intensities gathered from each raster.

The first step in this process is to look for density sensitive line ratios using the lines available in the observations performed for this work. Despite the large number of observed lines during the joint observations of $17^{th}$ April 2009, only three density sensitive line ratios are not affected by known blends. From an atomic point of view, the choice of these ratios is related to the density sensitivity of the population ratio, which can be due to the competing importance of collisional and radiative de-excitation from the upper level or to the dependence on density of the population of the lower levels from which the upper level is populated.

Looking through the isoelectronic sequences, the first density sensitive line ratio which has been investigated belongs to the Be-like system. Figure 6.3 shows a partial diagram of atomic levels for O V. The first excited configuration $2s2p$

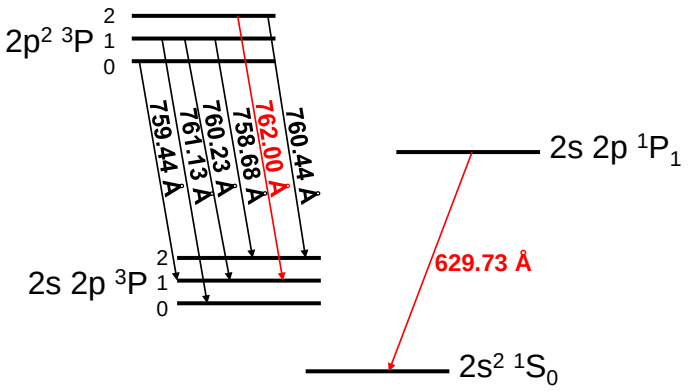


Figure 6.3: Partial level diagram for O V. The transitions which give rise to the two O V lines employed for a density diagnostics are marked in red.

results in a $^1P$ and a $^3P$ term. The $^1P$ term is excited from the ground state $^1$S and produce the strong resonance line at 629.73 Å, observed both by CDS and SUMER in the second order. The $2s2p\,^3P$ term is also excited by the ground state, but it is metastable. As a consequence, lines related to collisional excitations from it are density sensitive. The SUMER sequence allows observation of the $2p^2\,^3P_1 - 2s2p\,^3P_2$ line at 762.00 Å. The I(762.00)/I(629.73) ratio gives an estimate of the electron density at $\log(T_e/\mathrm{K})$~5.40.

The second line ratio is less common. It involves two Si VII lines observed by EIS and belonging to the O-like isoelectronic sequence. They are the $2s^22p^4\,^3P_2 - 2s2p^5\,^3P_2$ at 275.35 Å and the $2s^22p^4\,^3P_1 - 2s2p^5\,^3P_1$ at 275.67 Å. In general, the $2s^22p^4\,^3P - 2s2p_5\,^3P$ transitions give rise to six closely spaced lines (figure 6.4) which, for higher ions such as $Si^{+6}$, show some relative density sensitivity. The I(275.35)/I(275.67) ratio allows one to estimate the electron density at $\log(T_e/\mathrm{K})$~5.75.

Finally, the third ratio belongs to the P-like isoelectronic system. The circumstances are similar to the O V case. The term $3s^23p^3\,^2D$ is, in fact, metastable and, therefore, lines which involve this term are density sensitive. The transitions between the $^2D$ and $^2F$ terms produce three lines. EIS allows observation of the line 186.88 Å, which is a self-blend of the $3s^23p^3\,^3D_{5/2} - 3s^23p^23d\,^2F_{7/2}$ transition with the $3s^23p^3\,^3D_{3/2} - 3s^23p^23d\,^2F_{5/2}$ transition[1]. The other line, marked in red in figure 6.5, is a strong resonance line at 193.51 Å between the ground state and the $3s^23p^23d\,^4P_{3/2}$ level. The I(193.51)/I(186.88) ratio provides a good density diagnostic at $\log(T_e/\mathrm{K})$~6.10.

The three density sensitive line ratios, which as been chosen for this work are listed in table 6.1. This table reports the peak temperature of line formation and the density and pressure values deduced by the plots in figure 6.6. The theoretical ratios have been calculated within ADAS, using the equation 6.41 and plotted as a function of electron density. The temperatures of line formation have been established as the temperature where the contribution functions peak. The data points, marked in red in the plots in figure 6.6, show the measured ratios of the lines discussed above.

[1]Other two lines of $O^{+3}$ ion may contribute to the blend. However, table 6.6 shows that they contribute for less than 0.01% to the blend. So, they can be safely neglected.

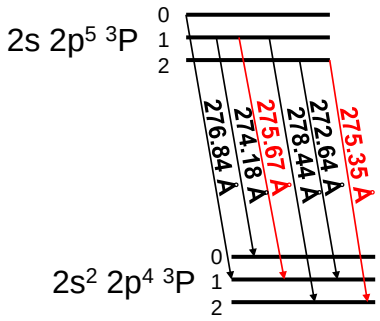


Figure 6.4: Partial level diagram for Si VII. Again, the transitions which provide the two Si VII lines used for a density diagnostics are marked in red.

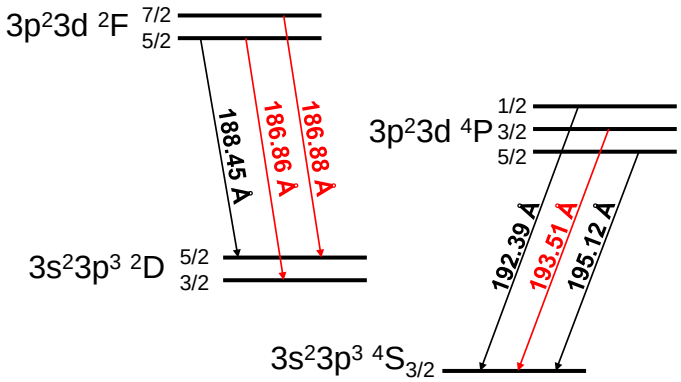


Figure 6.5: Partial level diagram for Fe XII. The three transitions marked in red are used for the density diagnostics. EIS observes the two lines at 186.86 Å and 186.88 Å between the $^2D$ and $^2F$ terms as a blend at the wavelength of 186.88 Å. So they are used as a "single line" in the ratio here investigated.

To minimise the errors which arise from the calibration and fitting procedures (data reduction and calibration, co-alignment and cross-calibration and fitting), every line intensity is averaged over the entire raster. Firstly the line ratio from each raster has been investigated separately and then the average density value has been derived. The O V I(762.00)/I(629.73) ratio is characterised by seven observational data points. The line at 762.00 Å, as said, is observed by SUMER in the first raster, while the line at 629.73 Å is observed both by SUMER (in the second order) in the second raster and by CDS through its set of five rasters, which were taken simultaneously with the two SUMER rasters (see chapter 4 for details). For reducing the problems due to the temporal misalignment and cross-calibration, the ratio between the 762.00 Å and 629.73 Å line intensities both from SUMER have been plotted together with the

| Ion | Ratio (Å) | $\log(T^{peak})$ | $\log(N_e)$ | $\log(P_e)$ |
|---|---|---|---|---|
| $O^{+4}$ | 762.00/629.73 | 5.40 | $10.0^{\pm 0.2}$ | $15.4^{\pm 0.2}$ |
| $Si^{+6}$ | 275.35/275.67 | 5.75 | $9.4^{\pm 0.3}$ | $15.1^{\pm 0.3}$ |
| $Fe^{+11}$ | 193.51/186.88 | 6.10 | $8.9^{\pm 0.1}$ | $15.0^{\pm 0.1}$ |

Table 6.1: Selected density sensitive line ratios for the evaluation of the kernels. $T^{peak}$ is the peak temperature of line formation, $N_e$ the density values deduced from the plots in fig. 6.6, using the ADAS database to calculate the theoretical ratios, and $P_e$ the pressure values respectively.

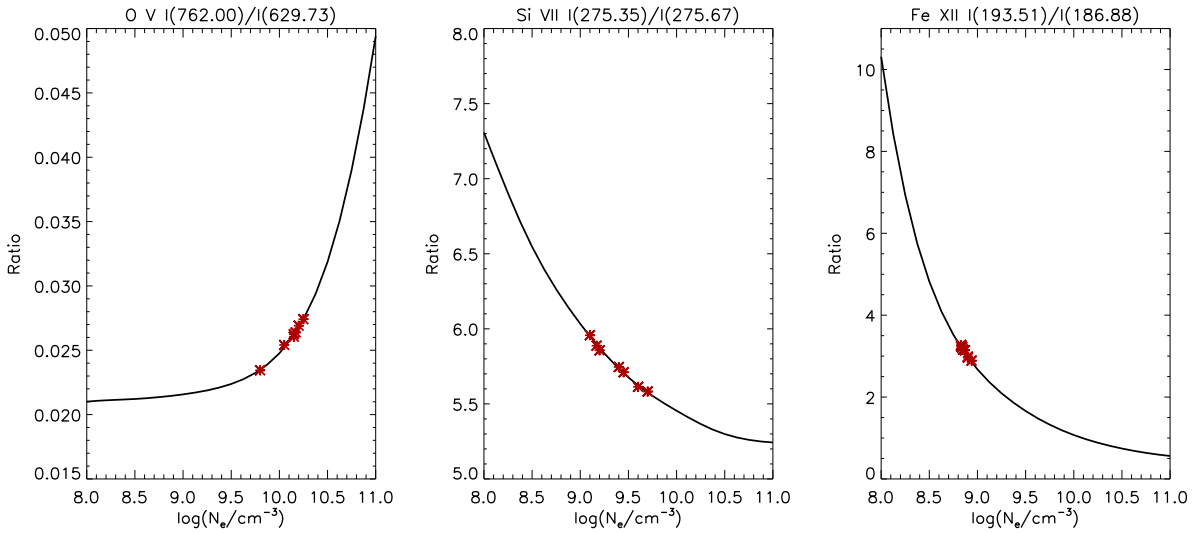


Figure 6.6: Plots of line ratios as a function of density for the three density diagnostic pairs, observed by SUMER, CDS and EIS. The observed ratios are compared to the theoretical ratios derived from ADAS database at the temperature where the contribution functions peak. The larger point spread for O V and Si VII line ratios is due to the Y-scale adopted.

five ratios between the 762.00 Å line intensity from SUMER and the 629.73 Å line intensities gathered by the CDS rasters. Also, the ratio between the 762.00 Å line intensity from SUMER and the averaged intensity of SUMER and CDS 629.73 Å line has been plotted for completeness. The O V ratio suggests a density of about $10^{10}$ cm$^{-3}$. Regarding the Si VII I(257.35)/I(275.67) and Fe XII I(193.51)/I(186.88) ratios, the whole set of lines involved is observed by EIS and collected in nine rasters. However, for Si VII the ratios from the first two rasters have been excluded from the density diagnostic analysis because of some discrepancy probably due to underestimated intensity of the line at 275.67 Å during the fitting procedure. The Si VII and Fe XII ratios indicate an electron density of about $3 \times 10^9$ cm$^{-3}$ and $8 \times 10^8$ cm$^{-3}$ respectively.

The electron densities which have been inferred from the comparison of the measurements with the theoretical ratios, would lead to the conclusion that the plasma is closer to having constant $P_e$ rather than constant $N_e$. The most likely pressure indicated by table 6.1 is around $10^{15}$ cm$^{-3}$ K. However, due to the non-negligible scatter especially in the O V I(762.00)/I(629.73) and Si VII I(257.35)/I(275.67) ratios, a larger grid of uniform $P_e$ will be considered for the evaluation of the kernels, dwelling on the following three values: $P_e^{(1)} \simeq 5 \times 10^{14}$ cm$^{-3}$ K, $P_e^{(2)} \simeq 1 \times 10^{15}$ cm$^{-3}$ K and $P_e^{(3)} \simeq 4 \times 10^{15}$ cm$^{-3}$ K. Additionally, in order to investigate the consequences of assuming a constant electron density, constant $N_e$ approximation for evaluation of the contribution functions will be used, by setting the electron density at a value equal to $10^{10}$ cm$^{-3}$.

### 6.1.4 Si II, C II and C III line intensities

A general problem related to the solar models of the upper chromosphere/lower transition region arises from the uncertain structure of these atmosphere layers. The present observations include five Si II lines, which sample progressively higher layers of the upper chromosphere reaching the lower transition region. Therefore, they provide useful constraint on these atmospheric layers and permit deduction of information on the behaviour of other lines formed in these regions, such as He I and He II lines. From the modelling point of view, the analysis of the Si II resonance multiplets, performed by (149), led to the conclusion that the lines belonging to the $3s^2 3p\,^2P - 3s3p^2\,^2S$ and $3s^2 3p\,^2P - 3s^2 3d\,^2D$ multiplets are moderately optically thick. This affects the observed intensities, which may result lower than the intensities in the pure optically thin case. Since an appropriate DEM analysis requires that the lines involved in the integral inversion are strictly optically thin, these Si II lines should be rejected or their intensities have to be adjusted to be consistent with an optically thin study. In this thesis, the latter solution has been adopted. In addition, several lines of C II and C III are observed. The multiplets to which they belong have been extensively examined by (5) and the spec-

tral lines emitted by these two carbon ions have been classified according to how much they are affected by opacity. The work of (5) has been taken as point of reference to derive the correction factors for the silicon line intensities and as source for the intensity corrections applied to the C II and C III lines included in the present observations. They analysed the emergent fluxes using an escape probability model to deduce the optical thickness of the considered lines. This technique is a relatively simple approach because it allows one to avoid the need to solve the full set of radiative transfer equations. It adopts the basic idea, established by (208), of extracting optical depths from observed intensity ratios of lines arising from a common upper level, together with the escape probability model introduced by (209) and (7). Returning to eq. 5.1, the radiative transfer equation for the photon intensity $I_\nu$ was given by the expression:

$$dI_\nu = -I_\nu \chi_\nu \rho ds + j_\nu \rho ds \tag{6.42}$$

where the emissivity coefficient is:

$$j_\nu = \frac{1}{4\pi\rho} A_{j\to i} N_j \psi_\nu^{(e)} \tag{6.43}$$

if stimulated emission is ignored, and the absorption coefficient is specified by:

$$\chi_\nu = \frac{h\nu}{4\pi\rho} B_{i\to j} N_i \psi_\nu^{(a)} \tag{6.44}$$

where $\psi_\nu^{(e)}$ and $\psi_\nu^{(a)}$ are the emission and absorption profiles and $B_{i\to j}$ is the Einstein coefficients for absorption. The $N_i$ and $N_j$ population densities refer to the lower level $i$ and the upper level $j$ between which the considered spectral line arises. The two extreme cases with $\tau_\nu = \chi_\nu \rho D \ll 1$ (opticaly thin case) and $\tau_\nu = \chi_\nu \rho D \gg 1$ (optically thick) have been discussed, focussing on the optically thin plasma condition. For intermediate optical depths, the absorption coefficient cannot be neglected and the solution of radiative transfer for the intensity averaged over direction, under the whole set of assumptions discussed in chapter 5, is:

$$I_\nu = \frac{j_\nu}{\chi_\nu} (1 - e^{-\tau_\nu}) \tag{6.45}$$

using the same form as eq. 5.3. Using the expressions for the emission and absorption coefficients (equations 6.43 and 6.44), the source function $j_\nu/\chi_\nu$ can be re-written as:

$$\frac{j_\nu}{\chi_\nu} = \frac{2\nu^2}{c^2} \frac{\omega_i}{\omega_j} \frac{N_j}{N_i} \frac{\psi_\nu^{(e)}}{\psi_\nu^{(a)}} \tag{6.46}$$

where all quantities have been previously defined. Assuming that the source function is independent of frequency, $\psi_\nu^{(e)} = \psi_\nu^{(a)} = \psi_\nu$, so that the ratio $\psi_\nu^{(e)}/\psi_\nu^{(a)}$ is equal to 1. Also, it is assumed that the line profiles are mainly determined by Doppler effect. This allows one to introduce the absorption line profile, with the central frequency $\nu_0$ (corresponding to the wavelength $\lambda_0$ at the peak of the spectral line), using the following relation:

$$\psi_\nu = \frac{1}{\sqrt{\pi}\Delta\nu_D} e^{-\left(\frac{\nu-\nu_0}{\Delta\nu_D}\right)^2} \tag{6.47}$$

with

$$\Delta\nu_D = \sqrt{\frac{2RT}{\mu c^2}} \nu_0 \tag{6.48}$$

where $R$ is the gas constant, $T$ is the temperature of the emitting ion and $\mu$ is its atomic weight. For $\nu = \nu_0$ the optical depth is:

$$\begin{aligned} \tau_0 &= \chi_{\nu_0} \rho D = \frac{h\nu_0}{4\pi\rho} B_{i\to j} N_i \psi_{\nu_0} \rho D = \frac{h\nu_0}{4\pi\rho} B_{i\to j} N_i \frac{1}{\sqrt{\pi}\Delta\nu_D} \rho D \\ &= \frac{1}{4\pi} \frac{1}{\sqrt{\pi}\Delta\nu_D} N_i D \frac{\omega_j}{\omega_i} \frac{c^2}{2\nu_0^2} A_{j\to i} = \frac{e^2}{4\epsilon_0 m_e c} \frac{1}{\sqrt{\pi}\Delta\nu_D} D f_{ij} \end{aligned} \tag{6.49}$$

where $e$ is the electron charge, $\epsilon_0$ the permittivity of free space, $m_e$ the electron mass. In addition, the relation $B_{i\to j}/A_{j\to i} = (c^2\omega_j)/(2h\nu^3\omega_i)$, between A- and B- Einstein coefficients and the relation $A_{j\to i} = (2\pi e^2 \nu_0^2 \omega_i f_{ij})/(\epsilon_0 m_e \omega_j c^3)$ between A-value and absorption oscillator strength $f_{ij}$ are used. Hence:

$$\tau_\nu = \tau_0 e^{-\left(\frac{\nu-\nu_0}{\Delta\nu_D}\right)^2}. \tag{6.50}$$

Substituting equations 6.46 and 6.50 into equation 6.45, the expression for the intensity becomes:

$$I_\nu = \frac{2\nu^2}{c^2}\frac{\omega_i}{\omega_j}\frac{N_j}{N_i}\left(1 - e^{-\tau_0 e^{-\left(\frac{\nu-\nu_0}{\Delta\nu_D}\right)^2}}\right) \tag{6.51}$$

A usual effect of opacity is to decrease the observed line intensity, along the line of sight, compared to the optically thin case. This is essentially due to the loss of photons out of the line of sight and the modification to the population structure caused by the photo-absortion. For a collisional-radiative model plasma in which there may be radiation trapping, the population rate equations (see eq. 5.12) have to be modified in order to include a term which takes into account the absorption of the radiation. Taking into account explicitly the first two terms only, by way of illustration, the population of excited level $j$ of an ion in a specific ionisation stage is described as follows:

$$\frac{dN_j}{dt} = -N_j A_{j\to i} + N_i B_{i\to j}\int_0^\infty I_\nu \psi_\nu d\nu + \text{other collisional-radiative terms.} \tag{6.52}$$

Using the relation between $A_{j\to i}$ and $B_{i\to j}$ and the equation 6.51which specifies the photon intensity, equation 6.52 can be written as:

$$\begin{aligned}
\frac{dN_j}{dt} &= -N_j A_{j\to i}\left(1 - \frac{c^2}{2\nu^2}\frac{\omega_j}{\omega_i}\frac{N_i}{N_j}\int_0^\infty I_\nu\psi_\nu d\nu\right) + \text{other collisional-radiative terms} \qquad (6.53)\\
&= -N_j A_{j\to i}\left(1 - \frac{1}{\sqrt{\pi}}\int_{-\infty}^{+\infty} e^{-x^2}\left(1 - e^{-\tau_0 e^{-x^2}}\right)dx\right) + \text{other collisional-radiative terms}\\
&= -N_j A_{j\to i} g(\tau_0) + \text{other collisional-radiative terms}
\end{aligned}$$

where $x = (\nu - \nu_0)/\Delta_D$, $\tau_0$ is the mean optical depth at the central frequency of the line and $g(\tau_0)$ is the *escape factor*. In other words, the effect of opacity can be described with a correction factor applied to the radiative transition probability $A_{j\to i}$, so that $A^{thick}_{j\to i} = A^{thin}_{j\to i} g(\tau_0)$. In terms of intensity, equation 5.7 becomes:

$$I^{thick}_{j\to i} = \frac{1}{4\pi A}\int A^{thin}_{j\to i} g(\tau_0) N_j dV = g(\tau_0) I^{thin}_{j\to i} \tag{6.54}$$

assuming that $g(\tau_0)$ depends only on the optical depth at the centre of the line. The purpose of such an approach is to derive suitable correction factors which account for the photon-absorption along the line of sight and use them to adjust the observed intensity for those lines that need to be included in the DEM analysis. Calling $I^{obs}$ the observed intensity of a line and $I^{corr}$ the intensity of the same line in an optically thin regime, from eq. 6.54 one obtains:

$$I^{corr} = \frac{I^{obs}}{g(\tau_0)}. \tag{6.55}$$

Once the previous relation has been deduced, the escape factor $g(\tau_0)$ has to be estimated for the five silicon lines included in this work. Following the idea of (208), implemented by (5) and (4), an intensity ratio between two lines which originate from a common upper level $u$ in conditions of moderate opacity is:

$$\frac{I_{u\to l_1}}{I_{u\to l_2}} = \frac{A_{u\to l_1} g(\tau_{0,l_1\to u})}{A_{u\to l_2} g(\tau_{0,l_2\to u})} \tag{6.56}$$

and from eq. 6.49 the ratio between $\tau_{0,l_1\to u}$ and $\tau_{0,l_2\to u}$ can be derived as follows:

$$\frac{\tau_{0,l_1\to u}}{\tau_{0,l_2\to u}} = \frac{N_{l_1}}{N_{l_2}}\frac{f_{l_1 u}}{f_{l_2 u}} \tag{6.57}$$

where $l_1$ and $l_2$ represent the lower levels of the two transitions. The equation 6.57 shows that the ratio between the two optical depths, $\tau_{0,l_1\to u}$ and $\tau_{0,l_2\to u}$, depends on known quantities: the lower level population densities ($N_{l_1}$ and $N_{l_2}$) and the oscillator strengths related to the two transitions ($f_{l_1 u}$ and $f_{l_2 u}$). Equations 6.56 and 6.57 provide the route for estimating the optical depths of the two lines and the respective escape factors, as defined in equations 6.49 and 6.53.

Practically, the first step is the choice of the Si II lines suitable for applying such a procedure. Figure 6.7 displays a partial diagram for the Si II lines observed by SUMER. The key doublet components that can be used for the opacity analysis are $3s^2 3p\,^2P_{1/2} - 3s3p^2\,^2S_{1/2}$ and $3s^2 3p\,^2P_{3/2} - 3s3p^2\,^2S_{1/2}$, which give rise to the lines at 1304.37 Å and 1309.28 Å respectively. The common upper level is:

$$u = 3s\,3p^2\,^2S_{1/2}$$

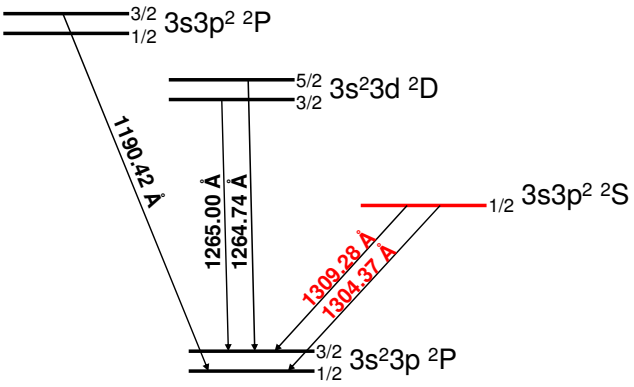


Figure 6.7: Partial level diagram for Si II. The two lines at 1304.37 Å and 1309.28 Å arise from the same upper levels, indicated in red, and have been used to calculate the escape factors.

while the lower levels are:

$$\begin{aligned} l_1 &= 3s^2 3p\,^2P_{1/2} \\ l_2 &= 3s^2 3p\,^2P_{3/2}. \end{aligned} \tag{6.58}$$

In order to calculate $\tau_{0,l_1\to u}/\tau_{0,l_2\to u}$, some consideration on the the lower levels has to be done. Assuming that distribution of their population densities is given by the Boltzmann equation and considering the energy difference between the two levels and the temperature of line formation, $N_{l_1}/N_{l_2}$ can be estimated as follows:

$$\frac{N_{l_1}}{N_{l_2}} = \frac{\omega_{l_1}}{\omega_{l_2}} e^{-\left(\frac{E_1-E_2}{kT}\right)} = \frac{1}{2} e^{0.016} \simeq \frac{1}{2} \tag{6.59}$$

and

$$\frac{\tau_{0,l_1\to u}}{\tau_{0,l_2\to u}} = 0.58 \tag{6.60}$$

Also, the observed ratio is:

$$\frac{I^{obs}_{SiII1304}}{I^{obs}_{SiII1309}} = \frac{A_{u\to l_1} g(0.58 \times \tau_{0,l_2\to u})}{A_{u\to l_2} g(\tau_{0,l_2\to u})} = 0.61 \tag{6.61}$$

Table 6.2 shows the results obtained by solving eq. 6.61, from which $g(\tau_{0,l_2\to u})$ can be derived and then $\tau_{0,l_1\to u}$ and $\tau_{0,l_2\to u}$. Once the escape factors are known for these two lines, those of all the other silicon lines can be evaluated using

| Transition | $\lambda$/Å | f | $\tau_0$ | $g(\tau_0)$ |
|---|---|---|---|---|
| $3s^2 3p\,^2P - 3s3p^2\,^2S$ | | | | |
| 1/2 - 1/2 | 1304.37 | 0.093 | 0.38 | 0.77 |
| 3/2 - 1/2 | 1309.28 | 0.080 | 0.53 | 0.64 |

Table 6.2: Si II doublet selected to classify the observed silicon lines according their opacity and to derive the intensity correction factors.

the following relation between observed ratios, $R^{obs} = I^{obs}_1/I^{obs}_2$ and the theoretical ratios in optically thin conditions, $R^{thin} = I^{thin}_1/I^{thin}_2$:

$$R^{obs} = \frac{g(\tau_1)}{g(\tau_2)} R^{thin}. \tag{6.62}$$

The final table 6.3 lists the whole set of lines to which the optically thick correction has been applied and the corresponding enhanced intensity indicated by $I^{corr}$. In this treatment, it has been assumed that all the observed Si II lines originate from the same atmospheric layer. However, as pointed out by (149), the region of formation of the Si II multiplets embraces regions with different depth of formation. This can affect the results obtained for the two observed components of the Si II 1265 Å multiplet and the line at 1190.42 Å. For this reason, the strongest component of the $3s^2 3p\,^2P - 3s3p^2\,^2S$ multiplet has been selected to perform the integral inversion, while the other Si II lines have been used in the forward sense, in order to test the reliability of this approach.

| Line | | $g(\tau_0)$ | $I^{obs}$ | $I^{corr}$ |
|---|---|---|---|---|
| | | | $ph\,cm^{-2}s^{-1}sr^{-1}$ | $ph\,cm^{-2}s^{-1}sr^{-1}$ |
| *b*C III | 538.20 Å | 0.99[a] | 3.428e+11 | 3.463e+11 |
| C III | 1174.93 Å | 0.93[a] | 2.552e+12 | 2.744e+12 |
| C III | 1175.26 Å | 0.94[a] | 2.155e+12 | 2.292e+12 |
| C III | 1176.37 Å | 0.93[a] | 2.412e+12 | 2.594e+12 |
| Si II | 1190.42 Å | 0.61 | 1.195e+12 | 1.953e+12 |
| Si II | 1264.74 Å | 0.27 | 7.621e+12 | 2.804e+13 |
| Si II | 1265.00 Å | 0.95 | 3.102e+12 | 3.267e+12 |
| Si II | 1304.37 Å | 0.77 | 3.419e+12 | 4.433e+12 |
| Si II | 1309.28 Å | 0.64 | 5.600e+12 | 8.693e+12 |
| C II | 1334.53 Å | 0.73[a] | 5.467e+13 | 7.489e+13 |
| C II | 1335.66 Å | 0.84[a] | 4.152e+12 | 4.943e+12 |
| C II | 1335.71 Å | 0.64[a] | 6.871e+13 | 1.074e+14 |

Table 6.3: Intensity corrected using the escape factor $g(\tau_0)$ for those lines which are affected by moderate opacity. The note (*a*) indicates the escape factors taken from (5). For the silicon lines the escape factors have been calculated using the same procedure as (5). Note that the multiplet of C III at ~538 Å, which results in a blend, is classified as optically thin, because its escape factor is almost equal to the unity and so its optical thickness is close to zero. However, it is added to the table for completeness.

### 6.1.5 Elemental abundances

As mentioned in section 6.1.2, one of the three main input data for calculating DEM and reconstructing line intensities is the set of abundances relative to hydrogen for all the 13 elements included in the present observations. These elements are listed in table 6.4 and their atomic abundances are given using a common logarithmic astronomical scale. The value for an element E on this scale is designated as A(E)=log$N$(E) and the number of hydrogen atoms is set to A(H)=log$N$(H)=12, so that A(E)=log$N$(E)= log[$N$(E)/$N$(H)]+12. The elements in the table can be divided into two

| Element | FIP/eV | Ph. ab. | Cor. ab.[fm] | Cor. ab.[m] | Hyb. ab.[fd] | Cor. ab.[p] | New ab. |
|---|---|---|---|---|---|---|---|
| H | 13.6 | 12.00 | 12.00 | 12.00 | 12.00 | 12.00 | 12.00 |
| He | 24.6 | 10.90 | 10.93 | 10.99 | 10.80 | 10.90 | 10.99 |
| C | 11.3 | 8.58 | 8.52 | 8.37 | 8.41 | 8.58 | 8.16 |
| N | 14.5 | 8.02 | 7.92 | 7.59 | 7.81 | 8.02 | 7.10 |
| O | 13.6 | 8.88 | 8.83 | 8.39 | 8.74 | 8.88 | 8.80 |
| Ne | 21.6 | 8.10 | 8.11 | 7.55 | 7.94 | 8.10 | 8.00 |
| Na | 5.1 | 6.30 | 6.62 | 6.44 | 6.63 | 6.90-7.10 | 7.50 |
| Mg | 7.6 | 7.55 | 7.88 | 7.57 | 7.90 | 8.15 | 7.90 |
| Si | 8.2 | 7.54 | 7.86 | 7.59 | 7.87 | 8.14 | 7.58 |
| S | 10.4 | 7.34 | 7.33 | 6.94 | 7.32 | 7.34 | 6.94 |
| Ar | 15.8 | 6.45 | 6.59 | 6.33 | 6.39 | 6.45 | 6.50 |
| Ca | 6.1 | 6.34 | 6.65 | 6.47 | 6.66 | 6.94-7.14 | 7.30 |
| Fe | 7.9 | 7.47 | 7.80 | 7.59 | 7.83 | 8.07 | 7.55 |

Table 6.4: Elemental abundances in the solar photosphere and corona, using the logarithmic astronomical scale, for the 13 elements included in the present observations. Photospheric abundances are from the recent collection of (190). The solar upper atmosphere abundances come from the coronal values of (204) (fm), (71) (m), (190) (p) and the hybrid values of (205) (fd). In addition, the relative abundances derived in the present work or adopted from literature are listed in the last column.

groups. The first group includes the non-volatile elements Na, Mg, Si, S, Ca, Fe. The second group includes the volatile elements H, C, N, O and the noble gases He, Ne, Ar. The abundances of the non-volatile elements can be obtained directly from the analysis of a particular class of meteorites (C I carbonaceous chondrite meteorites). It is thought that these formed together with the rest of the solar system and did not undergo any further processes. For this reason, (210) suggested that their elemental composition agrees with the solar photosphere composition. For volatile elements, the photosphere is the best source to derive their abundance values. Direct measurements from the chondrite

meteorites are more difficult in this case, because volatile elements are not completely retained in meteoritic material. Noble gases are not well represented in photospheric spectra, so their abundances can be taken from measurements of spectra emitted by the solar upper atmosphere. A recent revised list of laboratory-derived abundances of the C I carbonaceous chondrites has been published by (211) and adopted as main source of photospheric abundances by (190) (photospheric abundance values in table 6.4). These recent reviews and earlier analysis (see for instance (212) and (213)) show that the abundances of the solar photosphere have been measured accurately and are known with low uncertainties (on the order of 15%). Different consideration applies to the solar upper atmosphere composition. The solar transition region and corona are, in fact, highly dynamic and inhomogeneous leading to variation in the chemical composition in various coronal structures. Differences between elements from photospheric measurements appear to be related to the first ionisation potential (FIP) of the atoms. (71) reviewed the literature published before 1984 regarding elemental abundances in the solar upper atmosphere and established that elements with FIP ≥10 eV (high-FIP) are depleted by a factor of four to six compared to their photospheric values, while elements with FIP ≤10 eV (low-FIP) retain photospheric abundances. In a series of later papers (214), he changed his view, concluding that the low-FIP elements are enhanced with respect to their photospheric values instead of a high-FIP element depletion. This second model has been the preferred option for most of the subsequent analysis reviews, such as (215), (216), (204) and (217). A combination of the two models (low-FIP enhancement as well as high-FIP depletion) has been examined by (205), leading to hybrid abundance values. A unified picture of the FIP effects in the solar corona has been illustrated by (218). He demonstrated that the absolute magnitude of any enhancement or depletion factor depends sensitively on the chromospheric wave energy density and changes with the solar plasma conditions. Here coronal abundances from the three different models have been investigated: low-FIP enhancement from (204) (indicated by (fm) in table 6.4), high-FIP depletion from (71) (indicated by (m) in table 6.4) and hybrid from (205) (indicated by (fd) in table 6.4). Also, the recent collection of (190) (indicated by (p) in table 6.4) has been included. In addition, a further analysis to provide new relative abundances has been performed and the results are listed in the last column of table 6.4. A DEM curve has been obtained using each coronal set of abundances and plotted in figure 6.8. A constant electron pressure model has been used with $P_e$=$10^{15}$ cm$^{-3}$ K. The preferred set of new abundances values gives the dashed DEM curve.

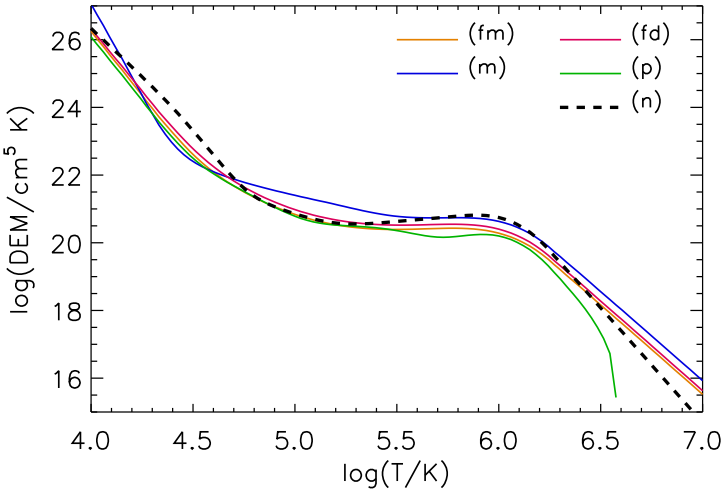


Figure 6.8: Comparison of DEM curves obtained using the different abundance sets listed in table 6.4. The new abundances are indicated by (n). For further description see table 6.4 caption.

In order to deduce relative elemental abundances from the present observations, two elements have been selected as starting point: oxygen, which is a high-FIP element, and silicon, which is a low-FIP element. Firstly, for the available ions of each of these two elements, lines which do not show evident blend or problems in atomic data have been selected. A preliminary DEM analysis has been performed independently for oxygen and silicon. This is necessary to check whether the relative intensities of the ions of oxygen and silicon are well calibrated and their theoretical reconstruction is reliable within the observational uncertainties, without involving abundance values. Then, oxygen and silicon ions have been analysed together, by means of DEM. In evaluating their abundances, it has been assumed that the oxygen abundances (with respect to hydrogen) in the transition region and corona is the same as in the photosphere.

The initial value, on the logarithmic scale defined above, has been taken from the photospheric abundances of (190). The silicon abundance have been adjusted in order to get the minimum deviation from observations. Once the relative abundance between oxygen and silicon has been estimated, the available neon ions have been added to the analysis. Following the suggestion of (217), the neon abundance as been assumed to be ~0.15 of the oxygen abundance. Thus a decrease in the oxygen abundance implies a similar decrease in the neon abundance. Again the three abundance values have been adjusted using the observations through the DEM approach. The values obtained by this analysis are the following: A(O)=8.80, A(Ne)=8.00 and A(Si)=7.58. After the abundances of oxygen, neon and silicon have been established, available ions from carbon and iron have been added and their abundance have been determined using the same procedure. For the other elements included in the present observations (Mg, Na, S, N, Ar and Ca), but which cannot be included in the set of lines used to perform the integral inversion, the abundances have been estimated comparing their observed intensities with the predicted intensities. For helium, the abundance from (71) has been adopted. The new abundances values are displayed in figure 6.9 together with the (190) coronal abundances for comparison. The abundances are shown as ratios to their photospheric values, taken from (190). A big discrepancy

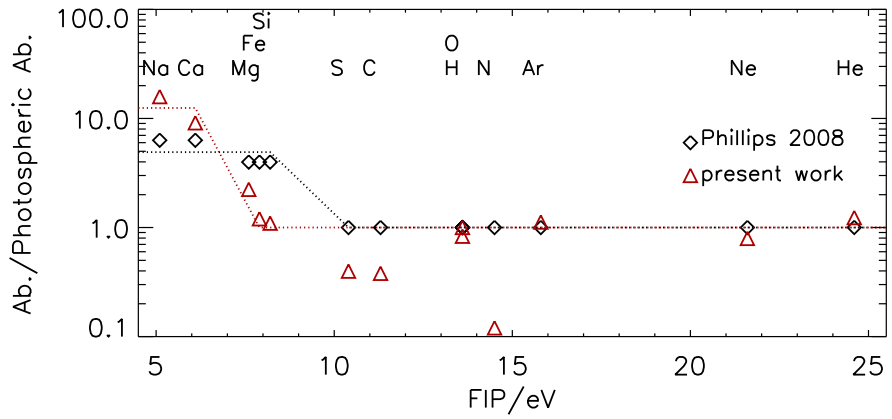


Figure 6.9: Elemental abundances for the SUMER/CDS/EIS joint observations of April 2009 compared with the (190) coronal abundances. The target is a quiet Sun region (see chapter 4). Abundances are plotted as ratios with the photospheric values taken from the recent collection of (190).

is found for N abundance. However, the determination of its abundance is quite uncertain because it is based on N II lines only. Although atomic data come from the preferred R-matrix calculations, these lines may be affected by opacity. However, a detailed examination of these lines is outside the scope of this work. Interesting results are found for Si and Fe abundances. Their values are close to photospheric values, even if their FIP values are lower than 10 eV. Similar results have been found by (95) in the analysis of data of an active region observed by SERTS-89. Here, the same behaviour of Si and Fe abundances is found for the quiet Sun too, suggesting a lower cut-off for the FIP effect.

### 6.1.6 Analysis of SUMER/CDS/EIS spectra

Once the elemental abundances have been evaluated using the preferred constant pressure model with $P_e$=$10^{15}$ cm$^{-3}$ K and tested using both a constant pressure and a constant density model (with their values obtained in section 6.1.3), a proper DEM approach can be followed. It will be used to estimate the intensities of all lines included in the set of observations performed by the three EUV spectrometers SUMER, CDS and EIS together. The main goal is the reconstruction of helium line intensities in the optically thin case and the estimate of new enhancement factors. However, this requires a more general analysis of the spectra gathered by the three instruments here employed, in order to ensure the reliability of the method currently adopted. The DEM approach will be supported by line ratio diagnostics as will be described in next section for several selected ions.

The preliminary analysis performed in section 6.1.3 for deducing electron density and pressure had the further purpose to eliminate lines known to be affected by blends or inconsistent with density-insensitive line ratio, in order to help to select lines suitable for the integral inversion. The choice of these lines is of fundamental importance to obtain

an accurate line intensity reconstruction and requires caution to avoid erroneous results. The main criteria for the selection of suitable lines are essentially the following:

1. free from blends;
2. optically thin;
3. density insensitive;
4. corresponding accurate atomic data;
5. large temperature range coverage.

Such criteria give critical constraints to the number of lines that can be used and would lead to a too small set of lines for the integral inversion. For this reason, it is not always possible to apply the full set of criteria listed above. However, the joint use of the complete set of the EUV spectrometers available at the time of observations allow to fill the missing line gap and make possible to apply nearly all of the criteria. The lines used in the present integral inversion and in the evaluation of elemental abundances for C, O, Ne, Si and Fe are listed in table 6.5.

| Line | | $\log(T^{peak})$ | $I^{obs}$ | $err^{obs}$ | $I^{rec}(P_e^{(1)})$ | $I^{rec}(P_e^{(2)})$ | $I^{rec}(P_e^{(3)})$ | $I^{rec}(N_e)$ |
|---|---|---|---|---|---|---|---|---|
| Si II | 1309.276[N] | 4.30 | 131.889 | 42.252 | 131.898 | 131.890 | 131.889 | 131.893 |
| C III | 1174.933[N] | 4.85 | 46.395 | 15.582 | 46.230 | 46.364 | 46.393 | 46.370 |
| O III | 599.598[N] | 4.95 | 42.718 | 13.866 | 42.828 | 42.743 | 42.719 | 42.729 |
| Ne IV | 543.886[E] | 5.20 | 8.094 | 2.694 | 8.047 | 8.065 | 8.093 | 8.082 |
| O IV | 279.631[N] | 5.25 | 1.964 | 0.813 | 2.348 | 2.278 | 2.063 | 2.255 |
| O V | 629.732[N] | 5.35 | 458.502 | 128.282 | 454.190 | 457.300 | 457.631 | 456.299 |
| O VI | 184.117[N] | 5.45-5.50 | 8.098 | 2.291 | 7.819 | 7.941 | 8.150 | 8.212 |
| Fe VIII | 186.601[N] | 5.70 | 21.674 | 5.216 | 22.003 | 21.809 | 21.685 | 21.723 |
| Si VII | 275.667[N] | 5.75 | 2.776 | 0.891 | 2.847 | 2.814 | 2.776 | 2.774 |
| Fe XII | 193.509[N] | 6.15 | 43.276 | 9.538 | 43.179 | 43.185 | 43.241 | 43.152 |
| Si XII | 520.662[E] | 6.25 | 3.663 | 1.310 | 3.689 | 3.702 | 3.676 | 3.705 |

Table 6.5: Lines used for integral inversion. The wavelengths used are the preferred laboratory wavelengths in Å (N is for NIST; E is for Edlèn,1983-1985). $T^{peak}$ is the peak temperature of line formation: in this case it is the temperature of the G(T) peak. $I^{obs}$ and $err^{obs}$ are the observed intensities and the respective uncertainty (fit+calibration). Reconstructed intensities are given in four cases where the G(T) functions are computed in the uniform pressure approximation ($P_e^{(1)} = 5 \times 10^{14}$ cm$^{-3}$ K, $P_e^{(2)} = 1 \times 10^{15}$ cm$^{-3}$ K and $P_e^{(3)} = 4 \times 10^{15}$ cm$^{-3}$ K) and uniform density approximation ($N_e = 10^{10}$ cm$^{-3}$). Intensities are in $erg\,cm^{-2}s^{-1}sr^{-1}$ instead of $photons\,cm^{-2}s^{-1}sr^{-1}$ in order to make easier the comparison between numbers.

For SUMER and CDS, the numerous spectral analysis performed in the previous literature (e.g. (60) for SUMER, (18) for CDS) are used as a starting point for lines and blend identification and selection. More care must be taken for EIS. As reference, the paper of (219) is used to select the five lines included in the integral inversion. Their reconstructed values are well within the observational uncertainties, supporting their choice. For Si II and C III lines the corrected intensities, derived in section 6.1.4, are used, to satisfy the second criterion. Also, it should be noted that the use of more than one line within $\Delta\log(T^{peak})$=0.05, where $T^{peak}$ is the temperature at which the G(T) peaks), is avoided. This limitation is adopted because the selection of lines forming at overlapping temperatures makes the $H_{ij}$ matrix (eq. 6.27) numerically ill-conditioned, resulting in a over-smoothed solution which fails to reproduce the observed intensities within the observational uncertainties. This would implies the selection of one line per ion at most. Figure 6.10 shows the DEM obtained assuming a uniform $P_e$ model in the evaluation of the contribution functions compared with the DEM obtained assuming uniform $N_e = 10^{10}$ cm$^{-3}$. Three pressure values have been tested: $P_e^{(1)} = 5 \times 10^{14}$ cm$^{-3}$ K, $P_e^{(2)} = 1 \times 10^{15}$ cm$^{-3}$ K and $P_e^{(3)} = 4 \times 10^{15}$ cm$^{-3}$ K. The difference of the DEM derived from the three constant $P_e$ approximations and the constant $N_e$ model is within 15%, except for the temperature ranges log(T/K)=4.40-4.60 and log(T/K)=5.90-6.10, where the model using $P_e^{(3)}$ and $P_e^{(2)}$ depart from the uniform $N_e$ approximation between 30-40%. For the spectral lines not included in the integral inversion, the intensities predicted using the DEMs of fig. 6.10 are compared with the observed intensities. A full list of the results is shown in table 6.6. The analysis is presented for each instrument, beginning from the shorter wavelengths (lines observed by EIS) up to the longer wavelengths (lines observed by SUMER).

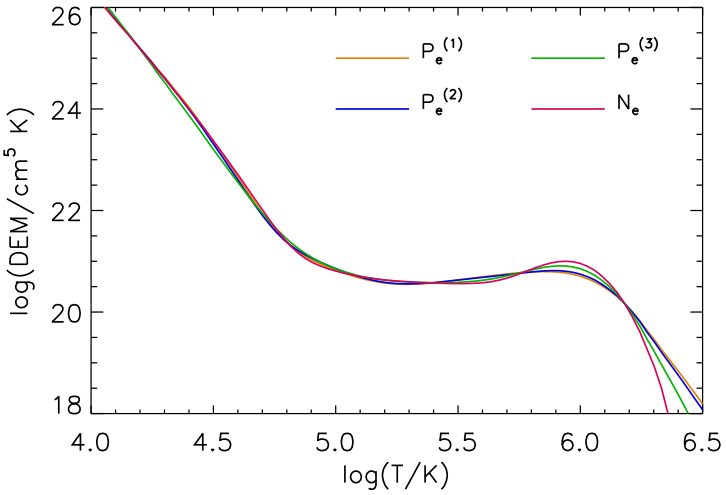


Figure 6.10: Differential emission measure (DEM) for the averaged solar quiet region using EUV line intensities observed by SUMER, CDS and EIS. The DEMs are derived assuming uniform $P_e$ or $N_e$ in the evaluation of contribution functions. Following the discussion in section 6.1.3, uniform $P_e$ models at $P_e^{(1)} = 5 \times 10^{14}$ cm$^{-3}$ K, $P_e^{(2)} = 1 \times 10^{15}$ cm$^{-3}$ K and $P_e^{(3)} = 4 \times 10^{15}$ cm$^{-3}$ K and a uniform $N_e$ model at $N_e = 10^{10}$ cm$^{-3}$ are considered.

Table 6.6: Comparison of the observed intensities with those derived from the DEM. See table 6.5 for description.

| Line | | $\log(T^{peak})$ | $I^{obs}$ | $err^{obs}$ | $I^{rec}(P_e^{(1)})$ | $I^{rec}(P_e^{(2)})$ | $I^{rec}(P_e^{(3)})$ | $I^{rec}(N_e)$ |
|---|---|---|---|---|---|---|---|---|
| **EIS** | | | | | | | | |
| O VI | 183.937[N] | 5.45 | 4.283 | 1.518 | 3.913 | 3.975 | 4.079 | 4.110 |
| Fe X | 184.542[N] | 6.00 | 73.458 | 16.363 | 30.473 | 31.873 | 36.236 | 41.957 |
| *b*Fe XII | 186.856[N] | 6.10 | | | 1.704 | 2.836 | 7.828 | 14.827 |
| *b*Fe XII | 186.880[N] | 6.10 | | | 8.920 | 12.336 | 19.831 | 27.309 |
| *b*O IV | 186.868[N] | 5.25 | | | 0.001 | 0.001 | 0.001 | 0.001 |
| *b*O IV | 186.884[N] | 5.25 | | | 0.000 | 0.000 | 0.000 | 0.000 |
| bsum | | | 13.563 | 3.364 | 10.626 | 15.175 | 27.663 | 42.140 |
| *b*Fe XI | 192.819[N] | 6.05 | | | 7.765 | 8.078 | 8.674 | 9.359 |
| *b*O V | 192.751[N] | 5.35 | | | 0.695 | 0.700 | 0.743 | 0.693 |
| *b*O V | 192.799[N] | 5.35 | | | 1.271 | 1.290 | 1.421 | 1.302 |
| *b*O V | 192.799[N] | 5.35 | | | 0.522 | 0.526 | 0.558 | 0.520 |
| bsum | | | 22.895 | 5.188 | 10.253 | 10.594 | 11.395 | 11.874 |
| *b*O V | 192.904[N] | 5.35 | | | 3.995 | 3.987 | 4.034 | 3.856 |
| *b*O V | 192.911[N] | 5.35 | | | 0.423 | 0.429 | 0.472 | 0.433 |
| *b*O V | 192.915[N] | 5.35 | | | 0.035 | 0.035 | 0.037 | 0.035 |
| bsum | | | 7.883 | 1.982 | 4.452 | 4.451 | 4.543 | 4.323 |
| *b*He II | 256.317[N] | 4.95 | | | 28.162 | 29.046 | 29.796 | 28.715 |
| *b*Si X | 256.384[N] | 6.15 | | | 8.629 | 8.604 | 9.154 | 10.572 |
| *b*Fe XIII | 256.420[N] | 6.20 | | | 0.373 | 0.389 | 0.436 | 0.477 |
| *b*Fe X | 256.410[N] | 5.95 | | | 1.584 | 1.766 | 2.322 | 2.851 |
| bsum | | | 222.829 | 47.383 | 38.748 | 39.805 | 41.708 | 42.615 |
| Si VII | 275.353[N] | 5.75 | 16.239 | 3.854 | 17.338 | 16.436 | 15.343 | 15.132 |
| O IV | 279.933[N] | 5.25 | 3.555 | 1.270 | 4.699 | 4.558 | 4.129 | 4.513 |
| **CDS** | | | | | | | | |
| He I | 515.620[N] | 4.50 | 13.623 | 4.310 | 15.928 | 15.574 | 13.885 | 14.801 |
| He I | 522.213[N] | 4.50 | 24.968 | 7.975 | 14.819 | 14.570 | 14.942 | 14.011 |
| O III | 525.797[N] | 4.95 | 23.685 | 7.526 | 18.387 | 18.463 | 18.246 | 18.107 |
| Ar VIII | 526.496[E] | 5.55 | 0.697 | 0.406 | 0.128 | 0.130 | 0.131 | 0.128 |
| He I | 537.030[N] | 4.50 | 71.831 | 22.949 | 44.553 | 40.230 | 34.076 | 44.528 |
| *b*O II | 538.100[N] | 4.70 | | | 7.959 | 7.079 | 6.185 | 8.469 |
| *b*C III | 538.080[N] | 4.85 | | | 0.584 | 0.595 | 0.625 | 0.603 |
| *b*C III | 538.149[N] | 4.85 | | | 1.755 | 1.786 | 1.876 | 1.811 |
| *b*C III | 538.312[N] | 4.85 | | | 2.928 | 2.980 | 3.131 | 3.023 |
| bsum | | | 12.783 | 4.408 | 13.227 | 12.441 | 11.818 | 13.908 |
| Ne IV | 542.070[E] | 5.15 | 5.310 | 1.816 | 5.372 | 5.382 | 5.400 | 5.394 |
| O IV | 553.329[N] | 5.20 | 30.322 | 9.752 | 32.302 | 32.378 | 30.954 | 32.232 |
| O IV | 554.076[N] | 5.20 | 56.026 | 18.797 | 63.452 | 63.676 | 61.122 | 63.440 |
| O IV | 554.513[N] | 5.20 | 135.686 | 42.961 | 161.696 | 162.084 | 154.973 | 161.354 |
| O IV | 555.263[N] | 5.20 | 30.178 | 9.825 | 32.792 | 32.907 | 31.585 | 32.785 |
| *b*Ne V | 572.112[E] | 5.40 | | | 3.038 | 2.989 | 2.796 | 2.684 |
| *b*Ne V | 572.334[E] | 5.40 | | | 19.039 | 18.736 | 17.525 | 16.825 |
| bsum | | | 11.231 | 3.672 | 22.084 | 21.733 | 20.327 | 19.516 |
| Ca X | 574.007[E] | 5.80 | 8.599 | 2.855 | 8.665 | 9.189 | 11.048 | 12.506 |
| Ca VIII | 582.845[N] | 5.70 | 16.932 | 8.044 | 5.578 | 5.379 | 5.095 | 4.743 |
| He I | 584.334[N] | 4.45 | 638.842 | 203.928 | 1278.445 | 1158.110 | 904.674 | 1267.226 |
| Ar VII | 585.754[N] | 5.50 | 5.325 | 3.734 | 5.754 | 5.736 | 5.338 | 4.954 |
| He I | 591.412[N] | 4.45 | 0.160 | 0.081 | 0.104 | 0.094 | 0.073 | 0.103 |
| O III | 597.818[N] | 4.95 | 2.793 | 1.191 | 2.510 | 2.520 | 2.491 | 2.472 |
| Si XI | 303.326[E] | 6.20 | 395.668 | 205.699 | 34.204 | 35.320 | 38.223 | 42.699 |
| He II | 303.780[N] | 4.90 | 5383.697 | 1717.610 | 409.286 | 419.531 | 431.826 | 426.598 |
| *b*Mg X | 609.790[E] | 6.05 | | | 60.857 | 66.255 | 82.608 | 102.371 |
| *b*O IV | 609.829[N] | 5.15 | | | 47.179 | 47.487 | 45.807 | 47.232 |
| bsum | | | 93.087 | 31.571 | 108.039 | 113.745 | 128.418 | 149.606 |
| **SUMER** | | | | | | | | |
| O V | 761.128[N] | 5.30 | 0.674 | 0.336 | 0.704 | 1.040 | 3.002 | 1.734 |
| O V | 762.004[N] | 5.30 | 8.835 | 2.897 | 8.175 | 8.580 | 10.659 | 9.294 |
| Mg VIII | 762.650[N] | 5.90 | 0.310 | 0.159 | 0.268 | 0.280 | 0.327 | 0.357 |
| Ne VIII | 770.409[N] | 5.75 | 96.682 | 30.682 | 100.893 | 104.051 | 117.232 | 126.033 |
| *b*O IV | 779.736[N] | 5.20 | | | 0.140 | 0.142 | 0.146 | 0.144 |
| *b*O IV | 779.821[N] | 5.20 | | | 1.217 | 1.235 | 1.269 | 1.252 |
| *b*O IV | 779.912[N] | 5.20 | | | 1.875 | 1.901 | 1.962 | 1.926 |
| *b*O IV | 779.997[N] | 5.20 | | | 0.138 | 0.140 | 0.145 | 0.142 |
| bsum | | | 1.875 | 0.691 | 3.372 | 3.419 | 3.532 | 3.465 |
| Ne VIII | 780.324[N] | 5.75 | 42.421 | 13.283 | 50.127 | 51.692 | 58.240 | 62.594 |
| O IV | 787.711[N] | 5.15 | 75.372 | 29.572 | 90.725 | 92.726 | 92.557 | 91.951 |
| Na VIII | 789.810[N] | 5.85 | 2.131 | 1.918 | 2.217 | 2.350 | 2.828 | 3.201 |
| *b*O IV | 790.109[N] | 5.15 | | | 17.394 | 17.777 | 17.744 | 17.630 |
| *b*O IV | 790.199[N] | 5.15 | | | 163.838 | 167.145 | 166.095 | 165.631 |
| bsum | | | 147.152 | 45.895 | 181.251 | 184.941 | 183.857 | 183.280 |
| S IV | 1072.990[N] | 5.00 | 7.122 | 2.266 | 1.327 | 1.377 | 1.437 | 1.302 |
| S IV | 1073.530[N] | 5.00 | 0.542 | 0.223 | 0.127 | 0.132 | 0.137 | 0.124 |
| S III | 1077.140[N] | 4.80 | 2.799 | 0.907 | 3.195 | 2.999 | 2.721 | 3.228 |
| N II | 1083.990[N] | 4.65 | 7.570 | 2.442 | 8.929 | 8.505 | 7.322 | 8.513 |
| He II | 1084.940[N] | 4.95 | 12.822 | 5.911 | 0.368 | 0.380 | 0.389 | 0.377 |
| *b*N II | 1085.540[N] | 4.65 | | | 6.484 | 6.173 | 5.311 | 6.184 |
| *b*N II | 1085.700[N] | 4.65 | | | 37.363 | 35.557 | 30.579 | 35.644 |

Table 6.6: – continued

| Line | | $\log(T^{peak})$ | $I^{obs}$ | $err^{obs}$ | $I^{rec}(P_e^{(1)})$ | $I^{rec}(P_e^{(2)})$ | $I^{rec}(P_e^{(3)})$ | $I^{rec}(N_e)$ |
|---|---|---|---|---|---|---|---|---|
| bsum | | | 42.848 | 16.725 | 43.852 | 41.735 | 35.894 | 41.834 |
| He I | 584.334$^{N}$ | 4.45 | 574.081 | 177.362 | 1278.445 | 1158.110 | 904.674 | 1267.226 |
| C III | 1175.263$^{N}$ | 4.80 | 38.744 | 13.238 | 37.652 | 37.825 | 37.899 | 37.733 |
| C III | 1176.370$^{N}$ | 4.80 | 43.797 | 8.431 | 46.897 | 47.114 | 47.204 | 46.996 |
| C I | 1189.450$^{N}$ | 4.15 | 0.228 | 0.202 | 0.308 | 0.317 | 0.353 | 0.333 |
| C I | 1189.630$^{N}$ | 4.15 | 1.115 | 0.566 | 1.086 | 1.110 | 1.187 | 1.176 |
| S III | 1190.170$^{N}$ | 4.75 | 1.993 | 0.781 | 2.312 | 2.088 | 1.781 | 2.380 |
| Si II | 1190.416$^{N}$ | 4.30 | 32.595 | 10.505 | 44.324 | 43.870 | 41.979 | 44.222 |
| O V | 629.732$^{N}$ | 5.30 | 411.784 | 132.277 | 454.190 | 457.300 | 457.631 | 456.299 |
| Si II | 1264.738$^{N}$ | 4.35 | 440.459 | 142.331 | 482.279 | 479.455 | 465.925 | 482.461 |
| Si II | 1265.002$^{N}$ | 4.35 | 51.296 | 17.315 | 56.964 | 56.634 | 54.992 | 56.947 |
| Si II | 1304.370$^{N}$ | 4.35 | 67.516 | 23.973 | 66.606 | 66.604 | 66.605 | 66.610 |
| O I | 1304.860$^{N}$ | 4.15 | 644.659 | 205.397 | 77.691 | 75.992 | 63.085 | 83.470 |
| C II | 1334.532$^{N}$ | 4.45 | 1114.748 | 367.886 | 1506.441 | 1478.155 | 1355.413 | 1399.470 |
| C II | 1335.660$^{N}$ | 4.45 | 73.515 | 36.650 | 297.302 | 291.707 | 267.506 | 276.179 |
| C II | 1335.708$^{N}$ | 4.45 | 1596.661 | 523.752 | 2708.936 | 2655.672 | 2433.413 | 2521.212 |

The EIS line intensities are reproduced within the observational uncertainties except for Fe X 184.54 Å, the blend of Fe XI 192.82 Å+O V 192.7 Å multiplet and the blend of O V 192.9 Å multiplet. Their reconstructed intensities are underestimated by a factor 1.7-2.4 for Fe X, 1.9-2.2 for Fe XI+O V and 1.7-1.8 for O V. Regarding Fe X, atomic data for this line come from the recent assessment of (130), as reviewed in chapter 5. Excluding that the discrepancy is due to the fit, and assuming a good quality of atomic data, a possible unknown blend may explain the higher observed Fe X intensity. On the other hand, Fe XI+O V and O V lines are seven components (one from Fe XI and six from O V) of a complex blend. As discussed by (219), the Ca XVII 192.82 Å line is in that region. It can affect the two observed blends resolved by the fitting procedure, increasing the observed intensity. Its contribution has not been estimated here, because data for Ca XVII have not been reviewed yet. Future work will be carried out in order to check and eventually fix these inconsistencies. In addition, a big discrepancy is found in the blend that includes one of the resonance lines of He II, which will be discussed in section 6.3.

The comparison between observed and reconstructed intensities for CDS lines is good for most of the lines (within observational uncertainties). Some discrepancy is found for the two weak lines of Ar VIII 526.50 Å and Ca VIII 582.84 Å, which are underestimated by the DEM reconstruction, likely because of fit problems. In fact, these two lines lie in the wings of the much more intense lines of O III 525.80 Å and He I 584.33 Å. After the SoHO loss, the line profile was altered resulting in an additional loss of spectral resolution. This makes less reliable the fit for such small lines. Another problem is encountered in the prediction of the blend of two components of the Ne V $2s^2 2p^2\ ^3P - 2s2p^3\ ^3D$ multiplet (at around 572 Å). This multiplet is overestimated by the DEM reconstruction by around 50%. The same discrepancy was found by (220). An improvement of more than 10% compared with the value presented by (220) is obtained, probably due to the more accurate atomic data here used (R-matrix from (110) instead of DW from (114)). However, the discrepancy is not clarified and a more detailed investigation is required. A further inconsistency is found in the reconstructed intensity of Si XI 303.33 Å line, which is observed in the second order. For this line, $I^{obs}/I^{rec} \sim 13 - 15$. Again, this discrepancy is consistent with (95; 220) spectral analysis, where $I^{obs}/I^{rec} \sim 10$. Possible blends were investigated by (220), but none of those considered contribute appreciably to the observed intensity. Moreover, this Si XI line may suffer from radiative pumping due to the its close vicinity to the strong He II 303.78 Å doublets. However, another cause may be sought in the CDS calibration at the second order, after the SoHO loss. Obviously, this can affect the He II line too, which will be discussed in section 6.3, together with other helium lines.

Most of the observed SUMER lines are predicted within the observational uncertainties. As for CDS, some fitting problems are found for small lines in the wings of much more intense lines. This is the case of the O IV multiplet at around 779.8 Å. Other discrepancies, which are found for the two S IV lines (at 1072.99 Å and 1073.53 Å) and for the O I line (at 1304.86 Å), are essentially due to the lack of accurate atomic data and possible opacity effects, especially in the case of neutral oxygen. Regarding the two C II lines at 1335.66 Å and 1335.71 Å, as discussed in subsection 4.2.1, the cut between the two spectral windows affects strongly the line at 1335.66 Å providing an observed intensity overestimated by a factor 3, that makes its observed intensity not reliable. Moreover, the cut between the two spectral windows affects slightly the observed intensity of the line at 1335.71 Å, resulting in a overestimate by a factor 1.5-1.6. The biggest problem in the analysis of SUMER line intensities is with the He II 1084.94 Å. This is not a resonance line, as the other He I and He II lines observed by CDS and EIS, and its predicted intensity is underestimated by a huge factor ($\sim 33$), which cannot be explained only by the underlying atomic physics or errors in the observations. Possible unknown blends may help to clarify the issue. However, this line would require a more robust analysis using different set of observations which include active regions and coronal holes too. Here, the helium problem is concentrated on the study of the helium resonance lines and the intercombination line of He I at 591.41 Å, so that the He II 1084.94 Å will be not included in further discussion.

Finally, as support of the present analysis, a comparison with the DEM distribution, performed by (221) is shown in figure 6.11. He investigated quiet Sun regions using SUMER and CDS observations in the period between 1996 and 1997, near the minimum in the solar activity cycle. A uniform pressure model was adopted to calculate the emissivity, with $P_e = 3 \times 10^{14}$ cm$^{-3}$ K, and the elemental abundances from (71) (decreasing the Mg abundance by 10% and increasing the Si abundance by 30 %) were used. Figure 6.11 shows that a discrepancy of more than 50% for temperature log(T/K)< 4.55 and between 10% and 50% in the range log(T/K)=4.55-5.40 is found between the present work and the (221) DEM. Also, a big inconsistency is visible for temperature log(T/K)> 5.2. The Warren DEM peaks at around log(T/K)~6.00, while the current DEM shows a peak at a slightly lower temperature. The reliability of DEM analysis discussed in this work is supported by the constraints given by the EIS lines which allow a good coverage in the temperature range log(T/K)=5.45-6.30, together with CDS lines, and by the reviewed atomic data discussed in chapter 5. Also, the (221) DEM analysis pointed out that lines from Li-like and Na-like ions present

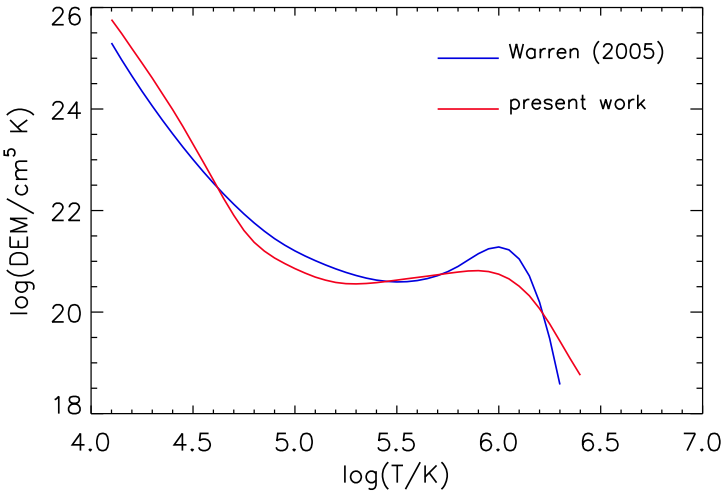


Figure 6.11: Comparison between the DEM curves derived by (221) and by the present analysis. The electron pressure has been fixed at $3 \times 10^{14}$ cm$^{-3}$ K and the abundances from (71) have been used for the Warren distribution. For the present work, the preferred DEM distribution, using $P_e^{(2)} = 10^{15}$ cm$^{-3}$ and the new abundance set, has been adopted.

evident deviations. He found that their observed intensities are greater than the calculated intensities by factors ranging from 2.1 to 3.6. The same conclusions have been already discussed by (207). The analysis presented here includes four ions belonging to the Li-like iso-electronic sequence and two ions belonging to the Na-like sequence. Three Li-like lines (O VI 184.12 Å, Ne VIII 770.41 Å and Si XII 520.66 Å) have been used for the integral inversion. The other Li-like and Na-like lines have been examined in the forward sense. Their reconstructed intensities are all within the observational uncertainties except for Ar VIII 526.47 Å, which is underestimated by a factor $\sim 5$. However, as said, this line lies in the wing of the more intense O III 525.80 Å line, leading to unreliable fit. Another group of lines near log(T/K)=4.60 are not in agreement with the Warren DEM distribution. They are lines from ions such as $N^{+1}$, $O^{+1}$ and $Si^{+2}$. In Warren analysis, their predicted intensities are all significantly lower than those predicted by the DEM. In the current analysis, only a few lines from these ions are observed: N II 1083.99 Å, a blend of N II at 1085.54 Å and 1085.70 Å from SUMER and the O II 538.10 Å multiplet observed by CDS in a blend with a C III multiplet. In the DEM reconstruction presented in this thesis, the predicted intensities of these lines are within the observational uncertainties.

## 6.2 Comparative line ratios

Because the solar upper atmosphere is highly structured, any line of sight observed in the EUV contains plasma over a considerable range of temperatures and spans different density regimes. In particular, on the disk - which is the case of the current observations - this range includes the atmosphere from the chromosphere to the corona. Since each ion is present over a generally narrow temperature range, individual structures are visible in different emission lines. Furthermore, if the plasma is in ionisation equilibrium, as has been assumed in the DEM analysis, the temperature range is narrow enough that it is possible to assign a formation temperature for each line. However, the solar upper atmosphere, in particular the transition region and corona, is highly dynamic and inhomogeneous, so that departures from ionisation equilibrium may affect line formation. In addition, time-dependent fluctuations in emission line intensities and/or both steady and impulsive mass motions, which may be present especially in the transition region, can lead to departures from ionisation equilibrium. Whichever is the cause, a lack of ionisation equilibrium can be revealed by significant systematic discrepancies in the DEM analysis and can affect sensitive-temperature line ratios. As seen in the previous section, the observational data examined for this thesis do not show clear evidences of non-equilibrium ionisation balance. As a support to the DEM analysis several line ratios are investigated. Firstly, He I and He II line ratios are examined. Then other two ions are selected, $C^{+2}$ and $O^{+3}$. The first one is chosen as a further means to check the reliability of the optically thick correction introduced in section 6.1.4. The second one is discussed

with the purpose to clarify the significant discrepancy, which has been found by (78) in the study of the ratio between O IV 787.71 Å and O IV 279.93 Å.

### 6.2.1 Helium line ratios

#### He I

CDS observes the $n = 2$ to $n = 5$ members of the $1s^2\,{}^1S - 1snp\,{}^1P$ series of neutral helium. A partial scheme of atomic transitions is reported in figure 6.12. As mentioned in section 2.2, (18) identified the intercombination line at 591.41 Å, which arises from the $1s^2\,{}^1S - 1s2\,{}^3P$ transition, using a position pattern method. He found that, although its position pattern has large error bars, it is consistent with that of the other He I lines. A comparison between measured

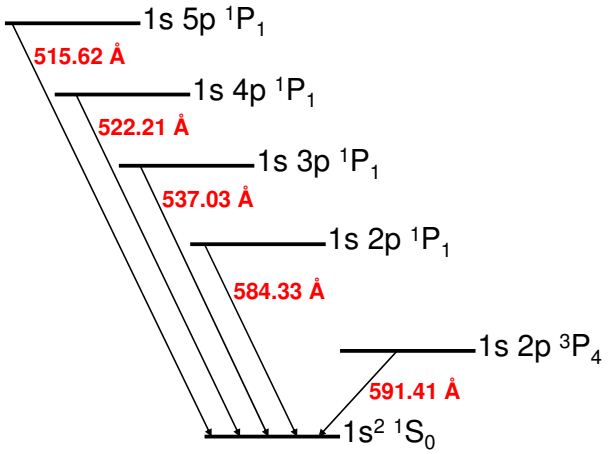


Figure 6.12: Partial term diagram for He I.

and predicted line ratios is made in table 6.7. The first line of the resonance series (He I 584.33 Å) is compared with the other resonance lines (He I 537.03 Å, 522.21 Å and 515.62 Å) and the intercombination line (He I 591.41 Å). It is expected that the He I resonance lines are affected by opacity, while the 591.41 Å line remains optically thin because of its very low A-value. Let us assume that the only effect of opacity is to deplete the observed intensities of these lines with respect to the predicted intensities in the optically thin approximation. Considering the relation 6.57, the optical thickness of He I 584.33 Å line is around 4, 10 and 20 times the optical thickness of He I 537.03 Å, 522.21 Å and 515.62 Å lines respectively. This would imply that the intensity of the first line of the He I resonance series is depleted more than the intensities of the other resonance lines and the intercombination line[2], which would lead to observed ratios (I(537)/I(584), I(522)/I(584), I(515)/I(584) and I(591)/I(584)) higher than the predicted ones. Table 6.7 shows that all measured ratios are enhanced by a factor $\sim 3$ compared to the reconstructed ratios, except for I(515)/I(584). The different behaviour of this ratio can be mainly due to the atomic data adopted for the transition $1s^2\,{}^1S - 1s5p\,{}^1P$ from which the He I 515.62 Å arises. The effective collision strength for this transition comes from the less accurate PWB approach instead of the preferred R-matrix calculations. This results in an overestimate of the reconstructed intensity for this specific line. Furthermore, in optically thick conditions, the radiation field also alters ther population densities with respect to the optically thin approximation. This effect is not taken into account here.

#### He II

Two EUV doublets of the He II resonance $1s\,{}^2S - np\,{}^2P$ (with $n = 2, 3$) series are included in the observations performed for this work. He II 303.78 Å is measured by CDS in second order in the NIS2 spectrum at 607.58 Å and

[2]Using, as first approximation, the relation between $\tau$ and the corresponding escape factor $g$, if $\tau_1 < \tau_2 \Rightarrow g(\tau_1) > g(\tau_2)$, so that the expression $I_1^{thick}/I_2^{thick} = (g(\tau_1)I_1^{thin})/((g(\tau_2)I_2^{thin}))$ (see eq. 6.54) implies that $I_1^{thick}/I_2^{thick} > I_1^{thin}/I_2^{thin}$.

| Ratio | Measured | Rec.($N_e$) | Rec.($P_e$) | $R^{obs}/R^{rec}$ |
|---|---|---|---|---|
| I(537)/I(584) | $(1.12 \pm 0.47)10^{-1}$ | $(0.32)10^{-1}$ | $(0.32 - 0.35)10^{-1}$ | 3.4 |
| I(522)/I(584) | $(3.49 \pm 1.61)10^{-2}$ | $(0.99)10^{-2}$ | $(1.04 - 1.48)10^{-2}$ | 3.0 |
| I(515)/I(584) | $(1.88 \pm 0.86)10^{-2}$ | $(0.93)10^{-2}$ | $(1.10 - 1.35)10^{-2}$ | 1.7 |
| I(591)/I(584) | $(2.54 \pm 1.94)10^{-4}$ | $(0.83)10^{-4}$ | $(0.81 - 0.83)10^{-4}$ | 3.1 |

Table 6.7: Observed and calculated He I line ratios. $R^{obs}/R^{rec}$ is the ratio between the observed ratio $R^{obs} = I^{obs}(i)/I^{obs}(584)$ and the predicted ratio $R^{rec} = I^{rec}(i)/I^{rec}(584)$, where $i = 537, 522, 515, 591$. A uniform $N_e$ model at $N_e = 10^{10}$ cm$^{-3}$ and uniform $P_e$ models at $P_e = P_e^{(1)}, P_e^{(2)}, P_e^{(3)}$ are considered, as described in section 6.1.3. Note that for uniform $P_e$ models only the minimum and maximum ratios are displayed.

is resolved from the two Si XI and O IV adjacent lines (see fig. 4.25). The 256.32 Å line lies in the EIS spectral range. Interpretation of the $1s\,^2S - 3p\,^2P$ doublet, observed as a single self-blended line, is complicated by blends with Si X 256.37 Å, Fe XIII 256.42 Åand Fe X 256.41 Å mainly (222) In addition, another possible component of this blend may be Fe XII 256.41 Å (219), but it has not been included in the present analysis because the lack of appropriate atomic data for the corresponding transition. For disk observations of quiet Sun, He II should dominate the feature contributing 80% at least to the blend. However, not all contributions to the blend are identified. Comparing the observed and reconstructed intensities, here it is assumed that He II contribution is 80% of the total intensity of the blend. A partial scheme of transitions is illustrated in figure 6.13. Table 6.8 shows the measured and calculated He II

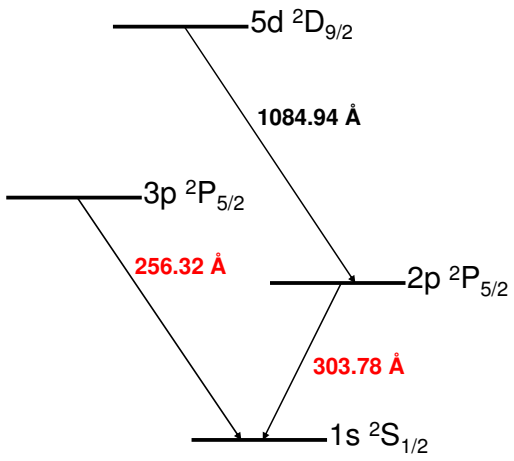


Figure 6.13: Partial term diagram for He II. The line between the excited term $2p\,^2P$ to $5d\,^2D$ is added for completeness, but not included in the line ratio analysis.

line ratios. Firstly, the observed intensity at 256.32 Å has been decreased by 20% and its ratio with He II 303.78 Å is compared with the theoretical ratio. Secondly, the intensity of the whole blend at 256.32 Å is compared with He II 303.78 Å intensity. In the latter case, the contribution from the other three lines of the blend at 256.32 Å has been included in the theoretical reconstruction. Applying the same arguments used in section 6.1.4 for Si II 1309.28 Å and 1304.37 Å, $\tau_{304} \sim 5\tau_{256}$ is obtained and the observed ratio I(256)/I(304) should be greater than the predicted ratio, but it is $R^{obs} \simeq 0.5R^{rec}$ instead. Several reasons may explain the discrepancy and each of them requires future investigation. First of all, as mentioned above, the components of the blend at 256.32 Å are not well defined. Therefore, even if for on disk quiet Sun observations He II should dominate the blend, the contribution due to other lines may be more than 20%. On the other hand, regarding the He II 303.78 Å doublet, it seems to show an enhancement of a factor 12-13, much bigger than the He II 256.32 Å enhancement (if the previous problem related to this blend is excluded). Possible cause can be found in the second order calibration of CDS after the SoHO loss. Also, a significant uncertainty in the second order CDS calibration would explain the Si XI 303.326 Å enhancement with respect to the predicted intensity. A further issue can be related with the partial lack of ionisation equilibrium, due to the plasma conditions in atmosphere layer where singly ionised helium ions are formed, which is presumably the lower transition region. Assuming as temperature of line formation that temperature where the line contribution function peaks ($T^{peak}$), any scatter from this temperature may reveal a departure from ionisation equilibrium. Figure 6.14 shows the measured

| Ratio | Measured | Rec.($N_e$) | Rec.($P_e$) | $R^{obs}/R^{rec}$ |
|---|---|---|---|---|
| I(256)/I(304) | $(2.79 \pm 1.64)10^{-2}$ | $(5.86)10^{-2}$ | $(5.80 - 5.84)10^{-2}$ | 0.5 |
| I($b$256)/I(304) | $(3.49 \pm 2.07)10^{-2}$ | $(8.70)10^{-2}$ | $(7.99 - 8.15)10^{-2}$ | 0.4 |

Table 6.8: Observed and calculated He II line ratios. $R^{obs}/R^{rec}$ is the ratio between the observed ratio $R^{obs} = I^{obs}(i)/I^{obs}(304)$ and the predicted ratio $R^{rec} = I^{rec}(i)/I^{rec}(304)$, where $i = 256, b256$. I(256) is the He I 256.32 Å intensity by subtracting the 20% from the observed intensity. I(b256) is the total intensity of the blend. A uniform $N_e$ model at $N_e = 10^{10}$ cm$^{-3}$ and uniform $P_e$ models at $P_e = P_e^{(1)}, P_e^{(2)}, P_e^{(3)}$ are considered, as described in section 6.1.3. Note that for uniform $P_e$ models only the minimum and maximum ratios are displayed.

ratio I(256)/I(304) (red dot) together with the theoretical ratio plotted as a function of temperature, calculated at $N_e = 10^{10}$ cm$^{-3}$. The vertical dotted line marks the temperature of line formation ($\log(T^{peak}/K) \simeq 4.90$). In addition,

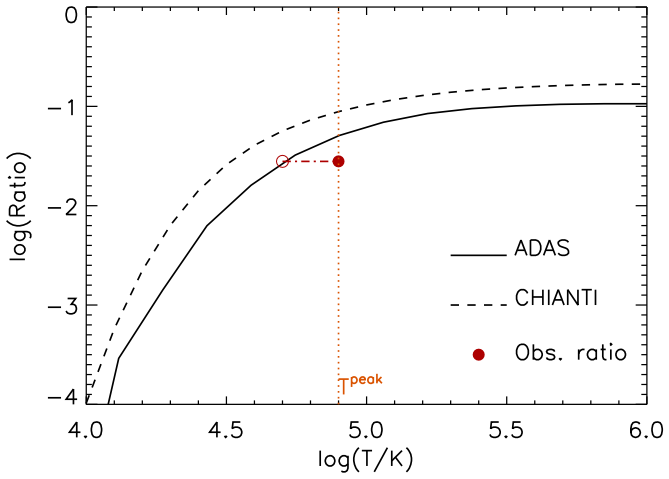


Figure 6.14: Line ratios as a function of electron temperature for He II 256.32 Å and 303.78 Å given in units of $photons\, cm^{-3} s^{-1}$. The theoretical line ratio is plotted at density $N_e = 10^{10}$ cm$^{-3}$, using atomic data from ADAS (solid line) and CHIANTI (dashed line). The vertical dotted line is at log(T/K)=4.90, which is the temperature where the G(T) peaks. The red dot represents the measured line ratios.

a comparison between the theoretical ratio derived by ADAS (solid line) and CHIANTI (dashed lines) is shown. As said in section 5.2.1, CHIANTI database includes data for transitions which involve the $1s$ and $2s$ configurations only. This gives a line ratio which is overestimated compared with the ADAS line ratio. Such difference in the atomic data does not clarify the discrepancy between observed and reconstructed ratios. Nevertheless, the measured ratio would agree with the theoretical ratio at log(T/K)$\simeq$ 4.70. This deviation from the established electron temperature $T^{peak}$ may be an indicator of non-equilibrium plasma conditions. However, as for He I ratios, the opacity effects on population densities are not taken into account, A more thorough discussion is deferred to section 6.3.

### 6.2.2 C III line ratios

Two C III multiplets are included in the observations of April 2009. SUMER observes the six components which arise from the $2s2p\,^3P - 2p^2\,^3P$ transitions. Unfortunately, as noticed in sec. 4.2.1 (fig. 4.10(a)), this multiplet is divided into two different spectral windows. Its partial reconstruction allows us to analyse only three lines of the multiplet: C III 1174.93 Å, which has been used for the integral inversion, C III 1175.26 Å and C III 1176.37 Å, which have been used in the forward sense. CDS observes the $2s2p\,^3P - 2s3s\,^3S$ multiplet at around 538 Å as a self-blend of its three components plus an O II component, which is estimated by the DEM analysis to be the 50-60% of the feature. The partial level diagram in figure 6.15 shows the lines examined here. As discussed in section 6.1.4, these lines are slightly affected by opacity and their observed intensities have been corrected using the factors listed in table 6.3.

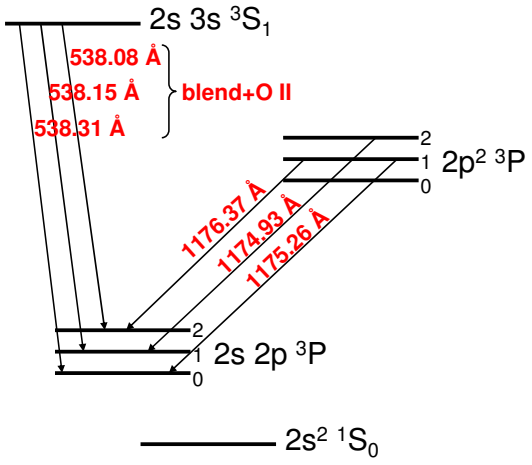


Figure 6.15: Partial level diagram for C III.

Table 6.9 shows both the measured and corrected line ratios and their comparison with the reconstructed ratios. Also,

| Ratio | Measured | Corrected | Rec.($N_e$) | Rec.($P_e$) | $\frac{R^{obs}}{R^{rec}}$ | $\frac{R^{cor}}{R^{rec}}$ |
|---|---|---|---|---|---|---|
| I(1174)/I(538) | (7.44 ± 5.51) | (7.92 ± 5.86) | 7.28 | 7.63-8.57 | 0.9 | 1.0 |
| I(1174)/I(1175) | (1.18 ± 1.01) | (1.20 ± 1.02) | 1.23 | 1.22-1.23 | 0.9 | 1.0 |
| I(1174)/I(1176) | (1.06 ± 0.83) | (1.06 ± 0.83) | 0.98 | 0.98-0.98 | 1.1 | 1.1 |

Table 6.9: Observed, corrected and calculated C III line ratios. $R^{obs}/R^{rec}$ is the ratio between the observed ratio $R^{obs} = I^{obs}(1174)/I^{obs}(i)$ and the predicted ratio $R^{rec} = I^{rec}(1174)/I^{rec}(i)$, where $i = 538, 1175, 1176$. $R^{cor}/R^{rec}$ is the ratio between the corrected line ratio and the predicted one. $R^{cor} = I^{cor}(1174)/I^{cor}(i)$, where the intensity values have been corrected using the factors listed in table 6.3. The ratio I(1174)/I(538) is calculate taking into account the whole set of components which contribute to the blend at ~538 Å. A uniform $N_e$ model at $N_e = 10^{10}$ cm$^{-3}$ and uniform $P_e$ models at $P_e = P_e^{(1)}, P_e^{(2)}, P_e^{(3)}$ are considered, as described in section 6.1.3. Note that for uniform $P_e$ models only the minimum and maximum ratios are displayed.

figure 6.16 illustrates, as an example, the ratio between C III 1174.37 Å and C III 1175.26 Å lines. The corrected ratio (red dot) shows a better agreement with the predicted one compared to the observed ratio without any correction (black dot), confirming the validity of such an approach.

### 6.2.3 O IV line ratios

The wavelength ranges of SUMER, CDS and EIS contains several lines which arise from the $O^{+3}$ ion. In particular, the joint observations carried out in April 2009 include three sets of O IV lines (essentially free from blend and useful for temperature diagnostics). Each set comes from one of the three instruments. SUMER allows observation of the O IV lines which arise from the $2s^2 2p\,^2P_{1/2,3/2} - 2s2p^2\,^2D_{3/2,5/2}$ transitions: $2s^2 2p\,^2P_{1/2} - 2s2p^2\,^2D_{3/2}$ gives rise to O IV 787.72 Å while $2s^2 2p\,^2P_{3/2} - 2s2p^2\,^2D_{3/2}$ and $2s^2 2p\,^2P_{3/2} - 2s2p^2\,^2D_{5/2}$ are a self-blend of the line at 790.11 Å and 790.19 Å observed at about 790.1 Å. CDS observes the $2s^2 2p\,^2P - 2s2p^2\,^2P$ multiplet, whose the four components are resolved by the fitting procedure. Finally, EIS observations include the two lines at 279.63 Å and 279.93 Å, which arise from the $2s^2 2p\,^2P_{1/2,3/2} - 2s^2 3s\,^2S_{1/2}$ transitions. The partial level diagram in figure 6.17 illustrates the three line sets observed by SUMER, CDS and EIS, with the corresponding transitions and energy levels. These three line sets provide a quite large combination of line ratios, which can involve both each instrument independently and two different instruments together. Some of these line ratios can be used to study the electron temperature of the plasma from which the lines involved are emitted. This is, for instance, the case of the ratio between the SUMER line at 787.72 Å and the EIS line at 279.93 Å. This line ratio has been analysed recently by (78), together with the O VI 1037.61/183.94 Å and O VI 1037.61/184.12 Å ratios. The SUMER O VI 1037.61 Å line has not been included in the

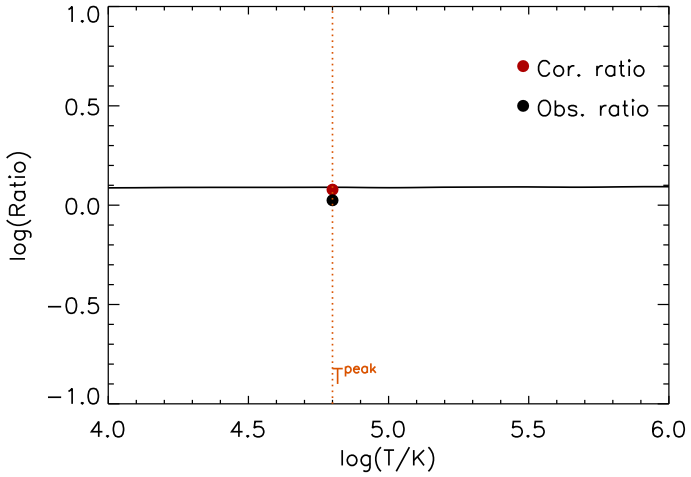


Figure 6.16: Line ratio as a function of electron temperature for C III 1174.37 Å and 1175.26 Å given in units of $photons\,cm^{-3}\,s^{-1}$. The theoretical line ratio is plotted at density $N_e = 10^{10}$ cm$^{-3}$ The vertical dotted line is at log(T/K)=4.80, which is the temperature where the G(T) peaks. The red dot represents the measured line ratios corrected for the opacity, the black dot is the measured ratio without any corrections.

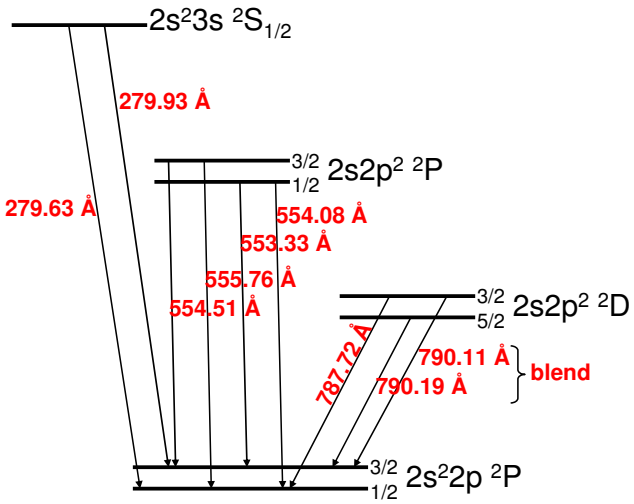


Figure 6.17: Partial level diagram for O IV.

present observations, hence only the O IV I(787)/I(279) ratio is examined in detail in this work and a comparison with (78) results is provided. Also, as support and cross-checking, I(787)/I($b$790) and I(787)/I(554) ratios are investigated. The former is the ratio of two SUMER lines, where $b$790 is, as said, a self-blend of the two lines at 790.11 Å and 790.19 Å. The latter involves the O IV 787.72 Å SUMER line and the strongest line of the CDS multiplet, O IV 554.51 Å, displayed in fig. 6.17. The observed and theoretical values of the three ratios here investigated are shown in table 6.10. (78) analysed data taken during the joint SUMER/EIS campaign of April 2007. They selected spectra obtained

| Ratio | Measured | Rec.($N_e$) | Rec.($P_e$) | $R^{obs}/R^{rec}$ |
|---|---|---|---|---|
| I(787)/I($b$790) | (0.59 ± 0.42) | 0.50 | 0.50-0.50 | 1.2 |
| I(787)/I(554) | (0.79 ± 0.56) | 0.81 | 0.80-0.85 | 1.0 |
| I(787)/I(279) | (59.67 ± 34.46) | 57.37 | 54.33-63.07 | 1.0 |

Table 6.10: Observed and calculated O IV line ratios. $R^{obs}/R^{rec}$ is the ratio between the observed ratio $R^{obs} = I^{obs}(787)/I^{obs}(i)$ and the predicted ratio $R^{rec} = I^{rec}(787)/I^{rec}(i)$, where $i = b790, 554, 279$. A uniform $N_e$ model at $N_e = 10^{10}$ cm$^{-3}$ and uniform $P_e$ models at $P_e = P_e^{(1)}, P_e^{(2)}, P_e^{(3)}$ are considered, as described in section 6.1.3. Note that for uniform $P_e$ models only the minimum and maximum ratios are displayed.

in quiet regions on the solar disk, including sometimes small-scale coronal bright points. The theoretical ratio between O IV 787.72 Å and O IV 279.93 Å lines has been calculated using the CHIANTI database for three different electron densities, $N_e = 10^9, 10^{10}$ and $10^{11}$ cm$^{-3}$. They found that all measured ratios were smaller by a factor 3-5 than the theoretical ratio and derived from those measurements an electron temperature in the range of log(T/K)=5.58-6.07. Such temperature values are much higher than the formation temperature values for this ion. In order to explain the anomalous behaviour of the I(787)/I(279) ratio, they investigated various possible causes, ranging from instrumental and observational effects to the presence of additional processes such as photoexcitation from photospheric black body radiation, self-absorption and non-Maxwellian distribution of the free electrons. However, they did not solve the discrepancy. Here the O IV I(787)/I(279) measured ratio has been compared with the revised atomic data, discussed in sec. 5.2.1. The results are given in table 6.10 and illustrated in figure 6.18. The black dashed line represents the

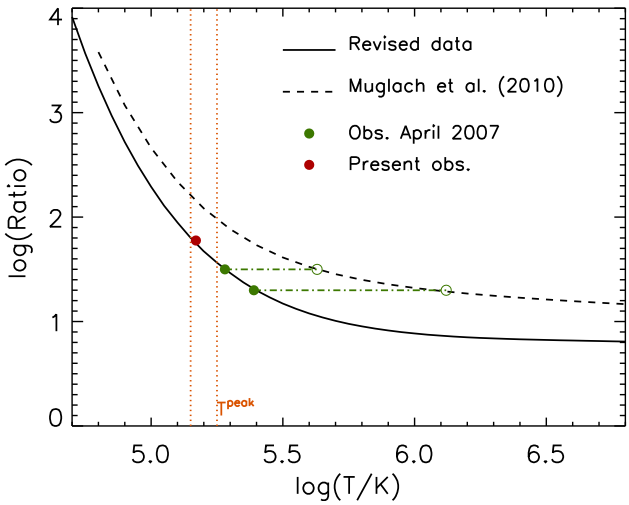


Figure 6.18: Line ratios as a function of electron temperature for O IV 787.72 Å and 279.93 Å given in units of $photons\,cm^{-3}s^{-1}$. The theoretical line ratio is plotted at density $N_e = 10^{10}$ cm$^{-3}$, using atomic data from ADAS (solid line) and CHIANTI (dashed line). The vertical dotted lines are at log(T/K)=5.15-5.25, which is the temperature ranges where the contribution functions peak. The red dot represents the measured line ratio derived from the present observations. The green dots are the measured line ratios derived from the (78) observations.

theoretical ratio obtained by (78), using the CHIANTI atomic data, while the black solid line comes from the atomic data for the $O^{+3}$ ion, which have been adopted for this thesis. The electron density has been fixed at $10^{10}$ cm$^{-3}$ for both the atomic datasets. The main difference is due to the number of transitions included in the atomic data. As said, in fact, only transitions which involve the first five energy levels have been taken into account in the CHIANTI dataset.

The additional transitions, taken from (106) calculations and included in the revised data, result in a decrease of the theoretical line ratio, providing a good agreement with observations. The dots in figure 6.18 show the measured ratio derived from the present observations (red dots) and the measured ratios derived from the observations of April 2007, as extracted by the (78) work. The dotted vertical lines indicate the range of formation temperature for the two lines examined. The electron temperature determined from the observations of April 2007, using the revised atomic data for O IV spectrum, is now in the range of log(T/K)=5.2-5.4, much closer to the ion formation temperature. This may clarify the (78) discrepancy for O IV line ratio. However, further investigation should be done for O VI line ratios too, in order to exclude or not departures from ionisation equilibrium conditions.

## 6.3 On enhancement factors

As thoroughly reviewed in section 2.3, the formation and behaviour of helium lines in the solar spectrum constitute an issue still open to debate and investigation. The early studies on helium formation mechanisms date back to 1939, but the first quantitative demonstration of anomalous high intensities of the neutral and single ionised EUV helium lines, based on emission measure distribution, comes from (34). She found that, under optically thin conditions, the reconstructed integrated emission of He I 584.33 Å is a factor 15 lower than the observed intensity, using disk-averaged solar spectra. Similarly, she derived an enhancement factor of 5.5 for He II 303.78 Å. These results were confirmed by (47), using spatially resolved observations of quiet regions performed by SoHO instrumentations (essentially SUMER and CDS to derive the emission measure distribution, combined with the Extreme-Ultraviolet Imaging Telescope, EIT, and the Michelson Doppler Imager, MDI), which allowed the analysis of supergranulation boundary and interior structures. They found that He I 584.33 Å and He II 303.78 Å lines are enhanced by factors of 10 and 13 respectively in the cell boundaries and by factors 14 and 25 respectively in the cell interiors. Hence, while the enhancement factors of He I 584.33 Å line are quite similar in the two studies, higher enhancements by a factor 2-4 were derived for He II 303.78 Å line. More recently, helium enhancement factors have been revised by (50). They noted that previous studies of helium enhancements recognised the need for a treatment of radiative transfer in the relatively opaque helium lines, but did not include the possible effects of opacity on the lines used in the underlying emission measure analysis. Using this issue as starting point, they performed new calculations of the intensities of lines of helium, carbon, oxygen and silicon, by the means of two different approaches. The first approach was analogous to the optically thin approximation used by (34), while in the second approach the non-LTE transfer equation was solved together with the statistical equilibrium equations. In order to perform their calculations, (50) used atomic models of helium, carbon, oxygen and silicon, taking energy levels, collisional and radiative data essentially from CHIANTI (v. 3-4) and ionisation data from (134) for ground level ionisation and from the general formula of (146) for excited level ionisation. Using optically thin calculations and taking some adjustment to account for the behaviour of other lines formed at similar temperatures as helium lines, they obtained enhancement factors of 3 and 13 for He I 584.33 Å and He II 303.78 Å respectively. In the second type of calculations, one-dimensional atmospheric models specifying thermal properties as a function of column mass were built up and full non-LTE transfer solutions were made using the MULTI code (19). The results obtained deriving line intensities from the full radiative transfer approach showed that He I 584.33 Å, He I 537.03 Å and He II 303.78 Å line are enhanced by factors 2-5, 4-7 and 2-9 respectively, depending on the elemental abundances assumed. The revisit of helium enhancements proposed by (50) shows an improvement of the ratio between observed and predicted intensities compared with the previous work of about a factor 3 for both He I and He II. While it is difficult to explain a discrepancy of a factor 10 or more between observed and predicted intensities only assuming that the atomic data and/or the observations are in error by such an amount, an enhancement of a factor 2 or more may suggest the need to review the atomic data used in the previous work and to perform new observations. Here, this idea has been taken as starting point for the complete revisit and update of atomic data, which have been done in chapter 5. From the observational point of view, the launch of the new space-borne satellite Hinode, which includes the EIS spectrometer, allowed to take into account a larger range of EUV emission lines suitable for diagnostics, providing a more accurate analysis (chapter 4). In addition, the He II 256.32 Å line has been coupled with He II 303.78 Å line to give more constraints to He II enhancement factor. Table 6.11 shows the enhancement factors derived using the DEM analysis, as discussed in the previous sections of this chapter. All the EUV He I and He II resonance lines observed by CDS and EIS have been included in this study. Also, the first line shown in tab. 6.11 is the intercombination line of He I observed by CDS at 591.41 Å. Because of its optically thin behaviour, a proper DEM analysis should give reliable results for its predicted intensity. It should be noted that it is a very weak line, with low integrated intensity, hence the uncertainties related to the fit and the calibration procedures are quite high compared to the observed flux. However, the reconstructed intensity for this line in within the observational uncertainties, suggesting that the main mechanism that can affect the resonance lines of neutral helium may be the

| Line | | R($N_e$) | R($P_e^{(1)}$) | R($P_e^{(2)}$) | R($P_e^{(3)}$) |
|---|---|---|---|---|---|
| He I | 591.41 Å | 1.549 ± 0.862 | 1.541 ± 0.764 | 1.709 ± 0.862 | 2.206 ± 1.125 |
| He I | 515.62 Å | 0.920 ± 0.313 | 0.855 ± 0.256 | 0.875 ± 0.271 | 0.981 ± 0.311 |
| He I | 522.21 Å | 1.782 ± 0.619 | 1.685 ± 0.517 | 1.714 ± 0.543 | 1.671 ± 0.538 |
| He I | 537.03 Å | 1.613 ± 0.563 | 1.613 ± 0.496 | 1.785 ± 0.566 | 2.108 ± 0.680 |
| cHe I | 584.33 Å | 0.504 ± 0.180 | 0.499 ± 0.158 | 0.551 ± 0.179 | 0.706 ± 0.230 |
| sHe I | 584.33 Å | 0.453 ± 0.157 | 0.449 ± 0.138 | 0.496 ± 0.155 | 0.635 ± 0.200 |
| He II | 303.78 Å | 13.017 ± 4.026 | 13.154 ± 4.123 | 12.832 ± 4.041 | 12.467 ± 3.954 |
| He II | 256.32 Å | 5.224 ± 1.313 | 5.746 ± 1.345 | 5.594 ± 1.320 | 5.339 ± 1.294 |

Table 6.11: Ratios between observed and predicted intensities for the intercombination line of He I and the resonance lines of He I and He II. A model with both uniform density (R($N_e$)) and uniform pressure (R($P_e^{(1)}$), R($P_e^{(2)}$) and R($P_e^{(3)}$)) have been used. The values of $N_e$ and $P_e$ have been established in sec. 6.1.3.

opacity. The comparison between observed and predicted intensities for the He I resonance lines does not show a real enhancement. Furthermore, the first line of the resonance series shows a depletion of a factor ~2, again supporting the opacity mechanisms. Table 6.12 allows a comparison of the present enhancement factors and the ones derived by (34), (47) and (50). Differences with ealier calculations for neutral helium arise mostly from the new revised atomic data employed not only for helium but also and mainly for the other ions used in deriving the DEM curve. Nevertheless, this analysis examines a quiet Sun region near the disk center only. As a consequence, any information on helium behaviour in active regions or coronal holes is not provided here. Further work will extend this analysis to a wider range of solar plasma conditions, in order to give more constraints to the new enhancement factors obtained for He I.

| Source | He I | He II |
|---|---|---|
| (34) | 15 | 5.5 |
| (47) | 10-14 | 13-25 |
| (50) | 2-5 | 2-13 |
| Present work | 0.5-2 | 5-13 |

Table 6.12: Comparison between the enhancement factors provided in literature and those derived by the present analysis.

By contrast, the computed enhancement for He II is not in disagreement with either that of (34) or (47). As suggested by (47), a full non-LTE radiative transfer calculations may give more reliable constraints to He II enhancement factor, without including *ad hoc* assumptions on the fractions of escaping photons. However, as mentioned in section 6.2.1, other issues may affect the intensities of both He I 303.78 Å and He II 256.32 Å lines, ranging from calibration uncertainty to line blending. Moreover, even if further unknown blends may explain enhancement of a factor 5-6 of He II 256.32 Å line, it is unlikely that instrument effects can clarify the higher enhancement of He II 303.33 Å. Assuming that the discrepancy for neutral helium is solved by a consistent analysis and the use of appropriate atomic data, the enhancement of He II may be explain by some processes which could selectively enhance ionised helium intensities. A suggestion may be sought in the relationship between the photospheric magnetic flux and the EUV emission, recently examined by (223) and (224) and related to coronal heating studies. In fact, the solar magnetic flux, generated in the convection zone, passes through the partially ionised photospheric and chromospheric plasma before it can appear high up in the upper transition region and solar corona. This connection between the lower and upper layers of the solar atmosphere might affect both the distribution of intensities and their integrated values of EUV transition region lines, providing different effects for neutral and ionised elements. A global relationship between the EUV integrated intensity and the total magnetic flux has been analysed by (223), concluding that the intensity of transition region lines in active regions depend on the photospheric magnetic flux density. However, they found that this relation is inadequate for determining coronal heating mechanisms. (224) extended this study, using both spatially resolved EUV intensities and spatially resolved magnetic flux densities. They focussed their work on the comparison between the intensity distribution of the O V 629.72 Å line and the resolved photospheric magnetic field, as observed in a series of active regions. They finally postulated the presence of a basal heating as a proof that the magnetic field is one of the major factors which contribute to the basal component of the coronal plasma heating. On the other hand, (3), following the suggestion of (57), proposed a new scenario which takes into account the spatial relationship among the observed chromosphere, transition region and corona. He speculated that cross-field diffusion and a subsequent

parallel conduction may affect line intensity values giving an explanation of helium enhancements. Here, it is proposed that the combined suggestions of (224), on the connection between line intensities and magnetic field, and of (3), on cross-field diffusion, might provide the final solution of helium enhancement problem. However, more spatially resolved observations are needed, especially for active regions together with magnetic field observations, in order to provide a solid support to this suggestion.

# Chapter 7

# Conclusions and future work

## 7.1 Objective of the thesis and general conclusions

The scope of this thesis is the use of spectroscopy to predict and reconstruct line intensity as a means of interpreting observational data. In particular, the main objective is to provide a complete and accurate approach to the investigation of the seventy year old problem of helium enhancement in the solar upper atmosphere, using as means the most up-to-date observational and atomic tools available. From the observational point of view, of all the solar missions in flight now, only three EUV spectrometers in space, SoHO/SUMER, SoHO/CDS and Hinode/EIS, are dedicated to solar physics studies. Hence, the first big advantage of this work is that it is concerned with the "full set" of available instruments. They cover all together a large range of temperatures (from about $10^4$ K to $10^7$ K), allowing a complete analysis of the solar atmosphere from the upper chromosphere to the hot corona. For the purpose of this thesis, in fact, it is essential to examine lines formed at the lower temperatures of the upper chromosphere/lower transition region, in order to investigate the plasma conditions of the atmospheric layer from where EUV helium lines are believed to originate. However, it is also important to include lines formed in the upper transition region and corona, to take into account the possible connection amongst the atmospheric layers, from the chromosphere to the corona. The new observation sequences written for this goal allowed selection of a large set of lines suitable for diagnostics, increasing the temperature coverage. In addition, the consistent results obtained in the cross-calibration procedure (sec. 4.2.4) can be taken as a proof of the reliability and accuracy of the analysis carried out in this thesis. Also, this adds confidence to any future work and joint observations which involve the three spectrometers together. In order to describe the particular phenomena which occur in the solar plasma and to propose solutions to unresolved problems, it is important to relate the observations to theoretical models. Even assuming a perfect calibration for the instruments involved in a specific set of observations, the reliability of every diagnostic analysis is strictly related to the understanding of the underlying atomic physics and the accuracy of the basic and derived atomic data adopted. In such context, this work is focussed on the review and update of light elements, concentrating on the precision and accuracy of the previous calculations and performing new computation to extend and top-up preferred data from literature (sec. 5.2). A recommendation of atomic data with appropriate accuracy is very important to avoid interpretation errors. An example is the O IV I(787)/I(279) theoretical line ratio (fig. 6.18) examined by (78), which shows a significant deviation from the observed ratio, caused by the insufficient number of transitions included in their atomic model (fig. 5.3). The additional transitions, taken from (106) calculations and included in the revised data, resulted in a decrease of the theoretical line ratio compared to that of (78), providing a good agreement with observations. Furthermore, other discrepancies regarding Li-like and Na-like ions (6.1.6) and He II line ratio (6.14), found in previous work, seem to be close to the solution when the revised set of atomic data is used. Additionally, the more accurate atomic data now available for iron ions and the updated atomic data for silicon ions (sec. 5.3.2) allowed confirmation of the results on silicon and iron abundances, which have been found by (95) in the analysis of data of an active region observed by SERTS-89. In the investigation of the quiet Sun region observed in April 2009, the silicon and iron abundances have been found to be close to photosphere values, suggesting a lower ($<$ 10 eV) cut-off for FIP effects in both quiet Sun and active regions. Also, new calculation for silicon ionisation, both for ground to ground state ionisation and metastable resolved have been performed (sec. 5.3). Because of its low formation temperature (log(T/K)$\leq$4.5), a key ion in the present analysis is $Si^{+1}$. From a collisional-radiative point of view and at chromospheric density, this places the problem in a finite density regime leading to redistribution amongst excited states and reducing the

effective recombination (especially the dielectronic part of it), due to re-ionisation of excited states. On this atomic side, the development of this work is within the ADAS project, which is designed to apply to all densities of plasma and is additionally orientated to dynamic plasmas. Hence, it lies in a more general context, with applications not only addressed to astrophysical plasmas but also to those of magnetic confinement fusion devices. Regarding the helium problem, the combined use of new specific observations and revised atomic data has lead to the suggestion that the main mechanism that affects the intensity behaviour of the resonance lines of neutral helium may be the opacity. The comparison between observed and reconstructed intensities for He I resonance lines and the intercombination line does not show a real enhancement. By contrast, the first line of the $1s^2\,{}^1S - 1snp\,{}^1P$ resonance series shows a depletion of a factor ~2, supporting the opacity mechanism. Different conclusion have been found for single ionised helium lines. The enhancement factors obtained here agree with those of previous work. The different behaviour of He I and He II lines may lead to proposal of some mechanism that affects ionised helium only. Some suggestion on the combined effects of the photospheric magnetic and cross-field diffusion has been proposed in section 6.3.

## 7.2 Areas of future work

This thesis deals with the analysis of a quiet Sun region near the disk centre only. As a consequence, any information on helium behaviour in active regions or coronal holes cannot be derived. Further work will extend this analysis to a wider range of solar plasma conditions in order to give more constraints to the new enhancement factors determined both for He I and He II line intensities. Also, new resolved spectral observations should be done together with magnetic field observations using active region targets, in order to investigate the possible connection with the stronger magnetic field and its relation with single ionised helium line intensities. A future development in this context will be the launch of Solar Orbiter, which will be dedicated to improving the understanding of fundamental physical processes common to all solar, astrophysical and laboratory plasmas, together with the study of the solar activity and its connection with the inner solar system. In particular, following CDS and SUMER, the new spectrometer onboard SPICE (SPectral Imaging of the Coronal Environment) will be able, in theory, to observe in the second order further lines belonging to the He I $1s^2\,{}^1S - 1snp\,{}^1P$ resonance series with $n$ from 6 to 14. It will permit a more detailed investigation of the behaviour of neutral helium and exclude or not the difference between He I and He II resonance line intensities found out in this work. On the atomic point of view, the new GCR ionisation calculation should be extended to other elements of astrophysical interest, such as magnesium, sulphur, calcium and iron. Especially magnesium and iron are becoming a priority. The new spacecraft SDO, launched in February 2010, allows observations of a series of magnesium lines, which require the preparation and revision of excitation and ionisation data suitable for their analysis. In addition, Hinode/EIS observes many lines which arise from different iron ions. Atomic data are becoming available and more reliable for many iron ions (within the iron project), but they are still incomplete. Also, the steps performed in this thesis for deriving fractional abundances (fig. 5.6) will need to be further automated, so that the work can be extended more easily to the elements above mentioned and eventually to further elements. This will be done particularly for the procedure described in section 5.3.1. An expert system will be developed to make automatic the calculations for ionisation resolved into ground and metastable initial and final states using the semi-empirical formula of (146). Finally, the atomic databases (in particular ADAS in the context of this thesis) have to be updated including the data revised for this work and the new GCR calculations for silicon and possibly for other elements, higher than neon, which are relevant in the astrophysics environment.

# Bibliography


[1] S. Patsourakos, P. Gouttebroze and A. Vourlidas. 'The quiet Sun network at subarcsecond resolution: VAULT observations and radiative transfer modeling of cool loops'. ApJ, **664** (2007) 1214

[2] J. M. Fontenla, E. H. Avrett and R. Loeser. 'Energy balance in the solar transition region. IV. Hydrogen and helium mass flows with diffusion'. ApJ, **572** (2002) 636

[3] P. Judge. 'An explanation of the solar transition region'. ApJ, **683** (2008) L87

[4] G. A. Fischbacher, S. D. Loch and H. P. Summers. 'A study of opacity in SOHO-SUMER and SOHO-CDS spectral observations. II. Atmospheric structure at the solar limb'. Astron. Astrophys., **357** (2000) 767–776

[5] D. H. Brooks, G. A. Fischbacher, A. Fludra, R. H. Harrison, D. E. Innes, E. Landi, M. Landini, J. Lang, A. C. L. andS. D. Loch, R. W. P. McWhirter and H. P. Summers. 'A study of opacity in SOHO-SUMER and SOHO-CDS spectral observations. I. Opacity deduction at the limb'. Astron. Astrophys., **357** (2000) 697–715

[6] D. H. Brooks, H. P. Summers, R. A. Harrison, J. Lang and A. C. Lanzafame. 'EUV Spectral Variability and Non-Equilibrium Ionisation in the Quiet Sun'. Astrophysics and Space Science, **261** (1999) 91

[7] R. W. P. McWhirter. 'Spectral Intensities'. In R. H. Huddlestone and S. L. Leonard (Editors), 'Plasma diagnostic techniques', Academic Press New York London (1965)

[8] H. P. Summers. *ADAS manual*. JET Joint Undertaking (1994)

[9] R. W. P. McWhirter and H. P. Summers. 'On radiated power from impurities in plasmas'. In C. F. Barnett and M. F. A. Harrison (Editors), 'Applied Atomic Collision Physics Vol. 2', volume 2, 51. Academic Press (1984)

[10] N. R. Badnell, M. G. O'Mullane, H. P. Summers, Z. Altun, M. A. Bautista, J. Colgan, T. W. Gorczyca, D. M. Mitnik, M. S. Pindzola and O. Zatsarinny. 'Dielectronic recombination data for dynamic finite-density plasmas I. Goals and methodology'. Astron. Astrophys., **406**(3) (2003) 1151–1165. doi:10.1051/0004-6361:20030816

[11] H. P. Summers, W. J. Dickson, M. G. O'Mullane, N. R. Badnell, A. D. Whiteford, D. H. Brooks, J. Lang, S. D. Loch and D. C. Griffin. 'Ionization state, excited populations and emission of impurities in dynamic finite density plasmas: I. The generalized collisional-radiative model for light elements'. Plasma Phys. Control. Fusion, **48**(2) (2006) 263–293. doi:10.1088/0741-3335/48/2/007

[12] S. D. Loch, M. S. Pindzola, C. P. Ballance and D. C. Griffin. 'The effects of radiative cascades on the x-ray diagnostic lines of $Fe^{16+}$'. J. Phys. B, **39**(1) (2006) 85–104. doi:10.1088/0953-4075/39/1/009

[13] G. Y. Liang, A. D. Whiteford and N. R. Badnell. 'R-matrix electron-impact excitation data for B-like Si and its application in cool stars'. Astron. Astrophys., **499** (2009) 943–954

[14] A. R. Foster. *On the Behaviour and Radiating Properties of Heavy Elements in Fusion Plasmas*. Ph.D. thesis, University of Strathclyde (2008). Available from: http://www.adas.ac.uk/theses/foster_thesis.pdf

[15] K. Wilhem, W. Curdt, E. Marsch, U. Schühle, P. Lemaire, A. Gabriel, J. C. Vial, M. Grewing, H. M. C. E, S. D. Jordan, A. I. Poland, R. J. Thomas, M. Kühne, J. G. Timothy, D. M. Hassler and O. H. W. Siegmund. 'SUMER-solar ultraviolet measurements of emitted radiation'. Solar Phys., **162** (1995) 189

[16] R. A. Harrison, E. C. Sawyer, M. K. Carter and coauthors. 'The Coronal Diagnostic Spectrometer for the Solar and Heliospheric Observatory'. Sol. Phys., **162** (1995) 233

[17] J. L. Culhane, L. K. Harra, A. M. James, K. Al-Janabi, L. J. Bradley, R. A. Chaudry, K. Rees, J. A. Tandy, P. Thomas and coauthors. 'The EUV Imaging Spectrometer for Hinode'. Solar Physics, **243** (2007) 19–61

[18] D. H. Brooks, G. A. Fischbacher, A. Fludra, R. A. Harrison, D. E. Innes, E. Landi, M. Landini, J. L. A. C. Lanzafame, S. D. Loch, R. W. P. McWhirter, H. P. Summers and W. T. Thompson. 'The quiet Sun extreme ultraviolet spectrum observed in normal incidence by the SOHO coronal diagnostic spectrometer'. Astron. Astrophys., **347** (1999) 277–312. ADS: http://adsabs.harvard.edu/abs/1999A%26A...347..277B

[19] M. Carlsson. 'A Computer Program for Solving Multi-Level Non-LTE Radiative Transfer Problems in Moving or Static Atmospheres'. Upps. Astron. Obs. Rep., **33** (1986) 1–165

[20] L. Goldberg. 'The Temperature of the Solar Chromosphere'. ApJ, **89** (1939) 673

[21] T. Hirayama. 'The abundance of helium in prominences and in the chromosphere'. Sol. Phys., **17** (1971) 50

[22] H. Zirin. 'The helium chromosphere, coronal holes, and stellar X-rays'. ApJ, **199** (1975) L63

[23] R. W. Milkey. 'Comments concerning the photoionization model for excitation of resonance lines of He I and He II in the solar chromosphere'. ApJ, **199** (1975) L131

[24] G. W. Cushman, L. Farwell, G. Godden and W. A. Rense. 'Solar line profiles of He I 584 A and He II 304 A'. J.Geophys.Res., **80** (1975) 482

[25] G. A. Doschek, W. E. Behring and U. Feldman. 'The Widths of the Solar he i and he II Lines at 584, 537, and 304 Å'. ApJ, **190** (1974) L141

[26] W. M. Neupert, G. L. Epstein, R. J. Thomas and W. T. Thompson. 'An EUV imaging spectrograph for high-resolution observations of the solar corona'. Sol.Phys., **137** (1992) 87

[27] V. Domingo, B. Fleck and A. I. Poland. 'The SoHO mission: an overview'. Solar Physics, **162** (1995) 1–37

[28] R. G. Athay and H. R. Johnson. 'The Excitation of he i in the Spectrum'. Astrophys. J., **131** (1960) 413–428. doi:10.1086/146846

[29] R. G. Athay. 'Theoretical Line Intensities. III. Solar UV Lines and Continua of h, he i, and he II and the Chromospheric Model'. Astrophys. J., **142** (1965) 755–766. doi:10.1086/148336

[30] R. W. Milkey, J. N. Heasley and H. A. Beebe. 'Helium Excitation in the Solar Chromosphere: He I in a Homogeneous Chromosphere'. ApJ, **186** (1973) 1043

[31] J. E. Vernazza, E. H. Avrett and R. Loeser. 'Structure of the solar chromosphere. Basic computations and summary of the results'. ApJ, **184** (1973) 605

[32] A. K. Dupree and E. M. Reeves. 'The extreme-ultraviolet spectrum of the quiet Sun'. ApJ, **165** (1971) 599

[33] C. C. Batalha and R. De La Reza. 'The helium line formation in late-type stars. I-The quiet sun'. MNRAS, **240** (1989) 23

[34] C. Jordan. 'The intensities of helium lines in the solar EUV spectrum'. MNRAS, **170** (1975) 429

[35] A. G. Hearn. 'The ultra-violet resonance lines of neutral helium from the Sun'. MNRAS, **142** (1969) 53

[36] A. G. Hearn. 'A suggestion for the measurements of He II line intensities emitted by the Sun'. MNRAS, **142** (1969) 259

[37] R. Shine, H. Gerola and J. L. Linsky. 'Diffusion effects on the line intensities of He I and He II in the solar transition region'. ApJ, **202** (1975) L101

[38] J. M. Fontenla, E. H. Avrett and R. Loeser. 'Energy balance in the solar transition region. III-Helium emission in hydrostatic, constant-abundance models with diffusion'. ApJ, **406** (1993) 319

[39] J. M. Fontenla, E. H. Avrett and R. Loeser. 'Energy balance in the solar transition region. I - Hydrostatic thermal models with ambipolar diffusion'. ApJ, **355** (1990) 700

[40] J. M. Fontenla, E. H. Avrett and R. Loeser. 'Energy balance in the solar transition region. II-Effects of pressure and energy input on hydrostatic models'. ApJ, **377** (1991) 712

[41] V. Andretta and H. P. Jones. 'On the Role of the Solar Corona and Transition Region in the Excitation of the Spectrum of Neutral Helium'. Astrophys. J., **489**(2) (1997) 375–394. doi:10.1086/304760

[42] P. J. D. Mauas, V. Andretta, A. Falchi, R. Falciani, L. Teriaca and G. Cauzzi. 'Helium Line Formation and Abundance in a Solar Active Region'. ApJ, **619** (2005) 604

[43] V. Andretta, P. J. D. Mauas, A. Falchi and L. Teriaca. 'Helium line formation and abundance during a C-class flare'. Astrophys. J., **681** (2008) 650–663

[44] E. H. Avrett and R. Loeser. *Line transfer in static and expanding spherical atmospheres*. in Methods in Radiative Transfer, ed. W. Kalkofen (Cambridge: Cambridge Univ. Press) (1984). ISBN 0-521-25620-8

[45] E. H. Avrett and R. Loeser. *Solar and Stellar Atmospheric Modeling Using the Pandora Computer Program*. in IAU Symp. 210, Modelling of Stellar Atmospheres, ed. N. Piskunov, W. W. Weiss, & D.F. Gray (Dordrecht: Kluwer) (2003)

[46] C. Jordan, G. R. Smith and E. R. Houdebine. MNRAS, **362** (2005) 411

[47] K. P. Macpherson and C. Jordan. MNRAS, **308** (1999) 510

[48] E. Landi and M. Landini. 'Simultaneous temperature and density diagnostics of optically thin plasma'. Astron. Astrophys., **327** (1997) 1230–1241

[49] P. Brekke, W. T. Thompson, T. N. Woods and F. G. Eparvier. ApJ, **536** (2000) 959

[50] A. Pietarila and P. G. Judge. 'On the formation of the resonance lines of helium in the Sun'. Astrophys. J., **606** (2004) 1239–1257

[51] V. Andretta, S. D. Jordan, J. W. Brosius, J. M. Davila, R. J. Thomas, W. E. Behring, W. T. Thompson and A. Garcia. 'The Role of Velocity Redistribution in Enhancing the Intensity of the HE II 304 Line in the Quiet-Sun Spectrum'. Astrophys. J., **535**(1) (2000) 438–453. doi:10.1086/308833

[52] A. F. Viñas, H. K. Wong and A. J. Klimas. ApJ, **528** (2000) 509

[53] J. D. Scudder. 'Ion and electron suprathermal tail strengths in the transition region: Support for the velocity filtration model of the corona'. ApJ, **427** (1994) 446

[54] G. R. Smith and C. Jordan. MNRAS, **337** (2002) 666

[55] C. Wahlstrøm and M. Carlsson. ApJ, **433** (1994) 417

[56] G. R. Smith. MNRAS, **341** (2003) 143

[57] P. G. Judge and A. Pietarila. 'On the formation of extreme-ultraviolet helium lines in the Sun: analysis of SoHO data'. Astrophys. J., **606** (2004) 1258–1275

[58] K. Wilhelm, B. N. Dwivedi, E. Marsch and U. Feldman. 'Observations of the Sun at vacuum-ultraviolet wavelengths from space. Part I: Concepts and instrumentation.' Space Science Reviews, **111**(3) (2004) 415–480. doi:10.1023/B:SPAC.0000032695.27525.54

[59] T. Kosugi, K. Matsuzaki, T. Sakao, T. Shimizu, Y. Sone, S. Tachikawa, T. Hashimoto, K. Minesugi, A. Ohnishi, T. Yamada, S. Tsuneta, H. Hara, K. Ichimoto, Y. Suematsu, M. Shimojo, T. Watanabe, S. Shimada, J. M. Davis, L. D. Hill, J. K. Owens, A. M. Title, J. L. Culhane, L. K. Harra, G. A. Doschek and L. Golub. 'The Hinode (Solar-B) mission: an overview'. Solar Physics, **243** (2007) 3–17

[60] W. Curdt, P. Brekke, U. Feldman, K. Wilhelm, B. N. Dwivedi, U. Schühle and P. Lemaire. 'The SUMER spectral atlas of solar-disk features'. Astron. Astrophys., **375** (2001) 591–613

[61] J. Lang, W. T. Thompson, C. D. Pike, B. J. Kent and C. Foley. In A. Pauluhn, M. C. E. Huber and R. von Steiger (Editors), 'The Radiometric Calibration of SOHO. ISSI Scientific Report SR-002', chapter 7, 105 (2002)

[62] J. Lang, D. H. Brooks, A. C. Lanzafame, R. Martin, C. D. Pike and W. T. Thompson. 'The in-flight monitoring and validation of the SOHO CDS Normal Incidence Spectrometer radiometric calibration'. Astron. Astrophys., **463** (2007) 339–951

[63] G. Del Zanna, V. Andretta, P. C. Chamberlin, T. N. Woods and W. T. Thompson. 'The EUV spectrum of the Sun: long-term variations in the SOHO CDS NIS spectral responsivities'. Astron. Astrophys., **518** (2010) A49

[64] P. R. Young, T. Watanabe, H. Hara and J. T. Mariska. 'High-precision density measurements in the solar corona. I. Analysis methods and results for Fe XII and Fe XIII'. Astron. Astrophys., **495** (2009) 587–606

[65] J. Lang, B. J. Kent, W. Paustian, C. M. Brown, C. Keyser, M. R. Anderson, G. C. R. Case, R. A. Chaudry, A. M. James, C. M. Korendyke, C. D. Pike, B. J. Probyn, D. J. Rippington, J. F. Seely, J. A. Tandy and M. C. R. Whillock. 'Laboratory calibration of the Extreme-Ultraviolet Imaging Spectrometer for the Solar-B satellite'. Applied Optics IP, **45** (2006) 8689–8705

[66] J. Lang, H. E. Mason and R. W. P. McWhirter. Sol. Phys., **129** (1990) 31

[67] W. T. Thompson. 'Post-recovery broadened line profiles'. CDS Software Note 53, NASA Goddard Flight Center (1999). Available from: http://solar.bnsc.rl.ac.uk/swnotes/cds_swnote_53.pdf

[68] A. Pauluhn, I. Rüedi, S. K. Solanki, J. Lang, C. D. Pike, U. Schühle, W. T. Thompson, J. Hollandt and M. C. E. Huber. Applied Optics, **38** (1999) 7035–7046

[69] A. Pauluhn, I. Rüedi, S. K. Solanki, U. Schühle, K. Wilhelm, J. Lang, W. T. Thompson and J. Hollandt. Applied Optics, **34** (2001) 6292–6300

[70] E. Landi and P. R. Young. Astrophys. J., **714** (2010) 636–643

[71] J. P. Meyer. Astrophys. J. Suppl. Ser., **57** (1985) 173–204

[72] R. Wilson. 'The spectroscopy of non-thermal plasmas'. J. Quant. Spectrosc. Radiat. Transfer, **2** (1962) 477–490

[73] M. S. Seaton. 'Excitation of coronal lines by proton impact'. ApJ, **127** (1964) 191–194

[74] A. V. Phelps. 'Collisions of H+, H+2, H+3, ArH+, H-, H, and H2 with Ar and of Ar+ and ArH+ with H2 for Energies from 0.1 eV to 10 keV'. J. Phys. Chem. Ref. Data, **21** (1992) 883

[75] R. Janev, G. Ivanovski and E. A. Solov'ev. 'Ionization of hydrogen atoms by multiply charged ions at low energies: The scaling law.' Phys. Rev. A, **49** (1994) 645–648

[76] A. C. Lanzafame. 'Diagnostic of stellar chromospheres and transition regions'. ASP Conferences Series, **158** (1999) 258–296

[77] J. G. Doyle, H. P. Summers and P. Bryans. A&A, **430** (2005) L29

[78] K. Muglach, E. Landi and G. A. Doschek. 'The electron temperature of the solar transition region as derived from EIS and SUMER'. Astrophys. J., **708** (2010) 550–559

[79] K. P. Dere, E. Landi, H. E. Mason, B. C. Monsignori-Fossi and P. R. Young. Astron. Astrophys. Suppl. Ser., **125** (1997) 149–173

[80] H. P. Summers, H. Anderson, M. G. O'Mullane and M. G. von Hellermann. 'Spectral Analysis of Highly Ionised Fusion Plasmas Using Beams'. Phys. Scr., **T92** (2001) 80–84. doi:10.1238/Physica.Topical.092a00080

[81] N. R. Badnell. 'On the effects of the two-body non-fine-structure operators of the Breit-Pauli Hamiltonian'. J. Phys. B, **30**(1) (1997) 1–11. doi:10.1088/0953-4075/30/1/005

[82] R. D. Cowan. *The Theory of Atomic Structure and Spectra*. University of California Press (1981). ISBN 0520038215

[83] W. M. Eissner, M. Jones and N. H. Comput. Phys Commun., **8** (1974) 270

[84] A. Bar-Shalom, M. Klapisch and J. Oreg. 'Electron collision excitations in complex spectra of ionized heavy atoms'. Phys. Rev. A, **38** (1988) 1773–1784

[85] M. F. Gu. Astrophys. J., **590** (2003) 1131–1140

[86] I. Bray and A. T. Stelbovics. Phys. Rev. A, **46** (1992) 6995–7011

[87] K. Bartschat and I. Bray. 'Electron-impact ionization of atomic hydrogen from the 1S and 2S states'. J. Phys. B, **29**(15) (1996) L577–L583. doi:10.1088/0953-4075/29/15/005

[88] D. C. Griffin, N. R. Badnell and M. S. Pindzola. 'R-matrix electron-impact excitation cross sections in intermediate coupling: an MQDT transformation approach'. J. Phys. B, **31**(16) (1998) 3713–3727. doi:10.1088/0953-4075/31/16/022

[89] P. H. Norrington and I. P. Grant. J. Phys. B: At. Mol. Opt. Phys., **20** (1987) 4869–4881

[90] C. P. Ballance, N. R. Badnell and E. S. Smith. J. Phys. B: At. Mol. Opt. Phys., **36** (2003) 3707–3719

[91] G. Lach and K. Pachucki. Phys. Rev. A, 042510

[92] I. D. Paton. *On the neutral gas puff as a tokamak edge diagnostic*. Ph.D. thesis, University of Strathclyde (2005). Available from: http://www.adas.ac.uk/theses/paton_thesis.pdf

[93] F. J. de Heer, R. Hoekstra and H. P. Summers. Atomic and plasma material interaction for fusion, **3** (1992) 47

[94] H. L. Zhang and D. H. Sampson. At. Data Nucl. Data Tables, **52** (1992) 143

[95] A. C. Lanzafame, D. H. Brooks, J. Lang, H. P. Summers, R. J. Thomas and A. M. Thompson. 'ADAS analysis of the differential emission measure structure of the inner solar corona . Application of the data adaptive smoothing approach to the SERTS-89 active region spectrum'. Astron. Astrophys., **384** (2002) 242–272

[96] R. W. P. McWhirter. 'An Assessment of Collision Strengths for Lithium and Lithium-Like Ions'. At. Data Nucl. Data Tables, **57** (1994) 39–70

[97] C. E. Moore. In J. W. Gallacher (Editor), 'Tables of Spectra of Hydrogen, Carbon, Nitrogen and Oxygen Atoms and Ions', CRC Series in Evaluated Data in Atomic Physics. CRC Press (1993)

[98] A. Hibbert. J. Phys. B, **13** (1980) 1721–1730

[99] N. Allard, M.-C. Artru, T. Lanz and M. L. Dourneuf. 'Compilation of atomic oscillator strengths for carbon, nitrogen and oxygen ions - The beryllium isoelectronic sequence (C III, N IV, and O V)'. Astron. Astrophys. Suppl. Ser., **84** (1990) 563–600

[100] H. L. Zhang, D. H. Sampson and C. J. Fontes. At. Data Nucl. Data Tables, **44** (1990) 31–77

[101] H. P. Muehlethaler and H. Nussbaumer. Astron. Astrophys., **48** (1976) 109–114

[102] K. A. Berrington. At. Data Nucl. Data Tables, **57** (1994) 71–95

[103] B. Edlén. Phys. Scripta, **28** (1983b) 48

[104] C. Froese Fischer. J. Phys. B., **16** (1983) 157

[105] G. Merkelis, M. J. Vilkas, G. Gaigalas and R. Kisielius. Phys. Scr., **51** (1994) 233

[106] D. H. Sampson, H. L. Zhang and C. Fontes. At. Data Nucl. Data Tables, **57** (1994) 97

[107] H. L. Zhang, M. Graziani and A. K. Pradhan. Astron. Astrophys., **283** (1994) 319

[108] W. L. Wiese, M. W. Smith and B. M. Glennon. 'Atomic Transition Probabilities (H through Ne — A Critical Data Compilation)'. Natl. Stand. Ref. Data Ser., Natl. Bur. Stand. (U.S.), NSRDS-NBS 4, vol. i (1966)

[109] K. M. Aggarwal and F. P. Keenan. 'Excitation rate coefficients for fine-structure transitions in O III'. Astrophys. J. Suppl. Ser., **123** (1999) 311–349

[110] D. C. Griffin and N. R. Badnell. 'Electron-impact excitation of Ne4+'. J. Phys. B: At. Mol. Opt. Phys., **33** (2000) 4389–4408

[111] K. M. Aggarwal. Astrophys. J. Suppl. Ser., **54** (1984) 1–15

[112] K. M. Aggarwal. Astrophys. J. Suppl. Ser., **58** (1985) 289–296

[113] K. M. Aggarwal. Astrophys. J. Suppl. Ser., **61** (1986) 699–717

[114] A. K. Bhatia and G. A. Doschek. Atomic Data and Nuclear Data Tables, **55** (1993) 315

[115] R. P. Stafford, K. L. Bell, A. Hibbert and W. P. Wijesundera. Mon. Not. R. Astr. Soc., **268** (1994) 816–820

[116] D. H. Brooks. Ph.D. thesis, University of Strathclyde (1997)

[117] B. M. McLaughlin and K. L. Bell. 'Analytical FITS for electron collisionally excited effective collision strengths of O II'. Astrophys. J. Suppl. Ser., **94** (1994) 825–827

[118] A. K. Bhatia and S. O. Kastner. ApJ, **332** (1988) 1063

[119] C. A. Ramsbottom, K. L. Bell and F. P. Keenan. 'Effective collision strengths for fine-structure forbidden transitions among the $2s^2 2p^3$ levels of Neiv'. Mon. Not. R. Astr. Soc., **293** (1998) 233–238

[120] D. H. Sampson, H. L. Zhang and C. Fontes. At. Data Nucl. Data Tables, **44** (1990) 209–271

[121] D. C. Griffin, N. R. Badnell, M. S. Pindzola and J. A. Shaw. 'Electron-impact excitation of Mg-like ions'. J. Phys. B, **32** (1999) 2139–2152

[122] S. S. Churilov and V. E. Levashov. Phys. Scr., **48** (1993) 425–435

[123] E. Landi, P. J. Storey and C. J. Zeippen. 'Atomic Data and Spectral Line Intensities for Ca VIII'. ApJ, **607** (2004) 640–652

[124] S. S. Tayal. 'Electron Collision Excitation of Fine-Structure Levels in S IV'. Astrophys. J., **530** (2000) 1091–1104

[125] S. S. Tayal and G. P. Gupta. 'Collision Strengths for Electron Collision Excitation of Fine-Structure Levels in S III'. Astrophys. J., **526** (1999) 544–548

[126] B. C. Fawcett and H. E. Mason. 'A slater parameter optimization method applied to the computation of collision strengths for Image XIII'. At. Data Nucl. Data Tables, **43** (1989) 245–258

[127] P. J. Storey, G. Del Zanna, H. E. Mason and C. J. Zeippen. 'Atomic data from the IRON Project'. Astron. Astrophys., **433** (2005) 717–730

[128] G. Del Zanna and H. E. Mason. 'Benchmarking atomic data for astrophysics: Fe XII'. Astron. Astrophys., **433** (2005) 731–744

[129] A. K. Bhatia and G. A. Doschek. At. Data Nucl. Data Tables, **64** (1996) 183–222

[130] G. Del Zanna, K. A. Berrington and H. E. Mason. 'Benchmarking atomic data for astrophysics: Fe X'. Astron. Astrophys., **422** (2004) 731–749

[131] M. Malinovsky, J. Dubau and S. Sahal-Brechot. 'Population processes of 3p/4/4s levels of Fe X'. Astrophys. J., **235** (1980) 665–677

[132] D. C. Griffin, M. S. Pindzola and N. R. Badnell. 'Electron-impact excitation of Fe7+'. Astron. Astrophys. Suppl. Ser., **142** (2000) 317–323

[133] M. C. Witthoeft and N. R. Badnell. 'Atomic data from the IRON Project. LXV. Electron-impact excitation of Fe6+'. Astron. Astrophys., **481** (2008) 543–551

[134] M. Arnaud and R. Rothenflug. 'An updated evaluation of recombination and ionization rates'. Astron. Astrophys. Suppl. Ser., **60** (1985) 425–457. Available from: http://adsabs.harvard.edu/abs/1985A%26AS..60..425A

[135] M. Arnaud and J. Raymond. 'Iron ionization and recombination rates and ionization equilibrium'. Astrophys. J., **398** (1992) 394–406. doi:10.1086/171864

[136] H. P. Summers. 'Tables and graphs of collisional dielectronic recombination and ionisation equilibra of H-like to A-like ions of elements'. 367, Appleton Laboratory (1974)

[137] A. K. Bhatia and E. Landi. At. Data Nucl. Data Tables, **93** (2007) 275–353

[138] A. K. Bhatia and E. Landi. Astrophys. J., **585** (2003) 587–597

[139] P. L. Dufton and A. E. Kingston. 'Effective collision strengths for SI II'. Mon. Not. R. Astr. Soc., **248** (1991) 827–828

[140] A. Burgess and H. P. Summers. 'The recombination and level populations of ions. I - Hydrogen and hydrogenic ions'. Mon. Not. R. Astr. Soc., **174** (1976) 345–391. ADS: http://adsabs.harvard.edu/abs/1976MNRAS.174..345B

[141] S. Loch, J. Munoz Burgos, C. Ballance, J. Ludlow, T.-G. Lee, M. Fogle, M. Pindzola, D. Griffin, A. Yumak, I. Yavuz and Z. Altun. 'Electron-impact ionization of atomic ions: Theoretical results'. J. Phys. Conference Series, **194**(1) (2009) 012021. doi:10.1088/1742-6596/194/1/012021

[142] W. Lotz. 'An empirical formula for the electron-impact ionization cross-section'. Z. Phys., **206** (1967) 205–211. doi:10.1007/BF01325928

[143] W. Lotz. 'Electron impact ionization cross-sections and ionization rate coefficients for atoms and ions from hydrogen to calcium'. Z. Phys., **216** (1968) 241–247. doi:10.1007/BF01392963

[144] K. P. Dere. 'Ionization rate coefficients for the elements hydrogen through zinc'. Astron. Astrophys., **466**(2) (2007) 771–792. doi:10.1051/0004-6361:20066728

[145] A. Burgess, H. P. Summers, R. W. P. McWhirter and D. M. Cochrane. 'Cross-sections for ionization of positive ions by electron impact'. Mon. Not. R. Astr. Soc., **179** (1977) 275–292

[146] A. Burgess and M. C. Chidichimo. 'Electron impact ionization of complex ions'. Mon. Not. R. Astr. Soc., **203** (1983) 1269–1280. Available from: http://adsabs.harvard.edu/abs/1983MNRAS.203.1269B

[147] H. Summers and M. B. Hooper. Phys. Plasmas, **25**(12) (1983) 1311–1344

[148] M. S. Pindzola, D. C. Griffin and C. Bottcher. 'Electron-ion collisions in the average-configuration distorted-wave approximation'. In F. Brouillard (Editor), 'Atomic Processes in Electron-Ion and Ion-Ion Collisions', volume 145, 75–91. Plenum, New York (1986)

[149] A. C. Lanzafame. 'Si II resonance multiplets in the Sun'. Astron. Astrophys., **287** (1994) 972–981

[150] S. N. Nahar. 'Oscillator Strengths for Dipole-Allowed Fine-Structure Transitions in Si II'. At. Data Nucl. Data Tables, **68** (1998) 183–201

[151] H. Nussbaumer. 'The SI II spectrum in quasi stellar objects'. Astron. Astrophys., **58** (1977) 291–293

[152] G. Y. Liang, A. D. Whiteford and N. R. Badnell. 'R-matrix electron-impact excitation data for the Na-like iso-electronic sequence'. Astron. Astrophys., **500** (2009) 1263–1269

[153] A. K. Bhatia and H. E. Mason. At. Data Nucl. Data Tables, **32** (1985) 435–469

[154] M. C. Witthoeft, A. D. Whiteford and N. R. Badnell. 'R-matrix electron-impact excitation calculations along the F-like iso-electronic sequence'. J. Phys. B: At. Mol. Opt. Phys., **40** (2007) 2969–2993

[155] M. Mohan and M. L. Dourneuf. 'Electron-impact excitation from the Si(5+) ground state, using the R-matrix method'. Astron. Astrophys., **227** (1990) 285–288

[156] H. E. Saraph and J. A. Tully. 'Atomic data from the IRON project. IV. Electron excitation of the $^2P^0_{3/2}$ – $^2P^0_{1/2}$ fine structure transition in fluorine-like ions'. Astron. Astrophys., **107** (1994) 29–38

[157] A. K. Bhatia, U. Feldman and G. A. Doscheck. Astron. Astrophys., **80** (1979) 22–26

[158] A. K. Bhatia and H. E. Mason. Mon. Not. R. Astr. Soc., **190** (1980) 925

[159] K. L. Bell, A. Matthews and C. A. Ramsbottom. Mon. Not. R. Astr. Soc., **322** (2001) 779

[160] H. L. Zhang and D. H. Sampson. At. Data Nucl. Data Tables, **72** (1999) 153–216

[161] A. K. Bhatia and E. Landi. At. Data Nucl. Data Tables, **85** (2003) 317–376

[162] I. Kink, L. Engstr$\acute{}$om and U. Feldman. 'New Identifications of Si VIII and S X Lines in the Solar Coronal Spectrum Measured by SOHO/SUMER'. Astrophys. J., **512** (1999) 496–499

[163] A. K. Bhatia and G. A. Doschek. At. Data Nucl. Data Tables, **55** (1993) 281

[164] K. M. Aggarwal. 'Electron collision strengths for transitions within the 1s/2/2s/2/2p/2/ configuration of Si IX'. J. Phys. B: At. Mol. Phys., **16** (1983) L59–L64

[165] H. L. Zhang and D. H. Sampson. At. Data Nucl. Data Tables, **258** (1994) 255–305

[166] K. A. Berrington, P. G. Burke, P. L. Dufton and A. E. Kingston. At. Data Nucl. Data Tables, **33** (1985) 345

[167] S. J. Goett and D. H. Sampson. At. Data Nucl. Data Tables, **29** (1983) 535–572

[168] D. H. Sampson, S. J. Goett and R. E. H. Clark. At. Data Nucl. Data Tables, **29** (1983) 467–534

[169] H. L. Zhang and D. H. Sampson. Astrophys. J. Suppl. Ser., **63** (1987) 487–514

[170] R. E. H. Clark, D. H. Sampson and S. J. Goett. Astrophys. J. Suppl. Ser., **49** (1982) 545–554

[171] K. M. Aggarwal and A. E. Kingston. 'Electron impact excitation of Si XIV: collision strengths and rate coefficients'. Phys. Scr., **46** (1992) 193–201

[172] F. A. Parpia and W. R. Johnson. Phys. Rev. A, **26** (1982) 1142–1145

[173] A. Burgess. 'Semi-classical theory of electron-atom collisions'. In 'Proceedings of the symposium on atomic collision processes in plasmas', AERE-R 4818 (1964). Culham Laboratory, UK. 14–16 September.

[174] P. Mazzotta, G. Mazzitelli, S. Colafrancesco and N. Vittorio. 'Ionization balance for optically thin plasmas: Rate coefficients for all atoms and ions of the elements H to Ni'. Astron. Astrophys. Suppl. Ser., **133**(3) (1998) 403–409. doi:10.1051/aas:1998330

[175] P. Bryans, N. R. Badnell, T. W. Gorczyca, J. M. Laming, W. Mitthumsiri and D. W. Savin. 'Collisional Ionization Equilibrium for Optically Thin Plasmas. I. Updated Recombination Rate Coefficients for Bare through Sodium-like Ions'. Astrophys. J. Suppl. Ser., **167** (2006) 343–356. doi:10.1086/507629

[176] P. Bryans, E. Landi and D. Savin. 'A New Approach to Analyzing Solar Coronal Spectra and Updated Collisional Ionization Equilibrium Calculations. II. Updated Ionization Rate Coefficients'. Astrophys. J., **691** (2009) 1540–1559. doi:10.1088/0004-637X/691/2/1540

[177] M. Mattioli, G. Mazzitelli, M. Finkenthal, P. Mazzotta, K. B. Fournier, J. Kaastra and M. E. Puiatti. 'Updating of ionization data for ionization balance evaluations of atoms and ions for the elements hydrogen to germanium'. J. Phys. B: At. Mol. Opt. Phys., **40** (2007) 3569–3599

[178] G. Mazzitelli and M. Mattioli. 'Ionization balance for optically thin plasmas: rate coefficients for Cu, Zn, Ga and Ge ions'. At. Data Nucl. Data Tables, **82** (2002) 313–356

[179] A. Burgess and J. A. Tully. 'On the Analysis of Collision Strengths and Rate Coefficients'. Astron. Astrophys., **254** (1992) 436–453. Available from: http://adsabs.harvard.edu/abs/1992A%26A...254..436B

[180] N. R. Badnell. Astrophys. J. Suppl. Ser., **167** (2006) 334–342

[181] N. R. Badnell. Astrophys. J., **651** (2006) L73–L76

[182] N. R. Badnell. J. Phys. B: At. Mol. Opt. Phys., **39** (2006) 4825–4852

[183] N. R. Badnell. Atomic and Molecular DiagnosticProcesses in Plasmas (Dept. Physics, Univ. Strathclyde) http://amdpp.phys.strath.ac.uk/tamoc/

[184] I. J. D. Craig and J. C. Brown. Astron. Astrophys., **49** (1976) 239

[185] I. J. D. Craig and J. C. Brown. *Inverse Problems in Astronomy*. Adam Hilger, Bristol (1986)

[186] J. C. Brown, B. N. Dwivedi, Y. M. Almleaky and P. A. Sweet. Astron. Astrophys., **249** (1991) 277

[187] P. G. Judge, V. Hubeny and J. C. Brown. 'Fundamental limitations of emission-line spectra as diagnostics of plasma temperature and density structure'. Astrophys. J., **475** (1997) 257–290

[188] R. W. P. McWhirter, P. C. Thonemann and R. Wilson. 'The heating of the solar corona. II - A model based on energy balance'. Astron. Astrophys., **40** (1975) 63–73

[189] R. A. Harrison and A. M. Thompson. 'Intensity integral inversion techniques: a study in preparation for the SoHO mission'. Technical Report 1991-092, RAL (1992)

[190] K. J. H. Phillips, U. Feldman and E. Landi. *Ultraviolet and X-ray spectroscopy of the solar atmosphere*. Cambridge University Press (2008)

[191] G. L. Withbroe. 'The analysis of XUV emission lines'. Solar Physics, **45** (1975) 301

[192] J. Sylwester, J. Schrijver and R. Mewe. 'Multitemperature analysis of solar X-ray line emission'. Solar Physics, **67** (1980) 285–309

[193] A. Fludra and J. Sylwester. 'Comparison of three methods used for calculation of the differential emission measure'. Solar Physics, **105** (1986) 323–337

[194] M. Siarkowski. 'A new method for the multitemperature analysis of solar X-ray line emission'. Solar Physics, **84** (1983) 131–138

[195] B. C. Monsignor-Fossi and M. Landini. 'Models for inner corona parameters'. Adv. Space Res., **11** (1991) (1)281–(1)292

[196] S. W. McIntosh. 'On the inference of differential emission measures using diagnostic line ratios'. Astrophys. J., **533** (2000) 1043–1052

[197] A. M. Thompson. 'Adaptive smoothing and its application to the inversion of the Crab synchrotron spectrum'. Astron. Astrophys., **240** (1990) 209–215

[198] V. Kashyap and J. J. Drake. 'PINTofALE: Package for the interactive analysis of line emission'. Bull. Astron. Soc. India, **28** (2000) 475–476. ADS: http://adsabs.harvard.edu/abs/2000BASI...28..475K

[199] C. T. H. Baker. *Numerical treatment of Integral Equation*. Oxford University Press, Oxford (1977)

[200] G. H. Golub, M. Heath and G. Wahba. 'Generalized cross-validation as a method for choosing a good ridge parameter'. Technometrics, **21** (1979) 215

[201] M. G. Cox and J. G. Hayes. 'Curve fitting: a guide and suite of algorithms for non-specialist user'. Technical Report 26, National Physical Laboratory, Teddington, Middlesex. (1973)

[202] M. G. Cox. 'The numerical evaluation of B-splines'. J. Inst. Math. Appl., **10** (1972) 134–149

[203] M. G. Cox. 'The numerical evaluation of a spline from its B-spline repre- sentation'. J. Inst. Math. Appl., **21** (1978) 135–143

[204] U. Feldman and K. G. Widing. 'Elemental abundances in the upper atmospheres derived by spectroscopic means'. Space Science Reviews, **107** (2003) 665–720

[205] A. Fludra and J. T. Schmelz. 'The absolute coronal abundances of sulfur, calcium, and iron from Yohkoh-BCS flare spectra'. Astron. Astrophys., **348** (1999) 286–294

[206] J. T. Mariska. *The solar transition region*. Cambridge University Press (1992)

[207] G. D. Zanna, M. Landini and H. E. Mason. 'Spectroscopic diagnostics of stellar transition regions and coronae in the XUV: AU Mic in quiescence'. Astron. Astrophys., **385** (2002) 968

[208] C. Jordan. 'The Relative Intensities of CI Lines in the Solar EUV Spectrum'. Solar Physics, **2** (1967) 441–450

[209] T. Holstein. 'Imprisonment of resonance radiation in gases'. Phys. Rev., **72** (1947) 1212–1233

[210] V. M. Goldschmidt. 'Geochemische Verteilungsgestze der Elemente, IX'. Math. Naturw, **4** (1937) 99

[211] K. Lodders. 'Solar systemabundances and condensation temperatures of the elements'. Astrophys. J., **591** (2003) 1220–1247

[212] E. Anders and N. Grevesse. 'Abundances of the elements - Meteoritic and solar'. Geochim. Cosmochim. Acta, **53**(1) (1989) 197–214. doi:10.1016/0016-7037(89)90286-X

[213] N. Grevesse and A. J. Sauval. 'The Composition of the solar photosphere'. Advances in Space Research, **30** (2002) 3–11

[214] J. P. Meyer. 'Elemental abundances in active regions, flares and interplanetary medium'. Advances in Space Research, **13** (1993) 377–390

[215] U. Feldman. 'Elemental abundances in the upper solar atmosphere'. Physica Scripta, **46** (1992) 202

[216] U. Feldman and J. M. Laming. 'Elemental abundances in the upper atmospheres of the Sun and stars: update of observational results'. Phys. Scr., **61** (2000) 222–252

[217] U. Feldman and K. G. Widing. 'Spectroscopic measurements of coronal compositions'. Space Science Reviews, **130** (2007) 115–126

[218] J. M. Laming. 'A unified picture of the first ionisation potential and inverse first ionisation potential effects'. Astrophys. J., **614** (2004) 1063–1072

[219] P. R. Young, G. Del Zanna, H. E. Mason, K. Dere, E. Landi, M. Landini, G. A. Doschek, C. M. Brown, L. Culhane, L. K. Harra, T. Watanabe and H. Hara. 'EUV Emission Lines and Diagnostics Observed with Hinode/EIS'. Publ. Astron. Soc. Japan, **59** (2007) S857–S864

[220] A. C. Lanzafame, D. H. Brooks and J. Lang. 'ADAS analysis of the differential emission measure structure of the inner solar corona. II. A study of the "quiet Sun" inhomogeneities from SOHO CDS-NIS spectra'. Astron. Astrophys., **432** (2005) 1063–1079

[221] H. P. Warren. 'A Solar Minimum Irradiance Spectrum for Wavelengths below 1200 Å'. Astrophys. J. Suppl. Ser., **157** (2005) 147–173

[222] C. M. Brown, U. Feldman, J. F. Seely, C. M. Korendyke and H. Hara. 'Wavelengths and Intensities of Spectral Lines in the 171-211 and 245-291 Ranges from Five Solar Regions Recorded by the Extreme-Ultraviolet Imaging Spectrometer (EIS) on Hinode'. Astrophys. J. Suppl. Ser., **176** (2008) 511–535

[223] A. Fludra and J. Ireland. 'Radiative and magnetic properties of solar active regions. I. Global magnetic field and EUV line intensities'. Astron. Astrophys., **483** (2008) 609–621

[224] A. Fludra and H. Warren. 'Radiative and magnetic properties of solar active regions. II. Spatially resolved analysis of O V 62.97 nm transition region emission'. Astron. Astrophys., **523** (2010) A47